Order Number 9209708

A study of one-dimensional nonlinear hydromagnetic waves and collisionless shocks

Lyu, Ling-Hsiao, Ph.D.

University of Alaska Fairbanks, 1991

U·M·I
300 N. Zeeb Rd.
Ann Arbor, MI 48106

A STUDY OF ONE-DIMENSIONAL NONLINEAR HYDROMAGNETIC WAVES AND COLLISIONLESS SHOCKS

A

THESIS

Presented to the Faculty

of the University of Alaska Fairbanks

in Partial Fulfillment of the Requirements

for the Degree of

DOCTOR OF PHILOSOPHY

BY

Ling-Hsiao Lyu, B.S., M.S.

Fairbanks, Alaska

September 1991

A STUDY OF ONE-DIMENSIONAL NONLINEAR HYDROMAGNETIC WAVES AND COLLISIONLESS SHOCKS

By

Ling-Hsiao Lyu

RECOMMENDED:

S.-I. Akasofu

N. N. Biswas

J. V. Olson

D. W. Swift

Advisory Committee Chair J. R. Kan

Department Head J. L. Morack

APPROVED:

Dean, College of Natural Sciences P. Reichardt

Dean of the Graduate School L. Proenza

8/1/91

Date

Abstract

A variety of nonlinear hydromagnetic waves have been observed in the collisionless solar wind plasma. A comprehensive theoretical study of nonlinear hydromagnetic waves, including rotational discontinuities and collisionless shocks, is carried out in this thesis by means of both analytical solutions and numerical simulations. Nonlinear hydromagnetic waves are governed by the interplay of the dispersion process, the collisionless dissipation process and the nonlinear steepening process. The purpose of this thesis is to understand the nonlinear behavior of hydromagnetic waves in terms of these fundamental processes.

It is shown that the rotational discontinuity structures observed in the solar wind and at the magnetopause are nonlinear Alfvén wave solutions of the collisionless two-fluid plasma equations. In these nonlinear wave solutions, nonlinear steepening is self-consistently balanced by dispersion.

Collisionless viscous dissipation is the dominant dissipation in high Mach number shocks, which converts the flow energy into thermal energy. Hybrid simulations show that the collisionless viscous dissipation can result from the reflection and pitch-angle scattering of incoming ions flowing through the magnetic structures in the shock transition region. Collisionless dissipations in hydromagnetic shocks is governed by the magnetic structures in the shock transition region. The dissipation in turn can modify the wave structures and balance the nonlinear steepening. However, such delicate balance of the dispersion, dissipation, and nonlinear steepening has been observed to break down momentarily in high Mach number quasi-parallel shocks. This leads to the so-called cyclic shock front reformation seen in the hybrid simulations. The shock front reformation can be explained in terms of momentary off-balance

between the dispersion-dissipation on the one hand and the nonlinear steepening on the other hand. The off-balance occurs after a significant fraction of incoming ions are reflected. Each off-balance lasts a few ion gyro periods, which governs the shock front reformation time scale.

Table of Contents

List of Figures

List of Tables

Acknowledgments

I wish to thank Professor Joseph R. Kan, my Ph.D. thesis adviser. He taught me how to do research and how to write scientific papers. He encouraged me to follow my own thoughts and to develop my own ideas, which are essential to being creative and original. However, when I had no idea on how to solve a particular problem, he did point out the right direction for me to start. For instance, he suggested that I use a two-fluid plasma model to study non-MHD phenomena in the nonlinear hydromagnetic waves observed in the solar wind. By following his suggestion, I was able to start my thesis research in the right direction from the beginning.

My deepest appreciation also extends to members of my thesis advisory committee: Professors Dan Swift, John Olson, Syun Akasofu, and Niren Biswas. Their questions and comments resulted in the improved presentation of my thesis. Thanks are also due to Professor Dan Swift and Dr. Mark E. Mandt for the use of their hybrid simulation codes. Finally, I wish to thank Ms. Jeanne Hume for her skillful proof-reading of my thesis.

My acknowledgment would be incomplete without recording my heartfelt thanks to my former teachers who introduced me to the field of space physics. In particular, I wish to thank Ms. Tseng, my high school teacher of Earth Science, and Professor J. K. Chao, who was my Master thesis adviser at the National Central University in Taiwan. I learned my first lesson on collisionless shock from Professor Chao. He taught me that the essence of shock wave study is to understand how the nonlinear steepening is balanced by dispersion and dissipation in the shock transition region. This lesson has been the guideline of my research work in collisionless shocks.

Chapter 1

Introduction

By way of introduction, I want to say a few words about the definition of a *plasma* for the benefit of the general reader. A plasma, as discussed in this thesis, is not the colorless fluid in the blood but a low density ionized gas that exhibits collective behavior [e.g., *Krall and Trivelpiece*, 1973; *Chen*, 1974, 1984]. The plasma state is also called the fourth state of matter. More than 99 percent of the known universe is in the plasma state. Outer space, such as the earth's magnetosphere, interplanetary space, interstellar space, and intergalactic space, are all filled with plasma. The solar wind discussed in this thesis is the plasma which fills interplanetary space.

Like most space plasmas, the solar wind is considered a collisionless plasma, because the collision mean free path in the solar wind is much longer than the scale length of observed nonlinear waves in the solar wind, such as shocks, discontinuities, and Alfvénic fluctuations. The thickness and the structure of nonlinear waves (shocks or discontinuities) depend on the dissipation scale length and/or the dispersion scale length of the medium. In ordinary gas dynamics, the thickness of shock waves is governed by the collision mean free path, because dissipation, which results in increase of entropy across the shock, is due to particle collisions. In collisionless plasmas, the thickness of hydromagnetic shock waves and discontinuities is of the order of 1–100 ion inertial lengths c/ω_{pi}, where c is the speed of light and ω_{pi} is the ion plasma frequency. The scale length of the shock waves indicates that wave-particle interactions associated with nonlinear waves with scale lengths near ion inertial lengths can provide anomalous dissipation for the formation of collisionless shocks. Characteristics

of these nonlinear waves and their interactions with plasma particles will be studied in this thesis.

1.1 Reviews

In this section, we shall briefly review earlier studies and recent developments of one-dimensional nonlinear hydromagnetic waves in collisionless plasmas. Nonlinear constant-profile hydromagnetic waves have been studied extensively based on a magnetohydrodynamic (MHD) plasma model [e.g., *Kantrowitz and Petschek*, 1966], which is good for studying long-spatial-scale and low-frequency plasma phenomena. The MHD plasma model has successfully provided a theoretical explanation of certain observed features. For instance, collisionless shocks and other discontinuities approximately satisfy the jump conditions obtained from the MHD Rankine-Hugoniot (R-H) equations. [e.g., *Kantrowitz and Petschek*, 1966; *Chao*, 1970]. The MHD model can also predict the propagation of interplanetary shocks in the solar wind. However, the purpose of this study is not to predict the propagation of nonlinear waves and shocks in the large scale interplanetary space but to understand the dispersive and dissipative processes of these collisionless nonlinear waves. The dispersion and dissipation processes are governed by the fine structures in the transition region of collisionless shocks or discontinuities. The scale length of these fine structures ranges from 1–100 ion inertial lengths, which usually cannot be described by the MHD plasma model. Observed non-MHD phenomena in collisionless shocks and other nonlinear hydromagnetic waves will be discussed later in section 1.1.2. To help the discussion of the non-MHD properties, an introduction to MHD wave characteristics is given in the following section.

1.1.1 Magnetohydrodynamic Waves

The magnetohydrodynamic (MHD) plasma model is a simplified one-fluid plasma model under long-spatial-scale and low-frequency approximations. The pressure of the MHD plasma is assumed to be isotropic and follows an adiabatic process. A brief review on the MHD waves, shocks, and discontinuities is given in this section. Readers who are familiar with this subject can skip this section.

(A) *Linear Waves*

A dissipationless magnetohydrodynamic (MHD) plasma satisfies the frozen-in-flux condition, which can be written (in Gaussian units) as

$$c\mathbf{E} = \mathbf{V} \times \mathbf{B} \tag{1.1.1}$$

where c is the speed of light, $\mathbf{E}$ is the electric field, $\mathbf{B}$ is the magnetic field, and $\mathbf{V}$ is the flow velocity of the MHD plasma. Four fundamental linear wave modes can be obtained in the dissipationless MHD plasma. They are fast mode, Alfvén mode, slow mode and entropy waves [e.g., *Kantrowitz and Petschek*, 1966]. All of them are nondispersive waves; i.e., the wave phase speed (ω/k) is independent to the wave number (k). The phase speed of an entropy wave is equal to zero. The phase speed of the MHD Alfvén mode (sometimes called intermediate mode) is

$$V_{AX} = C_A \cos\theta \tag{1.1.2}$$

where θ is the wave propagation angle with respect to the ambient magnetic field,

$$C_A = B/\sqrt{4\pi\rho} \tag{1.1.3}$$

is the Alfvén speed, B is the magnitude of the ambient magnetic field, and ρ is the plasma density. The phase speed of the fast mode is

$$V_F = \left[(C_A^2 + C_S^2 + C_{AS}^2)/2\right]^{1/2} \tag{1.1.4}$$

and the phase speed of the slow mode is

$$V_{SL} = \left[(C_A^2 + C_S^2 - C_{AS}^2)/2\right]^{1/2} \tag{1.1.5}$$

where C_{AS} is defined by

$$C_{AS}^4 = (C_A^2 + C_S^2)^2 - 4C_A^2 C_S^2 \cos^2\theta \tag{1.1.6}$$

$$C_S = \sqrt{\gamma p/\rho} \tag{1.1.7}$$

is the sound speed which is obtained based on the assumption of an adiabatic process in the MHD plasma, p is the thermal pressure of the plasma, and $\gamma = 5/3$ for an adiabatic process. The fast mode and the slow mode are named based on the fact that for a given set of θ, C_A, and C_S the fast mode speed is always faster than the Alfvén mode and slow mode speeds, whereas the slow mode speed is always slower than the fast mode and Alfvén mode speeds. Characteristics of these MHD waves can be briefly summarized as follows. Alfvén mode is an incompressible wave in which the wave magnetic field is perpendicular to both wave vector **k** and the ambient magnetic field **B**. Fast mode and slow mode are compressible waves in which the wave magnetic field is perpendicular to the wave vector **k** but lying in the plane containing **k** and **B**. The variations of density and magnetic field magnitude are in phase for the fast mode but out of phase for the slow mode [e.g., Figure 6.3 in *Kantrowitz and Petschek*, 1966].

(B) *MHD Shocks and Discontinuities*

Jump conditions of one-dimensional (planar) MHD shocks and discontinuities can be obtained from the Rankine-Hugoniot (R-H) equations. The R-H equations consist of the time-independent Maxwell equations and equations for conservation of

mass, momentum and energy fluxes in a MHD plasma [e.g., *Kantrowitz and Petschek*, 1966; *Chao*, 1970]. MHD shocks and discontinuities obtained from the R-H equations include fast shocks, slow shocks, intermediate shocks, rotational discontinuities (RDs), tangential discontinuities (TDs), and contact discontinuities (CDs, also called entropy discontinuities) [*Kantrowitz and Petschek*, 1966; *Chao*, 1970]. The intermediate shocks consist of Alfvén shocks, fast-Alfvén shocks, fast-Alfvén-slow shocks, and Alfvén-slow shocks. These MHD shocks are named based on the changes of their normal flow speed across the shock. The characteristics of the upstream and the downstream normal flow speeds in the shock rest frame are summarized in Figure 1.1 and Table 1.1.

Figure 1.1 sketches Friedrichs' diagrams of MHD waves with (*a*) $C_A > C_S$ and (*b*) $C_A < C_S$. The Friedrichs' diagram displays the dependence of three MHD wave phase speeds (radial coordinate) on their angle of propagation with respect to the ambient magnetic field (the angular coordinate measured from the vertical axis). MHD shock waves can be found with upstream state in areas 1, 2, and 3 and with downstream state in areas 2, 3, and 4 as listed in Table 1.1. The brief notations of each shock wave solution listed in Table 1.1 are obtained based on its upstream and downstream states and the corresponding areas shown in Figure 1.1. The normal flow speed in the shock rest frame always decreases across the shock. As a result, plasma density always increases across the shock layer. The normal flow speed is zero across TDs and CDs, so that the density on the two sides of the TDs or CDs can be any value, as long as the total pressure is balanced across the discontinuity. The normal flow speed is constant and equal to the Alfvén mode speed across RDs. The RD is also characterized by equal density, equal thermal pressure, equal field magnitude across the discontinuity. According to the R-H equations, the tangential components

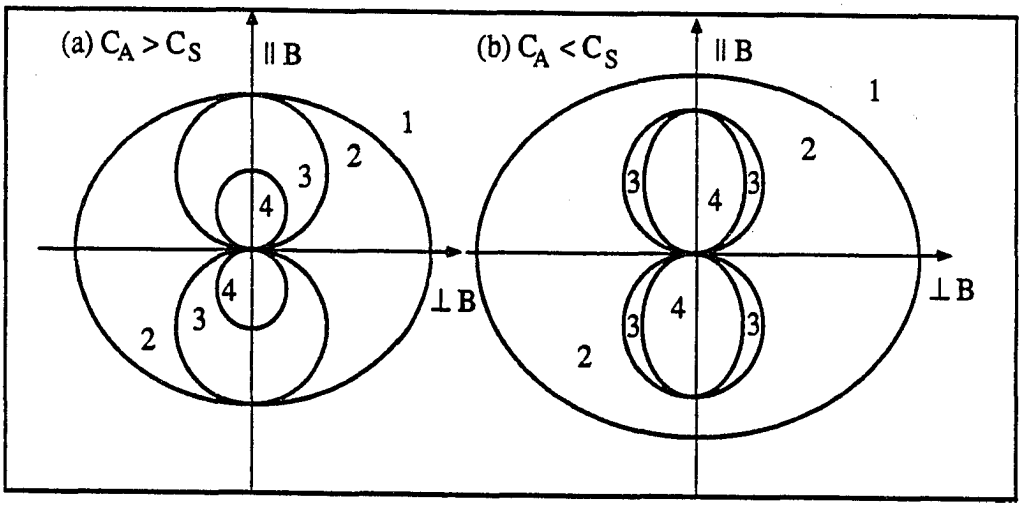

Figure 1.1 Friedrichs' diagrams of MHD waves with (*a*) $C_A > C_S$ and (*b*) $C_A < C_S$. The Friedrichs' diagram displays the dependence of three MHD wave phase speeds (radial coordinate) on their angle of propagation with respect to the ambient magnetic field (the angular coordinate measured from the vertical axis). MHD shock waves can be found with upstream state in areas 1, 2, and 3 and with downstream state in areas 2, 3, and 4 as listed in Table 1.1.

Table 1.1 Upstream and downstream normal flow speed of MHD shock waves

Shock Types	Brief Notations	Upstream Flow Speed	Downstream Flow Speed
Fast	$1 \rightarrow 2$	$V_{F1} < V_{N1}$	$V_{AX2} < V_{N2} < V_{F2}$
Fast-Alfvén	$1 \rightarrow 3$	$V_{F1} < V_{N1}$	$V_{SL2} < V_{N2} < V_{AX2}$
Fast-Alfvén-Slow	$1 \rightarrow 4$	$V_{F1} < V_{N1}$	$V_{N2} < V_{SL2}$
Alfvén	$2 \rightarrow 3$	$V_{AX1} < V_{N1} < V_{F1}$	$V_{SL2} < V_{N2} < V_{AX2}$
Alfvén-Slow	$2 \rightarrow 4$	$V_{AX1} < V_{N1} < V_{F1}$	$V_{N2} < V_{SL2}$
Slow	$3 \rightarrow 4$	$V_{SL1} < V_{N1} < V_{AX1}$	$V_{N2} < V_{SL2}$

V_{N1} is the normal upstream flow speed in the shock rest frame.
V_{N2} is the normal downstream flow speed in the shock rest frame.
Brief notations are obtained based on upstream and downstream states of each shock and the corresponding areas shown in Figure 1.1.

of the magnetic field in TDs or RDs can rotate to any angle across the discontinuity. The tangential component of magnetic field should be in the same direction across the fast and slow shocks, but rotates 180° across intermediate shocks. Namely, for shock waves, the downstream magnetic field must lie on the plane as defined by the normal vector and the upstream magnetic field. This is the coplanarity principle of shock waves [e.g., *Chao*, 1970].

1.1.2 Non-MHD Phenomena

If we consider a nonlinear wave profile as a series of small-amplitude step functions and each step is a small amplitude wave propagating in a medium which has been modified by previous waves (i.e., previous step functions), as suggested by *Kantrowitz and Petschek* [1966], then the magnetic field should remain coplanar over entire shock transition region for MHD fast shocks and slow shocks, whereas the density and total magnetic field should keep constant for MHD RDs and other nonlinear MHD Alfvénic fluctuations. The predicted structures of shock waves and RDs are consistent with MHD simulation results. However, the structures of the observed nonlinear waves and shocks in collisionless plasmas (such as the solar wind plasma) and in particle simulations are much more complicated than the structure of nonlinear waves and shocks obtained from the MHD simulations. For instance, a noncoplanar magnetic field is commonly observed in the transition region for both quasi-perpendicular and quasi-parallel fast shocks [e.g., *Goodrich and Scudder*, 1984, 1986; *Jones and Ellison*, 1987; *Gosling et al.*, 1988; *Friedman et al.*, 1990; *Kan and Swift*, 1983]. Variations in density and total magnetic field are also commonly observed in the transition region of RDs and Alfvénic fluctuations observed in the solar wind [e.g., *Unti et al.*, 1973; *Unti and Russell*, 1976; *Neugebauer et al.*, 1978; *Swift and Lee*, 1983; *Richter and*

Scholer, 1989]. Moreover, the angle of rotation in highly circularly polarized RDs appears to be limited to no more than 180° [*Sonnerup and Cahill*, 1968; *Swift and Lee*, 1983; *Lyu and Kan*, 1989*b*; *Neugebauer*, 1989], which is another feature that cannot be explained by MHD theory.

It may be noted that by including the effects of pressure anisotropy and non-zero heat flux across the shock or discontinuity, the jump condition of both shock waves and RDs can be modified [e.g., *Chao*, 1970; *Hudson*, 1971, 1973, 1974; *Lyu and Kan*, 1986]. However, those modifications can explain neither the noncoplanar magnetic field in the fast and slow shock transition region, nor the presence of upper limit of rotation angle (i.e., 180°) in highly circularly polarized RDs.

The causes of the non-MHD phenomena can be understood by examining the scale length of the nonlinear hydromagnetic waves. The observed thickness of collisionless fast shocks extends from a few ion inertial lengths for quasi-perpendicular fast shocks ($\theta_o \geq 45°$, where θ_o is the acute angle between upstream magnetic field and the shock normal direction) to a few tens of ion inertial lengths for quasi-parallel ($\theta_o < 45°$) fast shocks [e.g., *Greenstadt and Fredricks*, 1979; *Tsurutani and Rodriguez*, 1981; *Greenstadt*, 1985]. The thickness of RDs is about a few tens of ion thermal gyroradii (C_S/Ω_i) [*Martin et al.*, 1973; *Burlaga et al.*, 1977; *Lepping and Behannon*, 1986]. The scale length of Alfvénic fluctuations is ordinarily observed to be a few to a few tens of ion thermal gyroradii for Alfvénic fluctuations [*Unti et al.*, 1973; *Neugebauer*, 1975, 1976; *Unti and Russell*, 1976; *Neugebauer et al.*, 1978]. Since the ion thermal gyro radius ranges from the same as the ion inertial length in solar wind plasma, the scale length of observed shocks and RDs is of the order of 1–100 ion inertial lengths (c/ω_{pi}).

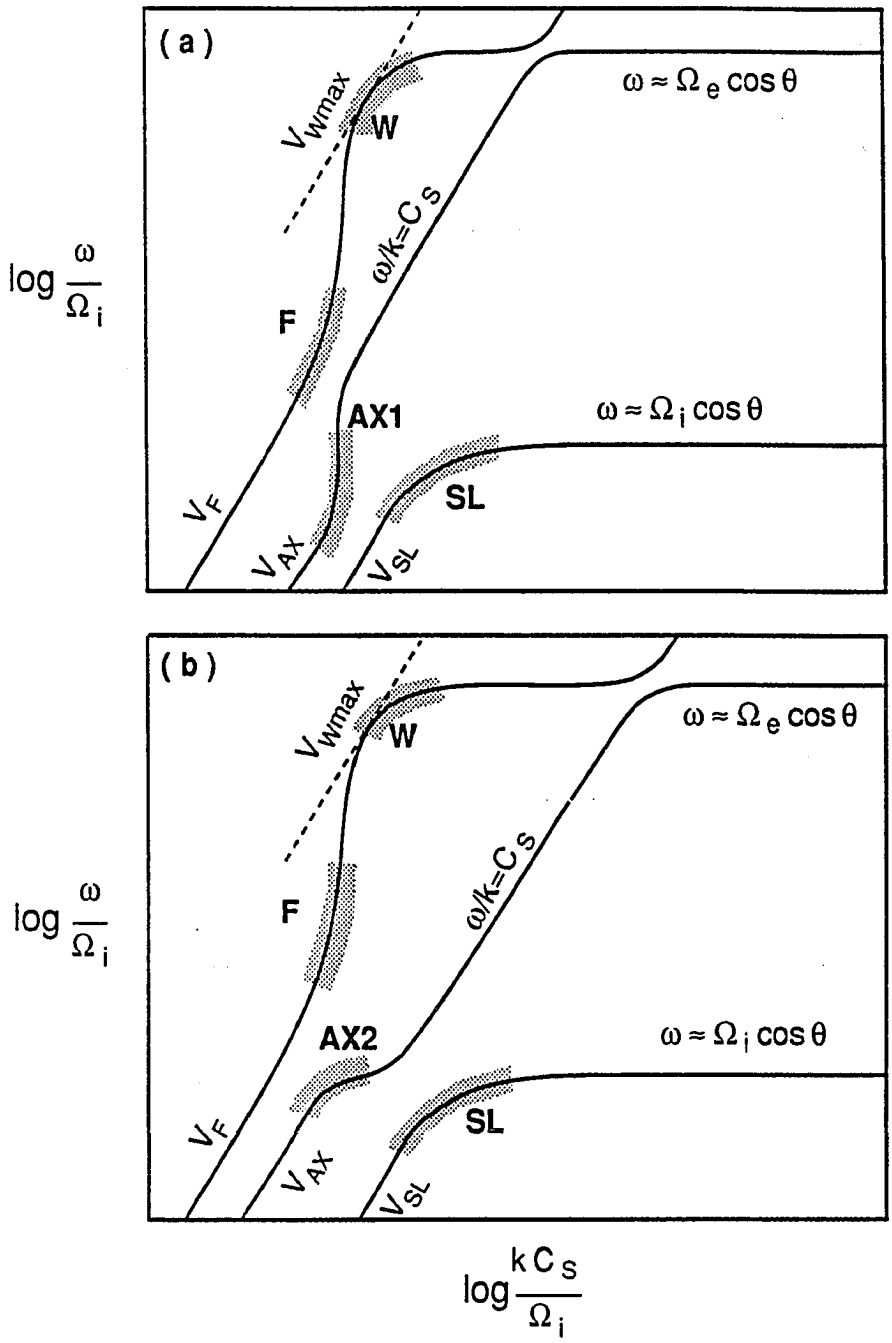

Figure 1.2 Sketches of two-fluid linear wave dispersion relation with oblique propagation under quasi-neutrality approximation, where (*a*) is for $C_S > V_{AX}$, and (*b*) is for $C_S < V_{AX}$ [adapted from *Stringer*, 1963; *Formisano and Kennel*, 1969].

When the spatial scale length is close to the ion inertial length, the MHD approximation (1.1.1) is no longer applicable. This can be seen from the dispersion relations obtained in a two-fluid (ion-fluid and electron-fluid) plasmas [e.g., *Stringer*, 1963; *Formisano and Kennel*, 1969]. Figure 1.2 sketches the two-fluid dispersion curves with oblique propagation under the quasi-neutrality approximation, where panel (*a*) is for $C_S > V_{AX}$ and panel (*b*) is for $C_S < V_{AX}$. The characteristic frequencies $\Omega_i = eB/m_ic$ and $\Omega_e = eB/m_ec$ are the gyro frequencies of ions and electrons, respectively. The two-fluid linear dispersion relation reduces to three fundamental MHD wave modes in the long wavelength limit. The plasma becomes a dispersive medium when the wavelength is shorter than about 100 times the ion inertial length ($c/\omega_{pi} \approx C_A/\Omega_i$, where $\omega_{pi} = \sqrt{4\pi ne^2/m_i}$ is the ion plasma frequency). The polarization of each wave mode becomes elliptical as the wavelength approaches to ion inertial length. Wave polarization is right-handed for the fast mode waves with wavelength in the shaded regions F or shorter, and for the Alfvén mode wave with wavelength in the shaded region $AX1$. Wave polarization is left-handed for the slow mode waves with wavelength in the shaded regions SL or shorter, and for the Alfvén mode wave with wavelength in the shaded region $AX2$. The elliptic polarization of these three modes indicates that all of them are compressible waves and all of them have a transverse magnetic field component. Thus, using the same step-function method, but based on two-fluid dispersion relation instead of an MHD approximation, noncoplanar magnetic fields are expected to be found in fast shock or slow shock transition region, and density (or total magnetic field) variations are expected to occur in Alfvénic fluctuations or the transition region of a rotational discontinuity.

Note that the wave dispersion shown in Figure 1.2 can be understood in the following way. Because the wave polarization at regions F and $AX1$ are right-handed,

the ion-fluid becomes less magnetized, leading to a decrease of ion mass loading on the magnetic field line [*Stringer*, 1963]. Thus, the wave speed increases with increasing k. An opposite dispersion occurs at regions $AX2$ and SL, because the wave polarization at these two shaded regions is left-handed. Likewise, the phase speed of the right hand polarized fast mode (whistler mode) wave slows down as the wavelength decreases toward the electron inertial length (c/ω_{pe}) at the shaded region W. It is important to note that the Alfvén mode (also called intermediate mode) waves will turn into electrostatic ion acoustic mode when phase speed approaches sound speed C_S [*Stringer*, 1963].

The linear dispersion relation of a two-fluid plasma shown in Figure 1.2 apparently can provide some non-MHD features, but lacking of the "nonlinearity," the two-fluid linear dispersion relation can never replace the MHD R-H jump conditions. Thus, one of the objectives of this study is to seek nonlinear hydromagnetic wave solutions in two-fluid plasmas analytically, so that both two-fluid dispersive effect and the nonlinear nature are fully included.

It may be noted that there are at least two types of mechanisms can lead to those observed non-MHD phenomena. One is the two-fluid dispersive effect near ion inertial length as discussed above, the other is the kinetic effect resulting from the interaction between large amplitude, short wavelength waves and individual particles. Various kinetic effects associated with the collisionless shock waves include: reflections of ions near the shock front, leakage of suprathermal ions and electrons from downstream of the shock front to the upstream side, and trapping of ions or electrons by large amplitude waves. The large amplitude, short wavelength waves, which lead to wave-particle interactions, may be generated by two-fluid dispersive effect or other type of kinetic wave-particle interactions. Thus, both two-fluid dispersive effects and kinetic

effects can directly or indirectly contribute to anomalous dissipation, which is essential to the formation of shock waves in collisionless plasma. In this study, we shall use quasi-parallel fast shocks as examples and use hybrid simulation (particle ions and fluid electrons) [e.g., *Kan and Swift*, 1983; *Mandt and Kan*, 1988; *Lyu and Kan*, 1990] as a tool to demonstrate the detail of nonlinear wave-particle interactions and to show the generation and preservation of large amplitude waves in a collisionless plasma.

1.1.3 Intermediate Shocks

The intermediate shock has been considered to be a nonevolutionary extraneous shock solution, for about 25 years [e.g., *Kantrowitz and Petschek*, 1966; *Liberman and Velikovich*, 1986], but was recently shown to be a real shock solution by theoretical arguments [*Kennel et al.*, 1989, 1990], and by both MHD [*Wu*, 1988*a*,*b*], and two-fluid simulations [*Lyu and Kan*, 1989*a*].

According to *Kantrowitz and Petschek* [1966], intermediate shocks are extraneous shock solutions because: (1) the MHD Alfvén mode is an incompressible wave, therefore a pure Alfvén wave cannot steepen to form a shock wave; (2) when MHD Alfvénic fluctuations pile-up into the shock layer, the coplanarity property of the shock will be destroyed [e.g., *Kantrowitz and Petschek*, 1966]; (3) intermediate shock solutions can be replaced by a fast shock and/or a slow shock combined with an RD of 180° [e.g., *Kantrowitz and Petschek*, 1966]. Therefore, in this analysis an intermediate shock would disintegrate into an RD and a fast shock and/or a slow shock within a short period of time. These predicted structures are consistent with simulation results obtained from MHD simulations, which are based on a conservation-law form and

the Lax-Wendroff equations [e.g., *Richtmyer and Morton*, 1967]. However, a non-disintegrating intermediate shock has been recently obtained from MHD simulations by *Wu* [1987, 1988*a*,*b*] when additional dissipation terms are employed.

The theoretical argument given by *Kennel et al.* [1989, 1990], which supports the existence of intermediate shocks, is based on the fact that the evolutionary arguments traditionally used against intermediate shocks may not be valid in the MHD system. This is because the evolutionary conditions are based on a hyperbolic system of differential equations in which all the wave modes propagate at different speeds and never couple to each other. The equations of classical MHD are not strictly hyperbolic. For linear waves, Alfvén mode can couple to fast mode or slow mode for parallel propagation, and couple to slow mode for perpendicular propagation. For nonlinear waves, coupling between Alfvén mode and fast mode (or slow mode) can also occur for oblique propagation. According to dissipative MHD simulations obtained from *Wu* [1987, 1988*a*,*b*], oblique nonlinear Alfvén waves can couple to fast mode or slow mode waves, and become a compressible wave as dissipation terms are included. For nonlinear waves in two-fluid plasmas, the Alfvén mode can couple to fast mode or slow mode even without dissipation, which will be discussed later in Chapter 2. Moreover, without wave-mode coupling, the Alfvén mode alone in the two-fluid plasma becomes a compressible wave when wavelength approaches the ion inertial length. The compressive Alfvén waves in the two-fluid plasma can be found in both linear-wave (as discussed in Figure 1.2) and nonlinear-wave (to be discussed later in Chapter 2) models. Thus, the intermediate shock may not disintegrate into an RD and a fast shock and/or a slow shock if (1) the wave-mode coupling is strong enough to tie them together, or (2) the shock wave is weak enough so that the compressibility in the two-fluid Alfvén mode (due to finite ion inertial length) alone can provide the

necessary compression in the shock transition region. The results of simulation studies of the intermediate shocks will be given in Chapter 4.

Figure 1.3 shows solution space and velocity contrast across intermediate shocks in Friedrichs' diagram format for a $\beta = 0.1$ plasma. Shock normal angle, which is the angle between the shock normal and the upstream magnetic field, is denoted by θ. Notations $1 \rightarrow 3$, $1 \rightarrow 4$, $2 \rightarrow 3$ and $2 \rightarrow 4$ shocks are the same as defined in Table 1.1. The contours shown in the diagrams (*b*) and (*d*) are measured by the ratio of downstream normal flow speed to upstream normal flow speed. These diagrams are reproduced from Figures 6 and 7 of *Kennel et al.* [1989]. Figure 1.3 shows that the solution space of $1 \rightarrow 3$ shocks and $2 \rightarrow 3$ shocks vary continuously to form a family. Solutions of $1 \rightarrow 4$ shock and $2 \rightarrow 4$ shock in Figure 1.3 also vary continuously to form a family.

There is another way to see the relationship between these shock wave families. Figure 1.4 shows velocity jump across various types of MHD shocks for $\beta = 0.1$, θ_{BN} = (*a*) 0°, (*b*) 20° and (*c*) 45°, where V_{N1} and V_{N2} are the upstream and downstream normal flow speed in the shock rest frame, respectively. θ_{BN} is the shock normal angle. Two curves of solutions can be found in each panel of Figure 1.3. Each of them can be seen as one family of shocks. Thus, intermediate shocks and slow shocks belong to one family of shocks, whereas the fast shocks are another family of shocks by themselves. The family of fast shocks becomes connected to the intermediate shocks at parallel propagation. Fast-Alfvén shocks and fast-Alfvén-slow shocks no longer exist when the two curves of shock families separate far enough at oblique propagation. According to the solution space diagrams shown in Figure 1.4, we can conclude that Alfvén-slow shock is always stronger (i.e., with greater density jump) than the Alfvén shock with the same upstream Mach number. Likewise, for

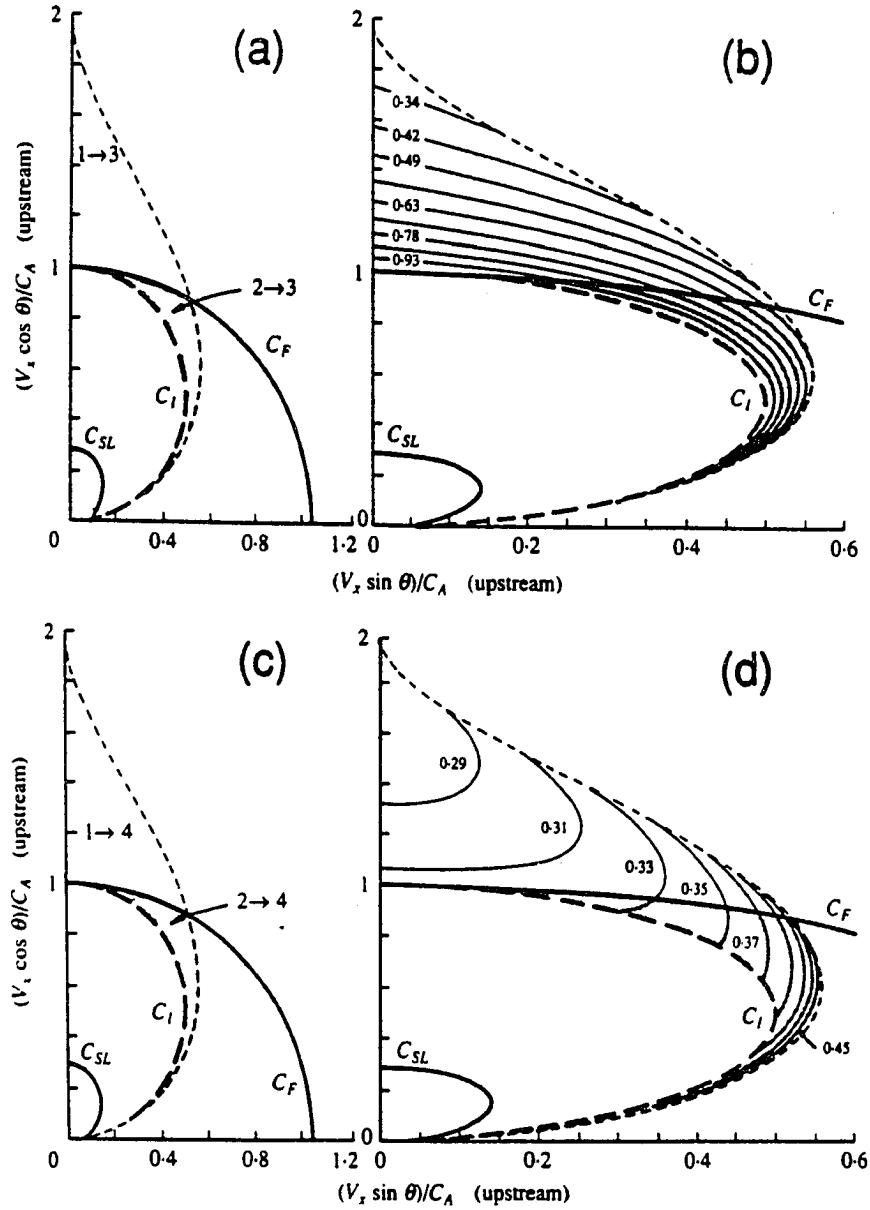

Figure 1.3 Solution space and velocity contrast across the intermediate shock in Friedrichs' diagram format for a $\beta = 0.1$ plasma. These diagrams are reproduced from *Kennel et al.* [1989], where diagrams (*b*) and (*d*) are plotted in an expended scale of diagrams (*a*) and (*c*), respectively. θ denotes the shock normal angle. Notations C_F, C_I, and C_{SL} are the same as notations V_F, V_{AX}, and V_{SL} used in this chapter. Notations $1 \rightarrow 3$, $1 \rightarrow 4$, $2 \rightarrow 3$ and $2 \rightarrow 4$ are the same as defined in Table 1.1. Thus, the solution space shown in diagrams (*a*) and (*b*) denotes a smooth transition from fast-Alfvén shock to Alfvén shock. The solution space shown in diagrams (*c*) and (*d*) denotes a smooth transition from fast-Alfvén-slow shock to Alfvén-slow shock.

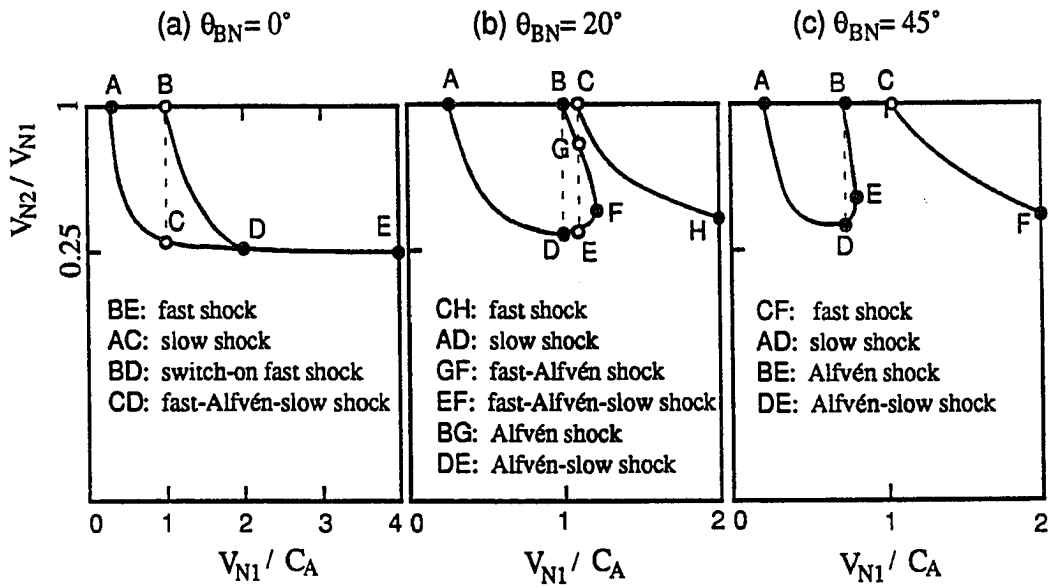

Figure 1.4 Velocity jump across various types of MHD shocks for $\beta = 0.1$, $\theta_{BN} =$ (*a*) 0°, (*b*) 20° and (*c*) 45°, where V_{N1} and V_{N2} are the upstream and downstream normal flow speed in the shock rest frame, respectively.

a given upstream Mach number, the fast-Alfvén-slow shock is always the strongest shock, and fast shock is always the weakest of the three shock wave solutions (i.e., the fast, fast-Alfvén, fast-Alfvén-slow shocks). It may be noted that the connection between the fast-Alfvén shock ($1 \rightarrow 3$ shock) and the fast-Alfvén-slow shock ($1 \rightarrow 4$) can also be seen from Figure 1.3. Namely, the contours in panels (*b*) and (*d*) should be continuously connected at the dashed curves for these two shocks.

It can be seen from Figure 1.4 that the switch-off shock at point D in panels (*b*) and (*c*) will become a singular solution if intermediate shock solutions were ruled out from the solution space. Without intermediate shock solutions, the switch-on shock will also become a singular solution, because a small amplitude fast mode perturbation on the upstream side may lead to a 180° rotation of the tangential magnetic field across the shock. By including intermediate shocks as part of legitimate shock wave

solutions, we can easily overcome the evolution problem of singular shock solutions of switch-off shocks and switch-on shocks as discussed by *Liberman and Velikovich* [1986].

1.2 Objectives of This Thesis Work

The purpose of this thesis is to study and to understand the non-MHD behavior of one-dimensional nonlinear hydromagnetic waves in collisionless plasmas. Particularly, this thesis work will focus on some outstanding problems in current research. This thesis consists of three parts, which will be presented in Chapters 2, 3 and 4.

Chapter 2 establishes a theoretical framework for nonlinear nondissipative hydromagnetic waves with scale length less than $\sim$ 100 ion inertial lengths [*Lyu and Kan*, 1989*b*]. Results obtained in Chapter 2 are essential in explaining the observed structures of rotational discontinuities and Alfvénic fluctuations in the collisionless solar wind and magnetospheric plasmas.

Chapter 3 is a simulation study of quasi-parallel fast shocks in collisionless plasmas. The purpose of this study is to understand the ion dynamics in the shock transition region and to identify the dissipation process in the collisionless quasi-parallel shocks. The hybrid code (particle ions and fluid electrons) simulation model [*Swift and Lee*, 1983; *Kan and Swift*, 1983; *Mandt and Kan*, 1988; *Lyu and Kan*, 1990] will be used in this study. An improved multiple-labeling diagnostic will be introduced in Chapter 3, which allows us to solve several controversial issues in current quasi-parallel shocks research, including (1) the identification of the source of upstream backstreaming suprathermal ions [e.g., *Thomsen*, 1985] and (2) the understanding of the physical process of various types of ion reflection events observed in high Mach number quasi-parallel shocks [e.g., *Gosling et al.*, 1982; *Gosling et al.*, 1989*b*]. A

comprehensive review of these controversial issues will be given in Chapter 3. A gyro-reflection model will be proposed in Chapter 3 to explain the various types of ion reflection events observed in high Mach number quasi-parallel shocks. Three critical Mach numbers for collisionless quasi-parallel shocks are proposed to synthesize the simulation results obtained in Chapter 3. The proposed critical Mach number model will improve the previous theoretical model on this subject [e.g., *Kennel et al.*, 1985].

Chapter 4 is a simulation study of rotational discontinuities, switch-off slow shocks, and intermediate shocks in collisionless plasmas. According to Figures 1.4*b* and 1.4*c*, one end of the intermediate shock solution curve connects to the rotational discontinuity solution while the other end of the solution curve connects to the switch-off shock solution. The purpose of putting the three different subjects in the same chapter is to show the similarities and systematic changes among these low Mach number nonlinear hydromagnetic waves. The purpose of studying rotational discontinuities is twofold. One is to confirm the theoretical prediction of the structures of rotational discontinuities given in Chapter 2, especially for rotational discontinuities with upstream $C_S < V_{AX}$. The other is to show how to generate an S-shaped RD without large amplitude wavetrains on the upstream or downstream side. The objective of studying the switch-off shock is to show that under appropriate initial conditions a subcritical switch-off shock can be formed without large-amplitude downstream wavetrain. A review of previous studies of S-shaped RDs and switch-off shock structures will be given in Chapter 4. Intermediate shocks studied in Chapter 4 include quasi-perpendicular Alfvén shock, Alfvén-slow shock, and quasi-parallel Alfvén shock, Alfvén-slow shock, fast-Alfvén shock, fast-Alfvén-slow shock. The purpose

of the study given in Chapter 4 is to explore the issue of possible existence of intermediate shocks in collisionless plasmas. The systematic changes among intermediate shocks, switch-off shocks, and rotational discontinuities will be demonstrated. The results of the intermediate shock studies obtained in Chapter 4 indicate that Alfvén shocks will not turn into rotational discontinuities, but some rotational structures may turn into Alfvén shocks, which is in contrast to the results obtained in a previous simulation study by *Lee et al.* [1989*a*]. The simulation results will be compared with several observed events in the solar wind and at planetary magnetopause.

Chapter 2

Nonlinear, Isentropic, Hydromagnetic Waves in Two-Fluid Plasmas

2.1 Introduction

Nonlinear, nondissipative, hydromagnetic wave solutions are obtained analytically in this chapter based on a two-fluid plasma model (ions and electrons). The two-fluid plasma model is the simplest model that contains non-MHD effects. The main difference between the MHD plasma model and the two-fluid plasma model is in the wave dispersion. The wave dispersion effects near ion inertial lengths are not included in the MHD plasma model but are fully included in the two-fluid plasma model, as discussed in Figure 1.2.

Nonlinear waves in a dispersive but nondissipative medium consist of solitons and wavetrains or wave-packets. Without dissipation, these nonlinear waves cannot turn into shocks. They are isentropic, nonlinear waves. A soliton is a solitary wave, which can travel at a constant speed and maintain a constant waveform. Solitons are formed when nonlinear steepening is balanced by dispersion. This is first demonstrated by the well-known Korteweg-deVries (KdV) equation [*Korteweg and deVries*, 1895].

Nonlinear, nondissipative, hydromagnetic wave solutions in two-fluid plasmas shown in this chapter consist of constant-profile solutions [*Lyu and Kan*, 1989*b*] and quasi-stationary nonlinear wave solutions, which are obtained from a classical pseudopotential method [e.g., *Lyu and Kan*, 1989*b*] and a multiple pseudopotential method, respectively. The improved multiple pseudopotential method is introduced in this chapter for the first time. Quasi-stationary, nonlinear wave solutions obtained from

the multiple pseudopotential method will allow us to explain the observed S-shaped rotational structures in the solar wind [*Neugebauer*, 1989; *Neugebauer and Buti*, 1990] without adding dissipation terms in our formulation. The multiple pseudopotential method will be introduced in Section 2.2 using the KdV equation. The KdV equation can be solved analytically based upon a simple model of one-dimensional fictitious particle motion in a pseudopotential well, which will pave the way for the more complicated two-dimensional fictitious particle motions on a pseudopotential surface to be discussed in Section 2.4 for the study of nonlinear waves in two-fluid plasmas.

The outline of this chapter is as follows. A brief review of the KdV equation, the classical pseudopotential method, and an introduction to the multiple pseudopotential method will be presented in Section 2.2. Two methods of solutions for nonlinear waves will be reviewed in Section 2.3. Formulation and analytic solutions of nonlinear hydromagnetic waves containing the full dispersion of the two-fluid plasmas will be presented in Section 2.4. These nonlinear wave solutions will be compared with available observations in Section 2.5.

2.2 Nonlinear Waves in a Korteweg-deVries Dispersive Medium

The Korteweg-deVries equation can be written as

$$\left\{\frac{\partial}{\partial t}+(C_o+V)\frac{\partial}{\partial x}+\xi\frac{\partial^3}{\partial x^2}\right\}V(x,t)=0 \qquad (2.2.1)$$

The linear dispersion relation associated with the KdV equation (2.2.1) is

$$\omega/k = C_o - \xi k^2 \qquad (2.2.2)$$

where ω is the wave angular frequency, k is the wave number, and C_o is the phase speed in the long wavelength limit. The dispersive characteristics of a KdV medium

depend on the sign of ξ. For $\xi > 0$, phase speed ω/k decreases with increasing k. For $\xi < 0$, phase speed increases with increasing k.

We look for constant profile nonlinear wave solution that propagates at a constant speed V_o in the lab frame, where the lab frame is defined as the frame where unperturbed medium is motionless. The nonlinear wave solution can be written as $V(x,t) = V(x - V_o t)$. Let $X = x - V_o t$, then (2.2.1) becomes

$$\left\{(-V_o + C_o + V)\frac{d}{dX} + \xi\frac{d^3}{dX^3}\right\} V(X) = 0 \,. \tag{2.2.3}$$

(2.2.3) can be integrated once, which yields

$$\frac{d^2V}{dX^2} = (V_o - C_o)\frac{V}{\xi} - \frac{V^2}{2\xi} \tag{2.2.4}$$

where we have taken the integration constant to be zero. Note that (2.2.4) has the same mathematical form as an equation of motion $m\ddot{x} = F(x) = -\nabla\mathcal{V}(x)$, where $\mathcal{V}(x)$ is a potential field. We can use the pseudopotential method [e.g., *Nicholson*, 1983] to solve (2.2.4). (2.2.4) can be rewritten as

$$\frac{d^2V}{dX^2} = -\frac{d\Psi(V)}{dV} \tag{2.2.5}$$

where

$$\Psi(V) = \frac{V^3}{6\xi} - (V_o - C_o)\frac{V^2}{2\xi} \tag{2.2.6}$$

is a pseudopotential. Equation (2.2.5) can be viewed as the "equation of motion" of a "fictitious particle" moving under the influence of a one-dimensional pseudopotential

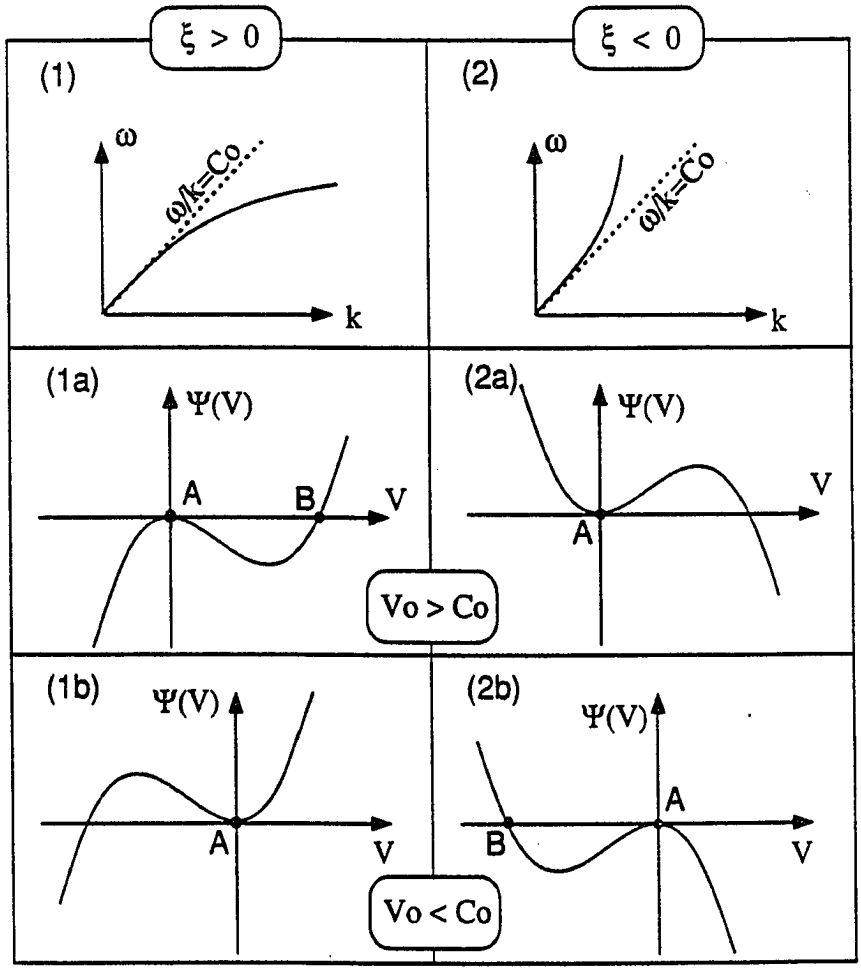

Figure 2.1 Sketches of linear dispersion curves and pseudopotentials of nonlinear constant-profile waves in KdV dispersive media.

field $\Psi(V)$. As a result, X, V, dV/dX, and d^2V/dX^2 will be denoted as the pseudo-time, pseudocoordinates, pseudovelocity, and pseudoacceleration, respectively, in the following discussion.

Figure 2.1 sketches dispersion curves and pseudopotentials for various types of KdV dispersive media, where the dispersion curves are for (*1*) positive-ξ and (*2*) negative-ξ KdV dispersive media. The pseudopotentials $\Psi(V)$ shown in the lower four panels are for (*1a*) $\xi > 0$, $V_o > C_o$; (*1b*) $\xi > 0$, $V_o < C_o$; (*2a*) $\xi < 0$, $V_o > C_o$;

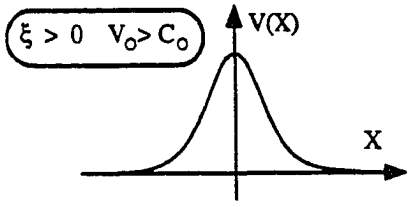

Figure 2.2 $V(x)$ profile of a compression soliton which can be obtained from pseudopotential field shown in panel (*1a*) of Figure 2.1.

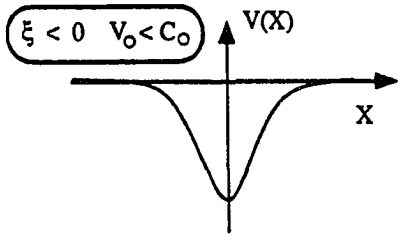

Figure 2.3 $V(x)$ profile of a rarefaction soliton which can be obtained from pseudopotential field shown in panel (*2b*) of Figure 2.1.

and (*2b*) $\xi < 0$, $V_o < C_o$. The motion of a fictitious particle under the influence of a pseudopotential as shown in panels (*1a*) and (*2b*) can result in soliton solutions. In order for the solutions to (2.2.3) vanish at infinity, $\partial\Psi/\partial V$ must be a local maximum. In the case of panel (*1a*), a fictitious particle can leave point A (where $V = 0$) by an infinitesimal displacement toward positive-V, falling once though the well to reach point B and then falling back through the well to return to point A. The $V(X)$ profile of this type of motion is sketched in Figure 2.2, which is a compression soliton solution. For the case shown in panel (*2b*) of Figure 2.1, the fictitious particle can leave point A by an infinitesimal displacement toward negative-V direction, falling once though the well to reach point B and then falling back through the well to return A. The $V(X)$ profile of this type of motion is sketched in Figure 2.3, which is a rarefaction soliton solution.

Note that to determined whether a soliton solution is a compression or rarefaction soliton, one can use the standard continuity equation to obtain density profiles based on the information of $V(X)$. It is easy to show that the spatial variations of density and velocity in the lab frame are in phase. Thus, the soliton solution in Figure 2.2 is a compression soliton, but a rarefaction soliton in Figure 2.3. No soliton solutions can be found when the pseudopotential Ψ has a local-minimum at $V = 0$ as the cases shown in panels (*1b*) and (*2a*) of Figure 2.1.

The soliton solutions in a KdV dispersive medium can also be obtained analytically by the following procedure. Multiplying (2.2.4) by dV/dX and integrating once, one obtains,

$$\frac{1}{2}\left(\frac{dV}{dX}\right)^2 = (V_o - C_o)\frac{V^2}{2\xi} - \frac{V^3}{6\xi} \tag{2.2.7}$$

where we have chosen the constant of integration to be zero because we are looking for the soliton solutions where $dV/dX = 0$ when $V = 0$ as shown in Figures 2.2 and 2.3. Then,

$$\frac{dV}{dX} = \left[(V_o - C_o)\frac{V^2}{\xi} - \frac{V^3}{3\xi}\right]^{1/2} . \tag{2.2.8}$$

(2.2.8) can be integrate once, to give

$$V(X) = 3(V_o - C_o)\mathrm{sech}^2\left[\sqrt{\frac{V_o - C_o}{4\xi}}X\right] . \tag{2.2.9}$$

Substituting $X = x - V_o t$ into (2.2.9), yields

$$V(x,t) = 3(V_o - C_o)\mathrm{sech}^2\left[\sqrt{\frac{V_o - C_o}{4\xi}}(x - V_o t)\right] . \tag{2.2.10}$$

To ensure the variable inside the square root in (2.2.9) and (2.2.10) is a positive value, the soliton solution can exist only if $(V_o - C_o)/\xi > 0$. This result is consistent with the

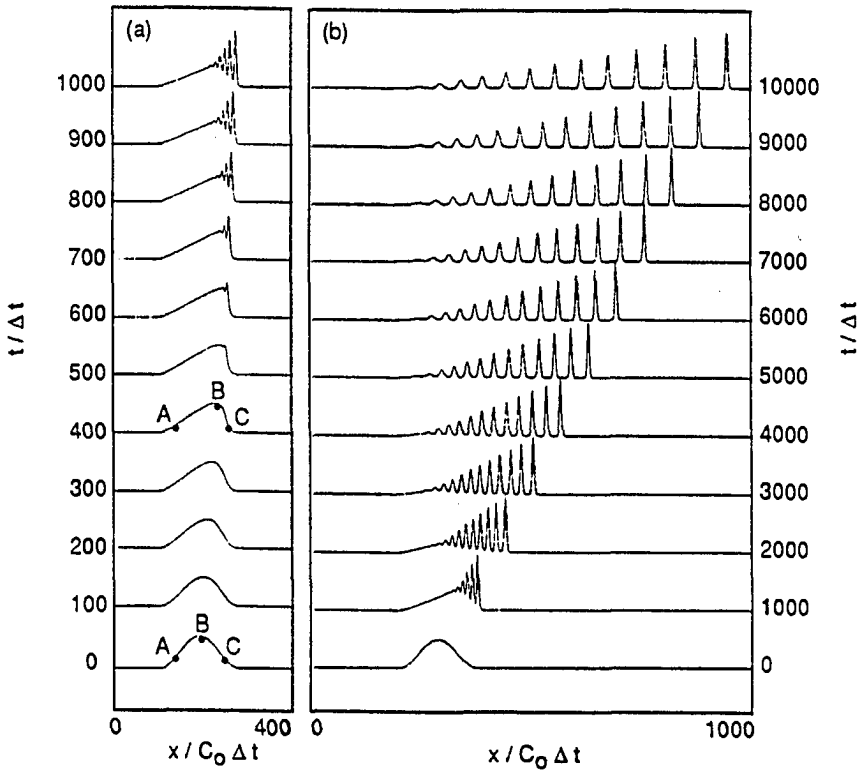

Figure 2.4 Evolution of a compression disturbance in a positive-ξ KdV dispersion medium.

result obtained from the pseudopotential method discussed above, since both panels (*1a*) and (*2b*) in Figure 2.1 are for $(V_o - C_o)/\xi > 0$.

To learn the effect of temporal variations on the nonlinear wave characteristics, numerical simulations are carried out to study the evolution of various density disturbances in different KdV dispersive media. Simulation results including solitons and wavetrains or wave-packets are given in Figures 2.4–2.7. Figure 2.4 shows evolution of a compression disturbance in a positive-ξ KdV dispersion medium. Figure 2.5 shows evolution of a rarefaction disturbance in a positive-ξ KdV dispersion medium. Figure 2.6 shows evolution of a compression disturbance in a negative-ξ KdV dispersion medium. Figure 2.7 shows evolution of a rarefaction disturbance in a negative-ξ

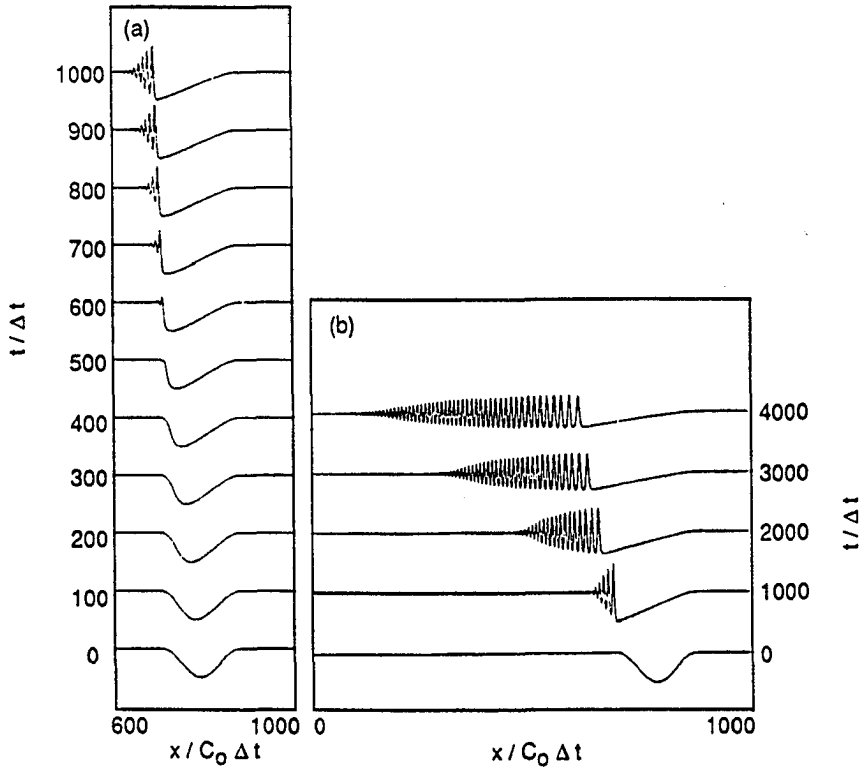

Figure 2.5 Evolution of a rarefaction disturbance in a positive-ξ KdV dispersion medium.

KdV dispersion medium. Each of these figures consists of two panels, where panel (*a*) shows the nonlinear steepening process at initial stage, and panel (*b*) shows the long-term evolution process as a result of balance between nonlinear steepening and dispersion effects. From panel (*a*) of each figure, we can see that the nonlinear steepening occurs at the upstream side of the initial profile for a compression disturbance, but at the downstream side of the initial profile for a rarefaction disturbance. A series of compressional solitons can be found in Figure 2.4*b*. A series of rarefaction solitons can be found in Figures 2.7*b*. No solitons but finite-extent wavetrains can be formed in Figures 2.5 and 2.6. For convenience, we choose our simulation frame moving at a constant speed $C_o\hat{\mathbf{x}}$ with respect to the lab frame (where the lab frame is defined as

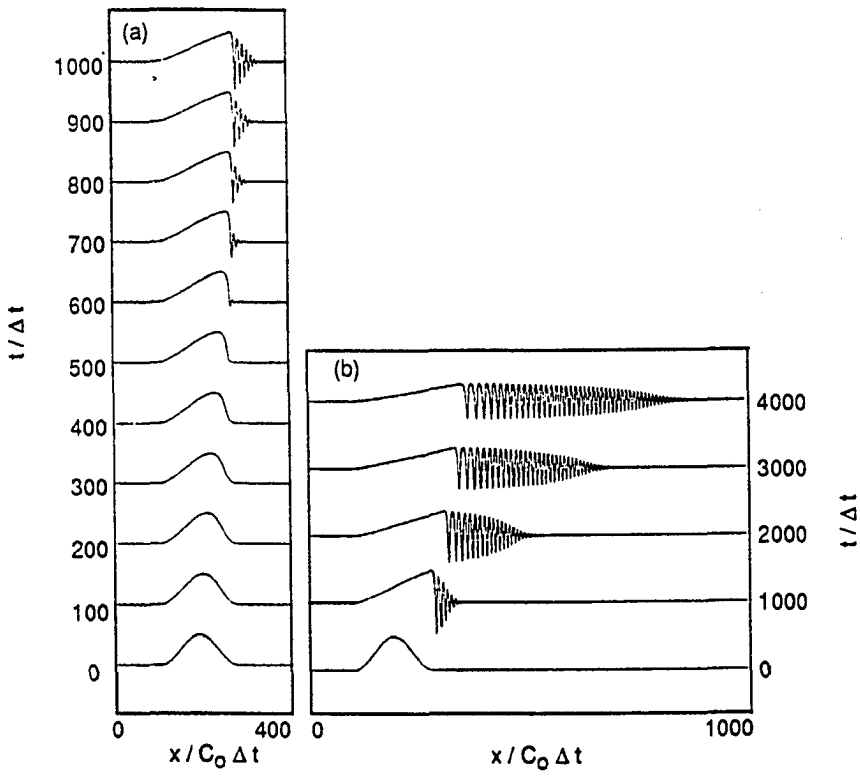

Figure 2.6 Evolution of a compression disturbance in a negative-ξ KdV dispersion medium.

the frame where unperturbed medium is motionless). Thus, wave propagation velocity in the lab frame ($V_o\hat{\mathbf{x}}$) can be obtained by

$$V_o\hat{\mathbf{x}} = V_{\text{simu}}\hat{\mathbf{x}} + C_o\hat{\mathbf{x}} \tag{2.2.11}$$

where $V_{\text{simu}}\hat{\mathbf{x}}$ is the wave propagation velocity observed in the simulation frame. From (2.2.11), we can conclude that the propagation speed of the nonlinear structures in Figures 2.4 and 2.6 is greater than C_o, whereas the propagation speed of the nonlinear structures in Figures 2.5 and 2.7 is less than C_o. Note that using numerical simulation, the evolution of nonlinear waves in a positive-ξ KdV dispersive medium has been studied by *Zabusky and Kruskal* [1965], *Berezin and Karpman* [1967], and *Berezin* [1968]. Their results are similar to the one shown in Figures 2.4 and 2.5.

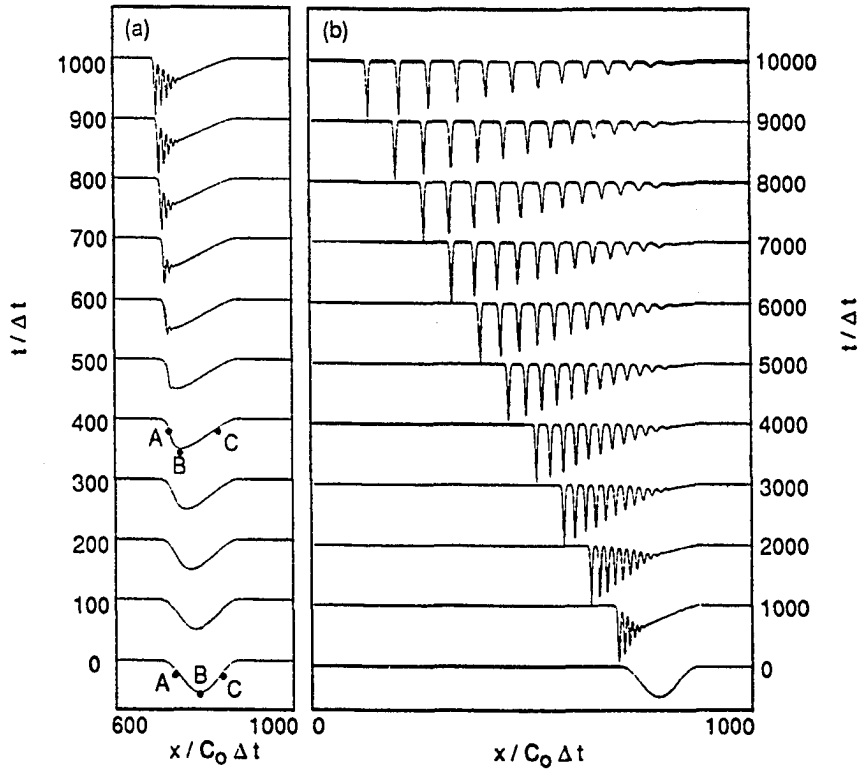

Figure 2.7 Evolution of a rarefaction disturbance in a negative-ξ KdV dispersion medium.

Figure 2.8 summarizes the evolution of nonlinear waves based on the simulation results shown in Figures 2.4–2.7. The evolution of nonlinear waves depends on the sign of ξ and the type of initial disturbance. Note that by assuming the time derivative exactly equal to zero and a uniform boundary condition, only two types of nonlinear wave solutions can be obtained as shown in Figures 2.2 and 2.3. The results shown in Figure 2.8 represent four basic types of KdV nonlinear wave solutions. The finite-extent wavetrains (or wave-packets) solutions shown in panels (*1b*) and (*2a*) of Figure 2.8 are not constant-profile nonlinear waves, because the shapes of the wave-packets vary slowly with time. Since the classical pseudopotential method

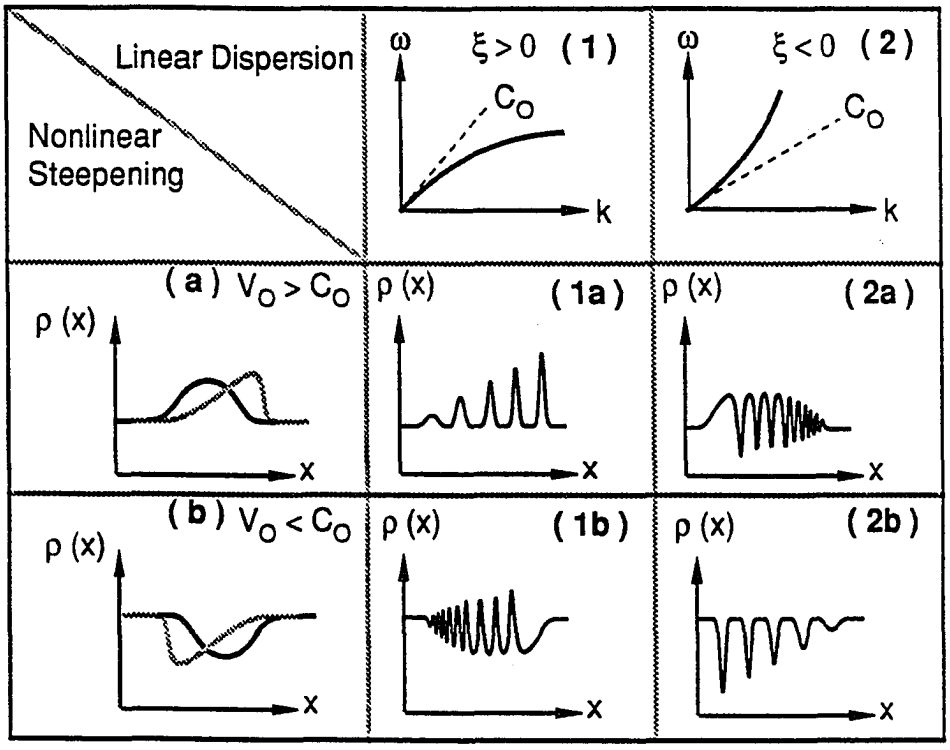

Figure 2.8 Summary of the initial condition dependence and ξ dependence on the nonlinear wave structures.

can only provide exactly constant-profile nonlinear wave solutions, an improved pseudopotential method will be introduced below to overcome the difficulty of solving quasi-stationary nonlinear wave problems analytically.

Time dependent nonlinear wave problems with $\partial/\partial t \ll V\,\partial/\partial x$ in the average wave moving frame can be treated approximately by a *multiple pseudopotential method*. A series of pseudopotentials with different values of V_o will be used in the multiple pseudopotential method. A fictitious particle is allowed to move through the series of pseudopotentials as pseudotime goes on. Note that different pseudotime represents different location in the real space. The different V_o of each pseudopotential denotes that the associated nonlinear wave is propagated at different speed V_o. To avoid the very transient state (i.e., $\partial/\partial t \geq V\,\partial/\partial x$ in the average wave moving frame)

due to nonlinear wave-wave interactions as a fast moving nonlinear wave catches on a slow moving nonlinear wave the fictitious particle is designed to move successively from large-V_o pseudopotentials to small-V_o pseudopotentials in the multiple pseudopotential system. As a result, fast moving waves will always propagate ahead of slow moving waves in the nonlinear wave solution obtained from this method. Furthermore, to ensure that $\partial/\partial t \ll V\,\partial/\partial x$ in the average wave moving frame, the difference between V_o of two successive pseudopotentials in the multiple pseudopotential system has to be much smaller than the average V_o of these two pseudopotentials. The condition of $\partial/\partial t \ll V\,\partial/\partial x$ in the average wave moving frame indicates that all the nonlinear wave solutions obtained from the multiple pseudopotential method are quasi-stationary. Note that when a nonlinear wave is at very transient state, such as when a fast moving nonlinear wave overtakes a slow moving wave, the change of the associated multiple pseudopotential system will be difficult to predict analytically due to the presence of nonlinear wave reflection and nonlinear wave interference. The multiple pseudopotential method is useless when the multiple pseudopotential system is unpredictable. Thus, the multiple pseudopotential method is only applicable to quasi-stationary nonlinear wave problems.

We shall use the simulation results shown in Figures 2.4–2.7 to demonstrate how to obtain quasi-stationary nonlinear wave solutions using the multiple pseudopotential method. It will be shown that the four basic types of KdV nonlinear wave solutions can be obtained analytically from the four types of KdV pseudopotential structures shown in Figure 2.1.

The series of solitons shown in Figure 2.8(*1a*) can be described by a fictitious particle moving through a series of pseudopotentials in the form similar to the one shown in Figure 2.1(*1a*). Figure 2.9 shows an example of such a multiple-pseudopotential

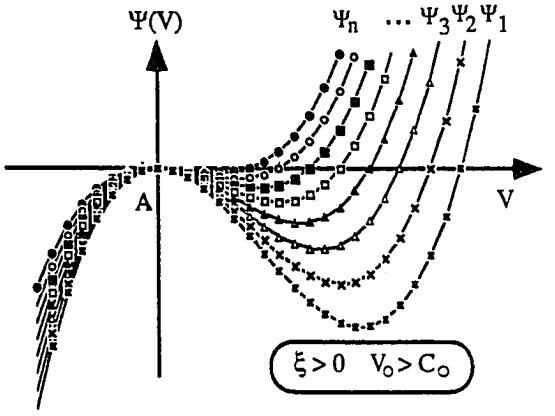

Figure 2.9 Multiple-pseudopotential system for compression soliton-train solution, in which the V_o of Ψ_1 is larger than the V_o of Ψ_2, ..., and so on. A fictitious particle moving successively from Ψ_1 to Ψ_2, to Ψ_3, ..., to Ψ_n can result in a series of solitons as shown in Figure 2.8(*1a*)

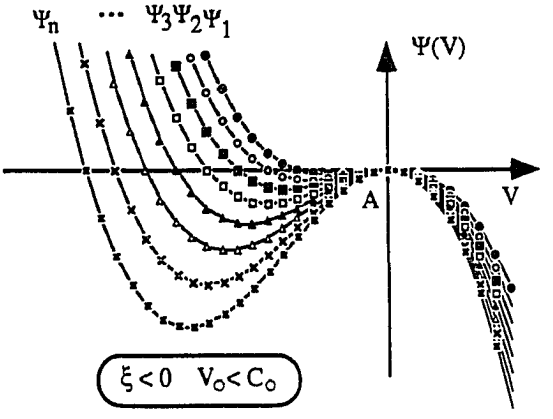

Figure 2.10 Multiple-pseudopotential system for rarefaction soliton-train solution. The V_o of each pseudopotential decreases successively, from Ψ_1 to Ψ_n. A fictitious particle moving successively from Ψ_1 to Ψ_n can result in a series of solitons as shown in Figure 2.8(*2b*).

system, in which the V_o of Ψ_1 is larger than the V_o of Ψ_2, ..., and so on. The fictitious particle moves successively from Ψ_1 to Ψ_2, to Ψ_3, ..., to Ψ_n. These pseudopotentials smoothly connect to one another at $V = 0$, where the potential gradient is zero.

Similarly, the soliton train structure shown in Figure 2.8(*2b*) can be described by a fictitious particle moving through a series of pseudopotentials in the form similar to the one shown in Figure 2.1(*2b*). Figure 2.10 shows an example of such a multiple-pseudopotential system. Again, the V_o of each pseudopotential decreases successively, from Ψ_1 to Ψ_n. These pseudopotentials connect to one another at $V = 0$, where the potential gradient is zero. The connection between two pseudopotentials at zero potential gradient will ensure a smooth transition on the fictitious particle motion, i.e., both pseudovelocity and pseudoacceleration will vary continuously across the connection point. A fictitious particle moving successively from Ψ_1 to Ψ_n can result in a series of solitons as shown in Figure 2.8(*2b*).

The finite-extent wavetrain or wave-packet solutions can also be obtained qualitatively from the multiple pseudopotential method. The finite-extent wavetrain or wave-packet solution shown in Figure 2.8(*2a*), can be obtained by considering a fictitious particle moving through a series of pseudopotentials in the form of Figure 2.1(*2a*). Figure 2.11 shows an example of such a multiple-pseudopotential system. Again, these pseudopotentials smoothly connect to one another at $V = 0$ and the V_o of each pseudopotential decreases successively, from Ψ_1 to Ψ_n. A fictitious particle moving from Ψ_1, ..., to Ψ_n successively can lead to a finite-extent wavetrain or wave-packet structures similar to the one shown in Figure 2.8(*2a*). Note that a small-amplitude short-wavelength perturbation of δV on the potential well Ψ_1 can lead to a finite change on $\delta\Psi$, as indicated by the dashed line. Since the potential well Ψ_2 is wider than Ψ_1, ..., and so on, the wave amplitude (δV) will increase as the

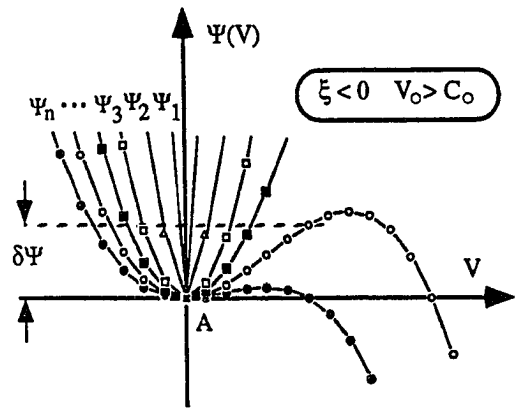

Figure 2.11 Multiple-pseudopotential system for quasi-stationary compression wave-train solution (see text for detail).

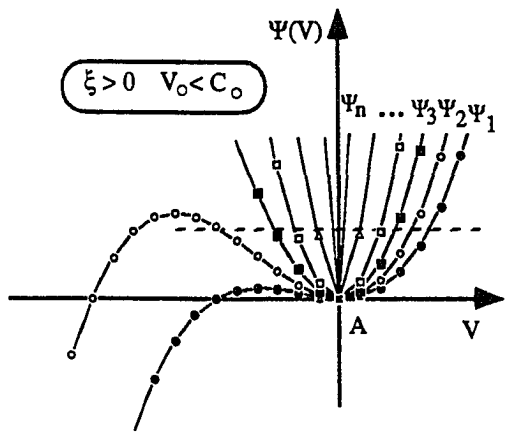

Figure 2.12 Multiple-pseudopotential system for quasi-stationary rarefaction wave-train solution (see text for detail).

fictitious particle moves from Ψ_1 to Ψ_n, due to the conservation of pseudoenergy, i.e., $\Psi + (dV/dX)^2 =$ constant. The highest point that the fictitious particle can reach, is determined by the pseudovelocity (i.e., the slope of $V(X)$) at the source region. The pseudovelocity at the source region increases as the slope of the source region increases. Thus, the location of the dashed line is not fixed, which will decrease with time as the slope of the profile connected to the source region decreases. Since the average slope of each pseudopotential well on the negative-V side is larger than the average slope on the positive-V side, the scale length of this nonlinear wave-packet in the negative-V half-period is shorter than the scale length in the other half-period of positive-V. This prediction is consistent with the simulation result.

Similarly, the finite-extent wavetrain or wave-packet solution shown in Figure 2.8(*1b*), can be obtained by considering a fictitious particle moving through a series of pseudopotentials in the form of Figure 2.1(*1b*). Figure 2.12 shows an example of such a multiple-pseudopotential system. Again, these pseudopotentials smoothly connect to one another at $V = 0$ and the V_o of each pseudopotential decreases successively, from Ψ_1 to Ψ_n. A fictitious particle moving successively from Ψ_1 to Ψ_n can lead to a finite-extent wavetrain or wave-packet structures similar to the one shown in Figure 2.8(*1b*). Again, due to the conservation of pseudoenergy, the wave amplitude δV will decrease toward downstream side as the fictitious particle moves to the inner part of these pseudopotentials; and due to the asymmetric nature of the potential well, the scale length of the wave-packet solution in the positive-V half-period will be shorter than the scale length in the other half-period of negative-V.

It is interesting to note that by including dissipative effects, a finite-extent wave-train solution can also be found by considering a fictitious particle moving dissipatively

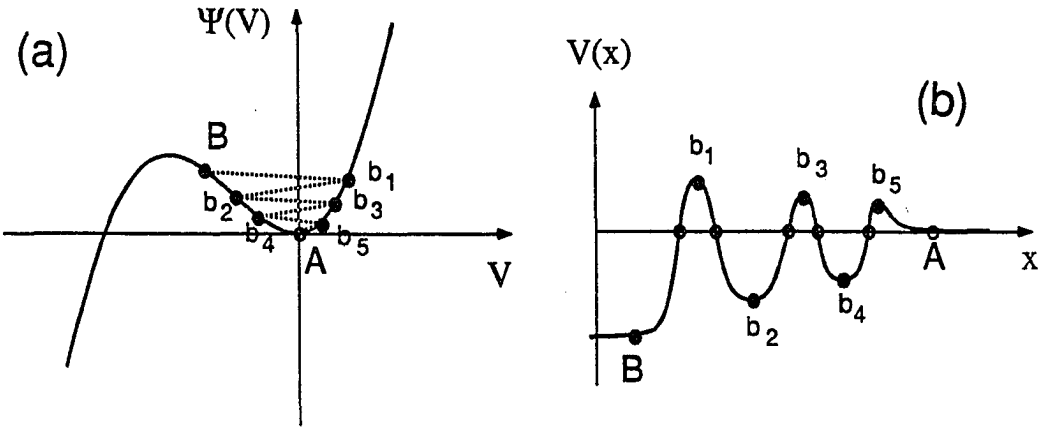

Figure 2.13 A sketch of formation of constant-profile dissipative wavetrain solution from a single pseudopotential well. Dashed lines in diagram (*a*) connect the highest points that a fictitious particle can reach after each bounce. Namely, the fictitious particle will move dissipatively on the potential well with trajectory of B–A–b_1–A–b_2–A–b_3–A–b_4–A–b_5–A. Diagram (*b*) is a sketch of the constant profile dissipative wavetrain solution obtained from the trajectory shown in diagram (*a*).

on a single pseudopotential well, as sketched in Figure 2.13 [e.g., *Sagdeev*, 1966; *Kennel and Sagdeev*, 1967*b*; *Biskamp*, 1973]. Dashed lines in Figure 2.13(*a*) connect the highest points that a fictitious particle can reach after each bounce. Diagram (*b*) in Figure 2.13 sketches the constant profile dissipative wavetrain solution obtained from the trajectory shown in Figure 2.13(*a*). Since the dissipative wavetrain or wave-packet is obtained from a single pseudopotential well, the entire wave-packet or finite-extent wavetrain will propagate at a constant speed and without changing its shape. This is in contrast to the nondissipative finite-extent wavetrain or wave-packet solution obtained above, which is only a quasi-stationary structure and should gradually spread out as time goes on.

Since we are going to discuss nondissipative nonlinear waves in two-fluid plasmas in this chapter, the idea of multiple pseudopotential method will allow us to obtain various types of quasi-stationary nonlinear wave solutions without introducing any

dissipative terms in our basic equations. It will be shown in section 2.5 that the quasi-stationary nonlinear wave solutions in two-fluid plasmas are very useful solutions in comparing with observations in collisionless space plasmas.

2.3 Methods of Nonlinear Wave Solutions

Two analytical methods of solving nonlinear wave problems will be discussed in this section, where the advantages of one method are often the disadvantages of the other, and vice versa. The first one to be discussed is the quasi-linear method. The theoretical background of the quasi-linear method can be summarized as follows: Soliton solutions are found to be the characteristic solutions of several well-known partial differential equations (PDEs) including the KdV equation, modified KdV (MKdV) equation, nonlinear Schrödinger (NLS) equation, derivative nonlinear Schrödinger (DNLS) equation, and so on. Under a suitable quasi-linear approximation (e.g., keeping a few high order terms in the Fourier transformed original governing equations) most dispersive waves can be approximated by one of these well-known PDEs. Therefore, the particular nonlinear wave problem can be solved according to the well-established analytical and numerical methods of solving these PDEs [e.g., *Taha and Ablowitz*, 1984*a*,*b*,*c*]. This is one of the conveniences of the quasi-linear method. Another convenience of using quasi-linear method is that one can easily associate or identify the quasi-linear wave solutions with a particular linear wave mode. On the other hand, it is also convenient to predict the nonlinear wave solution characteristics qualitatively based on a simple linear dispersion relation.

Examples of quasi-linear approaches can be easily seen by comparing Figure 1.2 with Figure 2.8. For instance, since the wave dispersions in the shaded regions F and $AX1$ in Figure 1.2 are similar to the one given in panel (2) of Figure 2.8,

compressive, finite-extent, wavetrains or wave-packets are expected to be found when the upstream flow speed is slightly larger than the fast mode speed, and rarefaction soliton is expected to be found when the upstream flow speed is slightly less than the fast mode speed. The proposed nonlinear wave solutions discussed above based on quasi-linear approximation are listed in Table 2.1. The prediction of nonlinear wave polarizations listed in Table 2.1 is obtained based on the linear wave polarization in each shaded region discussed in Figure 1.2. With a more rigorous quasi-linear formulation, these wave modes can resemble solutions of the MKdV equation, in which the variation of wave magnetic field is included [e.g., *Kennel et al.*, 1988].

However, in many cases, solutions obtained from the quasi-linear method can only apply to a weak nonlinear situation (i.e., V_o slightly different from C_o). The quasi-linear approximation may break down at highly nonlinear situation either because the approximated quasi-linear dispersion relation diverges from the exact dispersion relation in a certain wavelength interval, or because the nonlinear coupling effects between two wave modes are not included in the quasi-linear formulations. Figure 2.14 shows an example of large deviation between exact dispersion and approximate dispersion curves, where the solid curve is the Alfvén wave dispersion curve for $V_{AX} > C_S$, and the dashed curve is an approximate KdV-type dispersion curve. The deviation between two curves becomes significant as the Alfvén mode turns into ion sound mode in the short wavelength interval. Evidence of the ignoring wave-mode coupling effects in the quasi-linear formulation can be seen by comparing the dispersion curves in Figure 1.2 and Figure 2.8. Three different wave modes co-exist in each panel of Figure 1.2 but only one dispersion curve was considered each time (for each panel) in Figure 2.8. Thus, obviously nonlinear interactions between fast, Alfvén, and slow modes have been ignored in the discussion of Table 2.1.

Table 2.1 Prediction of nonlinear hydromagnetic wave solutions based on two-fluid linear wave dispersions.

Dispersions	Type of Nonlinear Waves	V_o	Polarization
F	compression wave trains	$> V_F$	right-handed
F	rarefaction solitons	$< V_F$	right-handed
SL	compression solitons	$> V_{SL}$	left-handed
SL	rarefaction wave trains	$< V_{SL}$	left-handed
$AX1$	compression wave trains	$> V_{AX}$	right-handed
$AX1$	rarefaction solitons	$< V_{AX}$	right-handed
$AX2$	compression solitons	$> V_{AX}$	left-handed
$AX2$	rarefaction wave trains	$< V_{AX}$	left-handed
W	compression solitons	$> V_{W\max}$	right-handed

Notations used in the column of dispersions are obtained based on the shaded dispersion curves shown in Figure 1.2.

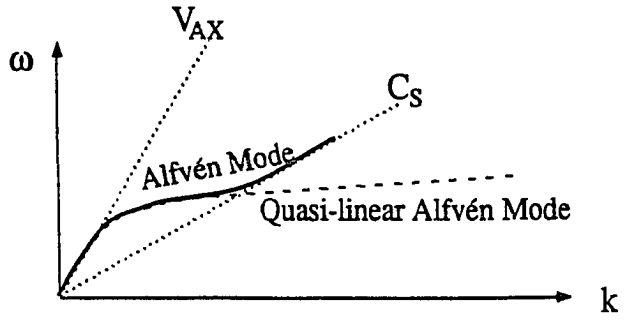

Figure 2.14 Sketches of Alfvén wave dispersion curve for $V_{AX} > C_S$ (solid curve) and a best-fit KdV-type dispersion curve (dashed curve). Large deviation between these two curves occurs after Alfvén mode turns into ion acoustic sound mode.

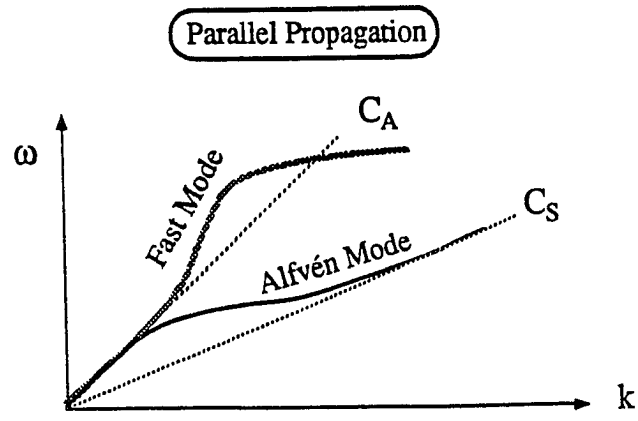

Figure 2.15 Sketches of fast-mode and Alfvén-mode linear wave dispersion curves with parallel propagation in a low β plasma ($C_A > C_S$).

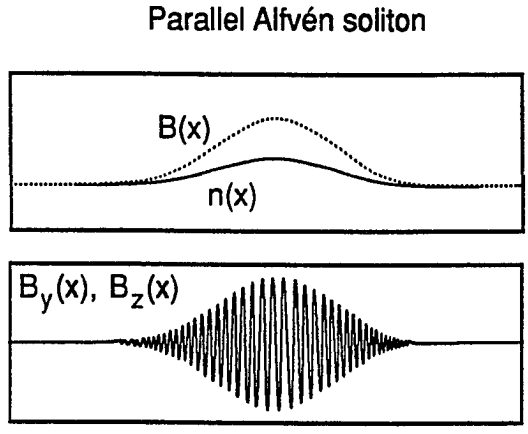

Figure 2.16 Sketches of spatial profiles of a parallel Alfvén envelope soliton solution.

But for some special cases, wave-mode coupling effects may be included in a suitable quasi-linear approximation if two wave modes are coupled to each other even in the linear wave limit. As an example, Figure 2.15 sketches the linear wave dispersion curves of Alfvén-mode and fast-mode with parallel propagation in a low temperature two-fluid plasma ($C_S < C_A$). The coupling between these two linear wave modes is characterized by an identical phase speed in the long wavelength limit. Under a suitable quasi-linear approximation the Fast-Alfvén wave modes with parallel propagation can be approximated by the DNLS equations [e.g., *Mio et al.*, 1976; *Spangler and Sheerin*, 1982; *Spangler et al.*, 1985; *Dawson and Fontán*, 1988; *Kennel et al.*, 1988]. Therefore, the coupling effect between the Fast-Alfvén modes is included in the quasi-linear envelope soliton solutions obtained from the DNLS equations.

Figure 2.16 sketches an idealized envelope soliton solution. Panel (*a*) shows the plasma density (solid curve) and the total magnetic field (dotted curve). Panel (*b*) shows one of the transverse components of the magnetic field. Note that the detail information of the short wavelength waves inside the envelope of the transverse magnetic field in Figure 2.16(*b*) is not included in the DNLS solutions. A quasi-stationary envelope soliton solution will be discussed later in Section 2.4.5 to show that the soliton solution is not a perfectly constant-profile nonlinear wave.

The second method of solving nonlinear wave problems is to solve the entire set of governing equations directly without any quasi-linear approximation. As a result, the nonlinear wave-mode coupling effects and wave-mode converting effects discussed above will be fully included. However, there are also weak points in this method, such as: there is no standard procedure to solve the nonlinear wave problem; there is no guarantee that an analytical form of the pseudopotential can be found; and there is

no guarantee that an analytical solution exists. But fortunately, based on the conservation principle of mass flux, momentum flux, and energy flux, an analytical form of pseudopotential for the two-fluid plasmas can be obtained, which will be studied in the next section. In addition, by comparing the fully nonlinear wave solutions with the predicted quasi-linear nonlinear wave solutions given in Table 2.1, the fully nonlinear wave solutions can be identified with one or two linear wave modes, which can help us to clarify the physical pictures behind the mathematical results, and to classify these nonlinear wave solutions based on those well-known linear wave modes.

2.4 Nonlinear Waves With Full Dispersion in Two-Fluid Plasmas

One-dimensional nondissipative nonlinear waves with full dispersion in two-fluid plasmas are studied systematically in this section based on the pseudopotential method [e.g., *Montgomery*, 1959; *Hain et al.*, 1960; *Crevier and Tidman*, 1970; *Lyu and Kan*, 1989*b*]. In the pseudopotential formulation, we shall choose the wave magnetic field as the pseudocoordinate. Since the wave magnetic field has two independent components, the pseudocoordinate will be a two-dimensional system, and the fictitious particle is moving on a two-dimensional pseudopotential surface. This result is different from the classical cases in which a fictitious particle is considered moving in a one-dimensional pseudopotential well, such as the pseudopotentials of the KdV dispersion medium as discussed in Section 2.2, and the Sagdeev pseudopotential of the electrostatic nonlinear waves [*Sagdeev*, 1966].

It may be noted that sections 2.4.1–2.4.3 are written based on the results of the paper *Lyu and Kan* [1989*b*]. Readers who are familiar with this paper may skip these three sections and go to the section 2.4.4.

2.4.1 Formulation

We look for constant-profile ($\partial/\partial t = 0$), one-dimensional ($\nabla = \hat{\mathbf{x}} d/dx$) nonlinear hydromagnetic wave solutions in a finite-temperature two-fluid plasmas. Since the hydromagnetic wave belongs to low-frequency ion waves, the quasi-neutrality approximation ($n_i \cong n_e = n$) is an adequate assumption for this study [e.g., *Chen*, 1984]. Under the quasi-neutrality assumption, the Poisson's equation will be ignored. Without the Poisson's equation, the longitudinal electric field will be determined from the momentum equation. The radiation term in the Ampere's law will also be ignored for hydromagnetic waves. Both ion and electron pressures are assumed to be isotropic and each of them follows an adiabatic process. The boundary condition on the upstream side ($x \to -\infty$) is assumed to be uniform; namely, all the derivatives vanish on the upstream side. No boundary condition will be imposed on the downstream side, because the downstream state can be determined for a given upstream state in this two-fluid model. Under above assumptions, the simplified two-fluid plasma equations are given below in Gaussian units.

The continuity equation (of the αth species, i.e., ions and electrons)

$$\nabla \cdot (\rho_\alpha \mathbf{V}_\alpha) = 0 \tag{2.4.1}$$

The momentum equation

$$\mathbf{V}_\alpha \cdot \nabla \mathbf{V}_\alpha + (1/\rho_\alpha)\nabla p_\alpha - (e_\alpha/m_\alpha c)(c\mathbf{E} + \mathbf{V}_\alpha \times \mathbf{B}) = 0 \tag{2.4.2}$$

The energy equation

$$(3/2)\mathbf{V}_\alpha \cdot \nabla p_\alpha + (5/2)p_\alpha \nabla \cdot \mathbf{V}_\alpha = 0 \tag{2.4.3}$$

The Maxwell equations

$$\nabla \cdot \mathbf{B} = 0 \tag{2.4.4}$$

$$\nabla \times \mathbf{E} = 0 \tag{2.4.5}$$

$$\nabla \times \mathbf{B} = 4\pi ne(\mathbf{V}_i - \mathbf{V}_e)/c \tag{2.4.6}$$

where ions are assumed to be protons, c is the speed of light, e_α, m_α, n_α, ρ_α, $\mathbf{V}_\alpha$, and p_α are respectively the charge, mass, number density, mass density, flow velocity, and thermal pressure of the αth species. All variables n_α, ρ_α, $\mathbf{V}_\alpha$, p_α, $\mathbf{E}$, and $\mathbf{B}$ are a function of x.

For wave propagation oblique to the upstream magnetic field, we can choose the coordinate system such that the upstream magnetic field ($\mathbf{B}_o$) is in the xy-plane, i.e., $\mathbf{B}_o = [B_{xo}, B_{yo}, 0]$, where subscript o indicates the upstream quantities. The wave normal angle with respect to the upstream magnetic field becomes $\theta_o = \cos^{-1}(B_{xo}/B_o)$ where $B_o = (B_{xo}^2 + B_{yo}^2)^{1/2}$ is the magnitude of the upstream magnetic field. We choose a moving frame such that the upstream flow velocity is in the x-direction, i.e., the normal incident frame [e.g., *Goodrich and Scudder*, 1984]. Based on the uniform boundary condition the current density must vanish on the upstream side, it follows that the flow velocities on the upstream side become $\mathbf{V}_{io} = \mathbf{V}_{eo} = \mathbf{V}_o = \hat{\mathbf{x}}V_o$. Without loss of generality and nonlinearity, we can write the total magnetic field to be the sum of the upstream magnetic field and the wave magnetic field $\mathbf{b}(x)$, i.e., $\mathbf{B}(x) = \mathbf{B}_o + \mathbf{b}(x)$. From (2.4.4), we have constant normal component of the magnetic field, i.e., $B_x = B_{xo}$ = constant, so that the wave magnetic field becomes

$\mathbf{b} = [0, b_y, b_z]$. As a result, relationships between B_y and b_y, and between B_z and b_z are given as follows:

$$B_y(x) = b_y(x) + B_{yo}$$

$$B_z(x) = b_z(x)$$

From (2.4.5), we have constant transverse electric field. It can be shown that the upstream electric field in the normal incidence frame is given by $\mathbf{E}_o = -\hat{z}V_oB_{yo}/c$, so that $E_y = E_{yo} = 0$ and $E_z = E_{zo} = -V_oB_{yo}/c$. The quasi-neutrality approximation, (2.4.1) leads to $V_{xi}(x) \cong V_{xe}(x) = V_x(x)$, which is required by (2.4.6) and the assumption of one-dimensionality. An isentropic equation of state for each species can be obtained from (2.4.3), i.e.,

$$p_\alpha V_x^\gamma = p_{\alpha o} V_o^\gamma \tag{2.4.7}$$

where $p_{\alpha o}$ are the upstream pressures of the αth species (ions or electrons), and $\gamma = 5/3$.

For constant-profile wave solutions, it is convenient to cast (2.4.1)–(2.4.6) into conservative forms. Under the uniform upstream boundary condition, the conservation equations are:

conservation of mass flux

$$[\rho_i(x) + \rho_e(x)]\, V_x(x) = \rho_o V_o \tag{2.4.8}$$

conservation of momentum flux

$$(p_i + p_e) + \rho_o V_o V_x + \frac{(B_{yo} + b_y)^2 + b_z^2}{8\pi} = p_o + \rho_o V_o^2 + \frac{B_{yo}^2}{8\pi} \tag{2.4.9}$$

$$(\rho_i V_{yi} + \rho_e V_{ye}) V_x - \frac{B_{xo} b_y}{4\pi} = 0 \tag{2.4.10}$$

$$(\rho_i V_{zi} + \rho_e V_{ze}) V_x - \frac{B_{xo} b_z}{4\pi} = 0 \tag{2.4.11}$$

and conservation of energy flux

$$\frac{5}{2}(p_i+p_e)V_x+\frac{1}{2}\left[\rho_i\left(V_x^2+V_{yi}^2+V_{zi}^2\right)+\rho_e\left(V_x^2+V_{ye}^2+V_{ze}^2\right)\right]V_x + \frac{V_\circ B_{y\circ}(B_{y\circ}+b_y)}{4\pi}=\frac{5}{2}p_\circ V_\circ+\frac{1}{2}\rho_\circ V_\circ^3+\frac{V_\circ B_{y\circ}^2}{4\pi} \qquad (2.4.12)$$

where $\rho_\circ=(m_i+m_e)n_\circ$ and $p_\circ=p_{i\circ}+p_{e\circ}$ are the total mass density and thermal pressure on the upstream side, and $n_\circ$ is the upstream number density of each species. Note that we have neglected the $E^2/B_\circ^2$ terms (of order $V_\circ^2/c^2\ll 1$) in (2.4.9) and (2.4.12).

We define a convective time τ as $\tau=\int V_x(x)^{-1}dx$. Using the notation $\dot{A}=dA/d\tau=V_x(dA/dx)$ to indicate convective time derivatives, the momentum equation (2.4.2) can be rewritten in the component form as

$$\dot{V}_{x\alpha}=+(e_\alpha/m_\alpha c)\left[cE_x+V_{y\alpha}b_z-V_{z\alpha}(B_{y\circ}+b_y)\right]-(1/\rho_\circ V_\circ)\dot{p}_\alpha \qquad (2.4.13)$$

$$\dot{V}_{y\alpha}=+(e_\alpha/m_\alpha c)\left[V_{z\alpha}B_{x\circ}-V_x b_z\right] \qquad (2.4.14)$$

$$\dot{V}_{z\alpha}=+(e_\alpha/m_\alpha c)\left[-V_\circ B_{y\circ}+V_x(B_{y\circ}+b_y)-V_{y\alpha}B_{x\circ}\right] \qquad (2.4.15)$$

where (2.4.8) has been used in (2.4.13). The $\dot{V}_{x\alpha}$ in (2.4.13) is equal to $\dot{V}_x$ for both ions and electrons species. Multiplying (2.4.6) by V_x leads to

$$\begin{aligned}\dot{b}_y&=+(4\pi e/c)n_\circ V_\circ\left(V_{zi}-V_{ze}\right)\\ \dot{b}_z&=-(4\pi e/c)n_\circ V_\circ\left(V_{yi}-V_{ye}\right)\end{aligned} \qquad (2.4.16)$$

Differentiating (2.4.16) once with respect to τ leads to

$$\begin{aligned}\ddot{b}_y&=+(4\pi e/c)n_\circ V_\circ\left(\dot{V}_{zi}-\dot{V}_{ze}\right)\\ \ddot{b}_z&=-(4\pi e/c)n_\circ V_\circ\left(\dot{V}_{yi}-\dot{V}_{ye}\right)\end{aligned} \qquad (2.4.17)$$

Solving (2.4.10), (2.4.11), (2.4.16), and making use of (2.4.8) yields

$$\begin{aligned}\frac{V_{yi,e}}{V_o} &= \frac{B_o^2}{4\pi\rho_o V_o^2}\left(\frac{B_{xo}}{B_o}\frac{b_y}{B_o} + \frac{e_{e,i}B_o}{m_{e,i}c}\frac{\dot{b}_z}{B_o}\right)\\ \frac{V_{zi,e}}{V_o} &= \frac{B_o^2}{4\pi\rho_o V_o^2}\left(\frac{B_{xo}}{B_o}\frac{b_z}{B_o} - \frac{e_{e,i}B_o}{m_{e,i}c}\frac{\dot{b}_y}{B_o}\right)\end{aligned} \tag{2.4.18}$$

Using (2.4.18) to eliminate the $V_{y\alpha}$ and $V_{z\alpha}$ in (2.4.14) and (2.4.15) and then substituting the latter results into (2.4.17), the governing equation for the wave magnetic field can be obtained in a dimensionless form as

$$\begin{aligned}\frac{\ddot{b}_y^*}{M_{Ao}^2\Omega_{io}^*\Omega_{eo}^*} = &-\left\{\left[\frac{B_{xo}^{*2}}{M_{Ao}^2} - V_x^*(b_y^*, b_z^*)\right](B_{yo}^* + b_y^*) - \left[\frac{B_{xo}^{*2}}{M_{Ao}^2} - 1\right]B_{yo}^*\right\}\\ &-\left(\frac{1}{\Omega_{io}^*} - \frac{1}{\Omega_{eo}^*}\right)\frac{B_{xo}^*}{M_{Ao}^2}\dot{b}_z^*\end{aligned} \tag{2.4.19}$$

$$\frac{\ddot{b}_z^*}{M_{Ao}^2\Omega_{io}^*\Omega_{eo}^*} = -\left\{\left[\frac{B_{xo}^{*2}}{M_{Ao}^2} - V_x^*(b_y^*, b_z^*)\right]b_z^*\right\} + \left(\frac{1}{\Omega_{io}^*} - \frac{1}{\Omega_{eo}^*}\right)\frac{B_{xo}^*}{M_{Ao}^2}\dot{b}_y^* \tag{2.4.20}$$

where $M_{Ao} = V_o/C_{Ao}$ and $C_{Ao} = (B_o^2/4\pi\rho_o)^{1/2}$ are the upstream Alfvén Mach number, and Alfvén speed. The dimensionless quantities denoted by the superscript $*$ are normalized by a characteristic quantity on the upstream side. They are defined as $B_{xo}^* = B_{xo}/B_o = \cos\theta_o$, $B_{yo}^* = B_{yo}/B_o = \sin\theta_o$, $b_y^* = b_y/B_o$, $b_z^* = b_z/B_o$, $V_x^* = V_x/V_o$, $x^* = x/x_o$, $\tau^* = \tau\Omega_o$, $\dot{A}^* = dA^*/d\tau^* = V_x^* dA^*/dx^*$, $\ddot{A}^* = d^2A^*/d\tau^{*2}$, $\Omega_{io}^* = \Omega_{io}/\Omega_o$, and $\Omega_{eo}^* = \Omega_{eo}/\Omega_o$, where $\Omega_{io} = eB_o/m_ic$ and $\Omega_{eo} = eB_o/m_ec$ are the upstream ion and electron cyclotron frequencies, and $\Omega_o = V_o/x_o$. The choice of the characteristic length x_o will be discussed later in the next section. The equation for $V_x^*(b_y^*, b_z^*)$ in (2.4.19) and (2.4.20) can be obtained from (2.4.9) in which p_i and p_e can be eliminated by (2.4.7). The resulting equation can be written as

$$\frac{\beta_o}{2M_{Ao}^2}V_x^{*-\gamma} + V_x^* + \frac{1}{2M_{Ao}^2}\left[\left(B_{yo}^* + b_y^*\right)^2 + b_z^{*2}\right] = \frac{\beta_o}{2M_{Ao}^2} + 1 + \frac{B_{yo}^{*2}}{2M_{Ao}^2} \tag{2.4.21}$$

where $\beta_o = p_o/\left(B_o^2/8\pi\right)$ is the plasma beta on the upstream side.

Multiplying m_α^2 to (2.4.13) and taking the difference between the resulting ion and electron equations, the expression of wave electric field $E_x(b_y, b_z)$ can be obtained upon eliminating $\dot{p}_\alpha$, $V_{y\alpha}$, and $V_{z\alpha}$ by (2.4.7) and (2.4.18). The result can be written in dimensionless form as

$$c^* E_x^*(b_y^*, b_z^*) = \frac{B_{xo}^* B_{yo}^* b_z^*}{M_{Ao}^2} + \left[\left(\frac{\dot{V}_x^*}{\Omega_{io}^*}\right) \Big/ \left(1 + \frac{T_{eo}}{T_{io}}\right)\right] \times \left[\left(1 - \frac{m_e}{m_i}\right) - \frac{\gamma\beta_o}{2M_{Ao}^2} \frac{1}{V_x^{*\gamma+1}} \left(1 - \frac{m_e}{m_i}\frac{T_{eo}}{T_{io}}\right)\right] \quad (2.4.22)$$

where $c^* = c/V_o$, $E_x^* = E_x/B_o$, and $T_{eo}/T_{io} = p_{eo}/p_{io}$ is the temperature ratio of electrons and ions on the upstream side. Both $V_x^*(b_y^*, b_z^*)$ and $\dot{V}_x^*(b_y^*, b_z^*)$ in (2.4.22) can be obtained from (2.4.21). By differentiating (2.4.21) once with respect to τ^* and solving $\dot{V}_x^*$, one obtains

$$\dot{V}_x^* = \frac{1}{2M_{Ao}^2}\left(\frac{d}{d\tau^*}\left[(B_{yo}^* + b_y^*)^2 + b_z^{*2}\right]\right) \Big/ \left(\frac{\gamma\beta_o}{2M_{Ao}^2}\frac{1}{V_x^{*\gamma+1}} - 1\right) . \quad (2.4.23)$$

By introducing the local sound speed $C_S = \sqrt{\gamma(p_i + p_e)/(\rho_i + \rho_e)}$ and the local sound Mach number $M_S = V_x/C_S$, it follows that

$$M_S = M_{Ao}\sqrt{2V_x^{*\gamma+1}/\gamma\beta_o} . \quad (2.4.24)$$

When $M_S = 1$, the denominator in (2.4.23) vanishes. In this case, $\dot{V}_x^*$ can be solved by differentiating (2.4.21) twice with respect to τ^*, which yields

$$\dot{V}_x^* = \pm\left\{\left(-\frac{d^2}{d\tau^{*2}}\left[(B_{yo}^* + b_y^*)^2 + b_z^{*2}\right]\right)\frac{V_x^{*\gamma+2}}{\gamma(\gamma+1)\beta_o}\right\}^{1/2} \quad (2.4.25)$$

where the sign is determined such that $\dot{V}_x^*$ is a continuous function. By introducing $B_\perp^* = [(B_{yo}^* + b_y^*)^2 + b_z^{*2}]^{1/2}$, it can be seen that $\dot{V}_x^*$ remains finite at $M_S = 1$ if $B_\perp^*$ is a maximum at $M_S = 1$ (i.e., $\dot{B}_\perp^* = 0$ and $\ddot{B}_\perp^* < 0$).

Equations (2.4.7), (2.4.8), (2.4.18)–(2.4.25) are the governing equations of nonlinear constant-profile waves. Equations (2.4.19), (2.4.20) and (2.4.23) are standard ordinary differential equations, which can be solved numerically for $\mathbf{b}(x)$, $\dot{\mathbf{b}}(x)$ and $V_x(x)$ when $M_S \neq 1$. The results can be substituted into (2.4.7), (2.4.8), (2.4.18), and (2.4.22) for the remaining variables $p_\alpha(x)$, $\rho(x)$, $V_{y\alpha}(x)$, $V_{z\alpha}(x)$, and $E_x(x)$. When M_S approaches 1, (2.4.23) must be replaced by (2.4.25). However, this step of replacement is difficult to handle numerically. This difficulty can be overcome by studying this nonlinear wave problem analytically based on the pseudopotential method as discussed in the next section.

2.4.2 Pseudopotential Method

According to the pseudopotential method [e.g., *Davis et al.*, 1958; *Montgomery*, 1959; *Hain et al.*, 1960; *Sagdeev*, 1966; *Crevier and Tidman*, 1970], (2.4.19) and (2.4.20) can be viewed as "equations of motion" of a fictitious particle with wave magnetic field $\mathbf{b}$ as its pseudocoordinate. Thus, the pseudovelocity of the fictitious particle is $\dot{\mathbf{b}}$ and the pseudoacceleration of the fictitious particle is $\ddot{\mathbf{b}}$. One can define a pseudovelocity-independent pseudopotential Ψ, such that the equations of motion (2.4.19) and (2.4.20) can be rewritten as

$$\frac{\ddot{b}_y^*}{M_{Ao}^2\Omega_{io}^*\Omega_{eo}^*} = -\frac{\partial\Psi(b_y^*,b_z^*)}{\partial b_y^*} - \left(\frac{1}{\Omega_{io}^*} - \frac{1}{\Omega_{eo}^*}\right)\frac{B_{xo}^*}{M_{Ao}^2}\dot{b}_z^* \qquad (2.4.26)$$

$$\frac{\ddot{b}_z^*}{M_{Ao}^2\Omega_{io}^*\Omega_{eo}^*} = -\frac{\partial\Psi(b_y^*,b_z^*)}{\partial b_z^*} + \left(\frac{1}{\Omega_{io}^*} - \frac{1}{\Omega_{eo}^*}\right)\frac{B_{xo}^*}{M_{Ao}^2}\dot{b}_y^* \qquad (2.4.27)$$

where Ψ is defined by

$$\frac{\partial\Psi(b_y^*,b_z^*)}{\partial b_y^*} = \left[\frac{B_{xo}^{*2}}{M_{Ao}^2} - V_x^*(b_y^*,b_z^*)\right](B_{yo}^* + b_y^*) - \left[\frac{B_{xo}^{*2}}{M_{Ao}^2} - 1\right]B_{yo}^* \qquad (2.4.28)$$

$$\frac{\partial\Psi(b_y^*,b_z^*)}{\partial b_z^*} = \left[\frac{B_{xo}^{*2}}{M_{Ao}^2} - V_x^*(b_y^*,b_z^*)\right]b_z^* \,. \qquad (2.4.29)$$

The function Ψ is a legitimate potential function, because the partial differentiation of (2.4.28) with respect to b_z^* is identical to the partial differentiation of (2.4.29) with respect to b_y^*.

(A) *Types of Fictitious Particle Trajectories*

The equations of motion (2.4.26) and (2.4.27) can be written in a vector form as follows.

$$C_1 \ddot{\mathbf{b}}^* = -\nabla_{\mathbf{b}^*}\Psi + C_2 B_{x_o}^* \hat{\mathbf{x}} \times \dot{\mathbf{b}}^* \tag{2.4.30}$$

where $C_1 = 1/M_{A_o}^2 \Omega_{i_o}^* \Omega_{e_o}^*$, $C_2 = (\Omega_{e_o}^* - \Omega_{i_o}^*)/M_{A_o}^2 \Omega_{i_o}^* \Omega_{e_o}^*$ and $\nabla_{\mathbf{b}^*} = \hat{\mathbf{y}}\partial/\partial b_y^* + \hat{\mathbf{z}}\partial/\partial b_z^*$. There are two types of pseudoforces in (2.4.30) to govern the motion of a fictitious particle. The first force term is the pseudopotential gradient force ($-\nabla_{\mathbf{b}^*}\Psi$) where the pseudopotential field Ψ is a two-dimensional potential surface field in the b_y-b_z space. The second force term in (2.4.30) is a pseudovelocity-dependent force ($C_2 B_{x_o}^* \hat{\mathbf{x}} \times \dot{\mathbf{b}}^*$) which always acts on the direction perpendicular to the pseudovelocity ($\dot{\mathbf{b}}$). Thus, it can only change the direction of particle motion but cannot affect the speed of the fictitious particle. Therefore, the sum of the kinetic energy and potential energy of the fictitious particle will be conserved.

Since the pseudocoordinate is the wave magnetic field $\mathbf{b}$, the trajectory of the fictitious particle can be seen as the hodogram of the wave magnetic field. The types of particle trajectories can be studied by analyzing (2.4.30) to see which two terms are the dominate terms to play the force balance. The magnitude of the three terms in (2.4.30) depends on the scale length of the nonlinear wave. For convenience, we define

$$L_i = (C_{A_o}/\Omega_{i_o}) \cdot (\cos\theta_o / M_{A_o})$$

as an ion scale length,

$$L_e = (C_{Ao}/\Omega_{eo})/(\cos\theta_o/M_{Ao})$$

as an electron scale length, and

$$L_h = (L_i L_e)^{1/2} = C_{Ao}/(\Omega_{io}\Omega_{eo})^{1/2}$$

as a hybrid scale length. The motion of the fictitious particle can be classified into three simple forms based on the three scale lengths.

When the wave spatial variation is of the order of the ion scale length, L_i, or longer, the inertia force term ($C_1\ddot{\mathbf{b}}^*$) in (2.4.30) is negligible. The balance between the pseudopotential gradient force term ($-\nabla_{\mathbf{b}^*}\Psi$) and the pseudovelocity dependent force term ($C_2 B_{xo}^* \hat{\mathbf{x}} \times \dot{\mathbf{b}}^*$) results in a "motion along equipotential contours." This type of trajectory will be called the ion-scale trajectory.

Figure 2.17 illustrates the magnetic field polarization associated with the ion-scale trajectory. It can be seen that the polarization with respect to $\hat{\mathbf{x}}B_{xo}$ have to be (*a*) left-handed when the equipotential contour bends around a low potential center, and (*b*) right-handed when the contour bends around a high potential center, so that the pseudovelocity dependent force ($C_2 B_{xo}^* \hat{\mathbf{x}} \times \dot{\mathbf{b}}^*$) can balance the pseudopotential gradient force ($-\nabla_{\mathbf{b}^*}\Psi$) in (2.4.30).

When the wave spatial variation is of the order of the electron scale length, L_e, the inertia force term will be large enough to balance the pseudovelocity dependent force term in (2.4.30), resulting in a right-handed "gyromotion." This type of trajectory will be called the electron-scale trajectory.

When the wave spatial variation is of the order of the hybrid scale length, L_h, the inertia force term can balance the potential gradient force term in (2.4.30), resulting

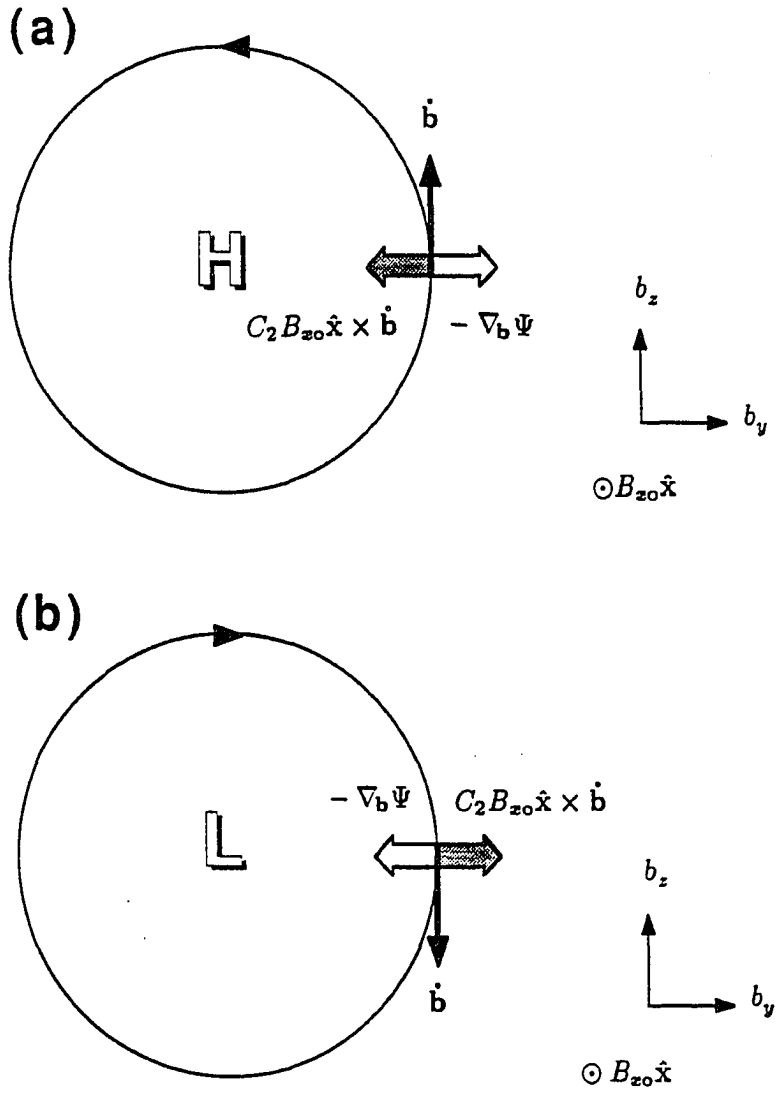

Figure 2.17 Force balance of the ion-scale trajectory. Ion-scale trajectory is characterized by a track of magnetic hodogram along equipotential contours. The magnetic field polarization has to be (*a*) left-handed when the equipotential contour curves around a low potential center, and (*b*) right-handed when the equipotential contour curves around a high potential center, so that the pseudovelocity dependent force term ($C_2 B_{xo}^{*}\hat{\mathbf{x}} \times \dot{\mathbf{b}}^{*}$) can balance the potential gradient force term ($-\nabla_{\mathbf{b}^{*}}\Psi$) in (2.4.30).

in trajectories that must cross equipotential contours. This type of trajectory will be called the hybrid-scale trajectory.

In general, the three types of trajectory can co-exist in the nonlinear wave solutions with one of them dominate to the others. The nonlinear wave of perpendicular propagation (i.e., $\theta_o = 90°$) is a special case in which the last term in (2.4.30) vanishes. As a result, the nonlinear wave will be completely governed by the hybrid-scale trajectory if $\theta_o = 90°$.

It can be shown that if $M_{Ao} \ll \cos\theta_o (m_i/m_e)^{1/2}$, the magnetic field variation is predominantly governed by the ion-scale trajectory, except for an extremely high beta plasma ($\beta_o \gg 1$). The electron-scale trajectory can coexist with the ion-scale trajectory. However, owing to the uniform boundary conditions ($d/dx = 0$) on the upstream side, it can be shown that the magnetic field variation described by the electron-scale trajectory is of small amplitude compared with B_o ($\delta b \approx B_o m_e/m_i$). Thus, we can obtain the magnetic hodogram of the nonlinear waves directly from the equipotential contours of the pseudopotential field without solving the (2.4.19), (2.4.20) and (2.4.23) numerically. It may be noted that although in most cases the pseudopotential gradient force perpendicular to a equipotential contour is non-uniform at different points along that equipotential contour. Thus, the ion scale trajectory cannot follow the equipotential contours exactly, but the deviation is usually very small, unless large amplitude nonlinear waves with electron scale trajectory are launched from upstream side or downstream side by an external source, which will be discussed later in Section 2.4.5. Without external forcing, the trajectory of the fictitious particle will deviate from the equipotential contour (i.e., the hybrid-scale trajectory) and shift toward the lower potential side by an amount $\delta b \approx B_o (m_e/m_i)^{1/2}$.

For $M_{Ao} \approx \cos\theta_o (m_i/m_e)^{1/2}$ (e.g., as θ_o slightly deviated from 90°, or if M_A is extremely large), the three terms in (2.4.30) are about the same magnitude. In these cases, we have to solve (2.4.19), (2.4.20) and (2.4.23) numerically to obtain the nonlinear wave solutions and magnetic field hodogram.

The condition of $M_{Ao} \ll \cos\theta_o (m_i/m_e)^{1/2}$ can be applied to most of the low Mach number nonlinear nondissipative hydromagnetic waves observed in the solar wind (such as the Alfvénic nonlinear hydromagnetic waves), except for some cases with highly perpendicular propagation. Thus, we can study these low Mach number nonlinear waves systematically by carefully examining the structure of pseudopotential Ψ for various upstream parameters.

(B) *Structure of the Pseudopotential*

The structure of pseudopotential Ψ can be obtained by two different approaches. A straightforward way to obtain the pseudopotential structure is to integrate (2.4.28) and (2.4.29) numerically. Using this method, one can easily obtain a cross section of Ψ at a constant b_y^* or b_z^*. But it will be a very complicated and difficult task to construct a pseudopotential in the two-dimensional b_y^*-b_z^* space. Instead of directly integrating, an analytic form of the pseudopotential can be obtained indirectly by the following procedures [e.g., *Hain et al.*, 1960; *Crevier and Tidman*, 1970; *Lyu and Kan*, 1989*b*].

Multiplying (2.4.26) by $\dot{b}_y^*$, (2.4.27) by $\dot{b}_z^*$, and adding the resulting equations, one obtains an equation that can be integrated once and written as

$$\frac{1}{2}\frac{\dot{b}_y^{*2} + \dot{b}_z^{*2}}{M_{Ao}^2 \Omega_{io}^* \Omega_{eo}^*} + \Psi(b_y^*, b_z^*) = 0 \qquad (2.4.31)$$

where $\Psi = 0$ has been chosen on the upstream side. Using (2.4.18) to eliminate $V_{y\alpha}$, $V_{z\alpha}$ and using (2.4.7) to eliminate p_i, p_e, the conservation of energy flux in (2.4.12) can be rewritten in a dimensionless form:

$$\frac{5\beta_o}{4}V_x^{*1-\gamma} + \frac{M_{Ao}^2}{2}V_x^{*2} + B_{yo}^*(B_{yo}^* + b_y^*) + \frac{B_{xo}^{*2}}{2M_{Ao}^2}\left(b_y^{*2} + b_z^{*2}\right) + \frac{1}{2}\frac{\dot{b}_y^{*2} + \dot{b}_z^{*2}}{M_{Ao}^2\Omega_{io}^*\Omega_{eo}^*}$$
$$= \frac{5\beta_o}{4} + \frac{M_{Ao}^2}{2} + B_{yo}^{*2}\,. \tag{2.4.32}$$

Comparing (2.4.31) and (2.4.32), the pseudopotential $\Psi(b_y^*, b_z^*)$ can be obtained analytically and written as

$$\Psi(b_y^*, b_z^*) = \frac{5\beta_o}{4}\left\{\left[V_x^*(b_y^*, b_z^*)\right]^{1-\gamma} - 1\right\} + \frac{M_{Ao}^2}{2}\left\{\left[V_x^*(b_y^*, b_z^*)\right]^2 - 1\right\}$$
$$+ B_{yo}^* b_y^* + \frac{B_{xo}^{*2}}{2M_{Ao}^2}\left(b_y^{*2} + b_z^{*2}\right) \tag{2.4.33}$$

where the equation for $V_x^*(b_y^*, b_z^*)$ is given by (2.4.21).

However, care must be taken in evaluating the equipotential contours of Ψ from (2.4.33), or integrating the potential gradients in (2.4.28) and (2.4.29). Because V_x^* is a double value function of (b_y^*, b_z^*), and so are Ψ and its gradients.

Figure 2.18 shows the double value nature of V_x^*, which has a pear-shaped surface. Diagram (*a*) shows the cross section of V_x^* at $b_z^* = 0$. Point Z indicates where $B_\perp^* = 0$ (i.e., $b_y^* = -B_{yo}^*$, $b_z^* = 0$). Point A is the "upstream point," where $b_y^* = b_z^* = 0$ and $V_x^* = 1$. It can be seen that points X and Y divide the closed curve into two parts: the solid-dotted curve and the open-dotted curve, each of them is a single value function of b_y^*. The characteristics of these two curves and the points X and Y can be obtained by the following procedures. Differentiating (2.4.21) once with respect to b_y^* yields

$$\frac{\partial V_x^*}{\partial b_y^*} = \frac{B_{yo}^* + b_y^*}{M_{Ao}^2} \Big/ \left(\frac{1}{M_S^2} - 1\right) \tag{2.4.34}$$

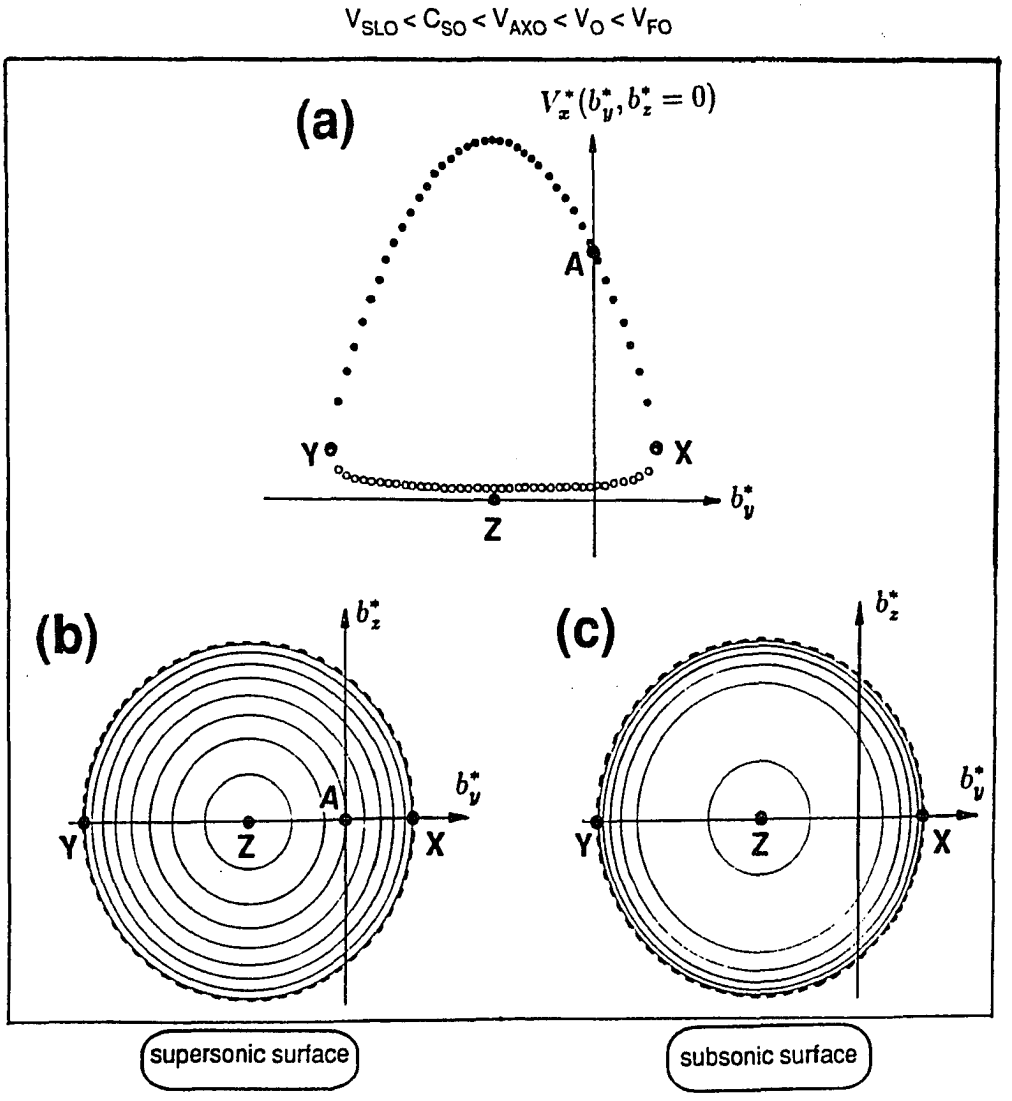

Figure 2.18 The double value nature of $V_x^*(b_y^*, b_z^*)$. (*a*) shows the cross section of V_x^* at $b_z^* = 0$, where A is the upstream point, X and Y are sonic points, and Z indicates where $B_\perp^* = 0$. The open-dotted curve is for $M_S < 1$ and the solid-dotted curve is for $M_S > 1$. (*b*) is the constant V_x^* contour diagram for $M_S > 1$. (*c*) is the constant V_x^* contour diagram for $M_S < 1$. This example is for $\beta_o = 0.01$, $\theta_o = 45°$, and $M_{Ao} = 0.76$.

where M_S is given in (2.4.24). According to (2.4.34) $\partial V_x^*/\partial b_y^* \rightarrow \infty$ as $M_S \rightarrow 1$, while from Figure 2.18*a* we can see the slope of the closed curve (i.e., $\partial V_x^*/\partial b_y^*$) approaches infinity at X and Y. Thus, we can conclude that points X and Y are for $M_S = 1$, which will be called the sonic points. According to (2.4.24), M_S increases with increasing V_x^*. Thus, the solid-dotted curve in Figure 2.18*a* is the supersonic curve ($M_S > 1$) and the open-dotted curve in Figure 2.18*a* is the subsonic curve ($M_S < 1$). Contour plots can be done only for a single value function. Therefore, the contour plots of constant V_x^* must be obtained for the supersonic and the subsonic surfaces separately. The diagram (*b*) in Figure 2.18 shows the contour plot of constant V_x^* on the supersonic surface ($M_S > 1$); and diagram (*c*) shows the contour plot of constant V_x^* on the subsonic surface ($M_S < 1$). All the contours are circles centered at point Z. This can be shown by (2.4.21) in which V_x^* is a function of $B_\perp^*$ only. The dashed circle at the outer boundary of each contour plot is the sonic circle of $M_S = 1$.

Figure 2.19 shows the pseudopotential structure and its gradient for the same example as given in Figure 2.18. Note that in this case the upstream characteristic speeds have the following relationship : $V_{F\circ} > V_\circ > V_{AX\circ} > C_{S\circ} > V_{SL\circ}$, where $V_{F\circ}$, $V_{AX\circ}$, $C_{S\circ}$, and $V_{SL\circ}$ are the upstream fast mode speed, Alfvén mode speed, sound speed, and slow mode speed, respectively. Diagram (*a*) in Figure 2.19 shows the cross section of $\partial\Psi/\partial b_y^*$ at $b_z^* = 0$, where arrows indicate the direction of increasing V_x^*. Diagram (*b*) shows the cross section of Ψ at $b_z^* = 0$. Diagram (*c*) sketches the three-dimensional structure of $\Psi(b_y^*, b_z^*)$. Notations in this figure are the same as those given in Figure 2.18. Points S and T in (*c*) are sonic points of $\Psi = 0$. The pseudopotential Ψ in (*c*) consists of a supersonic surface and a subsonic surface. The supersonic surface always lies above the subsonic surface. The two surfaces meet at

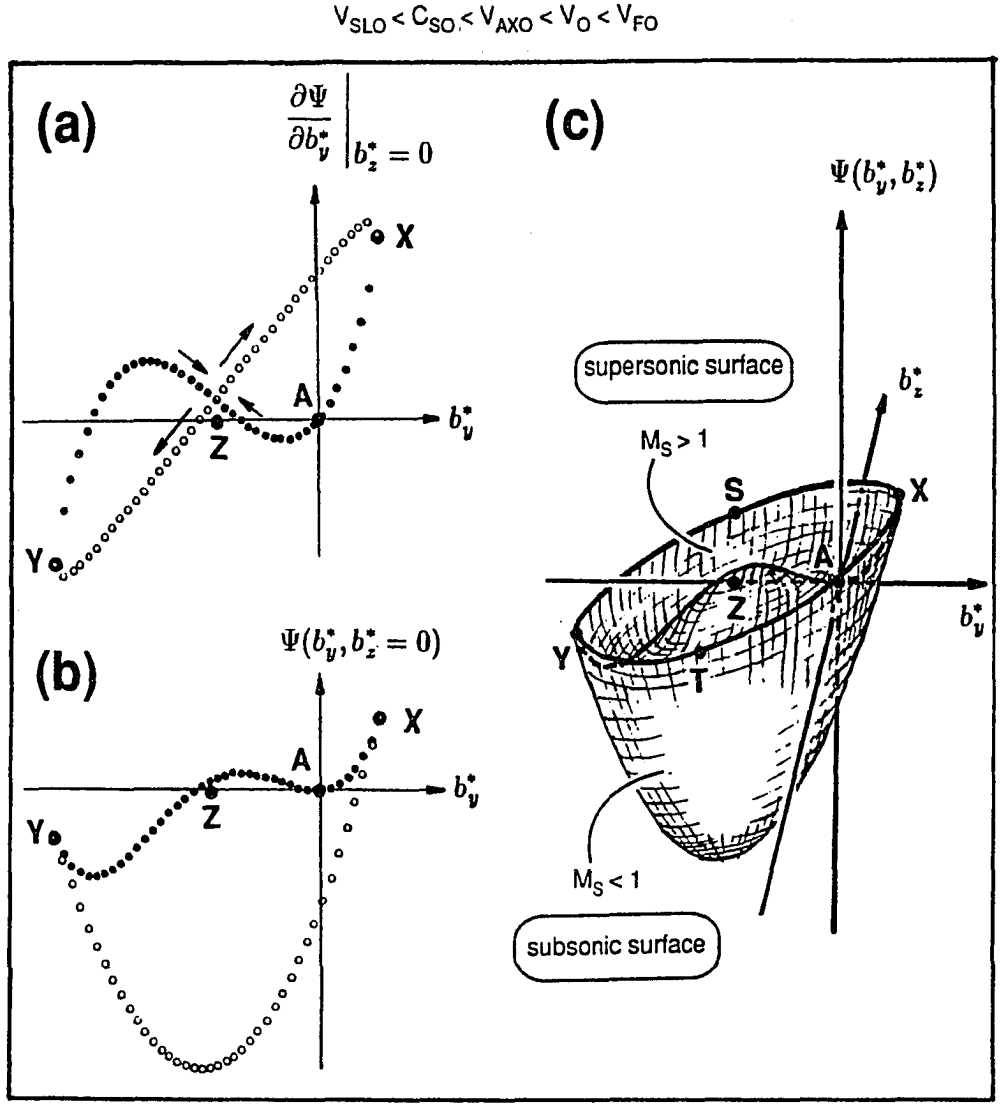

Figure 2.19 Structure of pseudopotential Ψ and its gradient. (*a*) shows the cross section of $\partial\Psi/\partial b_y^*$ at $b_z^* = 0$. (*b*) shows the cross section of Ψ at $b_z^* = 0$. (*c*) shows the three-dimensional structure of $\Psi(b_y^*, b_z^*)$. Notations and upstream parameters of this example are the same as in Figure 2.18. Points S and T in (*c*) are sonic points of $\Psi = 0$. Arrows in (*a*) indicate the increasing of V_x.

sonic loop where $M_S = 1$. For convenience, the surface that contained the upstream point A will be named as the upstream surface, which is the supersonic surface in this case. Note that the potential gradient in diagram (*a*) is a smooth and continuous function with a finite value at sonic points. Thus, the potential gradient force acting on the fictitious particle is of finite magnitude and varies smoothly and continuously, although the potential Ψ itself is not a smooth function at $M_S = 1$.

Figure 2.20 shows the contour plots of constant Ψ for the same example as shown in Figures 2.18 and 2.19. Since contour plots can only be obtained for a single value function, the contour plots of constant Ψ are obtained for (*a*) supersonic surface and (*b*) subsonic surface separately. By comparing the contours in Figure 2.20 with the cross section of Ψ in Figure 2.19*b*, we can conclude that the upstream point A is a saddle point on the supersonic surface in this case. Thick curves in Figure 2.20 indicate the equipotential contours of $\Psi = 0$. Points S and T are sonic points where $\Psi = 0$. The dashed circle at the outer boundary of each contour plot is the sonic circle as has been discussed in Figures 2.18*b* and 2.18*c*. The sonic circle is also the projection of the sonic loop (as discussed in Figure 2.19*c*) on the b_y^*-b_z^* plane. Since the sonic circle always centered at point Z with a constant and maximum value of $B_\perp^*$ and since the fictitious particle must lie on the pseudopotential surface, any motion that passes through the sonic loop must have a maximum value of $B_\perp^*$. Therefore, the condition required for a finite value of $\dot{V}_x^*$ discussed in (2.4.23)–(2.4.25) is always satisfied. This result together with the characteristics of potential gradient force, which varies smoothly and continuously at the sonic points as discussed in Figure 2.19, we can conclude that the solutions are of finite-value and vary continuously even at $M_S = 1$. This is in contrast with the previous studies [e.g., *Kakutani et al.*, 1967; *Crevier*

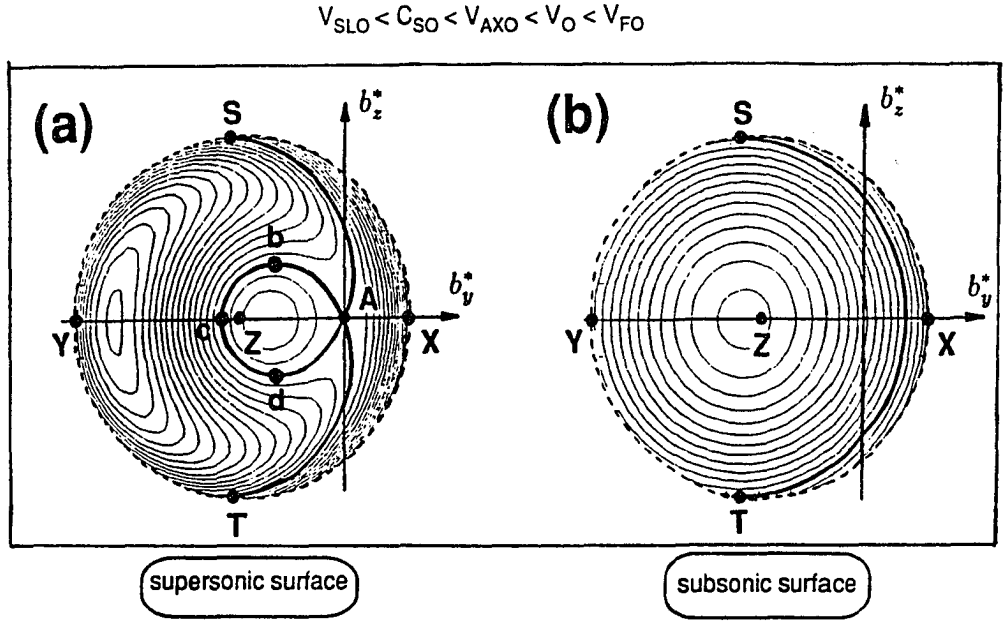

Figure 2.20 Plots of constant Ψ contours for the same example as given in Figure 2.19. (*a*) is for the supersonic surface and (*b*) is for the subsonic surface of Ψ. The dashed curve on the outer boundary of each contour plot is the sonic circle ($M_S = 1$). Thick curves indicate contours for $\Psi = 0$. Notations in this figure are the same as those given in Figures 2.18 and 2.19. A right-hand polarized, fast-mode rarefaction soliton solution can be found with magnetic hodogram along the inner-loop $\Psi = 0$ contour in panel (*a*), i.e., *A–b–c–d–A* for $B_{xo} > 0$. Density and field profiles of these soliton solutions are sketched in Figure 2.21. A two-fluid compressional nonlinear wave solution can be obtained from this figure, which is a rotational structure with magnetic field hodogram along the $\Psi = 0$ contour from A to T when $B_{xo} > 0$. (It is from A to S if $B_{xo} < 0$.) The fictitious particle will be trapped at point T with small amplitude waves on an electron-scale trajectory. The sonic point T is a trapping point for $B_{xo} > 0$, because the potential gradient force on both supersonic surface and subsonic surface can only allow an ion-scale trajectory starting from S toward T but not leaving T toward S. It can be shown that all the sonic points on the half sonic circle *X–T–Y* have the same characteristic as point T and all the sonic points on the half sonic circle *X–S–Y* have the same characteristic as point S. For $B_{xo} > 0$, sonic points on the half circle *X–T–Y* will be called *attracters* because an ion-scale trajectory can only reach to that point but are not allowed to leave. On the other hand, sonic points on the half circle *X–S–Y* will be called *emitters* for $B_{xo} > 0$, because the potential gradient force at that point only allows an ion-scale trajectory to leave but not to return nor to enter that point. The characteristics of attracters and emitters will be used later in Sections 2.4.4 and 2.4.5.

and Tidman, 1970] in which the solution is believed to diverge on the sonic loop due to the incorrect conclusion that $\dot{V}_x^* \to \infty$ as $M_S \to 1$.

The pseudopotential method will not only help us to overcome the difficulty raised from (2.4.23) when M_S approaches 1, but also enable us to study the nonlinear wave solutions qualitatively and systematically, even without solving (2.4.19), (2.4.20), and (2.4.23).

(C) *Qualitative Solutions*

We shall use the case shown in Figures 2.18–2.20 as an example to demonstrate how to obtain nonlinear wave solutions, qualitatively, without numerically integrating (2.4.19) and (2.4.20). From the discussion of (2.4.30), the magnetic field variation of nonlinear wave with $M_{A\circ} \ll \cos\theta_\circ (m_i/m_e)^{1/2}$ is predominantly governed by the ion-scale trajectory, which is characterized by motion along an equipotential contour with polarization described in Figure 2.17. Under a uniform upstream boundary condition, the nonlinear wave solution in ion-scale trajectory can be obtained when there is a finite-extent equipotential contour passing through the upstream point A. Using this guideline, a nonlinear wave solution can be found with magnetic field hodogram along the equipotential contour A–b–c–d–A in Figure 2.20 for $B_{x\circ} > 0$, or along A–d–c–b-A for $B_{x\circ} < 0$.

Figure 2.21 sketches the spatial profiles $B_y(x)$, $B_z(x)$, $B_\perp(x)$, and $\rho(x)$ of this solution A–b–c–d–A. The spatial gradients of these curves are determined based on the potential gradient perpendicular to the equipotential contour, which varies with minimum gradient near point A and maximum gradient at point c. Note that the fictitious particle moves faster when the potential gradient force is larger. The spatial profile of $B_\perp^*(x)$ is determined based on the distance from the equipotential contour to point Z, where $B_\perp^* = 0$, as denoted in Figure 2.20. The density profile is obtained

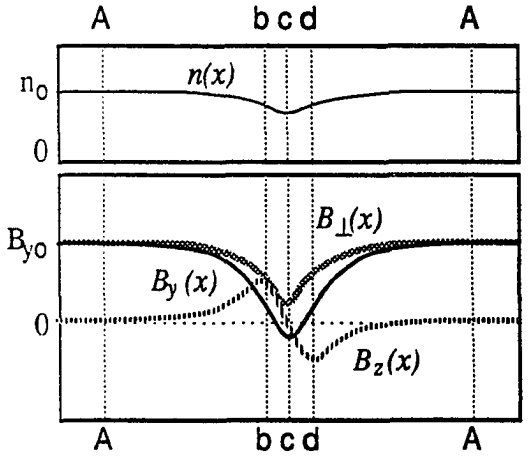

Figure 2.21 Sketched field and density profiles of soliton solution associated with the contour *A–b–c–d–A* shown in Figure 2.20.

based on the following procedure. According to the discussion in Figure 2.18, the constant V_x^* contours are circles centered at $B_\perp^* = 0$, where V_x^* is of maximum if $M_S > 1$, but of minimum if $M_S < 1$. Therefore, the variations of $V_x^*(x)$ and $B_\perp^*(x)$ are in phase if $M_S < 1$, but out of phase if $M_S > 1$. According to (2.4.8), the variations between density profile $\rho(x)$ and normal flow speed $V_x(x)$ are out of phase. Thus, we can conclude that the variations of $\rho(x)$ and $B_\perp(x)$ are in phase if $M_S > 1$, but out of phase if $M_S < 1$. Since the equipotential contour *A–b–c–d–A* is on the supersonic surface, the density profile in Figure 2.21 is sketched qualitatively to be in-phase with respect to $B_\perp(x)$. According to these spatial profiles, we can conclude that solution along *A–b–c–d–A* in Figure 2.20 is a right-hand polarized rarefaction soliton solution.

Another nonlinear wave solution can be obtained from Figure 2.20, which is a rotational structure with magnetic field hodogram along the $\Psi = 0$ contour from A to T when $B_{xo} > 0$. (It is from A to S if $B_{xo} < 0$.) The fictitious particle will be trapped at point T with small amplitude waves on an electron-scale trajectory. The sonic point T is a trapping point for $B_{xo} > 0$, because the potential gradient force on both

supersonic surface and subsonic surface can only allow an ion-scale trajectory starting from S toward T but not leaving T toward S. It can be shown that all the sonic points on the half sonic circle X–T–Y have the same characteristic as point T and all the sonic points on the half sonic circle X–S–Y have the same characteristic as point S. For $B_{x\circ} > 0$, sonic points on the half circle X–T–Y will be called *attracters* because an ion-scale trajectory can only reach to that point but are not allowed to leave. On the other hand, sonic points on the half circle X–S–Y will be called *emitters* for $B_{x\circ} > 0$, because the potential gradient force at that point only allows an ion-scale trajectory to leave but not to return nor to enter that point. The characteristics of attracters and emitters will be used later in Sections 2.4.4 and 2.4.5. The nonlinear wave solution along A–T is a compressional two-fluid rotational structure. It is a compression wave because the curve A–T is on the supersonic surface, and because the downstream transverse magnetic field magnitude (i.e., the distance between Z and T) is larger than it on the upstream side (i.e., the distance between Z and A). The two-fluid rotational structure was first obtained by *Lyu and Kan* [1989*b*].

2.4.3 Constant-Profile Nonlinear Wave Solutions With Uniform Upstream Boundary Conditions

Constant-profile, analytical nonlinear wave solutions in a finite-temperature, two-fluid plasma can be obtained from the pseudopotential method as discussed in the previous section. These nonlinear wave solutions will be discussed based on the upstream flow speed $V_\circ$ relative to several characteristic speeds on the upstream side, because structures of pseudopotentials are found to depend on the relative magnitude of $V_\circ$ in comparison with those characteristic speeds. Upstream characteristic speeds discussed here consist of sound speed $C_{S\circ}$, fast mode speed $V_{F\circ}$, slow mode speed

$V_{SL\circ}$, and Alfvén mode speed $V_{AX\circ}$. General definitions of those characteristic wave speeds have been given in equations (1.1.2)–(1.1.7).

Figure 2.22 shows the structure of pseudopotential Ψ for various upstream conditions as indicated on top of each panel. The upper diagram in each panel shows cross section of Ψ at $b_z^* = 0$. The lower diagram of each panel shows the equipotential contours on the upstream surface, except for panel (*g*) in which both surfaces of Ψ are shown. Notations used in this figure are the same as given in Figures 2.18–2.20. The helical curve with the arrow and label indicates hodogram and polarization direction of a constant-profile nonlinear wave magnetic field in ion-scale trajectory, for $B_{x\circ} > 0$. Properties of these constant-profile nonlinear wave solutions will be discussed later. A brief description on the characteristic structure of pseudopotentials shown in Figure 2.22*a–m* is given below.

For $V_{SL\circ} < V_\circ < V_{F\circ}$, as those shown in panels (*a*)–(*g*) of Figure 2.22 and the one shown in Figures 2.19–2.20, structure of pseudopotential for $V_\circ < C_{S\circ}$ and structure of pseudopotential for $V_\circ > C_{S\circ}$ are similar but are upside-down to each other. Likewise, structure of pseudopotential for $V_\circ \leq V_{SL\circ}$ and structure of pseudopotential for $V_\circ \geq V_{F\circ}$ are similar but are upside-down to each other, as shown in panels (*h*)–(*m*) of Figure 2.22. When $V_\circ = V_{AX\circ}$, structure of pseudopotential is symmetric to the point Z. Thus, all the equipotential contours are circles centered at point Z as shown in panels (*a*) and (*b*) of Figure 2.22. The Ψ becomes asymmetric to the Z on b_y^* direction when $V_\circ$ deviates from $V_{AX\circ}$. Namely, the pseudopotential tilts up on the side of Y with decreasing $V_\circ$ from $V_{AX\circ}$, but tilts down on the side of Y with increasing $V_\circ$ from $V_{AX\circ}$. The equipotential contour passing through points A and B in panels (*a*) and (*b*) splits into two loops when $V_\circ$ slightly deviates from $V_{AX\circ}$ as shown in panels (*c*)–(*f*) of Figure 2.22. The two loops have a common point at either

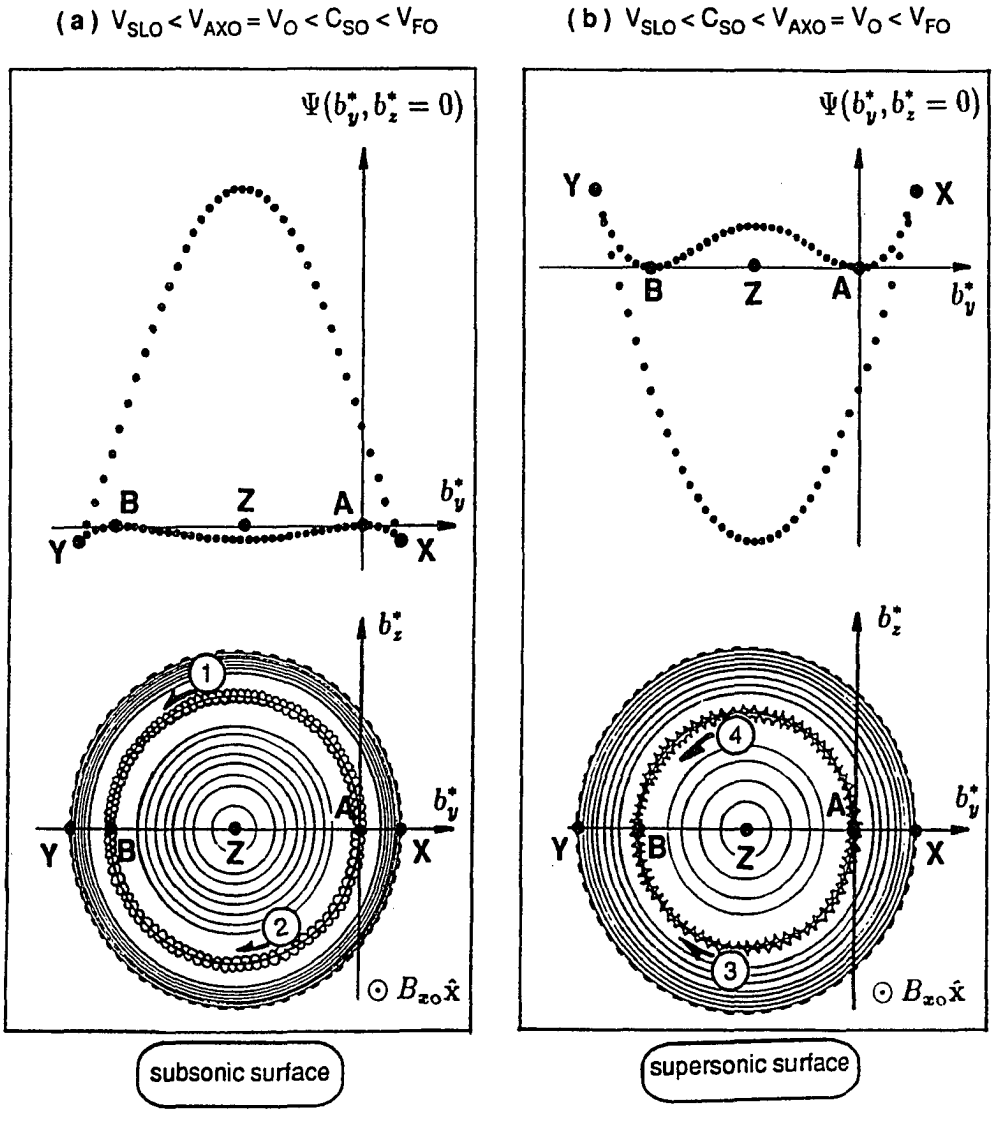

Figure 2.22 Illustrating of pseudopotential structure for different upstream parameters as denoted on top of each panel. The upper diagram shows the cross section of Ψ at $b_z^* = 0$. The lower diagram shows the equipotential contours of the upstream surface (except in panel (*g*) where both surfaces of Ψ are shown). Notations used in this figure are the same as given in Figures 2.17–2.19. Helical curves with arrows and labels indicate the magnetic field hodogram of nonlinear constant-profile wave solutions associated with the ion-scale trajectory for $B_{xo} > 0$. The example shown in panel (*a*) is for $\theta_o = 45°$, $M_{Ao} = 0.7071$, and $\beta_o = 1.8$. Example shown in panel (*b*) is for $\theta_o = 45°$, $M_{Ao} = 0.7071$, and $\beta_o = 0.01$. Solutions ①–④ are circularly polarized incompressible Alfvén wave train solutions of finite-extent or rotational structures with rotation angle less than 360°. Wavelength of these nonlinear waves is of the order of 500–1000 ion inertial lengths.

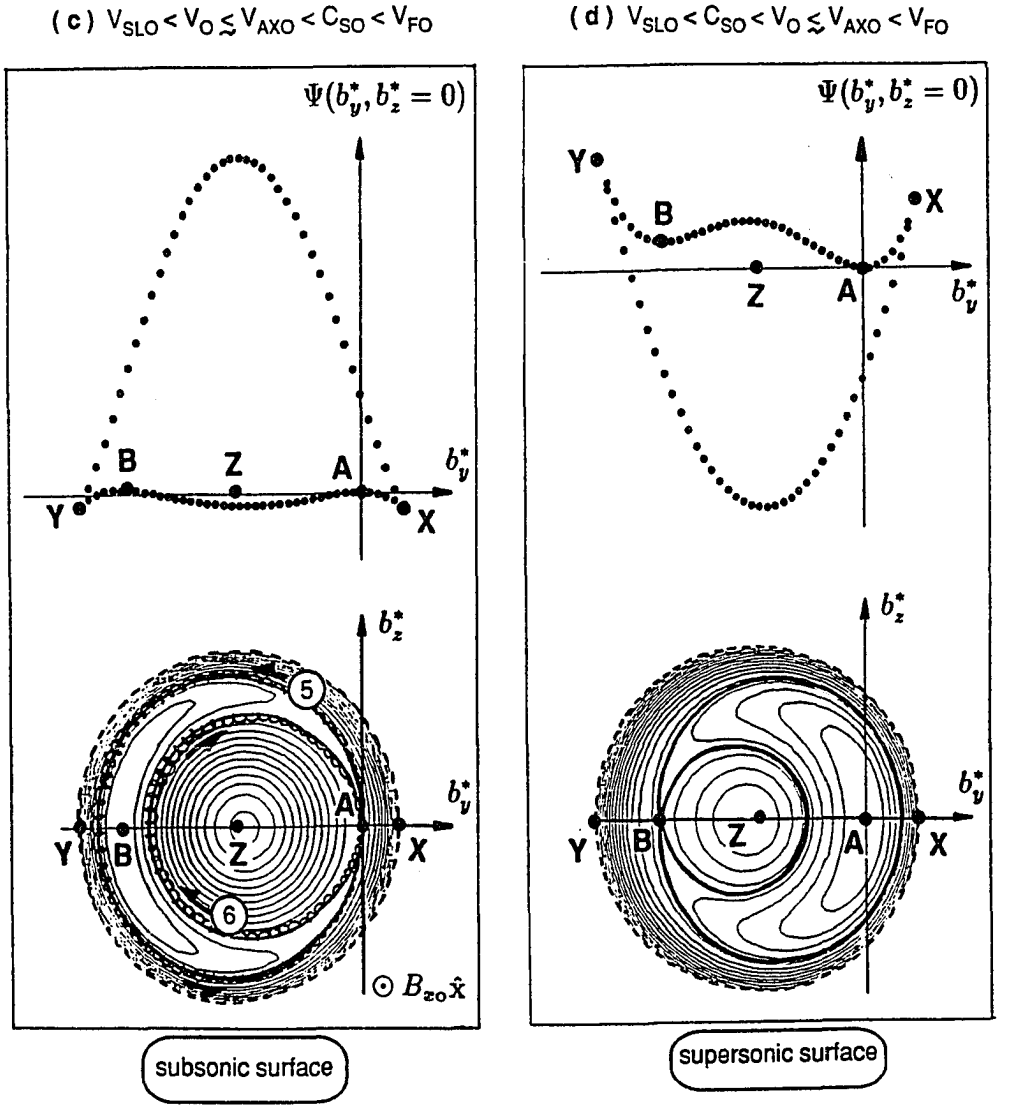

Figure 2.22 (Continued) Example shown in panel (*c*) is for $\theta_o = 45°$, $M_{Ao} = 0.705$, and $\beta_o = 1.8$. Example shown in panel (*d*) is for $\theta_o = 45°$, $M_{Ao} = 0.69$, and $\beta_o = 0.01$. Solution ⑤ along the outer-loop $\Psi = 0$ contour in panel (*c*) is a right-hand polarized rarefaction Alfvén-mode soliton solution. Solution ⑥ along the inner-loop $\Psi = 0$ contour in panel (*c*) is a left-hand polarized compression slow-mode soliton solution, which is strongly coupled with Alfvén mode in this example. Wavelengths of these nonlinear waves are of a few tens of ion inertial lengths. No constant profile nonlinear wave solutions with uniform upstream boundary conditions can be found in the case of panel (*d*). Quasi-stationary nonlinear wave solutions may be found in both cases shown in panels (*c*) and (*d*), which will be discussed later in Section 2.4.5.

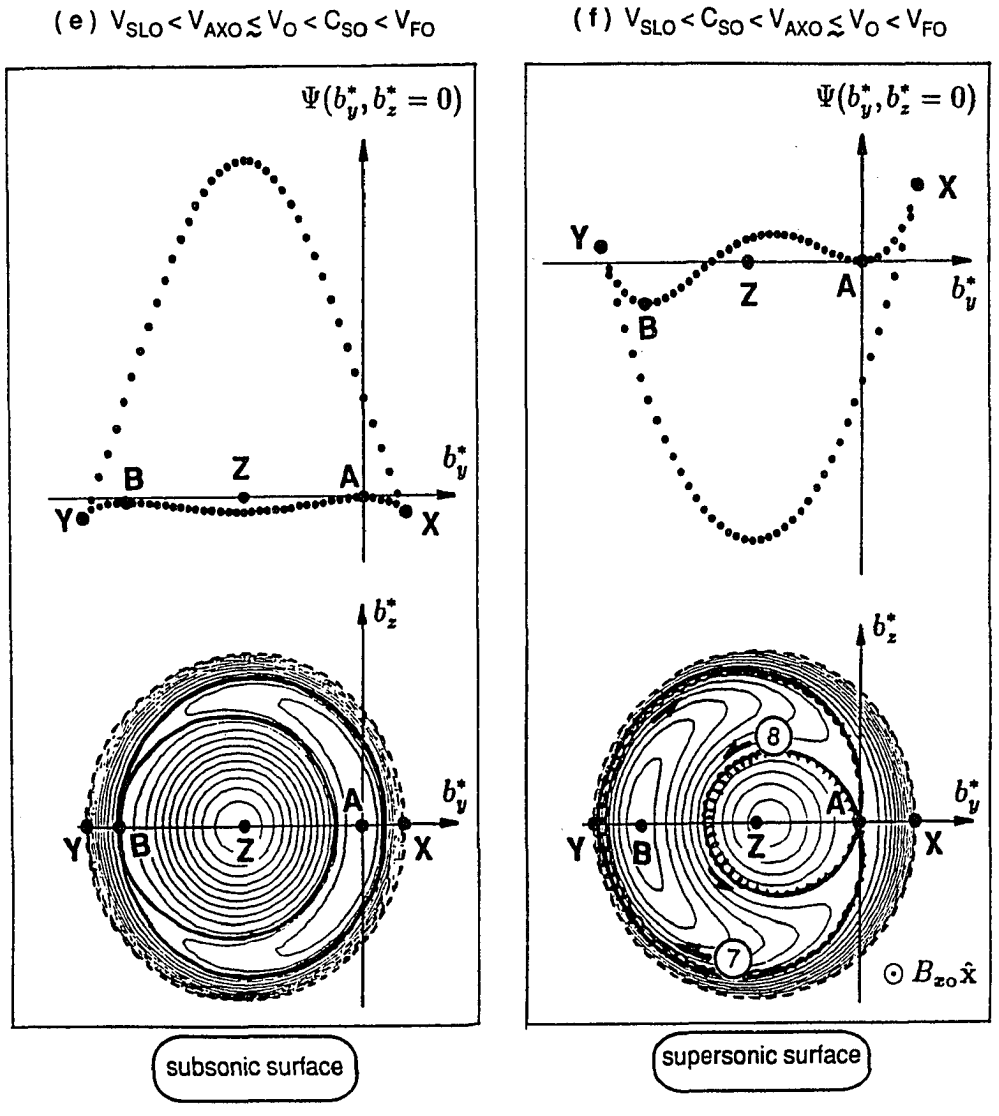

Figure 2.22 (Continued) Example shown in panel (*e*) is for $\theta_o = 45°$, $M_{Ao} = 0.709$, and $\beta_o = 1.8$. Example shown in panel (*f*) is for $\theta_o = 45°$, $M_{Ao} = 0.73$, and $\beta_o = 0.01$. Solution ⑦ along the outer-loop $\Psi = 0$ contour in panel (*f*) is a left-hand polarized compression Alfvén-mode soliton solution. Solution ⑧ along the inner-loop $\Psi = 0$ contour in panel (*f*) is a right-hand polarized rarefaction fast-mode soliton solution, which is strongly coupled with Alfvén mode in this example. Wavelengths of these nonlinear waves are of a few tens of ion inertial lengths. No constant profile nonlinear wave solutions with uniform upstream boundary conditions can be found in the case of panel (*e*). Quasi-stationary nonlinear wave solutions may be found in both cases of panels (*e*) and (*f*), which will be discussed later in Section 2.4.5.

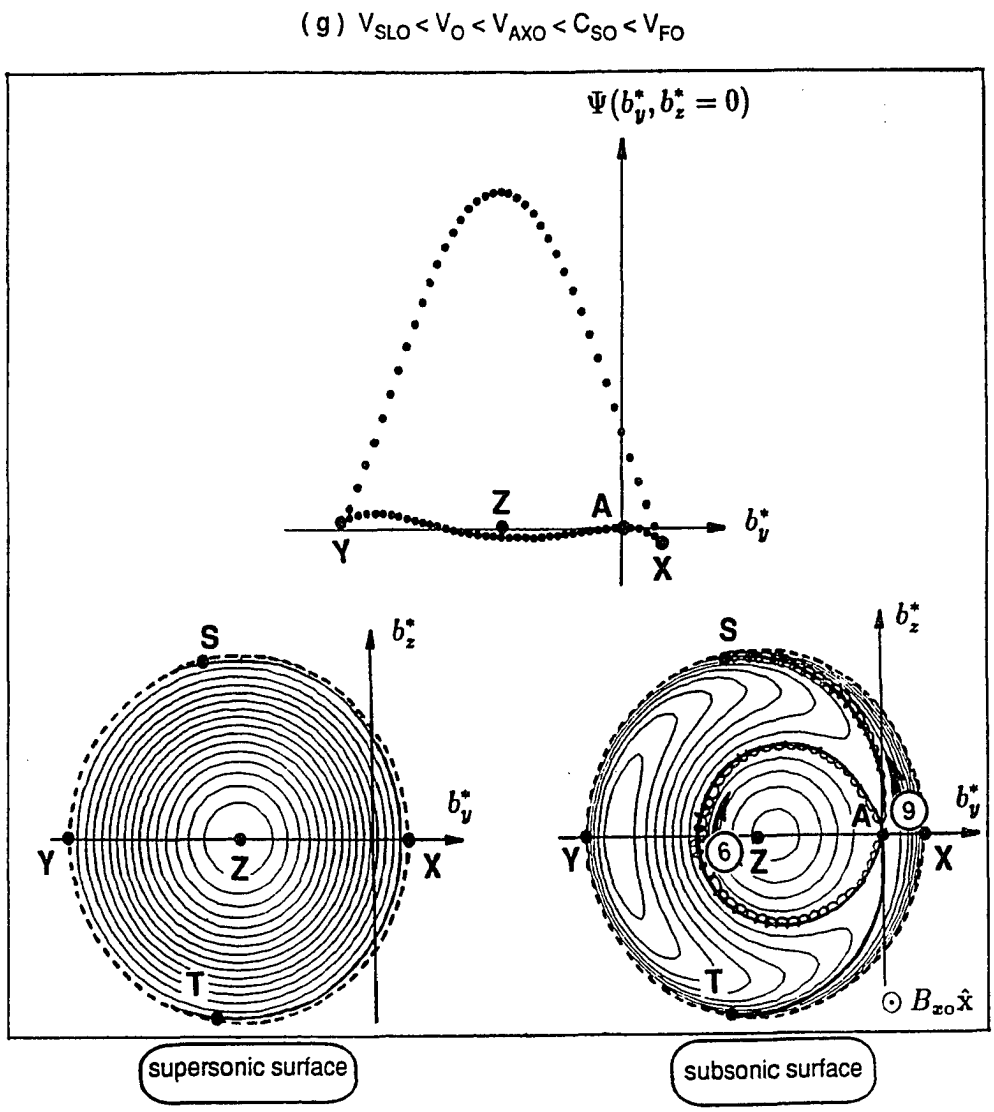

Figure 2.22 (Continued) Example shown in panel (*g*) is for $\theta_o = 45°$, $M_{Ao} = 0.697$, and $\beta_o = 1.8$. Solution ⑥ along the inner loop of $\Psi = 0$ contours is a left-hand polarized compression slow-mode soliton solution. Solution ⑨ along the arc of $\Psi = 0$ contours is a right-hand polarized rarefaction Alfvén-mode rotational structure. In this case, for $B_{xo} > 0$, all the sonic points on the half circle X–S–Y are attracters, and all the sonic points on the other half circle X–T–Y are emitters. Additional two-fluid rotational discontinuities can be found, which will be discussed later in Figures 2.25 and 2.28.

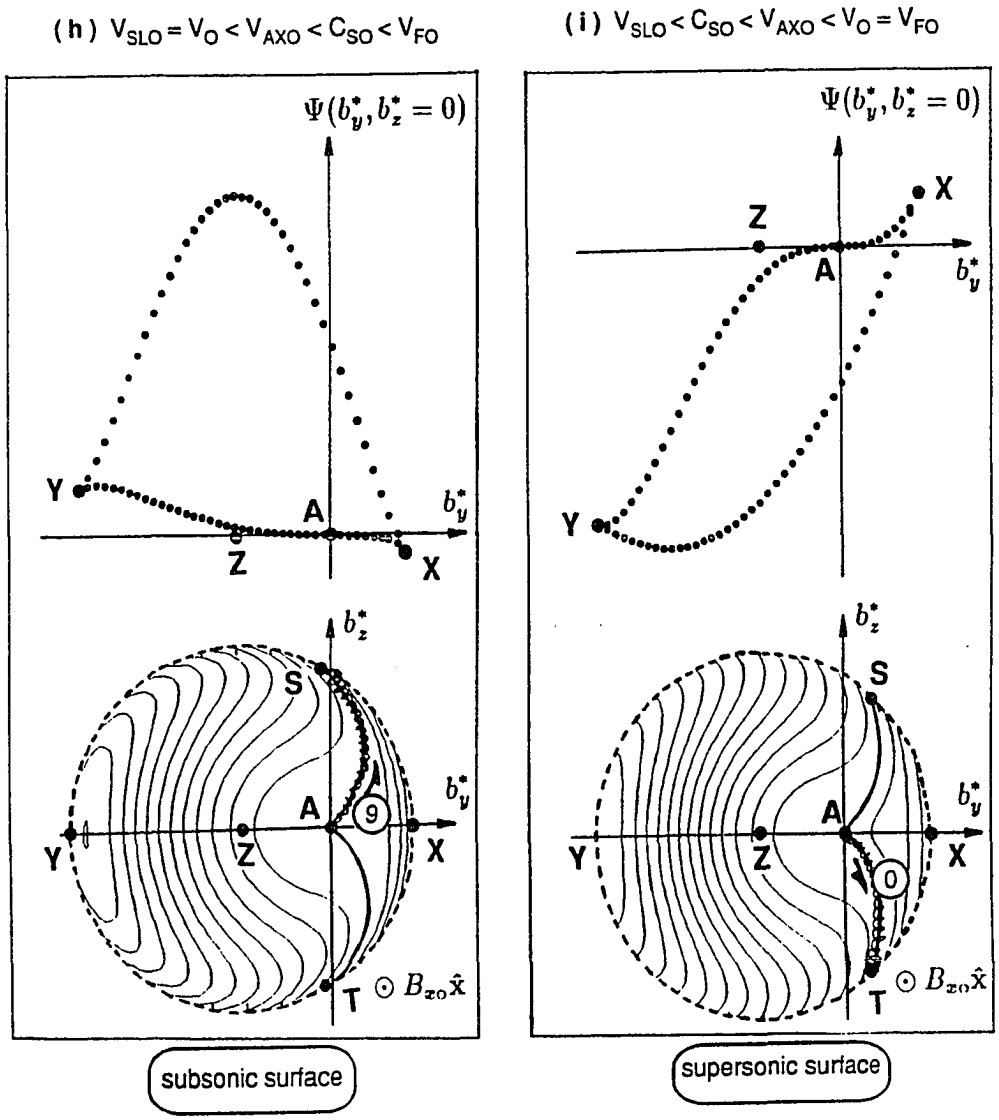

Figure 2.22 (Continued) Example shown in panel (*h*) is for $\theta_o = 45°$, $M_{Ao} = 0.63538$, and $\beta_o = 3$. Example shown in panel (*i*) is for $\theta_o = 45°$, $M_{Ao} = 1.002$, and $\beta_o = 0.01$. The amplitude of inner-loop soliton solutions vanishes as $V_o = V_{SLo}$ or $V_o = V_{Fo}$. But the Alfvén-mode soliton solutions ⑨ and ⓪, along the arc of $\Psi = 0$ contours in panels (*h*) and (*i*) may still of finite amplitude.

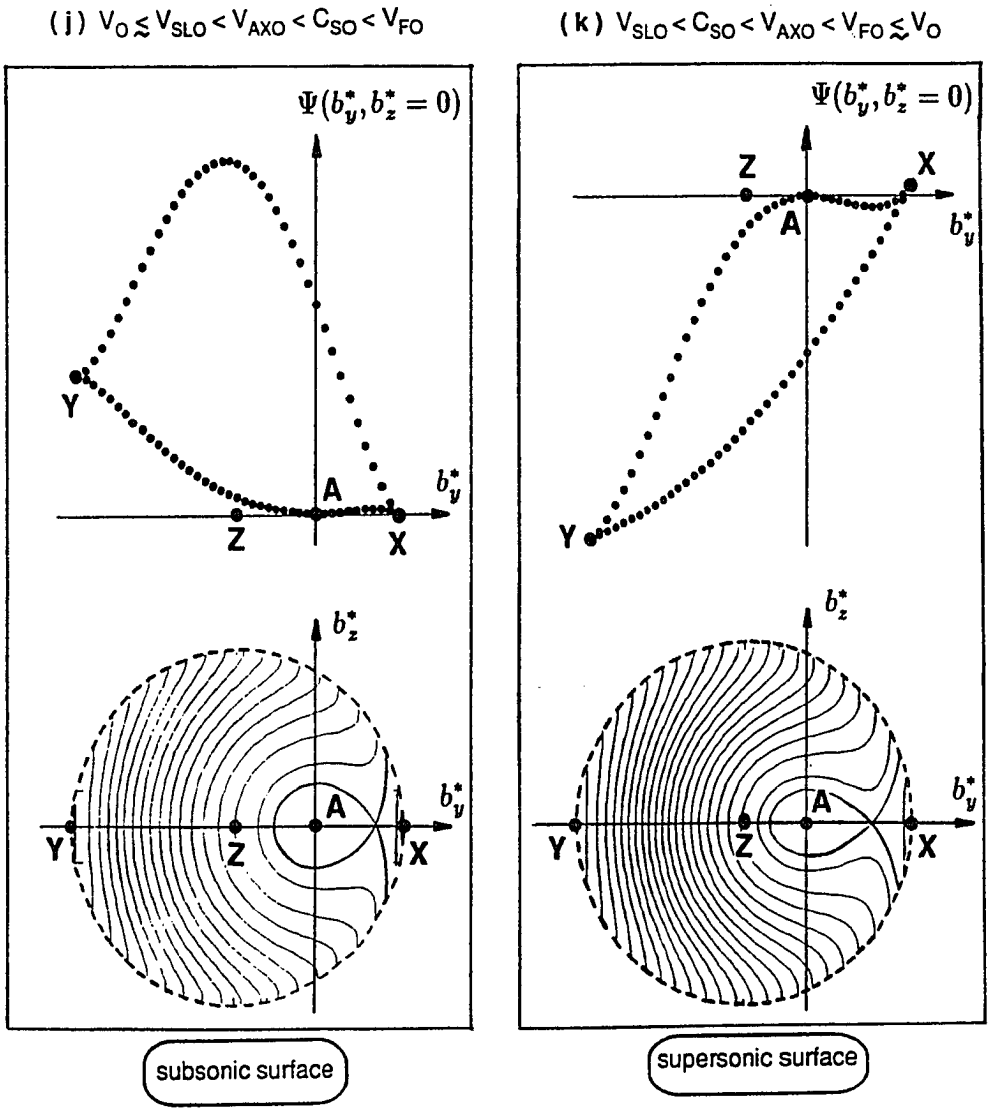

Figure 2.22 (Continued) Example shown in panel (*j*) is for $\theta_o = 45°$, $M_{Ao} = 0.52$, and $\beta_o = 3$. Example shown in panel (*k*) is for $\theta_o = 45°$, $M_{Ao} = 1.5$, and $\beta_o = 0.01$. No constant profile nonlinear wave solutions with uniform upstream boundary conditions can be found in these two examples. Quasi-stationary nonlinear wave solutions may be found in these two cases, which will be discussed later in Section 2.4.5.

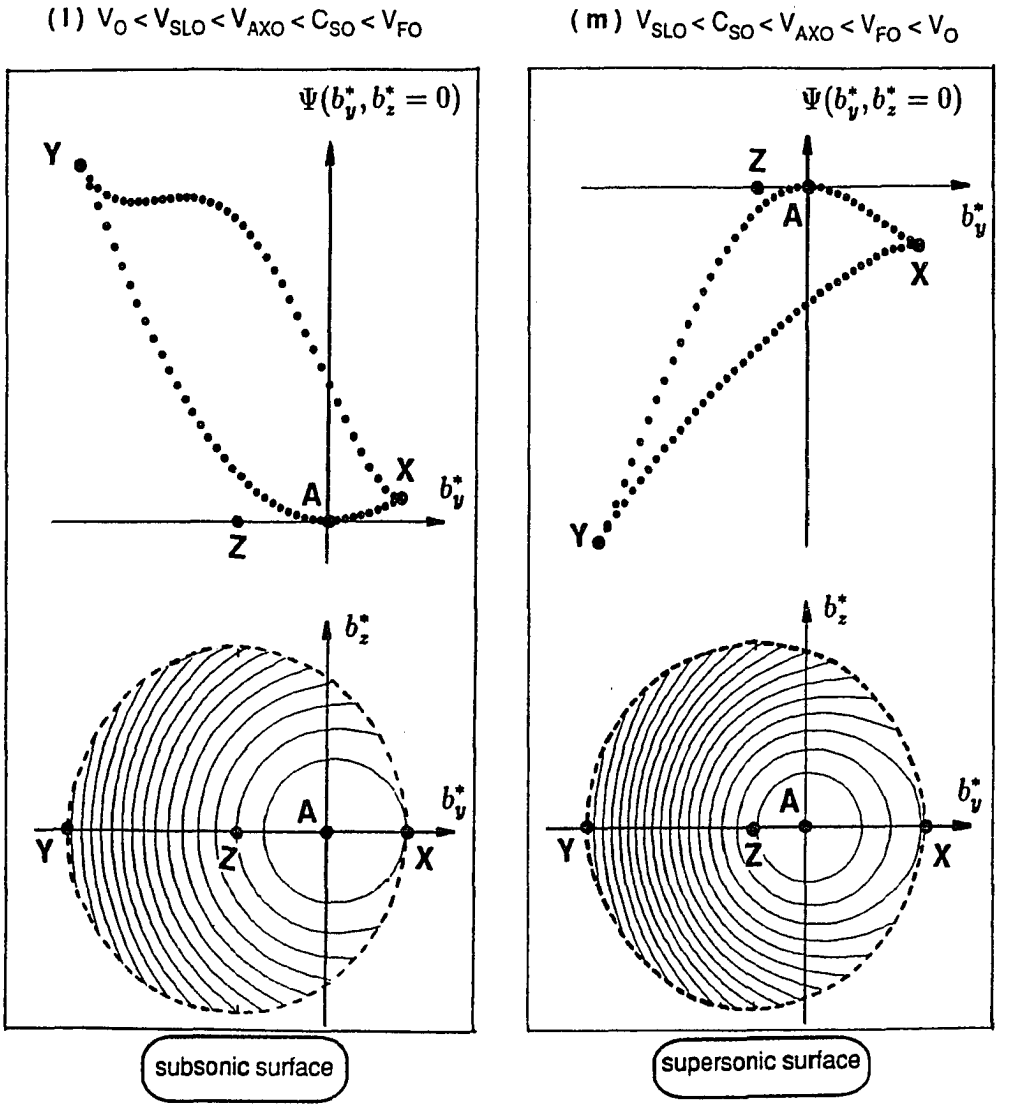

Figure 2.22 (Continued) Example shown in panel (*l*) is for $\theta_o = 45°$, $M_{Ao} = 0.295$, and $\beta_o = 1.8$. Example shown in panel (*m*) is for $\theta_o = 45°$, $M_{Ao} = 2.5$, and $\beta_o = 0.8$. No constant profile nonlinear wave solutions with uniform upstream boundary conditions can be found in these two examples. But quasi-stationary nonlinear wave solutions may be found in these two cases, which will be discussed later in Section 2.4.5.

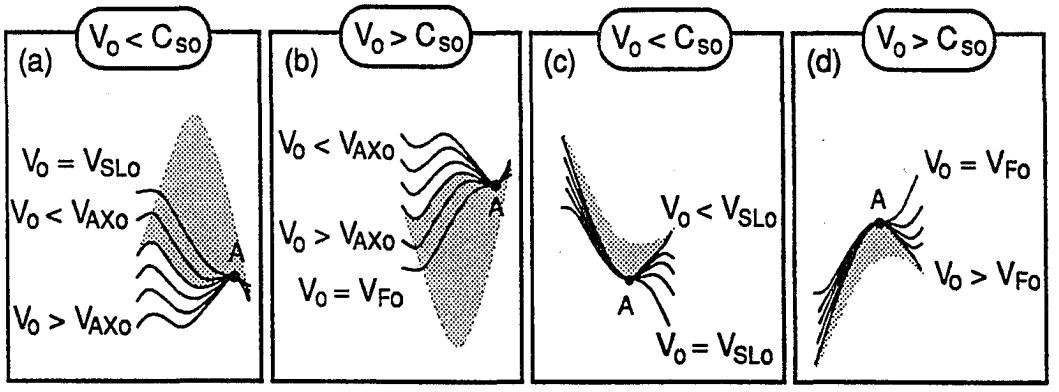

Figure 2.23 Characteristics of pseudopotential structures under various upstream conditions. The solid curves indicate the cross section of upstream surface of Ψ at $b_z = 0$.

point A or point B, which is also a saddle point. When V_o further deviates from V_{AXo}, the outer loop may intersect with the sonic circle (dashed circle). Two examples can be seen in Figure 2.20 and Figure 2.22*g*. They are evolved from panels (*f*) and (*c*) of Figure 2.22, respectively. Similar results can be obtained for the other two cases shown in panels (*d*) and (*e*). The upstream point A becomes a "chair point" when V_o is equal to V_{SLo} or V_{Fo}, as shown in panels (*h*) and (*i*). The saddle point shifts to the right-hand side of A, and A becomes a minimum point as V_o decreasing from V_{SLo}, but becomes a maximum point as V_o increasing from V_{Fo}, as shown in panels (*j*)–(*m*) of Figure 2.22.

It may be helpful to summarize the pseudopotential structures in a way as shown in Figure 2.23. Figure 2.23 sketches the cross section of the upstream surface of Ψ at $b_z = 0$, with various upstream conditions. Panel (*a*) is for $V_o < C_{So}$ and V_o varies from greater than V_{AXo} to equal to V_{SLo}. Panel (*b*) is for $V_o > C_{So}$ and V_o varies from less then V_{AXo} to equal to V_{Fo}. Panel (*c*) is for $V_o \leq V_{SLo}$. Panel (*d*) is for $V_o \geq V_{Fo}$.

These curves will give us useful information when we consider the quasi-stationary nonlinear wave solutions in Section 2.4.5.

Now, we shall go back to Figure 2.22 to examine the property of those constant-profile nonlinear wave solutions in the ion-scale trajectory as indicated by helical curves for $B_{xo} > 0$. Our conclusions on density and magnetic field variations for each nonlinear wave solution are obtained based on the general method introduced in Section 2.4.2(C).

(A) *Oblique Incompressible Alfvén Wavetrains and MHD Rotational Discontinuities*

When $V_o = V_{AXo}$, nonlinear oblique Alfvén wavetrain solutions exist as labelled by ①–④ in Figures 2.22*a* and 2.22*b*. The wavetrain solutions are characterized by constant density and circular polarization. Their wavelengths are much greater than the ion gyroradius (at least 600–1000 c/ω_{pi}). This means that these waves exist only in the MHD limit. The arrows in Figure 2.22 indicate the polarization directions for $B_{xo} > 0$. The polarization is right-handed for solutions ① and ④, but is left-handed for solutions ② and ③. These nonlinear Alfvén wavetrain solutions can be of finite extent if required by the boundary condition, because the equipotential contour associated with solutions ①–④ is on a flat circle passing through A and B. In addition to the constant-amplitude, finite-extent, wavetrain solutions, incompressible MHD rotational discontinuities can also exist when the rotation angle is less than 360°. Note that the thickness of these rotational discontinuities is at least a few hundred ion inertial lengths, which is much thicker than the observed rotational discontinuities in the solar wind or at the magnetopause.

(B) *Oblique Two-Fluid Soliton Solutions*

According to the discussion in Section 2.4.2(C), soliton solutions can be obtained when there is a finite-extent, closed-loop, equipotential contour passing through A,

with non-uniform potential gradient force along the equipotential contour and with minimum potential gradient at point *A*. According to this guideline, four types of soliton solutions, ⑤–⑧, are found in Figure 2.22. The characteristics of these soliton solutions are given below.

Soliton solution ⑤ in Figure 2.22*c* is a right-hand polarized rarefaction soliton solution with magnetic field hodogram along the outer-loop $\Psi = 0$ contour. Solution ⑤ exists when V_o is slightly less than V_{AXo} and $V_{AXo} < C_{So}$. Variations of density and total magnetic field are out of phase for this solution. Soliton solution with similar characteristics has been predicted by Table 2.1, based on the two-fluid dispersion at shaded region *AX*1 of Figure 1.2. Therefore, solution ⑤ can be called an Alfvén-mode rarefaction soliton. But this soliton solution can no longer exist if the outer-loop $\Psi = 0$ contour intersects with the sonic curve as V_o further increases and deviates from V_{AXo}. Apparently, this solution behavior has not been included in the quasi-linear solutions listed in Table 2.1.

Soliton solution ⑥ in Figures 2.22*c* and 2.22*g* is a left-hand polarized compression soliton solution with magnetic field hodogram along the inner-loop $\Psi = 0$ contour. Solution ⑥ exists when $V_{SLo} < V_o < V_{AXo} < C_{So}$. Variations of density and total magnetic field are out of phase for this solution. Soliton solution with similar characteristics as $V_o \rightarrow V_{SLo}$, has been predicted by Table 2.1, based on the two-fluid dispersion at shaded region *SL* of Figure 1.2. Therefore, solution ⑥ may be called a slow-mode compression soliton (especially, when $V_o \rightarrow V_{SLo}$). However, solution ⑥ is not fully identical to the slow-mode soliton solution predicted in Table 2.1, because nonlinear-coupling between slow-mode and Alfvén-mode takes place when $V_o \rightarrow V_{AXo}$. This coupling effect can be understood by considering the variation of density profile at different V_o. As V_o increases from V_{SLo} to V_{AXo}, the inner-loop

equipotential contour is enlarged from a small loop near A, to a large and highly circular loop centered at Z. Since the variations of $\rho(x)$ and $B_\perp(x)$ are out of phase, the maximum variations of $\rho(x)$ and $B_\perp(x)$ should occur when the inner-loop equipotential contour is connected to point Z. Thus, the amplitude of $\rho(x)$ does not increase monotonically with increasing V_o from V_{SLo} to V_{AXo}. The soliton characteristic is different from the one shown in Figure 2.8(*1a*). This result indicates the increasing influence of Alfvén-mode dispersion on the slow-mode soliton ⑥ as V_o approaches to V_{AXo}. The nonlinear-coupling effect between slow-mode and Alfvén-mode has certainly not been included in the quasi-linear solutions given in Table 2.1.

Soliton solution ⑦ in Figure 2.22*f* is a left-hand polarized compression soliton solution with magnetic field hodogram along the outer-loop $\Psi = 0$ contour. Solution ⑦ exists when V_o is slightly greater than V_{AXo} and when $V_{AXo} > C_{So}$. Variations of density and total magnetic field are in phase for this solution. A soliton solution with similar characteristics has been predicted by Table 2.1, based on the two-fluid dispersion at shaded region $AX2$ of Figure 1.2. Thus, solution ⑦ can be called the Alfvén-mode compression soliton. Again, this outer-loop soliton solution no longer exists, as the outer-loop equipotential contour intersects with the sonic curve. It will turn into a two-fluid rotational discontinuity as discussed in Figure 2.20.

Soliton solution ⑧ in Figure 2.22*f* is a right-hand polarized rarefaction soliton solution with magnetic field hodogram along the inner-loop $\Psi = 0$ contour. Solution ⑧ exists when $C_{So} < V_{AXo} < V_o < V_{Fo}$. Soliton solution ⑧ can also be found in Figure 2.20 associated with the inner-loop $\Psi = 0$ contour. Variations of density and total magnetic field are in phase for this solution. A soliton solution with similar characteristics as $V_o \rightarrow V_{Fo}$, has been predicted by Table 2.1, based on the two-fluid dispersion at shaded region F of Figure 1.2. Therefore, solution ⑧ may be named

as fast-mode rarefaction soliton (particularly, as $V_o \rightarrow V_{Fo}$). However, based on a similar argument as discussed in solution ⑥, the solution ⑧ is not fully identical to the fast-mode soliton solution predicted in Table 2.1. Namely, the fast-mode dispersion effect alone can lead to increasing density variation as V_o deviates from V_{Fo}; whereas, nonlinear-coupling between fast-mode and Alfvén-mode will lead to decreasing density variation as $V_o \rightarrow V_{AXo}$.

In addition to the soliton solution ⑤–⑧, there are two other types of soliton solutions, which are not shown in Figure 2.22, because they are not on ion-scale trajectory. One of them is the whistler soliton solution, which exists when $V_o > V_{W\max o}$. Whistler soliton is expected to be found according to Table 2.1. The pseudopotential structure for $V_o > V_{W\max o}$ is similar to the one given in Figure 2.22*m* but with a much larger potential gradient. Since, the condition of $V_o \geq V_{W\max o}$ is consistent with the condition $M_{Ao} \approx \cos\theta_o (m_i/m_e)^{1/2}$, which can lead to weak chaotic trajectory solitons. By solving (2.2.19), (2.2.20), and (2.2.23), it can be shown that the hodogram of the wave magnetic field in the whistler solitons can be described as follows. After an infinitesimal displacement near point *A*, the fictitious particle can fall down the potential surface on a hybrid-scale trajectory due to strong potential gradient force. After the fictitious particle picks up sufficient kinetic energy from the potential drop, the pseudoinertia term in (2.4.30) will become large enough to turn around the fictitious particle by an electron-scale trajectory motion and then the particle will return to the upstream point *A*, owing to the conservation of pseudoenergy as described by (2.4.31). Weak chaotic motion occurs when the fictitious particle unable to return to the same location under the same pseudovelocity as it left. Ignoring the weak chaotic motion,

the whistler soliton solution should be a compression right-hand polarized soliton solution with parallel propagation ($\theta_o = 0°$). The parallel whistler soliton solutions have been obtained in earlier studies [i.e., *Kellogg*, 1964; *Kakutani et al.*, 1967].

Another type of soliton solution, which has not been included in Figure 2.22, is the linearly polarized fast-mode compression soliton solution with perpendicular propagation. It can be found in hybrid-scale trajectory, when V_o is slightly greater than V_{Fo}. The pseudopotential structure of this soliton is similar to the one shown in Figure 2.22*k*.

(C) *Rotational Structures With Uniform Upstream Boundary Condition*

Based on the discussion given in Section 2.4.2(C), a highly circularly polarized two-fluid rotational structure or two-fluid RD can be found when the outer-loop $\Psi = 0$ contour passing though A intersects with the sonic circle as shown in Figures 2.20, 2.22*g*, 2.22*h*, and 2.22*i*. Since the pseudopotential Ψ is symmetric about the b_y^*-axis, so are the locations of points S and T. Thus, the rotation angle for the highly circularly polarized two-fluid RD should be no more than 180°.

The rotational structure solutions ⑨ in Figures 2.22*g* and 2.22*h* are a right-hand polarized rarefaction two-fluid RD with rotation angle no more than 180°, which may exist when $V_{SLo} \leq V_o < V_{AXo} < C_{So}$. The magnetic field hodogram of this solution is along $A \rightarrow S$ for $B_{xo} > 0$, but along $A \rightarrow T$ for $B_{xo} < 0$.

The rotational structure solutions ⓪ in Figures 2.22*i* and Figure 2.20 are a left-hand polarized compression two-fluid RD with rotation angle no more than 180°, which may exist when $C_{So} < V_{AXo} < V_o \leq V_{Fo}$. The magnetic field hodogram of this solution is along $A \rightarrow T$ for $B_{xo} > 0$, but along $A \rightarrow S$ for $B_{xo} < 0$.

It can be seen that the Alfvén soliton solution ⑤ may turn into rotational structure ⑨ if V_o decreases further from V_{AXo}; whereas, the Alfvén soliton solution ⑦ may

turn into rotational structure ⓪ if V_o increases further from V_{AXo}. These results can be understood by Figure 1.2 in which the Alfvén mode converts into electrostatic ion acoustic mode when the phase speed approaches the sound speed. Thus the magnetic field of the two-fluid rotational discontinuity stops rotating as $M_S \rightarrow 1$. This solution behavior has not been included in the quasi-linear solutions listed in Table 2.1, because the wave-mode conversion effect has not been included in a quasi-linear solution as discussed in Figure 2.15.

Note that the absence of highly circularly polarized rotational discontinuity with rotation angle greater than 180° has been reported by both magnetopause observations [*Sonnerup and Cahill*, 1968], and solar wind observations [*Neugebauer*, 1989]. It has also been demonstrated by the simulation results [*Swift and Lee*, 1983]. A possible theoretical explanation for absence of such rotational structures can be found here as a characteristic of the two-fluid rotational discontinuity solutions ⑨ and ⓪.

(D) *Summary*

To show the θ_o, M_{Ao}, and β_o dependence of the constant-profile nonlinear wave solutions, we place the solutions in the well-known Friedrichs' diagram [e.g., *Kantrowitz and Petschek*, 1966] for V_o less than V_{Fo}. Figure 2.24 shows the Friedrichs' diagram for (*a*) $C_{So} < C_{Ao}$ and (*b*) $C_{So} > C_{Ao}$. The radius of the polar plot indicates the upstream flow velocity ($V_o\hat{\mathbf{x}}$). The polar angle θ_o is measured from the vertical axis, which is parallel to the upstream magnetic field ($\mathbf{B}_o$). The solid curves indicate (from inside out) the slow-mode, the Alfvén-mode, and the fast-mode speeds. The dashed curve indicates $V_o = C_{So}$. The nonlinear constant-profile isentropic wave solutions ①–⑨ and ⓪, exist in the shaded regions as indicated by the legends. No constant-profile nonlinear wave solutions with uniform upstream boundary conditions have been found in the blank regions. Nonlinear solutions at the curves of fast-mode,

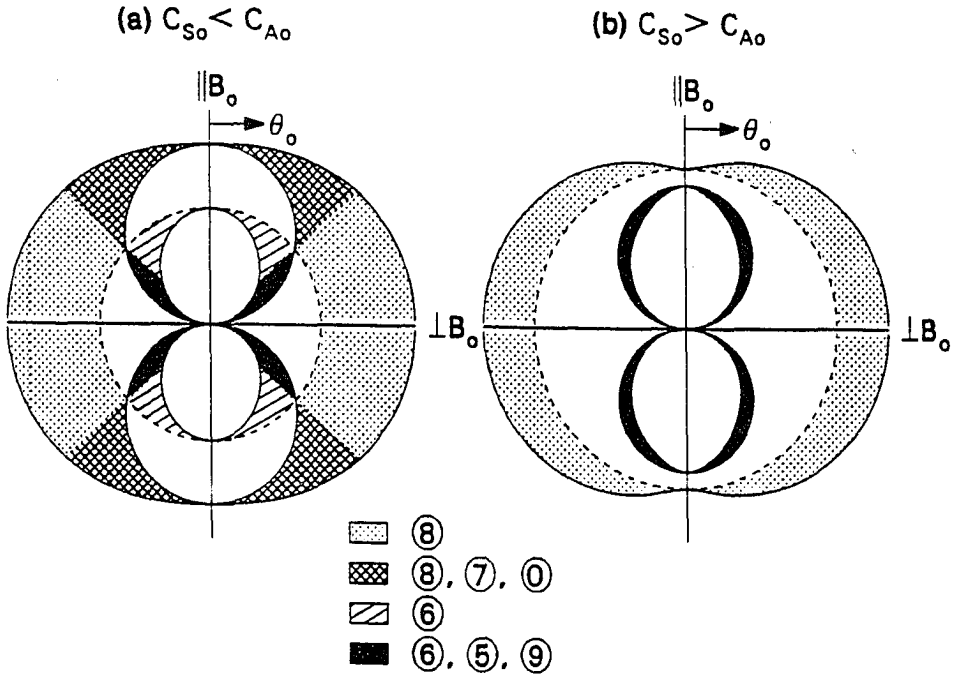

Figure 2.24 Summary of constant-profile, nonlinear hydromagnetic wave solutions in the Friedrichs' diagram, where (*a*) is for $\beta_o = 0.5$ and (*b*) is for $\beta_o = 1.8$. Nonlinear constant-profile isentropic wave solutions ①–⑨ and ⓪, exist in the shaded regions as indicated by the legends. No constant-profile nonlinear wave solutions with uniform upstream boundary conditions have been found in the blank regions.

slow-mode, Alfvén-mode and sound speed are summarized as follows. The amplitude of the inner-loop solutions ⑥ and ⑧ vanishes when $V_o = V_{SLo}$ or $V_o = V_{Fo}$ while the outer-loop (or arcs) solutions ⑤, ⑦, ⑨ and ⓪ may still be of finite amplitude (e.g., Figures 2.22*h* and 2.22*i*). On the other hand, when $V_o = C_{So}$, the amplitude of the outer-loop solutions vanishes but the inner-loop solutions may still be of finite amplitude. A circularly polarized incompressible Alfvén wavetrain or MHD rotational discontinuity can be found when $V_o = V_{AXo}$.

According to the results given in this section, we can conclude that all the left hand polarized solitons are compression solitons and all the right hand polarized solitons

are rarefaction solitons if soliton formation is due to the wave dispersion effect near ion inertial length; and so are the two-fluid rotational discontinuities. Opposite results can be obtained if soliton formation is due to the wave dispersion effect near electron inertial length. For instance, the compression whistler soliton is right-hand polarized nonlinear wave.

2.4.4 Two-Fluid Rotational Structures With Slightly Nonuniform Upstream Boundary Conditions

All the nonlinear wave solutions discussed in the last two sections satisfy the uniform upstream boundary condition. Thus, the magnetic field hodogram of each nonlinear wave has to start from point A. We now consider constant-profile nonlinear wave solutions with slightly non-uniform upstream boundary, i.e., non-uniform in the electron scale length but about uniform in the ion scale length. As have been discussed in Figure 2.21 and Figure 2.22g, sonic points can be classified into two groups. Half of them are attracters the other half of them are emitters. Magnetic field hodogram of a nonlinear wave solution can start from an emitter type of sonic point following along an equipotential contour, and end at the saddle point A or an attracter type of sonic point. It should be noted that if the magnetic field hodogram of a nonlinear wave solution does not start from point A, constants B_{yo}, p_o, ρ_o, V_o, ..., etc., will no longer be the upstream quantities. Only the combinations of these constants on the right-hand-side of equations (2.4.7)–(2.4.12) have well-defined physical meaning; they are the integration constants, representing the conservation of energy, momentum and mass fluxes.

Examples of constant-profile nonlinear waves with slightly non-uniform boundary conditions can be found in Figure 2.25. Figure 2.25 shows equipotential contours on

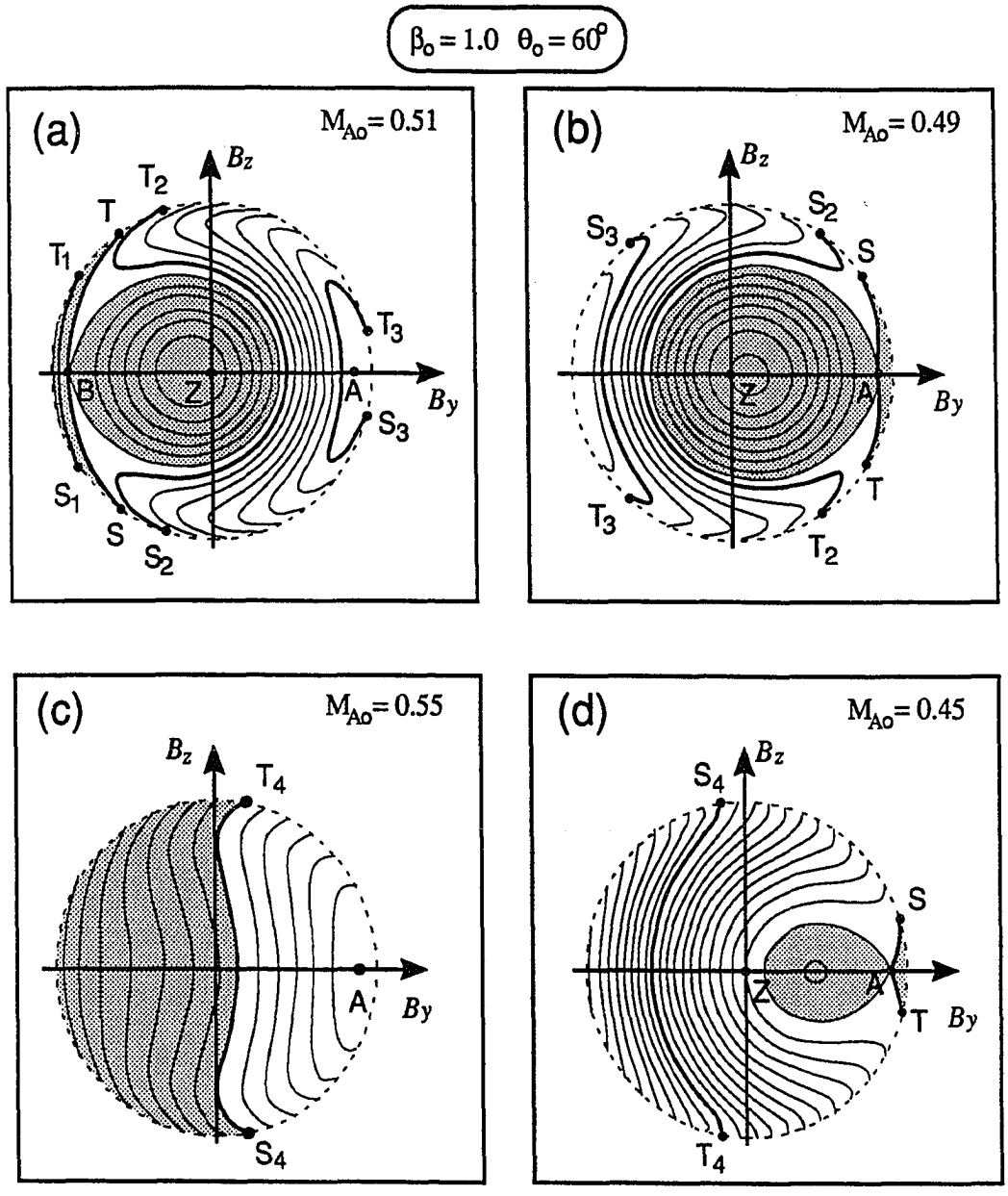

Figure 2.25 Equipotential contours on the subsonic surface for cases of $V_{AXo} < C_{So}$, and constant-profile two-fluid RD solutions with uniform or slightly non-uniform upstream boundary conditions. The pseudopotential on the shaded area is lower than that on the blank area. Polarization of highly circularly polarized RDs (e.g., $T \rightarrow A$, $T \rightarrow A \rightarrow S$, $A \rightarrow S$, $T \rightarrow B$, $T \rightarrow B \rightarrow S$, $B \rightarrow S$, and $T_1 \rightarrow S_1$, for $B_{xo} > 0$) is opposite to the polarization of Ω-shaped RDs (e.g., $T_2 \rightarrow S_2$), staple-shaped RDs (e.g., $T_3 \rightarrow S_3$), and RDs with very flat magnetic field hodogram (e.g., $T_4 \rightarrow S_4$).

the subsonic surface with $V_{AX_o} < C_{S_o}$, where (a) is for V_o slightly less than V_{AX_o}, (b) is for V_o slightly greater than V_{AX_o}, and (c) is for V_o further deviates from V_{AX_o}. The pseudopotential in the shaded area is lower than that in the blank area. By including nonlinear wave solutions with magnetic hodogram starting from a saddle point or an emitter type of sonic point, both left-hand polarized rotational structure solutions and right-hand polarized rotational structure solutions can be obtained. For convenience, we will only consider cases of $B_{x_o} > 0$ in the following discussions.

For $V_{AX_o} < C_{S_o}$, magnetic hodograms of right-hand polarized RDs are highly circular. Examples of these right-hand polarized RD solutions shown in Figure 2.25 include solutions along contours $T \rightarrow A$, $T \rightarrow A \rightarrow S$, and $A \rightarrow S$ in panels (b) and (c), and solutions along contours $T \rightarrow B$, $T \rightarrow B \rightarrow S$, $B \rightarrow S$, and $T_1 \rightarrow S_1$ in panels (a). Solution along $A \rightarrow S$ has been discussed in the last section as denoted by solution ⑨ in Figure 2.22g.

For $V_{AX_o} < C_{S_o}$, left-hand polarized rotational structures can be found with either a very flat magnetic hodogram or with hooked structures on upstream and downstream sides. RDs with two hooks at the ends of the hodogram can be found in panels (a) and (b) of Figure 2.25. They can further classify into two types. One of them is staple-shaped rotational structure (e.g., from T_3 to S_3) in which rotation angle is less than 180°. Another type of them is Ω-shaped rotational structure (e.g., from T_2 to S_2), in which the rotation angle is more than 180°. The principal arc of a staple-shaped RD is flatter than the right-hand polarized solutions ⑨. As V_o further deviates from V_{AX_o}, the principal arc of left-hand polarized RDs becomes much flatter and the hook structure at two ends diminishes. Examples of RDs with flat magnetic hodogram can be found in panels (c) and (d) of Figure 2.25 (e.g., from T_4 to S_4).

It may be noted that the deviation between V_o and V_{AXo} in cases (*a*) and (*b*) of Figure 2.25 is about 2 percent of V_{AXo}. Such small deviations between V_o and V_{AXo} may not be detectable by either observations or numerical simulations.

Similar results but with opposite polarizations can be found under $V_{AXo} > C_{So}$. For $V_{AXo} > C_{So}$, the left-hand polarized RD will have a highly circularly polarized magnetic field hodogram, whereas a right-hand polarized RD will have a staple-shaped, or Ω-shaped, or highly flat magnetic field hodogram.

It may be noted that earlier theoretical studies, either based on the characteristics of Alfvén-mode solitons [*Buti*, 1988; *Kennel et al.*, 1988; *Hada et al.*, 1989] or based on the characteristics of RD solutions with uniform upstream boundary conditions [*Lyu and Kan*, 1989*b*], predicated that the polarization of rotational discontinuities should depend on the sign of $1 - (\gamma\beta_o/2\cos^2\theta_o)$ (i.e., the sign of $(V_{AXo} - C_{So})$. However, observation shows very little dependence between them [*Neugebauer and Buti*, 1990]. By including constant-profile nonlinear wave solutions with slightly non-uniform upstream conditions (i.e., magnetic field hodogram starts from an emitter type of sonic point), both left-hand polarized RDs and right-hand polarized RDs can be found as legitimate solutions for cases of $V_{AXo} < C_{So}$ and for cases of $V_{AXo} > C_{So}$. Thus, the discrepancy between observations and earlier theoretical predictions can be resolved.

Several staple-shaped RDs are observed in the solar wind recently by *Neugebauer* [1989] and by *Neugebauer and Buti* [1990]. These observational results together with Ω-shaped RD obtained from an earlier simulation study by *Swift and Lee* [1983] motivated us to seek the nonlinear solutions with slightly non-uniform upstream boundary conditions. Thus, it is my pleasure to show that the theoretical solutions obtained in this section can be used to explain the characteristics of RD structures obtained

in observations [*Neugebauer*, 1989; *Neugebauer and Buti*, 1990] and in simulations [*Swift and Lee*, 1983].

Figure 2.26 shows observational results of staple-shaped RDs, where panels (*a*) and (*b*) are obtained from observations in the solar wind given by *Neugebauer* [1989] and panel (*c*) is given by *Neugebauer and Buti* [1990], where staple-shaped RD has been described as RD with angular overshoots at edges of the discontinuity [*Neugebauer*, 1989]. According to *Neugebauer* [1989], the "overshoot arcs always lie outside the principal arc." This remark accurately described the nature of staple-shaped RDs obtained theoretically from the two-fluid plasma model discussed above.

Figure 2.27 shows the simulation results of an Ω-shaped RD given by *Swift and Lee* [1983]. This Ω-shaped RD resulted from an initial left-hand polarized, 270° rotational structure. Another simulation run with an initial right-hand polarized, 270° rotational structure does not result in Ω-shaped RD. Their simulation results also show that for cases with rotation angle less than 180°, the magnetic field hodogram is highly circular for right-hand polarized RDs, but much flatter for left-hand polarized RDs. Since all the cases presented in *Swift and Lee* [1983] are for $\gamma\beta_o/2\cos^2\theta_o > 1$ (i.e., $V_{AXo} < C_{So}$), their simulation results are consistent with all the predicted features of RD solutions as discussed in Figure 2.25.

It may be noted that long after the theoretical solutions were obtained, additional RD simulation studies with $V_{AXo} > C_{So}$ were also carried out, which will be presented in Chapter 4. It again shows that the predictions given in Figure 2.25 are fulfilled. Namely, for $V_{AXo} > C_{So}$, the simulation results show that the magnetic field hodogram for a 180° RD is highly circular for a left-hand polarized RD, but much flatter for a right-hand polarized RD.

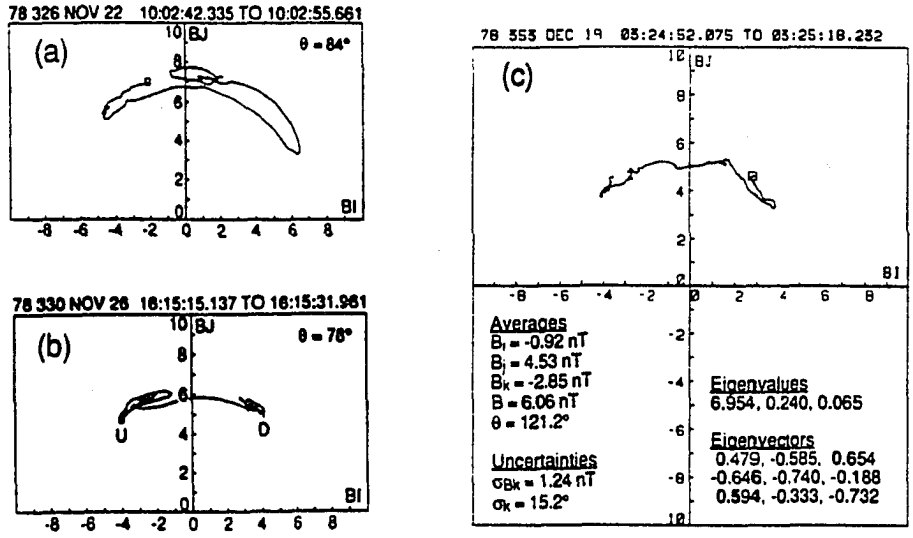

Figure 2.26 Observed staple-shaped RDs in the solar wind, where (*a*) and (*b*) are obtained from *Neugebauer* [1989]; (*c*) is obtained from *Neugebauer and Buti* [1990].

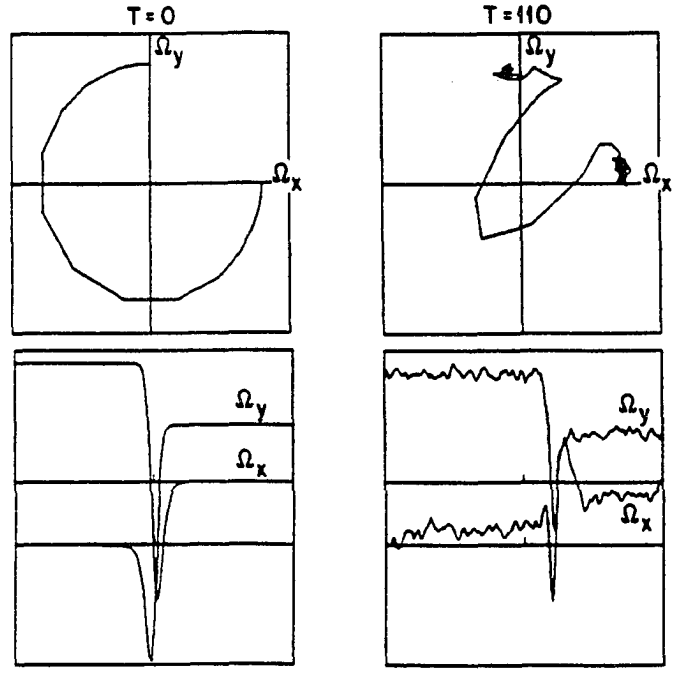

Figure 2.27 Simulation results of an Ω-shaped RD given by *Swift and Lee* [1983]. This simulation is for $\gamma\beta_o/2 > \cos^2\theta_o$, where $\cos\theta_o = 0.2$, $\beta_o = 0.33$, and the wave normal is along the z-axis.

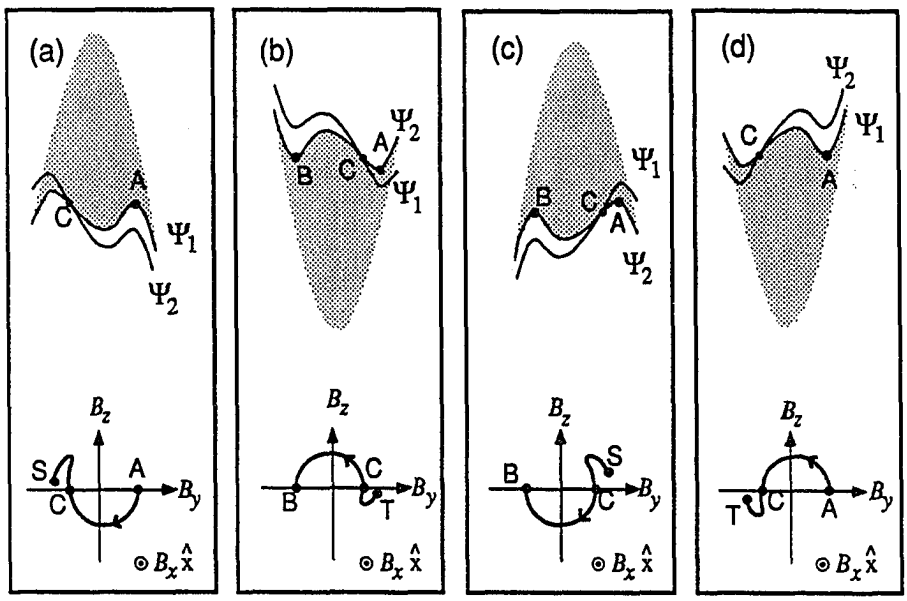

Figure 2.28 Sketches of four types of S-shaped RDs based on multiple pseudopotential method (see text for detail).

2.4.5 Quasi-Stationary Nonlinear Wave Solutions

Quasi-stationary nonlinear wave solutions in two-fluid plasmas can be obtained upon using the multiple pseudopotential method introduced in Section 2.2 and the pseudopotential structures shown in Figures 2.20 and 2.22. According to the multiple pseudopotential method, a fictitious particle is allowed to move through more than one pseudopotential with different V_0. In this section, we only single out several basic types of quasi-stationary isentropic nonlinear wave solutions that may exist in a finite-temperature magnetized two-fluid plasma. Interesting results to be discussed include S-shaped rotational structures, parallel Alfvén wave packets (or envelope solitons), highly linearly polarized banana-shaped oblique Alfvén wavetrain solutions, highly circularly polarized soliton-train solutions.

(A) *S-Shaped Rotational Discontinuity*

Figure 2.28 shows four types of S-shaped RDs, which can be obtained by considering a fictitious particle moving through two pseudopotentials, Ψ_1 and Ψ_2, of slightly different V_o. Top diagram of each panel sketches the cross section of the upstream surface of Ψ_1 and Ψ_2 at $B_z = 0$. Bottom diagram of each panel sketches the hodogram of the S-shaped RD solutions. The two pseudopotentials in each case have a similar saddle point (A or B), but with a different size of inner-loop equipotential contour passing the saddle point. For convenience, we will call the surface containing the saddle point A or B the *principle surface*, which is the subsonic surfaces in panels (a) and (c), but the supersonic surfaces in panels (b) and (d). By overlapping the equipotential contours of the principle surfaces of Ψ_1 and Ψ_2, the larger inner-loop contour on one pseudopotential is tangent to a staple-shaped contour on the other pseudopotential (which has a smaller inner-loop contour) at a point C. The tangent point C is a proper connection point for ion-scale trajectory motion on the two pseudopotentials, because the potential gradients of the two pseudopotentials at point C are in the same direction so that a fictitious particle can smoothly cross two pseudopotentials at this point (i.e., the pseudovelocity $\dot{\mathbf{b}}$ and the pseudoacceleration $\ddot{\mathbf{b}}$ can vary continuously across the two pseudopotentials at point C in both ion and electron scale lengths). Note that any discontinuities in the pseudovelocity will lead to discontinuous variations in the current profile in space. Thus, the condition of smoothly moving fictitious particle is to ensure a smooth and continuous current profile across the S-shaped RD transition region. After choosing point C as the connection point, S-shaped RD can be obtained as sketched in the lower diagram of each panel, which consists of a half inner-loop contour and a half staple-shaped contour. An example with pseudopotential structures similar to the one shown in panel (a) of Figure 2.28 is given in Figure 2.29 to demonstrate the contours-overlapping method discussed above. Figure 2.29 shows

color plots of equipotential contours of two principle surfaces separately as given in panels (*a*) and (*b*) and in an overlapped form as shown in panel (*c*). The blue contours are obtained from a pseudopotential of $\theta_o = 60°$, $\beta_o = 1.0$, and $M_{Ao} = 0.499$. The red contours are obtained from a pseudopotential of $\theta_o = 60°$, $\beta_o = 1.0$, and $M_{Ao} = 0.495$. The yellow curve *A–U–C–S* shown in panel (*c*) is the hodogram of the S-shaped RD solutions obtained for $B_{xo} > 0$, where point *S* is an attracter-type of sonic point. Note that the propagation speed of the upstream part of structure *A–U–C* is 0.499 C_{Ao} and the downstream part of structure *C–S* is 0.495 C_{Ao}. The Alfvén mode speed in this case is 0.5 C_{Ao}. Thus, the propagation speed of this RD is extremely close to the Alfvén mode speed. The speed difference between the upstream part and the downstream part of the S-shaped RD structure is also extremely small. Similar results can be obtained for the other three cases shown in Figure 2.28, except that RDs shown in Figure 2.28*b* and Figure 2.28*c* start from an emitter-type of sonic point *T* and end at a saddle point *B*.

From physical characteristics of these S-shaped RDs, we can classify the S-shaped RDs into two types.

(1) RDs shown in Figure 2.29, Figure 2.28*a* and Figure 2.28*b* are sub-Alfvénic S-shaped rotational structures ($V_o < V_{AXo}$). The characteristic speed V_o of Ψ_1 is greater than the characteristic speed V_o of Ψ_2, as the one shown in Figure 2.29. Thus, there will be no strong interaction between the two parts of the RD structure. The hodogram of these RDs is characterized by a left-hand polarized hodogram on the upstream side followed by a right-hand polarized hodogram on the downstream side. The density profile of these nonlinear waves can be obtained based on the method discussed in Section 2.4.2(C). Note that $B_\perp$ is maximum at the sonic point *S* or *T*, but minimum at point *C*. Thus, there will be a density overshoot in the cases shown in Figure 2.29

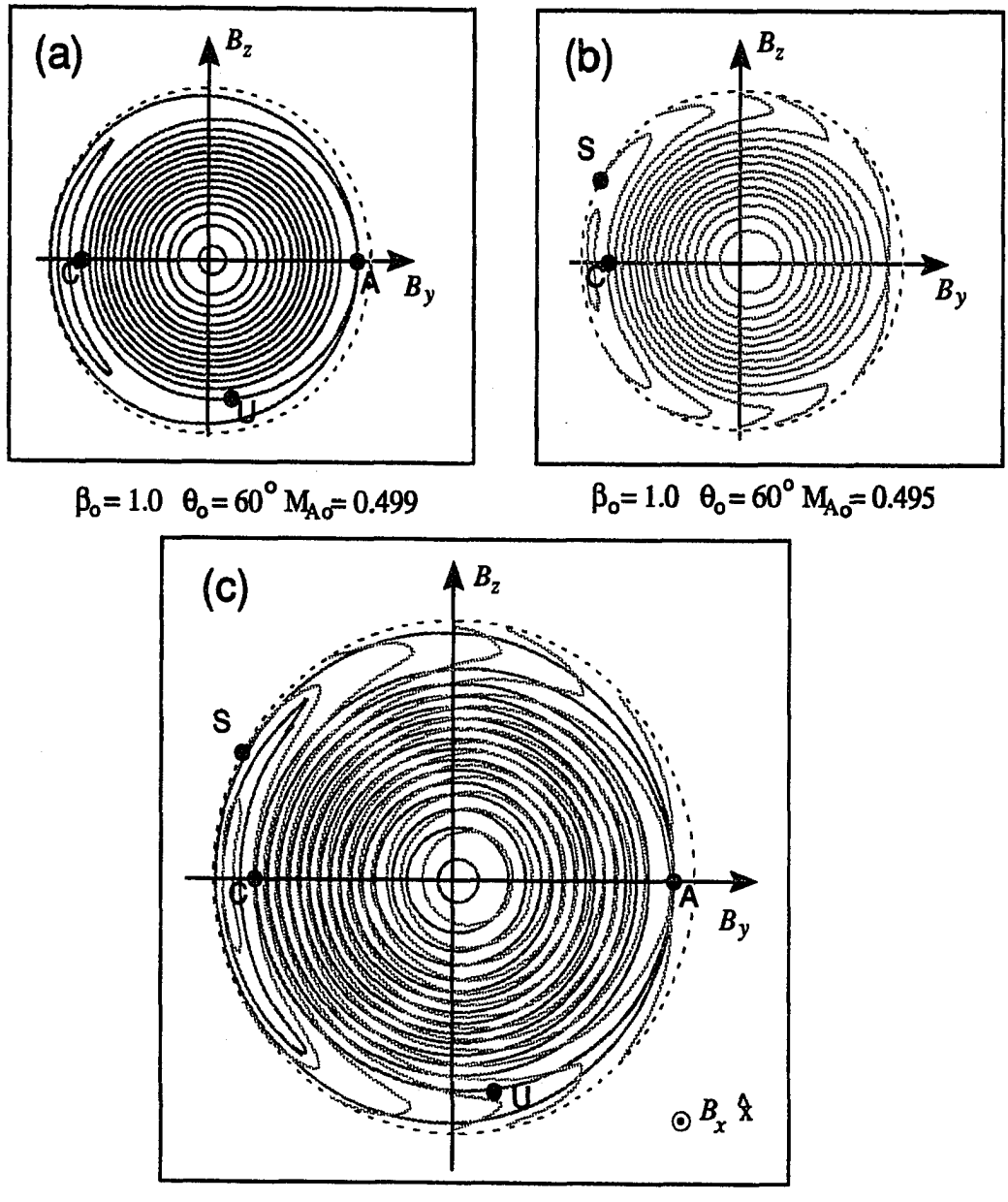

Figure 2.29 A demonstration of how to obtain the S-shaped RD solutions from contour plots of the principle surface of two pseudopotentials with structures similar to the one shown in Figure 2.28*a*. Panels (*a*) and (*b*) show the equipotential contours of two principle surfaces separately. Panel (*c*) shows an overlapping plot of the contours shown in panels (*a*) and (*b*). The yellow curve *A–U–C–S* shown in panel (*c*) is the hodogram of the S-shaped RD solutions obtained for $B_{xo} > 0$.

and Figure 2.28*a*, but a density undershoot in the case shown in Figure 2.28*b*. The net density jump decreases from upstream side to downstream side for all of these sub-Alfvénic S-shaped RD structures.

(2) RDs shown in Figure 2.28*c* and Figure 2.28*d* are super-Alfvénic S-shaped rotational structures ($V_o > V_{AXo}$). The characteristic speed V_o of Ψ_1 is less than the characteristic speed V_o of Ψ_2. Thus, the downstream part of the RD structure will eventually catch on the upstream part of the nonlinear wave as discussed in Section 2.2. Strong nonlinear interaction will occur for these super-Alfvénic S-shaped RD structures. However, for a characteristic speed difference of 0.004 C_A, a quasi-stationary rotational structure can last at least 100 ion gyro periods. The hodogram of these RDs is characterized by a right-hand polarized hodogram on the upstream side followed by a left-hand polarized hodogram on the downstream side. Again, there will be a density overshoot in the case of $V_{AXo} < C_{So}$ as shown in Figure 2.28*c*, but a density undershoot in the case shown in Figure 2.28*d*. The net density jump increases from upstream side to downstream side for these super-Alfvénic S-shaped RD structures. If dissipative process is present, these compression super-Alfvénic S-shaped RD structures may turn into an Alfvén shock before the downstream part of the rotational structure can overtake the upstream part of the rotational structure. This result is consistent with the previous simulation study of Alfvén shocks given by *Lyu and Kan* [1989*a*], in which they found that all the S-shaped Alfvén shocks are characterized by a right-hand polarized wave on the upstream side followed by a left-hand polarized wave on the downstream side. Note that an Alfvén-mode shock wave must be a compression wave with net rotational angle of 180°, which will be discussed later in Chapter 4.

Generally, the thickness of a nonlinear rotational structure depends on the average pseudopotential gradient, which is large if the deviation between V_o and V_{AXo} is large. Therefore, the thickness of an S-shaped RD with near 180° rotation is much less than the thickness of a highly circularly polarized rotational structure with a similar angle of rotation. Namely, with the same thickness, which is about a few ion inertial lengths, a highly circularly polarized RDs (such as solution ⑨ or ⓪ shown in Figure 2.22) can only afford a very small angle of rotation. However, since the S-shaped RD is only quasi-stationary over a long duration, we may expect the S-shaped RD either to relax into a highly circularly polarized RD or to steepen into an Alfvén shock.

Similarly, various RDs with S-shaped or asymmetrical staple-shaped magnetic hodogram can be obtained from a combination of two half staple-shaped contours on two pseudopotentials with slightly different V_o. A single hook (S-shaped) RD may also result from two arc-shaped contours (of outer-loop family) on two pseudopotentials connected at point A with different V_o (e.g., arcs in panels (*b*) and (*c*) of Figure 2.24). Note that the rotation angles of these RDs are often much less than 180°.

Figure 2.30 shows several observed and simulated S-shaped RDs, where panel (*a*) shows observed S-shaped rotational structures on the magnetopause [*Berchem and Russell*, 1982], panel (*b*) shows observed S-shaped rotational structures in the solar wind [*Neugebauer*, 1989], and panel (*c*) shows the simulated S-shaped rotational discontinuity by *Richter and Scholer* [1989]. Note that it may not be easy to distinguish some of the 180° RDs from Alfvén shocks. Thus, we shall leave this issue open at this time. Simulated S-shaped Alfvén solitons will be discussed later in Chapter 4. The very unsmoothed magnetic hodograms with very small θ_o shown in the solar wind observations may indicate that a fast-mode (or whistler-mode) wave packet is

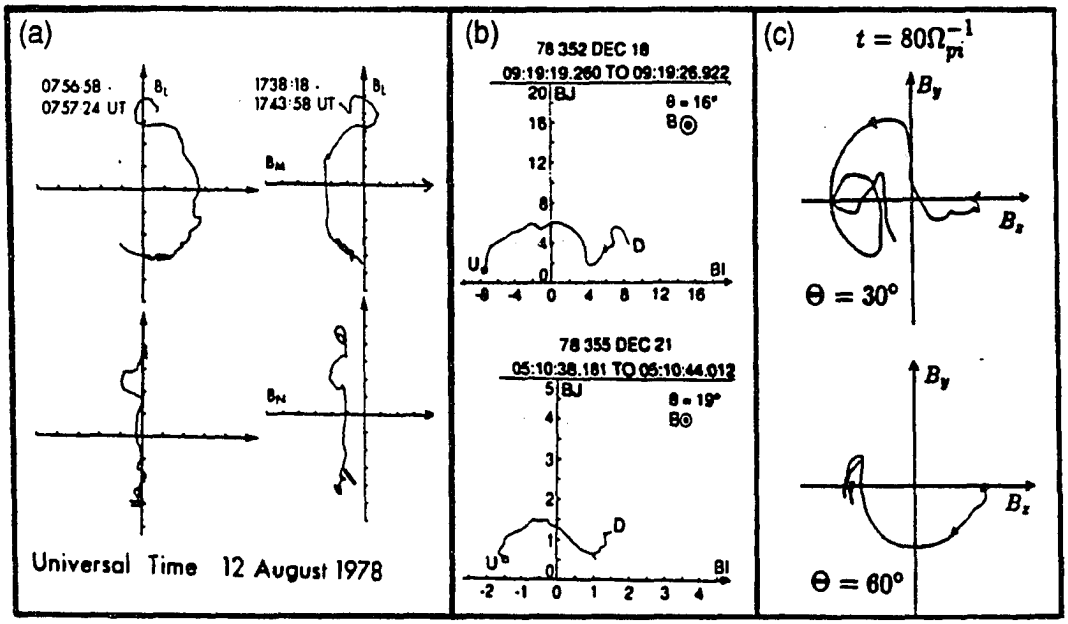

Figure 2.30 Example of observed and simulated S-shaped RDs, where (*a*) is obtained from the magnetopause observations of *Berchem and Russell* [1982], (*b*) is obtained from solar wind observation of *Neugebauer* [1989], and (*c*) is the simulation result obtained from *Richter and Scholer* [1989].

currently passing through the highly parallel nonlinear Alfvén wave. The fast-mode wave packet will be discussed later in this section.

(B) *Banana-Shaped Alfvén Wavetrain Solutions*

According to the discussion of S-shaped RD solutions given in Figure 2.28, quasi-stationary nonlinear wavetrain solutions of ion-scale trajectory can be formed with a magnetic hodogram gradually shifted to the neighboring equipotential contours by changing pseudopotential field rather than by introducing dissipative effect in the nonlinear wave solutions. As a result, Alfvén wavetrain solutions with a banana-shaped magnetic hodogram can be obtained as a combination of several banana-shaped equipotential contours around the maximum or minimum point located on the opposite side to the saddle point. One end of the wavetrain may connect to the maximum or

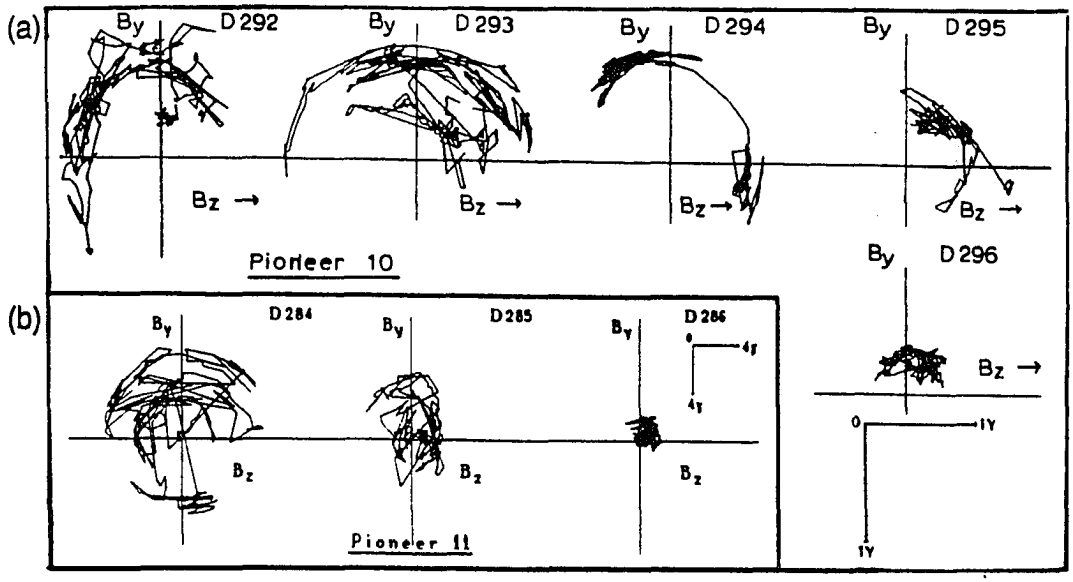

Figure 2.31 Observed Alfvén wavetrain structures in the solar wind given by *Mavromichalaki et al.* [1988].

minimum point at the center of the banana arc or a source region of the nonlinear perturbation. The other end of the banana-shaped RD may connect to the sonic point similar to the ending of a staple-shaped RD, or connect to the saddle point on the opposite side through the inner-loop equipotential contour or the outer-loop equipotential contour. Thus, these banana-shaped wavetrain structures may turn into a staple-shaped RD (if both ends are connected to the sonic points), or S-shaped RD (if one end is connected to the saddle point along the inner-loop contour), or even a single-hook RD with angular overshoot inside the principle arc (if one end is connected to the saddle point through the outer-loop contour, whereas the other end is near the source region around the minimum or maximum point). The last example of single-hooked RD has been reported by *Sonnerup and Ledley* [1974] in the magnetopause observations and has been found in intermediate shock simulation, which will be shown in Chapter 3.

Figure 2.31 shows observed Alfvén wavetrain structures in the solar wind given by *Mavromichalaki et al.* [1988]. Panel (*a*) is the observed events obtained from Pioneer 10 at $\sim$ 5 AU. Panel (*b*) is the observed events obtained from Pioneer 11 at $\sim$ 2.5 AU. According to the field profile plots versus time for these two data sets [*Mavromichalaki et al.*, 1988], the events D292 to D294 in panel (*a*) is about the counterpart of event D284 in panel (*b*). Event D295 is about the counterpart of event D285. Event D296 is roughly the counterpart of event D286. Apparently, the magnetic field hodograms of events D292, D293, D294, and D284 can be identified with the banana-shaped Alfvén wavetrain solutions discussed above, although the plots shown in Figure 2.31 have not been rotated to the principle coordinate yet [e.g., *Sonnerup and Cahill*, 1967]. *Mavromichalaki et al.* [1988] described these nonlinear waves as plane polarized (linearly polarized) nonlinear Alfvén waves (see Figure 3 of their paper). Their descriptions are consistent with the banana-shaped wavetrain solution. Note that the polarization of the banana-shaped wavetrain is right-handed (or left-handed) with respect to the center of the banana if it is a maximum point (or a minimum point), but the average polarization with respect to the normal magnetic field (i.e., point A, where $B_\perp = 0$) is highly linearly polarized. This result is consistent with the discussion of these observed nonlinear waves given in Figure 3 of *Mavromichalaki et al.* [1988].

(C) *Parallel Wave-Packet Solutions*

Parallel Alfvén wave-packet or envelope-soliton solutions have been obtained based on DNLS equations [e.g., *Mio et al.*, 1976; *Spangler and Sheerin*, 1982; *Spangler et al.*, 1985; *Kennel et al.*, 1988]. However, no constant-profile nonlinear waves with parallel propagation have been found as shown in the Friedrichs' diagrams in Figure 2.24. Preliminary simulation studies (not shown) also indicate the existence of envelope-shaped wave packets at small θ_o, which contains high frequency or short

wavelength waves. But simulation results also indicate that those wave packets are only quasi-stationary. Namely, the size of wave packet increases as time progresses. However, the simulation technique cannot determine unambiguously whether the non-stationary wave structure is a physical result or a result due to unaware numerical errors in the simulation. We shall use multiple pseudopotential method to show the existence of a quasi-stationary parallel or highly parallel Alfvén wave-packet solution as discussed below.

Figure 2.32 demonstrates how to obtain a parallel wave packet from a series of pseudopotentials of slightly different V_o. Top panels show pseudopotential structures near $V_o = C_{Ao}$ with $\theta_o = 0°$, where panel (*a*) is for $C_{Ao} > C_{So}$ and panel (*b*) is for $C_{Ao} < C_{So}$. These pseudopotentials connect at point *A*. A fictitious particle can move along an electron-scale trajectory passing through point *A* to a different pseudopotential surface. There can be two types of nonlinear wave solutions. One of them extends towards the downstream side, in which the fictitious particle moves from $M_{Ao} = 1$ surface to surfaces of $M_{Ao} < 1$ with decreasing pseudo-gyroradius as sketched in diagram (*c1*) in the middle panel. The other nonlinear wave extends towards the upstream side, in which the fictitious particle moves from surfaces of $M_{Ao} > 1$ to the surface of $M_{Ao} = 1$ with increasing of pseudo-gyro-radius as the one sketched in diagram (*c2*) in the middle panel. A combination of these two solutions leads to a wave-packet solution with magnetic hodogram as sketched in diagram (*c3*) of the middle panel. The average density and total magnetic field profiles of these wave-packet solutions are shown in the bottom panels, where panel (*d*) shows a compression envelope-soliton solution for $C_{Ao} > C_{So}$ and panel (*e*) shows a rarefaction envelope soliton for $C_{Ao} < C_{So}$.

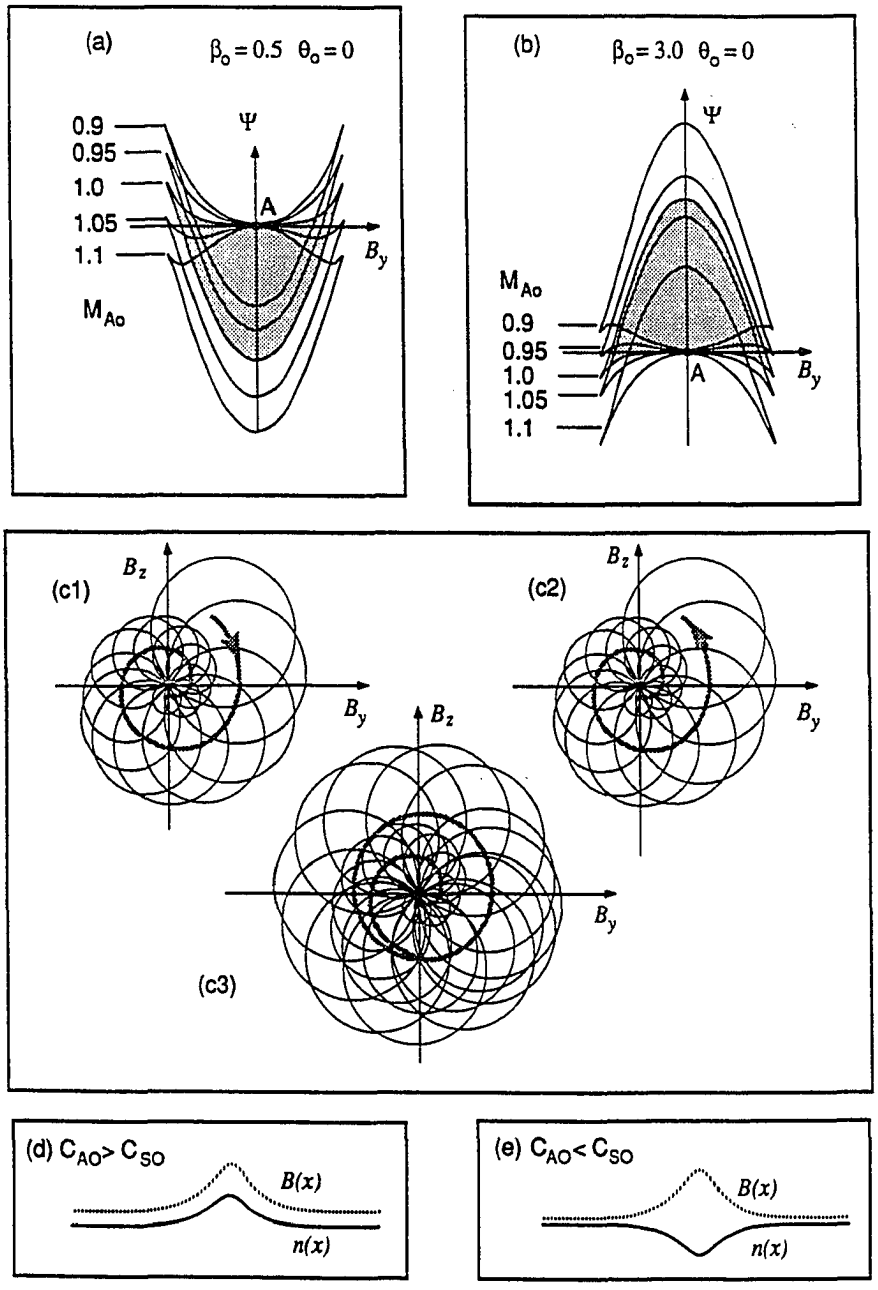

Figure 2.32 Quasi-stationary parallel wave-packet solutions obtained from multiple pseudopotential method. Top panels show multiple-pseudopotential structures near $V_o = C_{Ao}$. Middle panel sketches magnetic hodogram of the wave-packet solution. Bottom panels sketch the average density and total magnetic field profiles of envelope-soliton solutions.

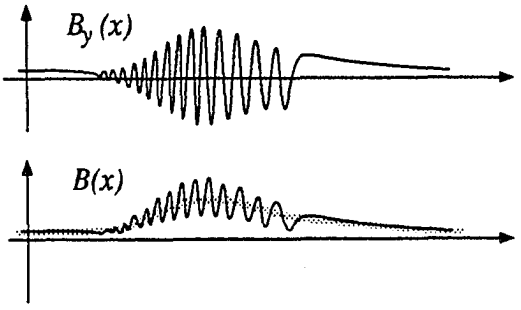

Figure 2.33 Spatial profiles of a fast-mode wave-packet solution with highly parallel propagation.

Note that fast-mode and Alfvén-mode linear wave dispersion curves for $C_{A\circ} > C_{S\circ}$ have been sketched in Figure 2.15. Similar results can be obtained for Alfvén-mode and slow-mode dispersion curves for $C_{A\circ} > C_{S\circ}$. Thus, we may identify the envelope-soliton solutions shown in panels (*d*) and (*e*) as fast-Alfvén envelope-soliton solution and Alfvén-slow envelope-soliton solution, respectively.

In the same manner, slow-mode and fast-mode wave packets with highly parallel propagation can be obtained from the cross sections of pseudopotentials shown in panels (*c*) and (*d*) of Figure 2.23. Figure 2.33 sketches the spatial profile of a fast-mode wave-packet solution with highly parallel propagation. Note that the decrease of wave amplitude after reaching a certain amplitude is due to the existence of a saddle point next to point *A* as shown in panel (*k*) of Figure 2.22, which can limit the wave amplitude of the nonlinear waves. A slow-mode wave packet can be obtained in the same way, but these electron-scale waves with phase speed less than the local sound speed in the slow-mode wave-packet solutions may be of highly damped, if kinetic effect is taken into account.

For oblique propagation, these wave-packet solutions may also be found if *A* is located far away from the sonic circle. Otherwise, the amplitude of the wave-packet

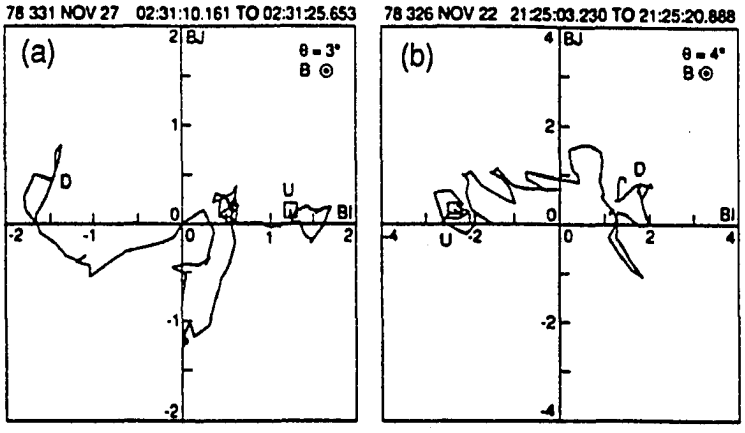

Figure 2.34 Observed highly parallel RDs with very jagged and irregular magnetic hodogram, which are obtained from *Neugebauer* [1989].

solutions should be limited by the sonic circle. These wave-packet solutions may be related to the quasi-stationary nonlinear finite-extent wavetrain solutions predicted in Table 2.1

Since the propagation speed of these fast-mode (which is also called the whistler-mode) wave packets is always faster than any of the MHD or two-fluid RD solutions and soliton solutions, these wave packets superposed on highly parallel RDs or solitons in ion-scale trajectory are expected to be found. We may use this result to explain the very jagged and irregular hodogram in highly parallel RDs shown in Figure 2.34, as obtained from solar wind observations [*Neugebauer*, 1989]. Similar results also show in our preliminary isentropic two-fluid simulations (not shown) and intermediate shock simulations (to be shown in the next chapter).

(D) *Soliton-Train Solutions*

In the same manner as shown in Figures 2.9 and 2.10, quasi-stationary soliton-train solutions can be obtained if we consider a series of pseudopotentials connected at point A (e.g., panels (a) and (b) in Figure 2.23) with different V_o, where $V_{SLo} <$

$V_o < V_{AXo} < C_{So}$ or $C_{So} < V_{AXo} < V_o < V_{Fo}$. Soliton-train solutions can be a set of outer-loop Alfvén solitons (i.e., solutions ⑤ or ⑦ shown in Figure 2.22), or a set of inner-loop solitons (i.e., solutions ⑥ or ⑧ in Figure 2.22), or a set of solitons with outer-loop and inner-loop solitons appeared alternately (i.e., a combination of soliton solutions ⑤ and ⑥ or a combination of solutions ⑦ and ⑧). Apparently, the mixed-type soliton-train is very similar to the banana-shaped wavetrain solutions. For example, the average polarization of a mix-typed soliton-train is also highly linear.

2.4.6 Comparison With Alfvénic Fluctuations Observed in the Solar Wind

It will be shown in this section that the characteristics of constant-profile, or quasi-stationary, nonlinear hydromagnetic waves in finite-temperature two-fluid plasmas obtained in this chapter can naturally explain many observed features of Alfvénic fluctuations in the solar wind.

Alfvénic fluctuations observed in the solar wind are characterized by large amplitude transverse magnetic field variations with a high correlation between wave magnetic field B and the solar wind velocity V [e.g., *Belcher and Davis*, 1971]. Both density and magnetic field intensity of purely Alfvénic fluctuations should be constant in a MHD plasma. However, non-zero fluctuations of magnetic field intensity and plasma density have been often found in observed solar wind Alfvénic fluctuations [e.g., *Burlaga and Turner*, 1976; *Neugebauer et al.*, 1978]. The variations of δB and δn are sometimes in phase but sometimes out of phase [*Neugebauer et al.*, 1978]. The polarization of the wave magnetic field in these observed Alfvénic fluctuation can be

right-handed and can be left-handed [*Neugebauer et al.*, 1978]. Apparently, our nonlinear wave solutions obtained in this chapter can provide a satisfactory explanation on these observed fluctuations on plasma density and magnetic field intensity.

The scale lengths of nonlinear wave solutions obtained in this chapter also consist with the scale lengths of observed nonlinear Alfvénic fluctuations in the solar wind. The thickness of highly circularly polarized nonlinear wave solutions ①–⑨ and ⓪ as discussed in Section 2.4.3 ranges from a few hundred ion inertial lengths (as $V_o \approx V_{AXo}$) to about a few tens of ion inertial lengths [e.g., *Lyu and Kan*, 1989*b*]. Since ion gyro period near 1 AU is about 10 seconds, these highly circularly polarized nonlinear wave solutions may contribute to those observed Alfvénic fluctuations with observed frequency of 10^{-5}–10^{-2} Hz [e.g., *Belcher and Davis*, 1971; *Burlaga and Turner*, 1976]. However, the scale length for other nonlinear wave solutions with larger δB and δn (such as strong soliton solutions or two-fluid RDs, or banana-shaped wavetrain solutions, highly parallel wave-packet solutions, etc.) may range from a few to a few tens of ion inertial lengths. This result is consistent with the thickness of observed RDs in the solar wind [e.g., *Martin et al.*, 1973; *Burlaga et al.*, 1977; *Lepping and Behannon*, 1986] and in the magnetopause [e.g., *Sonnerup and Ledley*, 1974]. It can be shown that a soliton solution with thickness of a few tens of ion inertial lengths can results in a power spectrum with a plateau structure near 0.01–0.1 Ω_i [*Lyu and Kan*, 1989*b*]. Thus, those nonlinear wave solutions with scale length range from a few to a few tens of ion inertial lengths can result in an enhanced power spectrum in the high frequency range, from 0.01–1 Ω_i as observed by *Unti et al.* [1973], *Unti and Russell* [1976], and *Neugebauer* [1975, 1976], which is corresponding to a structure with thickness of a few to a few tens of ion thermal gyroradii [*Neugebauer*, 1975, 1976]. Note that the differences between ion inertial length, C_{Ao}/Ω_{io}, and ion thermal

gyroradius, $C_{S\circ}/\Omega_{i\circ}$, is less than a factor of 2 if $0.3 < \beta_\circ < 4.8$. Thus, the ion inertial length, which has been used throughout this chapter, is about the same order of magnitude as the ion thermal gyroradius for most solar wind plasmas. Note that for very low β or very high β plasma, the nonlinear waves along the outer-loop contours and the nonlinear waves along the inner-loop contours with the same $V_\circ$, will have different thickness. In general, one of them is governed by the ion inertial length, and the other is governed by the ion thermal gyroradius. For a given $V_\circ$, the thickness of the outer-loop soliton is often thinner than the inner-loop solution. Namely, the outer-loop solutions are usually governed by the smaller characteristic length of the two.

Lyu and Kan [1989*b*] also showed that the nearly alignment between local average magnetic field and wave normal direction in the Alfvénic fluctuations as observed in both high-speed and low-speed solar wind streams at different heliographic distances [e.g., *Belcher and Davis*, 1971; *Daily*, 1973; *Solodyna and Belcher*, 1976; *Burlaga and Turner*, 1976; *Denskat and Neubauer*, 1982] can be naturally explained by the nonlinear wave solutions with thickness of a few hundred to a few tens of ion inertial lengths. According to the geometrical optics [e.g., *Hollweg*, 1975], the propagation direction of a planar nonlinear Alfvén wave should be refracted by the velocity shear in the solar wind. Therefore, the geometrical optics predicts that the distribution of the angle between the wave normal and the upstream magnetic field should vary with the location of the observer and cannot be expected to peak around zero degrees all the time. Under the commonly adopted assumptions that the "local average magnetic field" is equal to the "upstream magnetic field" and that the observed wave normal is parallel to the "local average magnetic field," one is led to the questionable conclusion that the wave normal is parallel to the "upstream magnetic field." This dubious conclusion is in

conflict with the prediction of the geometrical optics [e.g., *Solodyna and Belcher*, 1976; *Barnes*, 1981, 1983]. In an attempt to circumvent this conflict, the idea of turbulence is proposed to explain the preferential orientation of the wave normal along the average magnetic field direction [*Barnes*, 1981, 1983; *Matthaeus and Goldstein*, 1982]. On the other hand, *Solodyna and Belcher* [1976] argued that the conflict could be due to inapplicability of the minimum variance method [*Sonnerup and Cahill*, 1967]. They even suggest that the minimum variance method cannot determine the wave normal direction, but give the average magnetic field direction.

Recently, *Lyu and Kan* [1989*b*] showed that the local average magnetic field $\langle \mathbf{B} \rangle$ is different from the ambient magnetic field $\mathbf{B}_o$ for the oblique nonlinear two-fluid wave solutions. Figure 2.35 is reproduced from Figure 10 of *Lyu and Kan* [1989*b*] to show the field line structure and the directions of vectors $\langle \mathbf{B} \rangle$, $\mathbf{B}_o$ and $\hat{\mathbf{n}}$ in a finite-extent oblique Alfvén wavetrain structure, i.e., one of the solutions ①–④ as discussed in Section 2.4.3.

Figure 2.36 sketches the projection of a single field line on the yz-plane for (*a*) a left-hand polarized soliton train structure, (*b*) a right-hand polarized soliton train structure, (*c*) a mix-typed soliton-train solution, (*d*) a wavetrain structure with banana-shaped magnetic field hodogram with one end connect to the saddle point, and (*e*) an S-shaped RD with 180° rotation angle. According to Figure 2.35, a three-dimensional field line structure can be obtained by simply stretching its yz-plane projection along the x-axis. Similar results of the wavetrain solutions shown in Figures 2.35*a* and 2.36*d* have been obtained by *Mavromichalaki et al.* [1988]. Based on the field-line structure shown in Figure 2.36*d*, the wavetrain structure with banana-shaped magnetic field hodogram apparently can be either locally generated by the shear flow (i.e., amplified from Kelvin-Helmholtz instabilities) in the solar wind, or developed from a mix-typed

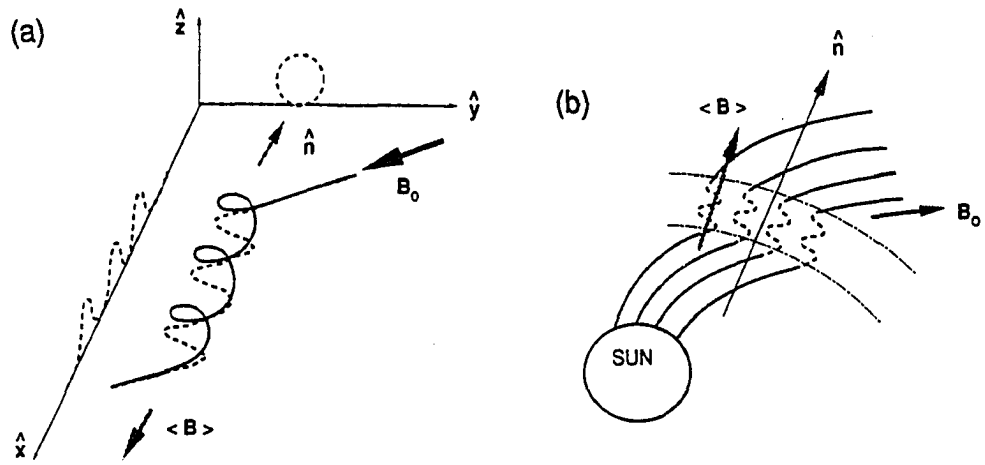

Figure 2.35 Sketches of (*a*) three-dimensional magnetic field line structure of a finite-extent Alfvén wavetrain and (*b*) the field line projection on the ecliptic plane for a nonlinear finite extent Alfvén wavetrain propagating outward from the sun. It can be seen that the local average magnetic field $\langle \mathbf{B} \rangle$ is aligned with the wave normal direction $\hat{\mathbf{n}}$, but different from upstream magnetic field $\mathbf{B}_o$.

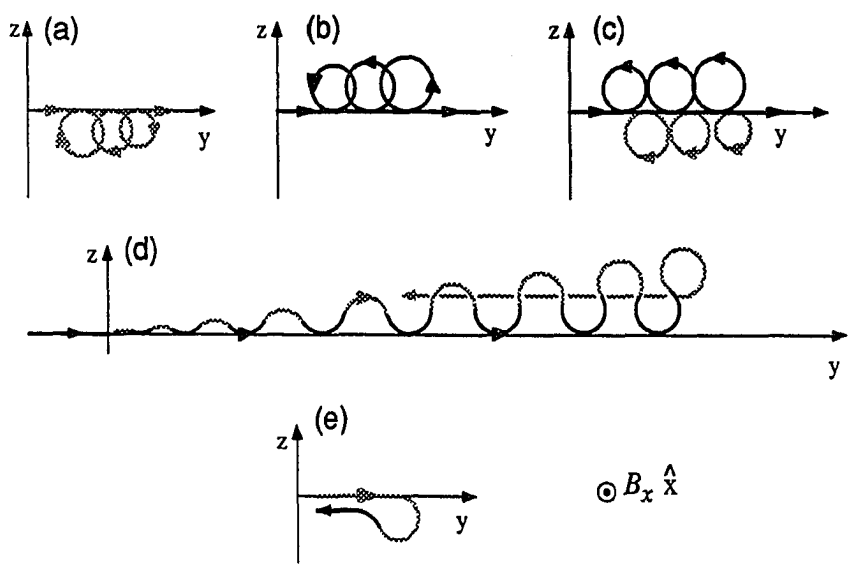

Figure 2.36 Sketches of the projection of a single field line on the *yz*-plane for (*a*) a left-hand polarized soliton train structure, (*b*) a right-hand polarized soliton train structure, (*c*) a mix-typed soliton-train solution, (*d*) a wavetrain structure with banana-shaped magnetic field hodogram with one end connect to the saddle point, and (*e*) an S-shaped RD with 180° rotation angle.

soliton-train (which may be generated at coronal hole due to the supergranulation motion on the photosphere) after being refracted by the velocity share in the solar wind.

2.5 Summary and Discussion

Nonlinear hydromagnetic waves in finite-temperature two-fluid plasmas are studied analytically based on pseudopotential method and multiple pseudopotential method. The results consist of constant-profile nonlinear wave solutions obtained from a single pseudopotential structure and quasi-stationary nonlinear wave solutions obtained from a multiple-pseudopotential system. Constant-profile nonlinear wave solutions consist of (1) circularly polarized incompressible MHD waves of very long wavelength (> 600 ion inertial lengths) propagating at Alfvén mode speed, which can be a finite-extent Alfvén wavetrain solution, or a rotational discontinuity with a rotation angle less than 360°; (2) soliton solutions which include right-hand polarized rarefaction Alfvén-mode soliton solution (i.e., solution ⑤), left-hand polarized compression slow-mode soliton solution (i.e., solution ⑥), left-hand polarized compression Alfvén soliton solution (i.e., solution ⑦), and right-hand polarized rarefaction fast-mode soliton solution (i.e., solutions ⑧); (3) highly circularly polarized two-fluid RD solutions ⑨ and ⓪, with rotation angle less than 180°); and (4) Ω-shaped RDs and staple-shaped RDs with slightly non-uniform upstream boundary conditions. The total angle of rotation of an Ω-shaped RD is more than 180°. The arcs of angular overshoot in staple-shaped RDs always lie outside its principal arc. For a given pseudopotential, the polarization sense of the principle arc of Ω-shaped and staple-shaped RDs is opposite to the polarization sense of highly circular RDs (e.g., solution ⑨ and ⓪ discussed in Figure 2.22).

To obtain parallel envelope-soliton solutions, which has been obtained based on DNLS equations [e.g., *Mio et al.*, 1976; *Spangler and Sheerin*, 1982; *Spangler et al.*, 1985; *Kennel et al.*, 1988], a multiple pseudopotential method is introduced in this chapter. The method is first tested using the simplest KdV dispersion medium. It successfully explains all the features of simulated quasi-stationary KdV wavetrain structures. It is then applied to study the nonlinear waves in two-fluid plasma. Consequently, we obtain not only the quasi-stationary parallel wave-packet solutions, but also various types of S-shaped RDs, banana-shaped oblique Alfvén wave trains, soliton-train solutions and highly parallel wave-packet solutions of fast-mode (or whistler-mode) and slow-mode.

Two-fluid RD solutions obtained in this chapter successfully explain many observed RD structures. The soliton or soliton-train solutions and banana-shaped Alfvén wavetrain solutions may contribute to the observed Alfvénic fluctuations in the solar wind (with observed period from a few minutes to an hour). The nearly alignment between local magnetic field and wave normal directions can also be naturally explained by these oblique propagated nonlinear wave solutions. Parallel and nearly parallel wave-packet solutions, strong solitons and RDs with very narrow transition region (e.g., a few ion inertial lengths) may contribute to the enhanced power spectrum near the proton thermal gyroradius in the observed solar wind fluctuations (with observed period of 0.3–80 seconds at 1 AU).

It may be noted that analytical solutions of quasi-stationary KdV wavetrains have been obtained by *Berezin and Karpman* [1967] based on a mathematical approximation (i.e., expressions obtained from Whitham's equations [*Whitham*, 1965] for slowly varying parameters). Although, both approximations, theirs and ours, share the same spirit, the intuitional multiple pseudopotential method is much more flexible, simple,

and conventional when it is applied to a nonlinear wave problem with more than one independent variable and with more than one dispersive wave mode.

Pseudopotentials obtained from (2.4.33), (2.4.21) together with the equation of motion (2.4.30) can be viewed as the simplest nonlinear dispersion relation of two-fluid plasmas. Solutions obtained in this chapter provide a basis of nonlinear phenomena that might occur in a finite-temperature, magnetized two-fluid plasmas. All the quasi-stationary nonlinear wave solutions should be obtainable from two-fluid simulations. Unfortunately, at this time I am not able to present simulation results of nonlinear two-fluid hydromagnetic waves systematically, similar to the KdV nonlinear wave simulations shown in Figures 2.4–2.7. My preliminary results indicate that the final nonlinear wave structure seems not only to depend on the thickness, the amplitude, the density profile of the initial disturbance, but also depend on the integrations of b_y and b_z over the initial disturbance (i.e., the vector potential differences across the initial disturbances). Further simulation studies need to be done to systematically determine the relationship between initial disturbances and resulting nonlinear wave solutions.

Kinetic effects have not been included in our fluid formulations. To determine the modification due to presence of kinetic effects, one can compare the two-fluid simulation results with particle code simulation results of nonlinear hydromagnetic waves. On the other hand, based on the result of two-dimensional simulations, one may obtain an additional set of nonlinear wave solutions in which the direction of wave normal is allowed to change slightly. Study of such quasi-planner and quasi-stationary nonlinear hydromagnetic waves may be a very interesting research topic. The results may provide a good explanation on the structures of some tangential discontinuities and rotational discontinuities observed in the solar wind. However, it should be noted that the formulations obtained in this study are not applicable to those solitary waves

generated by kinetic processes, such as a particular plasma distribution or multiple streaming effects, or formed as a fully two-dimensional nonlinear phenomenon. But the concept of multiple pseudopotential method may be still applicable to the study of these solitary waves if a pseudopotential field can be found.

Chapter 3

Ion Reflection, Ion Leakage, and Ion Heating in Quasi-Parallel Collisionless Fast Shocks

3.1 Introduction

Fast shocks are shock waves propagated in magnetized plasmas with upstream normal flow speed greater than the upstream fast-mode (or magnetosonic-mode) speed, and with downstream normal flow speed less than the downstream fast-mode speed but greater than the downstream Alfvén-mode speed. Planetary bow shocks in the solar system are fast shocks, because solar wind becomes super-magnetosonic beyond a radial distance greater than $\sim$ 0.3 AU. Interplanetary shocks in the solar wind are also mostly fast shocks. They are generated either by high-speed solar wind streams overtaking slow streams (i.e., the co-rotating shocks), or generated by solar flares or corona mass ejection events.

Observations of Earth bow shock by ISEE satellites indicate that shock structures not only depend on Mach number M_A but also depend on shock normal angle θ_{BN} [*Greenstadt*, 1985], where M_A is the Alfvén Mach number and θ_{BN} is the acute angle between the shock normal and the upstream magnetic field. Shocks with $\theta_{BN} < 45°$ are called quasi-parallel shocks. Shocks with $\theta_{BN} \geq 45°$ are called quasi-perpendicular shocks. The Mach number dependence can be seen from the presence of ion reflections. Ion reflection by a steep shock front can be found in high Mach number quasi-perpendicular shocks of $M_A > 3$ [e.g., *Pashmann et al*, 1981; *Leroy et al.*, 1981, 1982; *Lembege and Dawson*, 1987; *Burgess et al.*, 1989]. Ion reflections in high Mach number quasi-parallel shocks have also been found in observations [e.g., *Gosling et*

al., 1982, 1989*b*; *Onsager et al.*, 1990] and in simulation studies [e.g., *Lyu and Kan*, 1990; *Thomas et al.*, 1990]. Ion reflection can provide additional dissipation as needed for the formation of high Mach number collisionless shocks. Turbulent structures can be found downstream from high Mach number quasi-perpendicular shocks due to the presence of ion reflections at the shock front. Without ion reflection, low Mach number quasi-perpendicular shocks are mostly laminar shocks with transition region thickness of a few ion inertial lengths. On the other hand, large amplitude waves are often found in the quasi-parallel shock transition region even without ion reflection [e.g., *Greenstadt et al.*, 1968; *Greenstadt and Fredricks*, 1979; *Kennel et al.*, 1984*a*,*b*]. As a result, the average thickness of the quasi-parallel shock transition region is about a few tens of ion inertial lengths [e.g., *Scudder et al.*, 1984; *Greenstadt*, 1985]. Pitch angle scattering by these large amplitude waves can lead to ion heating in quasi-parallel shocks [*Kan and Swift*, 1983]. In addition to the large amplitude waves in the shock transition region, a large number of backstreaming suprathermal ions upstream from shock front is another unique characteristic of the observed collisionless quasi-parallel shocks [e.g., *Paschmann et al.*, 1981; *Thomsen*, 1985].

Quasi-parallel shocks have been studied extensively for more than a decade by both observations and numerical simulations. The general characteristics of wave structures and plasma distributions in the shock transition region are well established, but the physical processes associated with those phenomena are not yet fully understood. Simulation study of quasi-parallel shocks in collisionless plasmas will be carried out in this chapter based on the well-established hybrid code simulation model [e.g., *Swift and Lee*, 1983; *Kan and Swift*, 1983; *Mandt and Kan*, 1988; *Lyu and Kan*, 1990]. The purpose of this study is to understand ion dynamics and anomalous dissipation processes in the shock transition region of collisionless quasi-parallel shocks.

The four-group particle-labeling diagnostic designed by *Lyu and Kan* [1990] and an improved multiple-group particle-labeling diagnostic will be used in this study to assist us to see the ion dynamics in the shock transition region in greater details. Specifically, we shall focus on the following two issues: (1) the origin of the suprathermal backstreaming ions observed upstream from the shock front [e.g., *Edmiston et al.*, 1982; *Gosling et al.*, 1982; *Thomsen*, 1985], and (2) the physical processes of various types of ion reflection events observed in high Mach number quasi-parallel shocks [*Gosling et al.*, 1982, 1989*b*]. Other issues in current quasi-parallel shock researches such as shock front reformation processes [*Burgess*, 1989], ion heating processes, and formation of large amplitude hydromagnetic waves in the shock-transition region will also be discussed.

Outlines of this chapter are as follows: Controversial issues and outstanding problems in current quasi-parallel shock researches will be addressed in Sections 3.1.1–3.1.5. The simulation model and particle-labeling diagnostics will be introduced in Section 3.2. Simulation results of four quasi-parallel shocks of different Mach numbers will be presented in Section 3.3. A gyro-reflection model will be proposed in Section 3.4 to explain different types of ion reflection events obtained in high Mach number quasi-parallel shock simulation. In summary, three critical Mach numbers will be proposed in Section 3.5, based on the four cases studied in Section 3.3, to highlight the Mach number dependence in collisionless quasi-parallel shocks.

3.1.1 Origin of Upstream Suprathermal Backstreaming Ions

Upstream backstreaming suprathermal ions are commonly observed in quasi-parallel shocks. However, the origin of these backstreaming ions is still an open issue [e.g., *Thomsen*, 1985]. These suprathermal backstreaming ions may originate from

leakage of downstream hot ions [e.g., *Edmiston et al.*, 1982; *Krimigis et al.*, 1985; *Anagnostopoulos et al.*, 1986; *Sarris et al.*, 1987; *Sibeck et al.*, 1988] or directly come from reflected ions after being heated by upstream waves [e.g., *Paschmann et al.*, 1981; *Gosling et al.*, 1982].

Using the MHD Rankine-Hugoniot jump condition, *Edmiston et al.* [1982] showed that leakage of downstream ions can occur in quasi-parallel shocks, if the downstream ion thermal speed is greater than the downstream ion flow speed. However, the leakage ion density estimated by *Edmiston et al.* [1982] is about one order of magnitude higher than the backstreaming ion density observed upstream of quasi-parallel shocks [*Gosling et al.*, 1982]. The overestimation of leakage ion density may be due to the omission of interaction between leakage ions and large amplitude waves in the shock-transition region in their model. Moreover, *Edmiston et al.* [1982] assumed that the leakage process is adiabatic. Namely, both magnetic moment and kinetic energy are conserved during the leakage processes. Validity of this assumption is also an open issue for study of ion leakage process in quasi-parallel shocks [e.q., *Schwartz et al.*, 1983; *Thomsen*, 1985].

Paschmann et al. [1981] compared three types of observed ion distributions: (*a*) reflected ion beam distribution, (*b*) intermediate ion distribution, and (*c*) diffuse ion distribution, as shown in Figure 3.1. Diffuse ion distributions can be found upstream from quasi-parallel shocks. Intermediate ion distributions can be found upstream of both quasi-parallel and quasi-perpendicular shocks. The average velocity of these intermediate ion distributions and diffuse ion distributions observed upstream of quasi-parallel shocks are highly aligned with the average upstream magnetic field in the de Hoffman-Teller frame. Since reflected ion beam distributions observed upstream from quasi-perpendicular shocks are also highly field-aligned in the de Hoffman-Teller

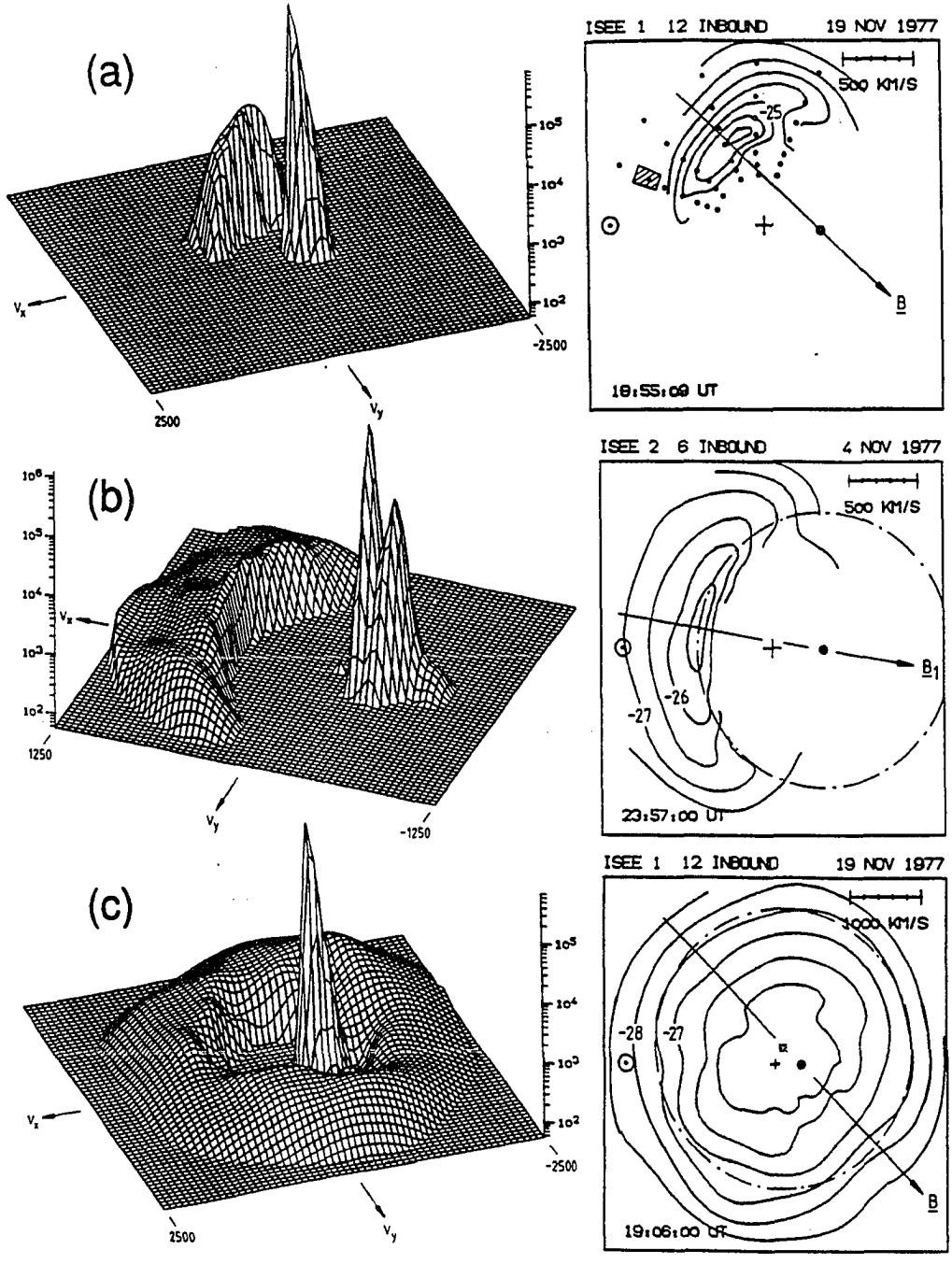

Figure 3.1 Relief plots and contour plots of observed three types of ion distributions: (*a*) reflected ion beam distribution, (*b*) intermediate ion distribution, and (*c*) diffuse ion distribution [after *Paschmann et al.*, 1981].

frame, *Paschmann et al.* [1981] suggested that reflected ions are the seed ions of both intermediate ion distributions and diffuse ion distributions. *Paschmann et al.* [1981] proposed that large amplitude hydromagnetic waves upstream from shock front may scatter a highly field-aligned reflected ion beam into an intermediate distribution. Further pitch-angle scattering of the intermediate ion distribution can result in a diffuse ion distribution.

From a different approach, *Gosling et al.* [1982] drew a similar conclusion on the origin of the upstream backstreaming ions as suggested by *Paschmann et al.* [1981]. *Gosling et al.* [1982] proposed that specularly reflected ions in quasi-parallel shocks can directly contribute to the suprathermal backstreaming ions upstream from the shock front. Specular reflection is defined by reflection in which normal velocity of the reflected ion changes its sign but does not change its magnitude, whereas the tangential velocity remains unchanged after reflection. It can be shown that the guiding center motion of a specularly reflected ion is directed downstream for $\theta_{BN} > 45°$ but directed upstream for $\theta_{BN} < 45°$ [*Gosling et al.*, 1982]. Figure 3.2 shows gyrating ion distributions observed upstream from a quasi-parallel shock [after *Gosling et al.*, 1982]. Panels (*a*) and (*b*) show observed gyrating ion distributions obtained from two successive 3-second measurements. Panel (*c*) shows observed total magnetic field profile where the short bar upstream from shock front denotes the time interval that ion distributions in panels (*a*) and (*b*) are obtained. *Gosling et al.* [1982] suggested that these gyrating ions are the evidence of specular reflection. Further scattering by upstream waves, these gyrating ions can contribute to the suprathermal backstreaming ions observed on the upstream side of quasi-parallel shocks.

From simultaneous measurements of energetic ions and electrons upstream from Earth's bow shock and within the Earth's plasma sheet, *Anagnostopoulos et al.* [1986]

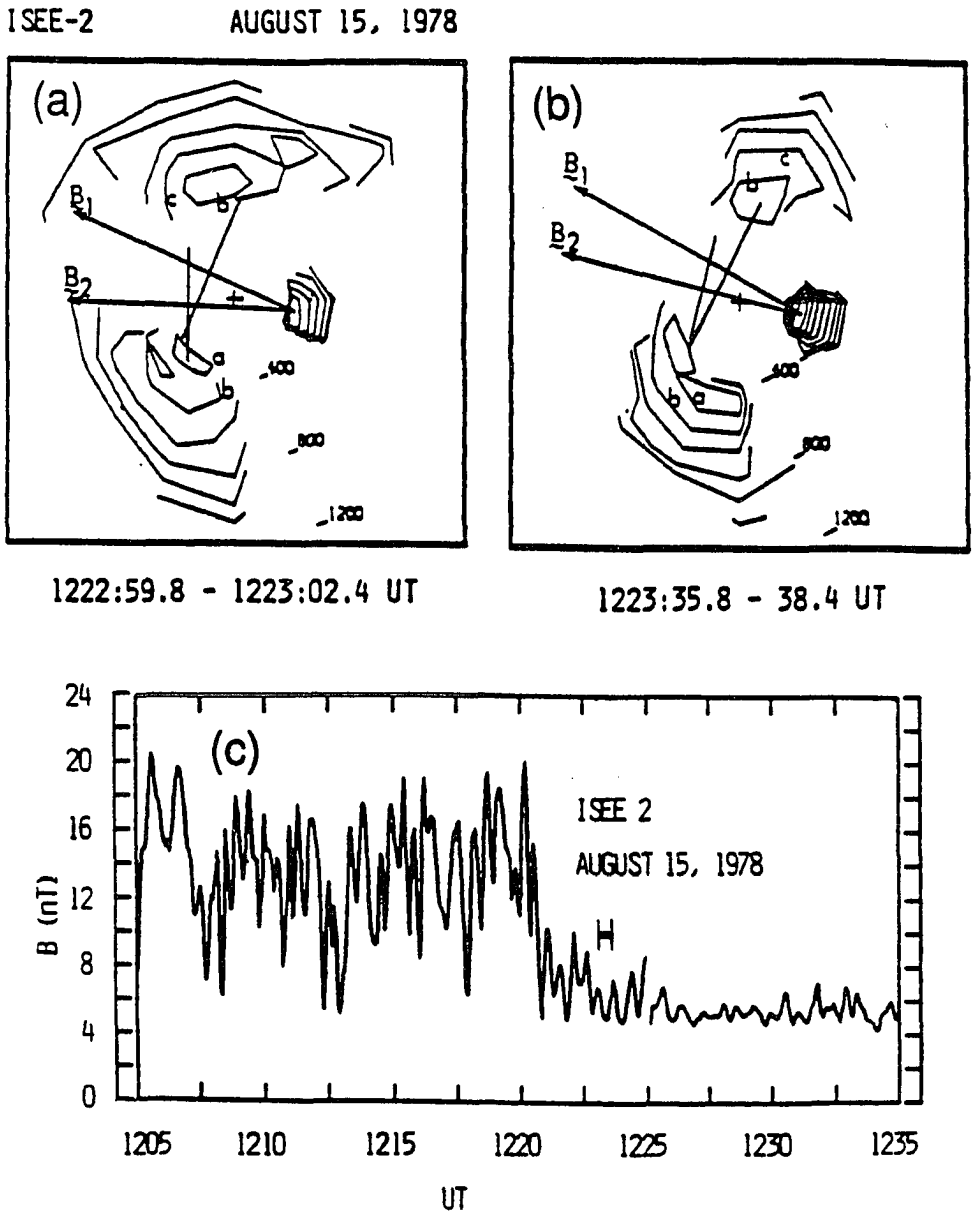

Figure 3.2 Gyrating ion distributions observed upstream from shock front in a quasi-parallel shock crossing [after *Gosling et al.*, 1982]. Panels (*a*) and (*b*) show observed gyrating ion distributions obtained from two successive 3-second measurements. Panel (*c*) shows observed total magnetic field profile, where the short bar upstream from shock front denotes the time interval that ion distributions in panels (*a*) and (*b*) are obtained.

and *Sarris et al.* [1987] suggested that the source of some upstream ion events (energetic ions) is indeed the Earth's magnetosphere, and no additional acceleration is necessary within the upstream medium.

Based on simultaneous magnetosphere, magnetosheath, and upstream energetic particle observations during two well-documented upstream events on November 1, 1984, *Sibeck et al.* [1988] showed that: (1) there are ion streams away from magnetopause toward the bow shock, (2) there are measurable fluxes of magnetospheric particles (O^+ and electrons) during portions of the events in the upstream region, and (3) the observed upstream and magnetospheric spectra had similar slopes. Thus, they concluded that magnetospheric leakage is a sufficient source for upstream particles during those two events. Similar results on the upstream ion spectra and compositions of energetic ions upstream of Jupiter's foreshock, magnetosheath, and magnetopause have also been reported by *Krimigis et al.* [1985]. But *Gosling et al.* [1989*a*] showed that the hot magnetospheric ions are not the only source for observed suprathermal upstream ions, because there are several upstream ion events in which the downstream magnetic field lines are clearly away from the magnetopause.

To identify the origin of upstream backstreaming suprathermal ions from satellite observations, one has to provide models or assumptions on ions' dynamics in the shock-transition region [e.g., *Schwartz et al.*, 1983; *Thomsen*, 1985]. However, most of these assumptions or models are not verified unless the origin of these backstreaming ions is known. A direct identification of the origin of the backstreaming ions is to trace all ions that have ever interacted with the shock layer. Since diagnostics can be devised more readily in numerical simulations, one can expect to determine the origin of backstreaming ions by simulation technique. A particle-labeling diagnostic used

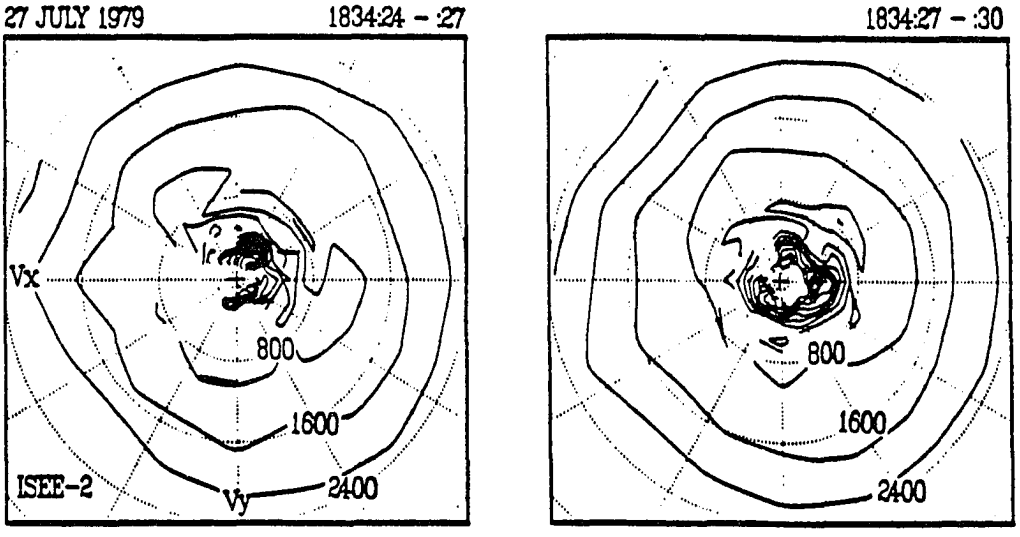

Figure 3.3 Contour plots of ion distributions observed downstream from shock front in two quasi-parallel shock crossings [after *Gosling et al.*, 1989*b*]. Ion distributions with secondary ion beam and multiple ion bunches shown in this figure are similar to the reflect-reentering ion distributions observed in high Mach number quasi-perpendicular shocks.

in this study will help us to study the origin of upstream backstreaming suprathermal ions in the simulated quasi-parallel shocks.

3.1.2 Two Types of Ion Reflection Events

Two types of ion reflection events have been observed at quasi-parallel shock crossings. One of them has been discussed in Figure 3.1*b* and Figure 3.2 in the previous section. Namely, highly field-aligned backstreaming intermediate ion distributions observed by *Paschmann et al.* [1981] and upstream gyrating ion distributions observed by *Gosling et al.* [1982]. Specular reflection model, which used to explain ion reflection processes in quasi-perpendicular shocks, can also explain these highly field-aligned intermediate ion distributions or gyrating ion distributions observed upstream from shock front [e.g., *Gosling et al.*, 1982; *Thomsen*, 1985].

The other type of ion reflections in quasi-parallel shocks has been reported by *Gosling et al.* [1989*b*] that a secondary ion beam or multiple ion bunches were observed downstream from shock front during several quasi-parallel shock crossings as shown in Figure 3.3. These observed ion distributions are similar to the ion distributions observed downstream from high Mach number quasi-perpendicular shocks. The reflect-reentering pictures proposed by *Gosling et al.* [1989*b*] are apparently in conflict with the specular reflection model proposed by *Gosling et al.* [1982], in which specularly reflected ions should direct upstream in quasi-parallel shocks. Thus, the physical mechanism of ion reflections is still an open issue in current quasi-parallel shock researches.

Both highly field-aligned ion reflections and reflect-reentering ion reflections are found in a high Mach number quasi-parallel shock simulation in this chapter. By examining the characteristics of magnetic field in the shock ramp, a unique relationship between the ramp field orientation and the type of ion reflections is obtained. Based on the simulation results, a model for the ion reflection processes in quasi-parallel collisionless shocks is proposed in this study. The proposed model can also provide a satisfactory explanation on the different types of ion distributions associated with ion reflection events observed during quasi-parallel shock crossings [*Gosling et al.*, 1982, 1989*b*].

3.1.3 Ion Heating

Several dissipation mechanisms in quasi-parallel and parallel shocks have been proposed prior to the ISEE age [see the review of *Kennel et al.*, 1985]. These include ion two-stream firehose instability [*Parker*, 1961], ion sound waves heating [*Moiseev and Sagdeev*, 1963], and theories containing both effects [e.g., *Kennel and Sagdeev*,

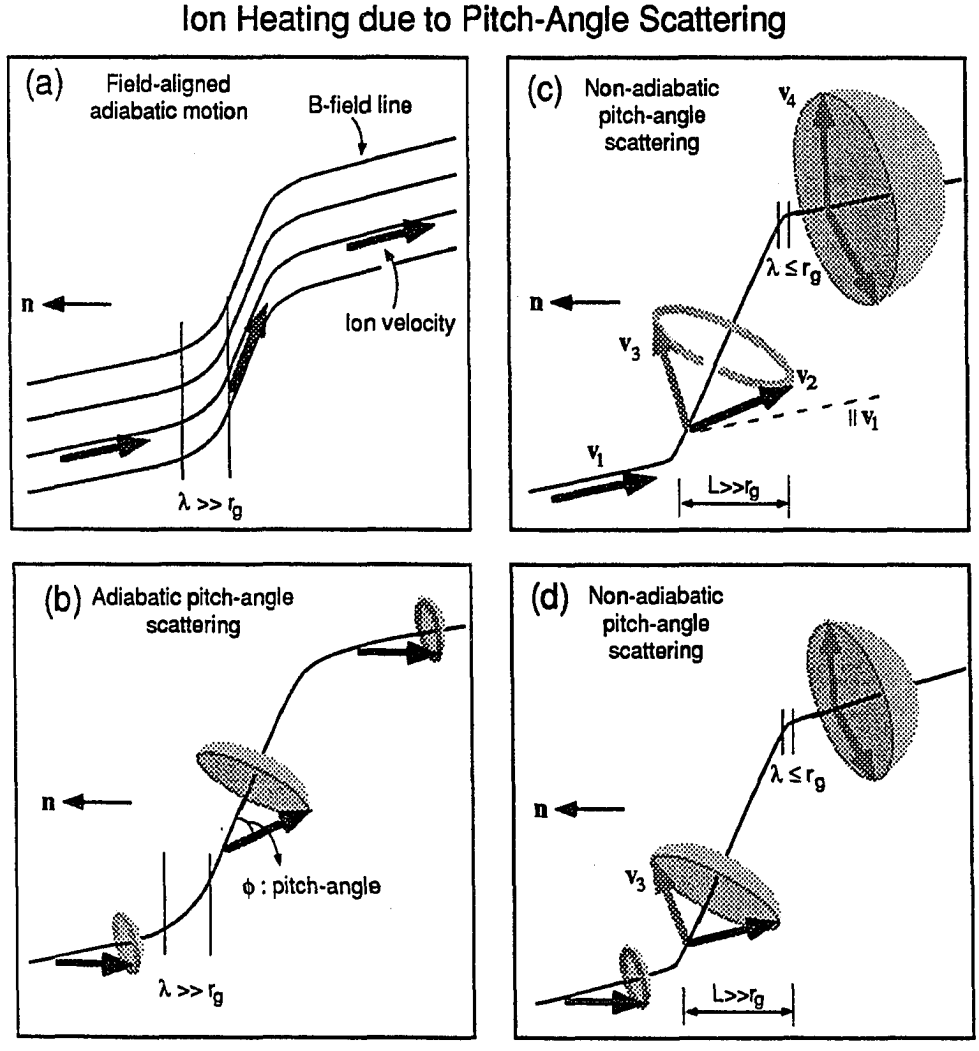

Figure 3.4 Sketches of ion heating processes due to adiabatic pitch-angle scattering and non-adiabatic pitch-angle scatterings. See text for discussion in detail.

1967*a*,*b*]. However, the complexity of the quasi-parallel shock structure obtained from ISEE *in situ* observations and numerical simulations indicate that the ion pitch-angle scattering in the shock-transition region must play an important role in the ion heating process [e.g., *Kan and Swift*, 1983; and *Quest et al.*, 1983], where pitch angle is the angle between the local magnetic field direction and the velocity direction of a moving ion.

Ion heating due to pitch-angle scattering can be discussed qualitatively as illustrated in Figure 3.4. Figure 3.4 sketches ion motions along curved magnetic field lines of a plane wave, where solid curves are the magnetic field lines, bold and shaded vectors denote the ion velocity, vector **n** denotes the normal direction of the plane wave, ϕ is the pitch angle, r_g is the ion gyro radius, λ is the scale length of the curved field line which is comparable to the radius of curvature of magnetic field line at the sharp turn, and L is the scale length between two sharp turns. The ion gyro radius r_g is defined by $r_g = v_\perp/\Omega_i$, where $\Omega_i = eB/m_ic$ is the ion gyro frequency, $v_\perp = v\sin\phi$ is the magnitude of ion velocity component perpendicular to the local magnetic field, and v is the magnitude of ion velocity. Since pitch angle ϕ changes during pitch-angle scattering, we shall re-define a pitch-angle independent ion gyro-radius $r_g = v/\Omega_i$, in this study. For simplicity, electric field effects will be ignored in the discussion of the four cases shown in Figure 3.4. Panel (*a*) shows an example of a cold, field-aligned ion beam moving adiabatically in a smoothly curved magnetic field line where the scale length λ of the curved field line is much greater than the ion gyro radius r_g. Since the pitch angle stays zero all the time, there is no pitch-angle scattering in this case. Panel (*b*) shows an example of adiabatic pitch-angle scattering, in which a bunch of warm ions with a cone-type pitch-angle distribution moves adiabatically in a smoothly curved magnetic field line. The thermal velocity of theses ions is assumed to be less than their average drift velocity. The magnetic moment is conserved during the adiabatic pitch-angle scattering. As a result, ion heating can be found when ions enter a strong magnetic field region; whereas, ion cooling can be found when ions enter a region with decreasing of magnetic field strength. This result is consistent with the MHD fast-mode wave characteristics. Panel (*c*) of Figure 3.4 shows an example of ion heating due to multiple non-adiabatic pitch-angle scatterings

when a cold and field-aligned ion beam moves in a magnetic field line with multiple sharp turns. The scale length λ of a sharply curved field line is less than or about the same as the ion gyro radius r_g, and the distance between two sharp turns is much greater than the ion gyro radius. Magnetic field may be smoothly curved in between two sharp turns, but for simplicity the magnetic field line between two sharp turns is assumed to be straight in Figure 3.4. The ion velocity changes from $\mathbf{v}_1$ to $\mathbf{v}_2$ as they moves across the first sharp turn in panel (*c*) of Figure 3.4. After ignoring the electric field effect, the scattered velocity $\mathbf{v}_2$ should lie in the sector region between the local magnetic field line and the dashed line. The dashed line is in the same direction as $\mathbf{v}_1$. The scattered velocity $\mathbf{v}_2$ should be in the same direction as $\mathbf{v}_1$ when the change of magnetic field is a step function, i.e., $\lambda \approx 0$. The velocity $\mathbf{v}_2$ should be aligned with the local magnetic field when $\lambda \gg r_g$ as the case shown in panel (*a*). Due to non-zero pitch angle of the scattered velocity $\mathbf{v}_2$, a ring-type ion velocity distribution will be formed after the beam ions move across the first sharp turn on the magnetic field line. The ring-type ion distribution will heat up after passing through additional sharp turns along the magnetic field line. It may be noted that a long distance between two sharp turns is an important condition for strong ion heating. If $L \approx \lambda \leq r_g$, such as the very short wavelength whistler waves, ions will move along the average magnetic field direction. Ions may be slow down and slightly preheated as they interact with these short wavelength waves. The pitch-angle scattering by a single sharp turn can result in effective ion heating if the incoming ions are slightly preheated as shown in panel (*d*) of Figure 3.4. The structure of magnetic field shown in Figure 3.4*d* is similar to the one shown in Figure 3.4*c* and the incoming ion distribution shown in Figure 3.4*d* is similar to the one shown in Figure 3.4*b*. In this case, ion heating occurs after the first sharp turn on the magnetic field line. Continuous ion heating can occur after the

second sharp turn on the magnetic field line with decreasing field magnitude. This result is in contract with the cooling due to adiabatic pitch-angle scattering shown in Figure 3.4*b*.

Strong pitch-angle scatterings can lead to ion reflection. Ion heating due to ion reflections has not been included in the discussion of Figure 3.4. However, one can see the possibility of ion reflection in panels (*c*) and (*d*) of Figure 3.4, where the vector $\mathbf{v}_3$ is directed upstream. A gyro-reflection model will be proposed in Section 3.4 based on the pitch-angle scatterings back and forth across the shock front by the ramp magnetic field and the upstream magnetic field in the quasi-parallel shocks.

Non-zero tangential electric field in the shock transition region can also result in non-adiabatic pitch-angle scattering. Since ion gyro radius r_g increases with increasing v, the non-zero tangential electric field can then result in changes of r_g, consequently it will affect pitch-angle scattering. The condition for ions to gain or loss kinetic energy is strongly dependent on the phase angle of the ion with respect to the phase angle of the tangential electric field. Thus, the ring-type ion distribution shown in Figure 3.4*c* will be heated up due to the presence of non-zero tangential electric field in the shock transition region. On the other hand, the presence of tangential electric field in the shock transition region but not on the upstream side indicates that there is a time-dependent variation on the magnetic field structure in the shock transition region. As a result, ions entering the shock transition region at different times will encounter different magnetic field structures and result in different pitch-angle scatterings. Thus, the non-zero tangential electric field in the shock transition region can contribute to the ion heating process in the collisionless shocks.

Ion heating due to pitch-angle scattering will be demonstrated in the simulation results to be discussed in Section 3.3. The above discussion will serve as a guide to

the conclusion that ion heating is due to pitch-angle scattering through the magnetic field structures in the shock transition region. The kinetic description of ion heating in the quasi-parallel shock demonstrated in this study will be used to reinforce previous macroscopic description on ion heating in terms of pressure anisotropy [*Kan and Swift*, 1983], and the ion equation of state [*Mandt and Kan*, 1988] in the quasi-parallel shocks.

3.1.4 Shock Front Reformation

Shock front reformation on the ion gyration time scale in supercritical quasi-parallel shocks was first discussed by *Burgess* [1989]. Recently, based on two-dimensional simulation results *Thomas et al.* [1990] showed that the cyclic reformation process can occur at different locations along the shock front. Since the long time average shock front structure is relatively stable, these simulation results still satisfy the MHD shock jump condition. Note that the MHD shock jump condition is obtained based on the MHD time scale. Thus, the MHD shock jump condition can only apply to time scale much longer than the ion gyro period. Due to the complex nature of quasi-parallel shocks, the cause-and-effect relationship of the shock front reformation processes is still not fully understood [e.g., *Winske et al.*, 1990].

3.1.5 Formations of Large Amplitude Waves in the Shock-Transition Region

Large amplitude waves in the shock-transition region are important to the ion dynamics associated with ion reflection, ion leakage and ion heating in the quasi-parallel shocks. Large amplitude whistler waves appear to be phase standing upstream from shock front [*Kan and Swift*, 1983; *Mandt and Kan*, 1988]. The large amplitude waves

in the high Mach number quasi-parallel shocks may be generated by the firehose instability in the shock layer [*Kan and Swift*, 1983]. *Quest* [1988] showed that the upstream waves in the parallel shock are not phase-standing but group-standing waves generated by ion beam-driven instability. *Omidi et al.* [1990] suggested that the downstream large amplitude waves may arise from the "old shock front" propagating downstream after a new shock front is formed in the reformation process. The formation of large amplitude waves in both low Mach number shocks and high Mach number shocks will be reexamined in detail in this chapter.

3.2 Simulation Model

Numerical simulations are performed using one-dimensional hybrid code, in which ions are treated as macro-particles while electrons are treated as a fluid subject to the adiabatic equation of state. This simulation code was originally developed by Professor Dan Swift in 1983 and modified by Dr. Mark Mandt in 1988. It has been used extensively since 1983 by the Space Physics Group of the Geophysical Institute at the University of Alaska Fairbanks. The validity and reliability of this code have been well established in the literature. A particle-labeling diagnostic developed by *Lyu and Kan* [1990] is used and further improved in this study. This new diagnostic can help us to study ion dynamics in the complex and highly dynamic shock-transition region. In addition, due to increasing concern on the validity of different simulation models [e.g., *Omidi and Winske*, 1990], a brief discussion of how to use our simulation model wisely and correctly will be given in Section 3.2.1. This discussion may serve as a guideline for those who are unfamiliar with our model but want to compare the performance of our simulation model with the performance of theirs.

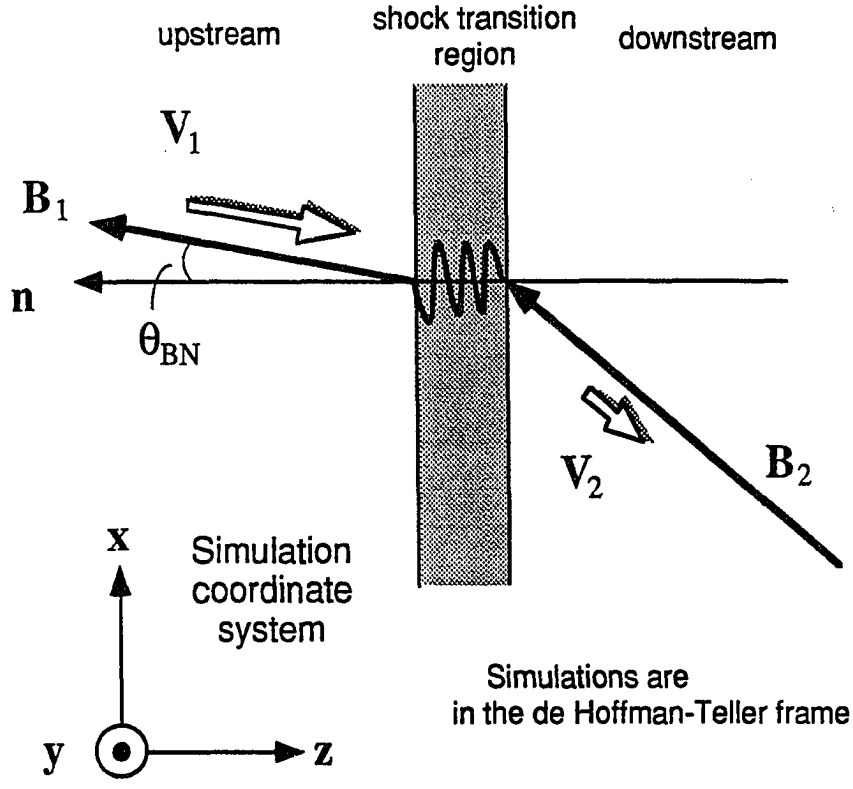

Figure 3.5 A sketch of the coordinate system used in the hybrid simulation study of quasi-parallel shocks shown in this chapter.

3.2.1 Boundary Conditions and Initial Conditions

Boundary conditions of this simulation code are fixed according to the Rankine-Hugoniot jump condition [e.g., *Kantrowitz and Petschek*, 1966]. A sketch of the coordinate system is given in Figure 3.5. Shock normal **n** is along the $-z$ direction. Upstream and downstream magnetic fields are in the x-z plane. The normal magnetic field component is chosen to be $B_z < 0$, and the initial tangential magnetic field is chosen to be $B_x > 0$. The initial flow velocity is antiparallel to the initial magnetic field everywhere in entire simulation domain. The simulations are performed in the de Hoffman-Teller frame, where tangential electric field vanishes on the upstream and downstream boundaries. Buffer zones are placed on the upstream and downstream

boundaries allowing ions to move in and out of the simulation domain and to maintain a constant particle flux at each boundary. Further information of the simulation code can be found in the Appendix of the Ph.D. Thesis by *Mandt* [1988].

Quasi-parallel shocks with upstream shock normal angle $\theta_{BN} = 10°$, upstream plasma beta $\beta = 0.5$, and upstream Mach number $M_A = 1.2$, 2, 4, and 6 are studied in this chapter, where the shock normal angle θ_{BN} is the acute angle between the shock normal direction and the upstream magnetic field direction, plasma β is the ratio of the plasma pressure to the magnetic pressure, and M_A is the ratio of the upstream normal flow speed to the upstream Alfvén speed C_A defined in Chapter 1. Choices of grid size, simulation system length and initial ramp thickness for each shock simulation are discussed below.

(*a*) *Grid Size.* For quasi-parallel fast shocks, whistler waves can disperse from an over-steepened shock front and propagate upstream. These upstream waves may play an important role in the shock heating processes. Thus, the grid size must be small enough to resolve these upstream waves. Since the wavelength of whistler waves decreases with increasing phase speed, and since only the waves with phase speed greater than the upstream flow speed can propagate upstream, we can estimate the grid size such that it is good enough to resolve the linear whistler waves with phase speed greater than the upstream flow speed. The resolution of grid size is estimated based on the following method. The accuracy of describing a period of sine wave by n data points may be estimated by the ratio of the area of a regular polygon with n sides to the area of its circumscribed circle. The estimated value is equal to $\sin(x)/x$, where $x = 2\,\pi/n$. A 90% accuracy indicates that there are at least eight grid points in each wavelength. For grid size $\Delta = 0.1\ c/\omega_{pi}$ is within 90% accuracy in resolving a linear whistler wave that propagates 10° to the ambient magnetic field with phase

speed equal to 7.5 C_A in a $\beta = 0.5$ plasma. Thus, in this study, we choose grid size $\Delta = 0.2\ c/\omega_{pi}$ for the $M_A = 1.2$ fast shock, but $\Delta = 0.1\ c/\omega_{pi}$ for the $M_A = 2$, 4, and 6 shocks, so that the grid size is small enough to resolve the upstream whistler waves in each case. It should be noted that linear whistler waves are only used to estimate the appropriate grid size. The upstream waves obtained in the quasi-parallel shock simulations are nonlinear, and their wavelength may be slightly different from the wavelength of linear waves for a given phase speed.

(*b*) *Simulation System Length.* The choice of simulation system length depends on the length of shock-transition region. According to early simulation results of $\theta_{BN} = 10°$ quasi-parallel shocks [e.g., *Kan and Swift*, 1983; *Mandt and Kan*, 1988], the length of shock-transition region is about 80 c/ω_{pi} for the $M_A = 2$ and 4 shocks. The length of simulation system is chosen to be 1536 grids, which is 307.2 c/ω_{pi} for the $M_A = 1.2$ fast shock, but 153.6 c/ω_{pi} for the $M_A = 2$, 4, and 6 shocks. The simulation system length used in this study is good enough to cover the entire shock-transition region for all four cases. However, this simulation study cannot resolve the characteristics of nonlinear wave and leakage ions in the far-upstream region due to finite length of the simulation box. Thus, the characteristics of backstreaming upstream ions and upstream waves discussed in this chapter can only apply to the near-upstream region with distance upstream from shock front no more than 50 c/ω_{pi}.

(*c*) *Initial Ramp Thickness.* The region connecting the upstream and downstream states is initialized by a hyperbolic tangent function with thickness D_W. Two different initial widths, $D_W = 3\ c/\omega_{pi}$ and $D_W = 30\ c/\omega_{pi}$, are used to study each of the aforementioned examples. For $D_W = 30\ c/\omega_{pi}$, evolution of shock ramp in all cases is governed by nonlinear steepening of a gentle compression wave. For $D_W = 3\ c/\omega_{pi}$, the shock is formed initially by a piston-like pulse, which is more like a magnetic

piston (i.e., large magnetic jump, but small pressure jump) for the low Mach number shocks but more like a hot-plasma piston (i.e., large pressure jump, but very small magnetic jump) for the high Mach number shocks. Due to nonlinear dispersive effects, the magnetic piston can emit large amplitude waves to initiate the shock formation. On the other hand, interactions between the hot-plasma piston and the upstream plasma can lead to ion beam-driven instabilities that may also initiate the shock formation. Simulations with different D_W of 3 c/ω_{pi} and 30 c/ω_{pi} lead to similar shock structures in all four cases after the shock front is fully developed and most of the initial transients propagated out of the simulation box. Simulations with a narrow initial ramp of D_W = 3 c/ω_{pi} usually take less simulation time to obtain a fully developed shock, except in the $M_A = 6$ shock simulation. Thus, resources are saved by chosing a narrow D_W. However, the amplitude of initial transient due to the initial profile increases with decreasing ramp thickness. Due to finite size of simulation domain, these initial transients may not be able to leave the simulation system completely without reflection. Thus, the simulation results obtained by nonlinear steepening of a gentle compression wave are more reliable than the one obtained from a narrow D_W.

For the $M_A = 6$ shock simulation, it takes more simulation time to obtain a fully developed shock structure when a narrow initial ramp $D_W = 3\ c/\omega_{pi}$ is used. To understand the cause, we carefully examine the shock front formation process from the beginning of the simulation. A large number of initially loaded downstream hot ions can leak across the initial shock ramp, before an overshoot magnetic field is formed, in the simulation study with $D_W = 3\ c/\omega_{pi}$. These initially leaked ions cannot only result in large amplitude initial transients on the upstream side but also lead to collapse of the initial plasma piston. The collapse of initial plasma piston lead to a very thick shock ramp, which takes a longer time for the nonlinear wave to grow.

By increasing the initial ramp thickness the number of initially leaked ions can be reduced. Consequently, it can reduce the amplitude of upstream transient generated by these initially leaked ions and prevent the collapse of initial shock front.

The reason that the number of initially leakage ions can be reduced by increasing initial ramp thickness can be understood as follows. Figure 3.6 shows Rankine-Hugoniot jump conditions as a function of the upstream Alfvén Mach number M_A for quasi-parallel shocks of $\theta_{BN} = 10°$ (sold curve), 20° (dashed curve), 30° (dotted curve), and upstream plasma $\beta = 0.5$. Panel (*a*) plots the ratio of downstream plasma density to the upstream plasma density. Panel (*b*) plots the ratio of downstream plasma pressure to the upstream plasma pressure. Panel (*c*) plots the ratio of downstream tangential magnetic field to the upstream tangential magnetic field. Panels (*d*) and (*e*) plot the ratio of downstream total magnetic field to the upstream total magnetic field. The solid dots with error bars shown in panel (*e*) indicate the overshoot magnetic field in the shock transition region obtained from the $M_A = 4$ and 6 shock simulations with $\theta_{BN} = 10°$. As we can see, the plasma density and plasma pressure on the downstream side increases with increasing Mach number for all three θ_{BN}. On the other hand, for the plot of magnetic field jump ratio shown in panels (*c*) and (*d*) only the $\theta_{BN} = 30°$ curve increases monotonically with increasing Mach number. For $\theta_{BN} = 10°$ and 20° shocks the ratio of magnetic field jump decreases with increasing Mach number as the Mach number greater than a certain value, which is at $M_A \approx 2$ for $\theta_{BN} = 10°$ but at $M_A \approx 3$ for $\theta_{BN} = 20°$. The magnitude of overshoot magnetic field shown in panel (*e*) increases with increasing Mach number. An overshoot of magnetic field is always present in a fully developed high Mach number shock [e.g., *Mandt*, 1988; *Mandt and Kan*, 1988]. Since the initial jump of the magnetic field is small but the jump of the plasma temperature is large in the high Mach number quasi-parallel shocks, hot

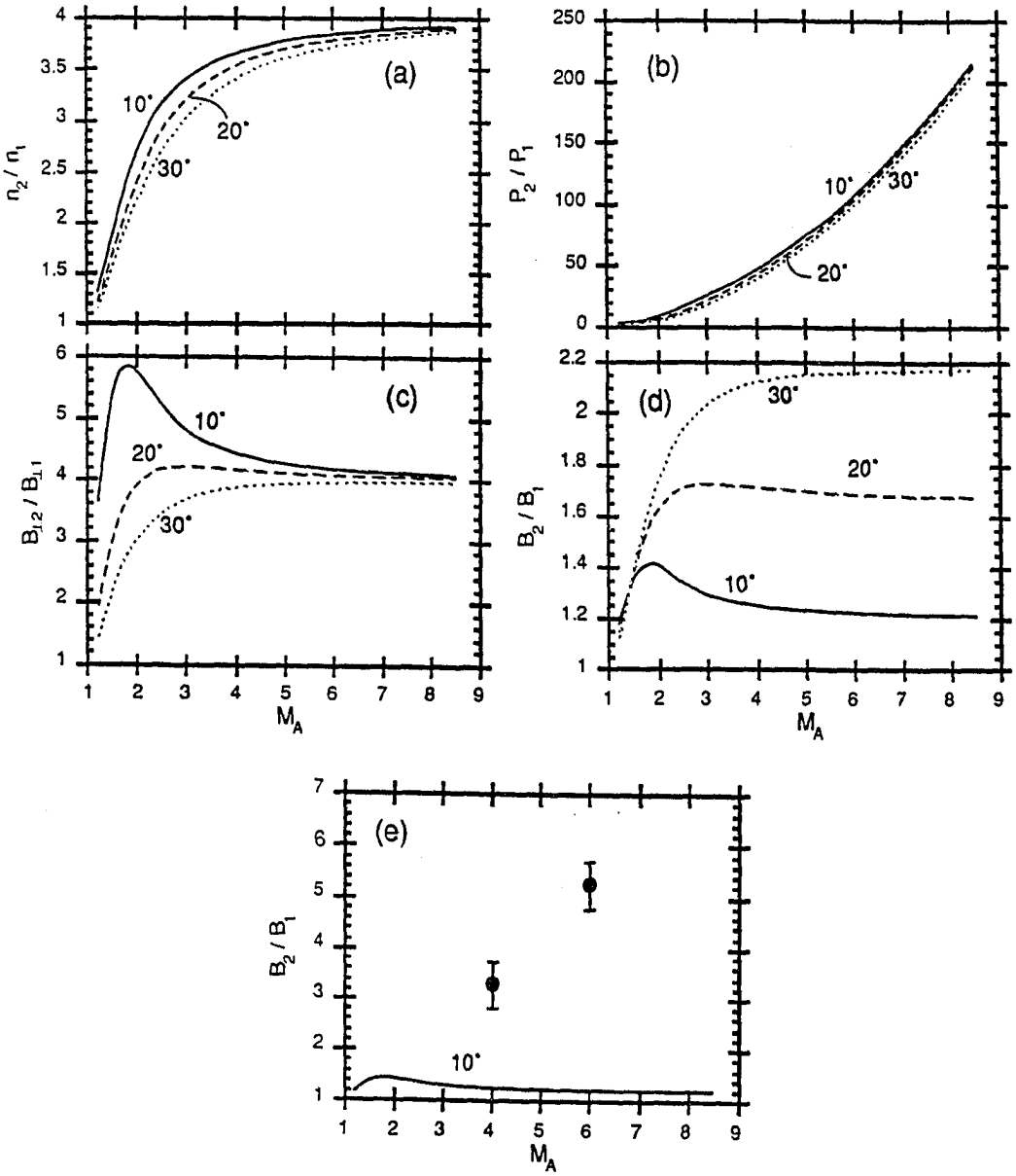

Figure 3.6 Plots of fast shock Rankine-Hugoniot jump conditions as a function of the upstream Alfvén Mach number M_A for quasi-parallel shocks with $\theta_{BN} = 10°$ (sold curve), 20° (dashed curve), 30° (dotted curve), and upstream plasma $\beta = 0.5$, where n, p, $B_\perp$, and B are the plasma density, the plasma pressure, the tangential magnetic field magnitude, and the total magnetic field, respectively. The subscripts 1 and 2 denote upstream quantity and downstream quantity, respectively. The solid dots with error bars shown in panel (e) indicate the overshoot magnetic field in the shock transition region obtained from the $M_A = 4$ and 6; $\theta_{BN} = 10°$ shock simulations.

downstream ions can freely enter the upstream region before the formation of overshoot magnetic field. The number of leakage ions from the downstream side are significantly reduced after the overshoot magnetic field is fully developed. However, it takes time for the overshoot magnetic field to develop. (Unfortunately, we have no idea on how to self-consistently make up an initial profile with overshoot magnetic field to reduce simulation time!) Since the density gradient and the temperature gradient are small in a wide initial ramp, it will take a longer time for the initial loaded downstream ions to leak out. As a result, in the large D_W simulation, only a small number of downstream ions can escape upstream before the overshoot magnetic field is fully developed.

The characteristic of adjustable initial ramp thickness is an important element of our simulation model. The above discussion can apply to other simulation studies of hydromagnetic shock with large temperature difference across the shock front, such as low β slow-mode shocks with upstream flow speed greater than the upstream thermal speed in the de Hoffman-Teller frame. Note that as mentioned before, due to increasing concern on the validity of different simulation models [e.g., *Omidi and Winske*, 1990], the above discussion may serve as a guide line for those who are not familiar with this model but want to study and compare the performance of this simulation model with the performance of others.

3.2.2 Particle-Labeling Diagnostics

To trace the origin of backstreaming ions on the upstream side, a four-group labeling technique was introduced by *Lyu and Kan* [1990] in which ions are divided into four groups: (1) the initially loaded upstream ions, (2) the initially loaded downstream ions, (3) the incoming streaming ions from the upstream boundary, and (4) the ions entering from the downstream boundary due to thermal motions. Ions in the

same group are labelled by a single number. The group number assigned to an ion is removed when the ion leaves the simulation domain. When the ion reenters the simulation box, it will be given a new label.

An improved multiple-group labeling scheme is introduced in this study since the four-group labeling scheme is not good enough to resolve the ion reflection process in high Mach number quasi-parallel shocks. This improved diagnostic enables us to see the dynamics of ion reflection in greater detail.

In the new scheme of multi-group labeling diagnostic, incoming ions are further divided into sub-groups based on the time interval that they enter the simulation box. The initially loaded ions can also be divided into several sub-groups based on their initial locations.

3.3 Simulation Results

Simulation results of $\theta_{BN} = 10°$, $\beta = 0.5$, $M_A = 1.2$, 2, 4 and 6 shocks will be present in this section, where M_A is the Mach number based on the upstream Alfvén speed C_A. The equivalent magnetosonic Mach numbers of the four cases are $M_F \approx$ 1.19, 1.98, 3.96, and 5.94, where M_F is the Mach number based on the upstream fast-mode speed V_F. Each of the four cases represents a group of quasi-parallel shocks that has unique wave structures and ion distributions in the shock transition region. Three critical Mach numbers can be drawn based on the simulation results of the four cases, which will be discussed later in Section 3.5.

3.3.1 $M_A = 1.2$ Fast Shock

Simulation results shown in this section are obtained from the $M_A = 1.2$ fast shock simulation with initial ramp thickness $D_W = 30\ c/\omega_{pi}$. Note that under the same upstream conditions of $\theta_{BN} = 10°$, $\beta = 0.5$, and $M_A = 1.2$, there are two more

shock solutions that can be obtained from the Rankine-Hugoniot jump conditions. They are the $M_A = 1.2$ fast-Alfvén-slow shock solution and the $M_A = 1.2$ fast-Alfvén shock solutions. The characteristics of these intermediate shocks will be discussed in the next chapter. To make the definition clear, we shall use "$M_A = 1.2$ fast shock" instead of "$M_A = 1.2$ shock" in our discussion throughout this chapter.

Figure 3.7 shows spatial profiles of ion normal flow velocity V_z, ion number density N_i, ion temperature T_i, tangential components of magnetic field B_x and B_y, and total magnetic field B, obtained from the $M_A = 1.2$ fast shock simulation at $t\Omega_{ni} = 100$, where Ω_{ni} is the ion gyro-frequency based on the normal component magnetic field. Normalized constants used in this figure are the upstream Alfvén speed C_A, upstream ion number density N_o, upstream ion temperature T_o, and normal magnetic field B_o. Profiles of ion density, ion temperature, ion normal flow velocity, and the total magnetic field indicate a laminar shock structure. Finite-amplitude whistler waves can be seen upstream from shock front in the plots of B_x and B_y. The amplitude of the dispersive wave is much smaller than the amplitude of the shock ramp.

Figure 3.8 plots the spatial profiles of B_x at successive times. Nonlinear steepening can be seen at the shock ramp when $t\Omega_{ni} < 50$. The final ramp thickness is about one half of the initial ramp thickness.

Figure 3.9 shows the magnetic hodograms of the $M_A = 1.2$ fast shock at different times as indicate. The upstream whistler waves can be easily distinguished from the shock ramp in the hodogram plots. The upstream whistler waves are characterized by a right hand polarized spiral-type magnetic hodogram. The magnetic hodogram at the shock ramp of the $M_A = 1.2$ fast shock is characterized by a hook-shaped structure due to change of polarization at downstream part of the shock ramp.

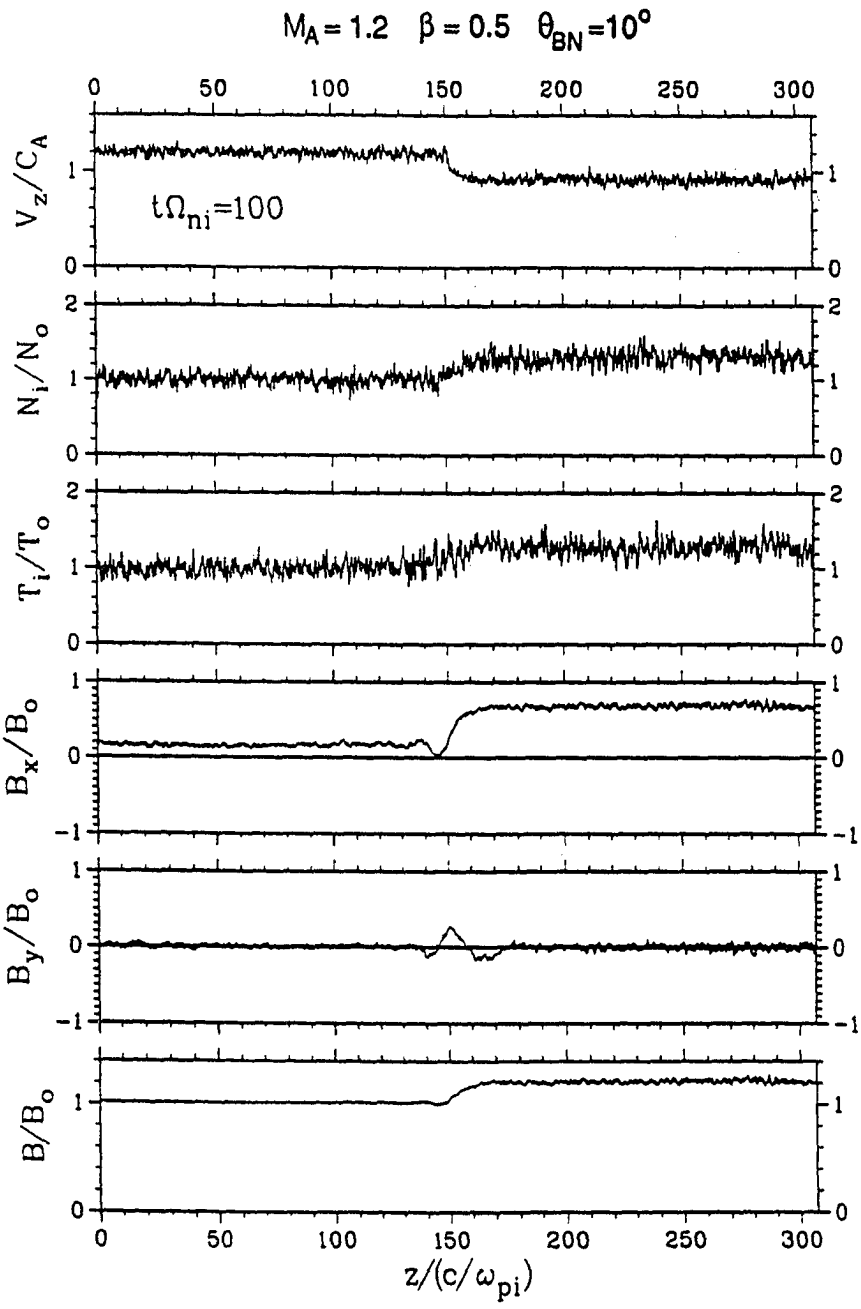

Figure 3.7 Spatial profiles of ion normal flow velocity V_z, ion number density N_i, ion temperature T_i, tangential components of magnetic field B_x and B_y, and total magnetic field B, obtained from the $M_A = 1.2$ fast shock simulation at $t\Omega_{ni} = 100$. Normalized constants used in this figure are the upstream Alfvén speed C_A, upstream ion number density N_o, upstream ion temperature T_o, and normal magnetic field B_o.

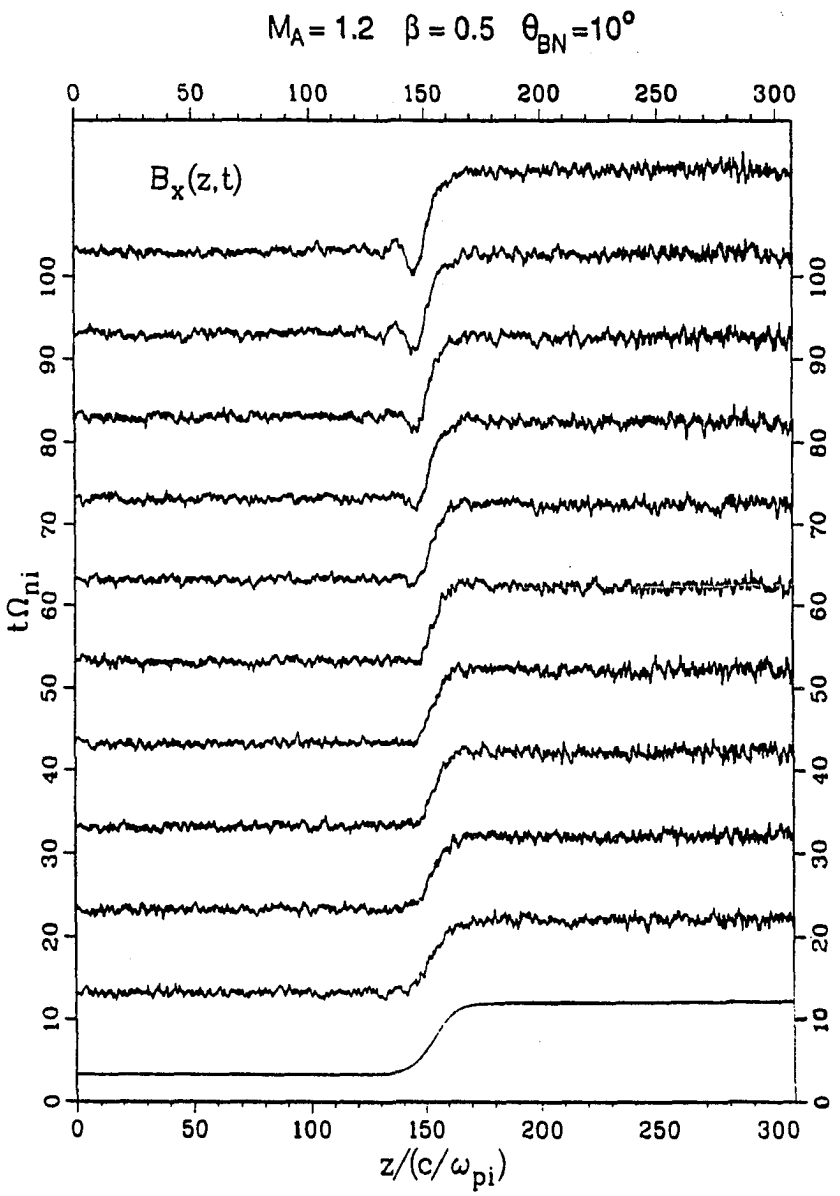

Figure 3.8 Spatial profiles of B_x plotted at successive times obtained from the $M_A = 1.2$ fast shock simulation. Nonlinear steepening can be seen at the shock ramp when $t\Omega_{ni} < 50$. The final ramp thickness is about one half of the initial ramp thickness.

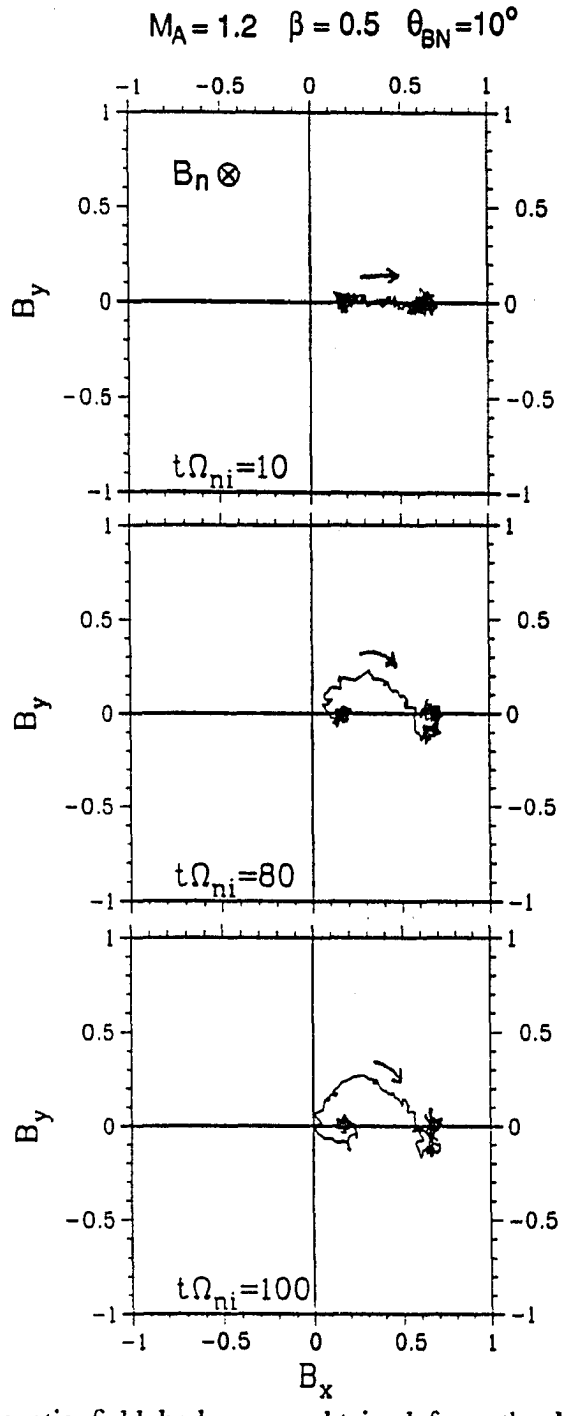

Figure 3.9 Magnetic field hodograms obtained from the $M_A = 1.2$ fast shock simulation at different times as indicated. Arrows are going in downstream direction. The upstream whistler waves are characterized by a right hand polarized spiral-type magnetic hodogram. The magnetic hodogram at the shock ramp is characterized by a hook-shaped structure due to change of polarization on the downstream side of shock front.

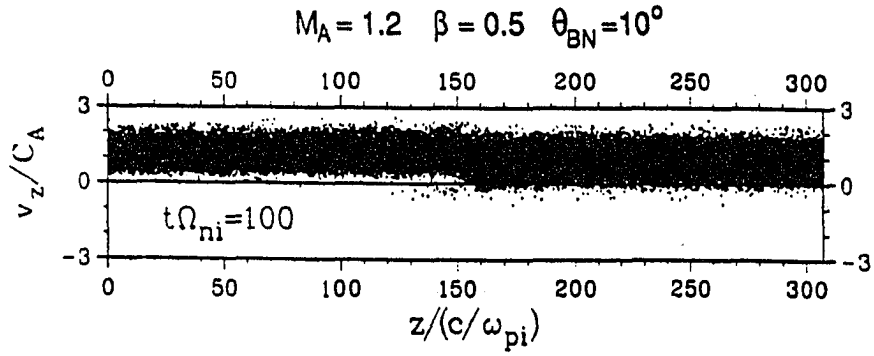

Figure 3.10 A scatter plot of ion distribution in the v_z-z space obtained from the $M_A = 1.2$ fast shock simulation at $t\Omega_{ni} = 100$. All the ions currently inside the simulation box are plotted. A small number of backstreaming diffuse ions can be found upstream from the shock front.

Figure 3.10 shows a scatter plot of ion distribution in the v_z-z space obtained from the $M_A = 1.2$ fast shock simulation at $t\Omega_{ni} = 100$. All the ions currently inside the simulation box are plotted. A small number of backstreaming diffuse ions can be found upstream from the shock front. To show these diffuse ions are leakage ions rather than upstream ions being scattered locally before entering the shock ramp, a special diagnostic is designed based on ion distributions in ϕ-z space, where ϕ is the ion pitch angle defined by the angle between ion velocity direction and local magnetic field direction. We choose to do the diagnostic in the ϕ-z space instead of the v_z-z space because it is easier to determine the direction of particle motion from the pitch angle than from the normal component of the particle velocity.

Figure 3.11 shows scatter plots of ion pitch angle distribution of three groups of ions in the ϕ-z space at $t\Omega_{ni} = 100$, where ions plotted in each panel are initially loaded in the region as denoted by the horizontal bar shown in each panel. Locations of these horizontal bars indicate that ions shown in panels (*a*) and (*b*) are initially loaded upstream ions, and ions shown in panel (*c*) are initially loaded downstream

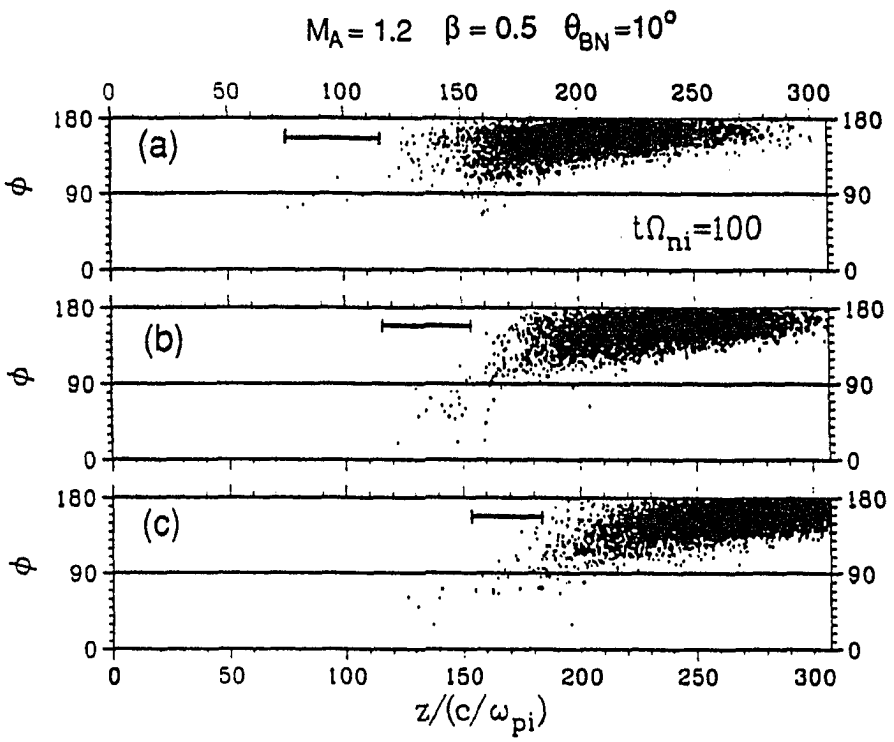

Figure 3.11 Scatter plots of ion pitch angle distribution of three groups of ions in the ϕ-z space at $t\Omega_{ni} = 100$ obtained in the $M_A = 1.2$ fast shock simulation. Ions plotted in each panel are initially loaded in the region as denoted by the horizontal bar shown in each panel. For $B_z < 0$, backstreaming ions can be identified by $\phi \ll 90°$. Backstreaming ions can be seen in panels (*b*) and (*c*), but not in panel (*a*).

ions. For $B_z < 0$, backstreaming ions can be identified by $\phi \ll 90°$. It can be seen that most of the backstreaming ions ($\phi \ll 90°$) appear in panels (*b*) and (*c*). Note that ions in panel (*b*) are initially loaded closer to the shock front than ions shown in panel (*a*). If the upstream diffuse ions are results of locally scattered upstream ions, they should appear in both panels (*a*) and (*b*). The absence of backstreaming ions in panel (*a*) indicates that a small number of backstreaming diffuse ions appeared on the upstream side are mostly leakage ions either from downstream hot ions as shown in panel (*c*) or from shock heated ions as shown in panel (*b*).

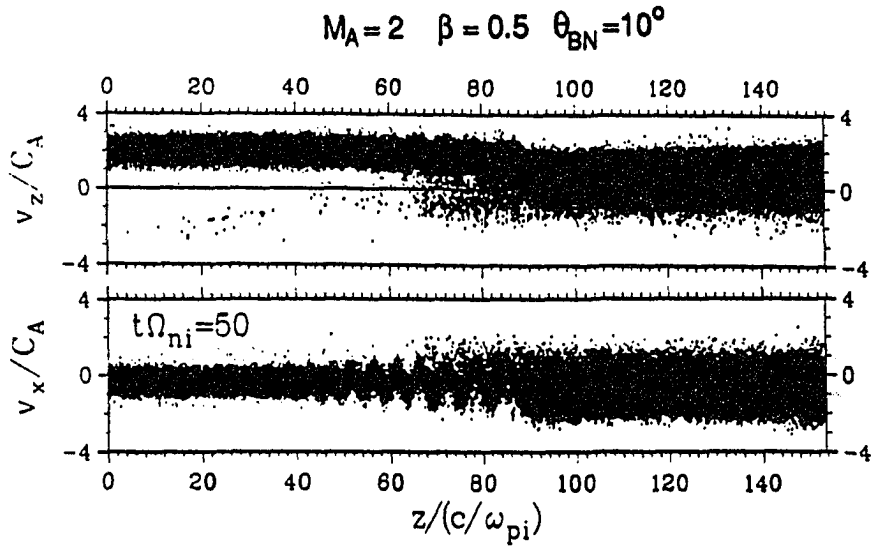

Figure 3.12 Scatter plots of ion distribution in (*a*) v_z-z space and (*b*) v_x-z space obtained from the $M_A = 2$ shock simulation at $t\Omega_{ni} = 50$. All the ions currently inside the simulation box are plotted. A large number of diffuse ions can be found in the region between $z \approx 60$–$80\ c/\omega_{pi}$.

3.3.2 $M_A = 2$ Shock

Simulation results shown in this section are obtained from the $M_A = 2$ shock simulation with initial ramp thickness $D_W = 30\ c/\omega_{pi}$.

Figure 3.12 shows scatter plots of ion distributions in v_z-z space (upper panel) and v_x-z space (lower panel) obtained from the $M_A = 2$ shock simulation at $t\Omega_{ni} = 50$. All ions currently inside the simulation box are plotted. A large number of diffuse ions can be found in the region between $z \approx 60$–$80\ c/\omega_{pi}$. In the following discussion, We use the same method as has been used in Figure 3.11 to identify the source of these diffuse ions.

Figure 3.13 shows scatter plots of ion pitch angle distribution of five groups of ions in the ϕ-z space at $t\Omega_{ni} = 50$ in the $M_A = 2$ shock simulation, where ions plotted in each panel are initially loaded in the region as denoted by the horizontal bar shown

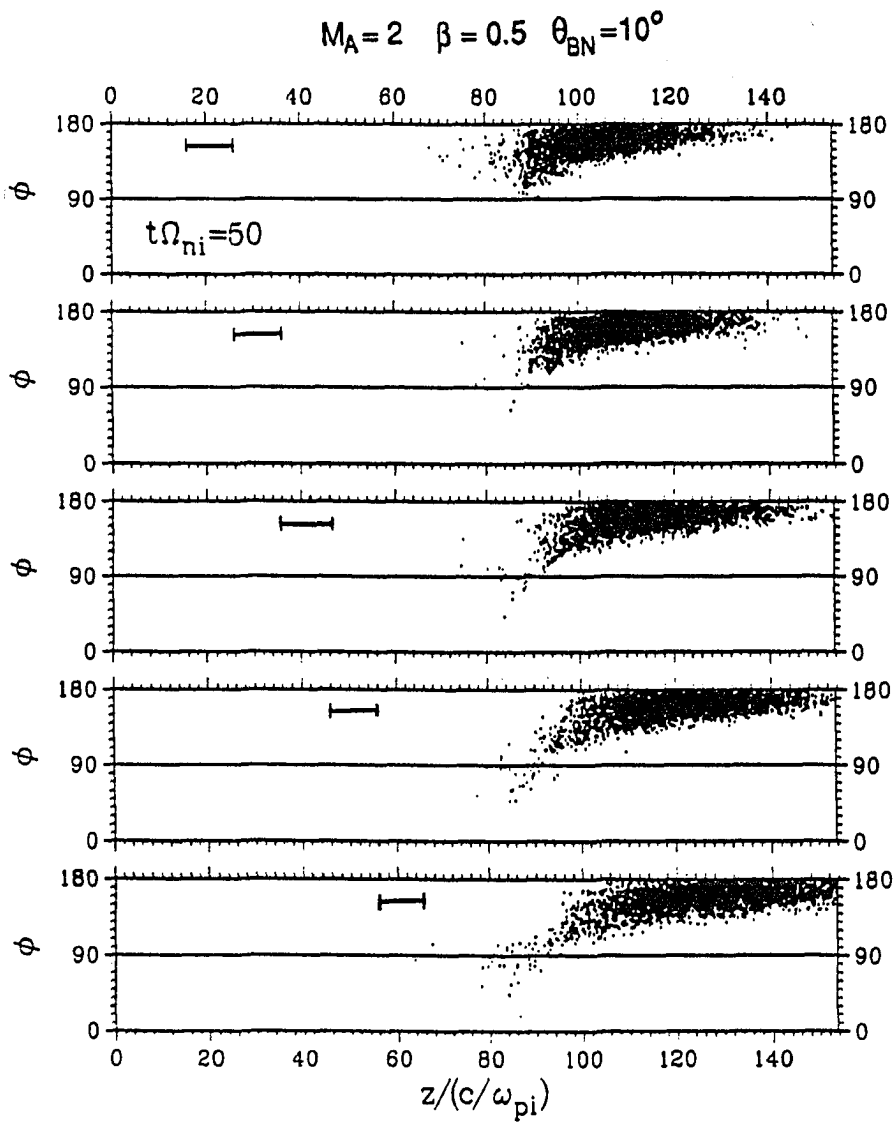

Figure 3.13 Scatter plots of ion pitch angle distribution of five groups of ions in the ϕ-z space at $t\Omega_{ni} = 50$ obtained in the $M_A = 2$ shock simulation. Ions plotted in each panel are initially loaded in the region as denoted by the horizontal bar shown in each panel. Backstreaming ions ($\phi \ll 90°$) can be seen in the lower four panels, but no backstreaming ions can be found in the top panel.

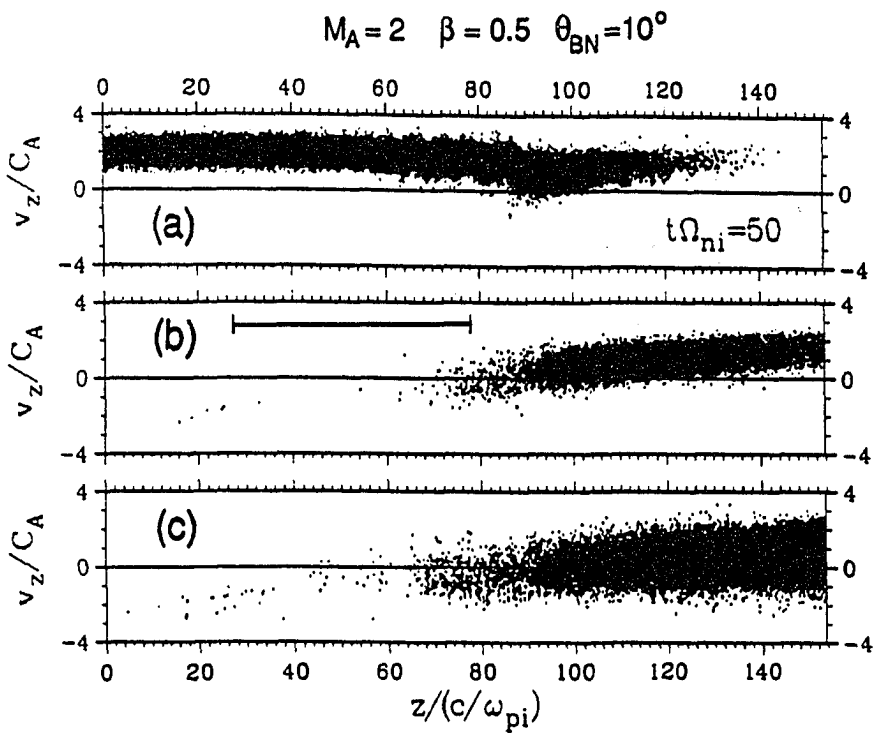

Figure 3.14 Scatter plots of ion distribution of three groups of ions in the v_z-z space obtained from the $M_A = 2$ shock simulation at $t\Omega_{ni} = 50$. Ions shown in panel (*a*) are incoming ions from upstream boundary after $t = 0$ and initially loaded ions that are located at $z \leq 26\ c/\omega_{pi}$. Ions plotted in panel (*b*) are initially loaded in the region as denoted by the horizontal bar. Ions shown in panel (*c*) are initially loaded ions and incoming ions from the downstream boundary. Flow slows down at $z \approx 86\ c/\omega_{pi}$, which will be denoted as the shock front. Leakage of shock heated ions and downstream hot ions can be found upstream from the shock front in panel (*b*) and panel (*c*), respectively. The separation of leakage ions from incoming upstream ion beam is achieved based on the information given in Figure 3.13.

in each panel. Backstreaming ions ($\phi \ll 90°$) can be seen in the lower four panels, but no backstreaming ions can be found in the top panel. Based on the information given in Figure 3.13, we are able to separate the diffuse ions from the cold upstream ion beam in Figure 3.12.

Figure 3.14 shows scatter plots of ion distribution in the v_z-z space of three groups of ions at $t\Omega_{ni} = 50$ obtained from the $M_A = 2$ shock simulation. Ions shown

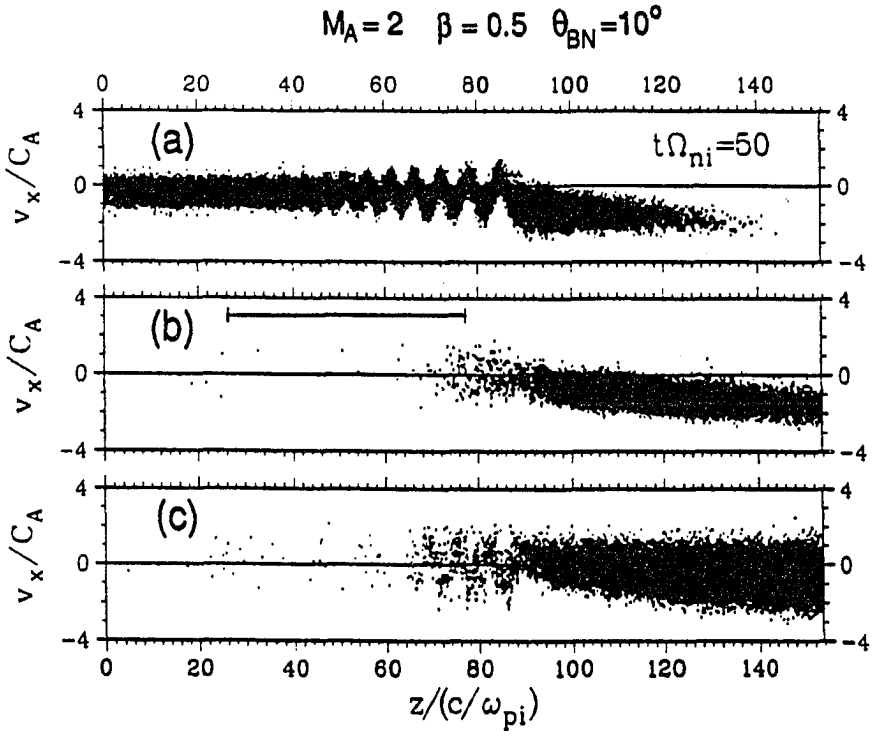

Figure 3.15 Scatter plots of ion distribution in the v_x-z space obtained from the $M_A = 2$ shock simulation at $t\Omega_{ni} = 50$ in the same format as shown in Figure 3.14.

in panel (*a*) are incoming ions from upstream boundary after $t = 0$ and ions initially loaded at $z \leq 26\ c/\omega_{pi}$. Ions shown in panel (*b*) are ions initially loaded in the region as denoted by the horizontal bar. Ions shown in panel (*c*) are initially loaded downstream ions and incoming ions from the downstream boundary. As one can see from panel (*a*), flow slows down at $z \approx 86$–$90\ c/\omega_{pi}$, where will be denoted as the shock front. Backstreaming ions ($\phi \ll 90°$) upstream from the shock front in panel (*b*) are from leakage of shock heated ions. Backstreaming ions ($\phi \ll 90°$) upstream from the shock front in panel (*c*) are from leakage of downstream hot ions. Scatter plots of ion distribution in the v_x-z space and ϕ-z space of the three groups of ions are shown in Figures 3.15 and 3.16 under the same format as shown in Figure 3.14.

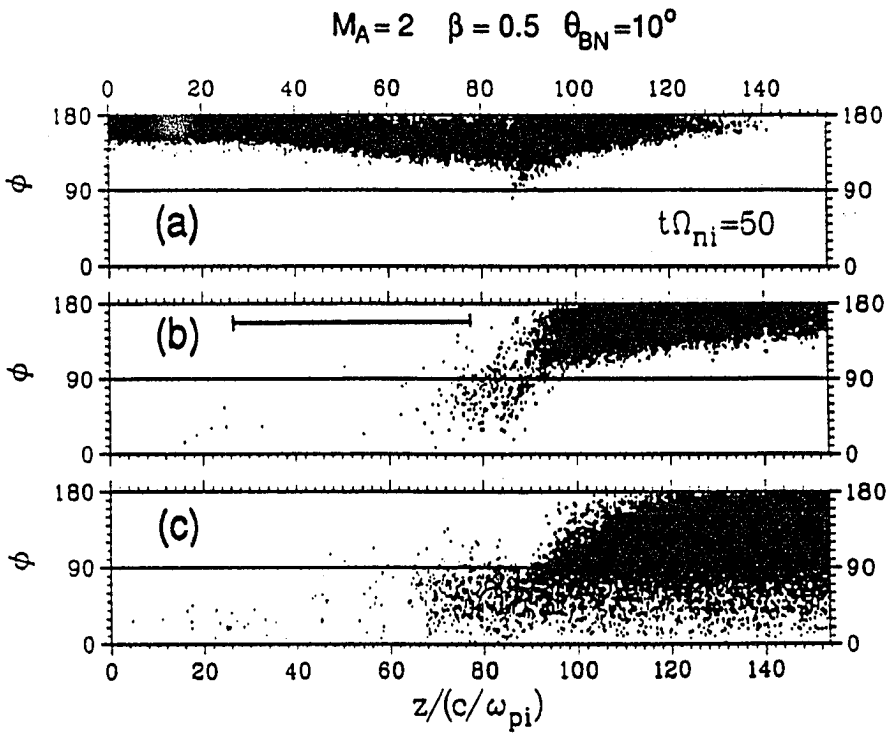

Figure 3.16 Scatter plots of ion distribution in the ϕ-z space obtained from the $M_A = 2$ shock simulation at $t\Omega_{ni} = 50$ in the same format as shown in Figure 3.14.

Figure 3.17 shows spatial profiles of V_z, N_i, T_i, $\log N_i^*$, B_x, B_y, and B obtained from the $M_A = 2$ shock simulation at $t\Omega_{ni} = 50$, where N_i^* is the ion density measured from ions shown in panels (*b*) and (*c*) of Figures 3.14–3.16. According to Figure 3.14, the shock front is located at $z \approx 86$–$90\ c/\omega_{pi}$. The principal jump of the V_z profile and the N_i profile in Figure 3.17 is also located at the shock front. However, the principal jump of the T_i profile appears upstream from the shock front due to the presence of leakage ions as can be seen from the plot of $\log N_i^*$ in Figure 3.17 and scatter plots shown in panels (*b*) and (*c*) in Figures 3.14–3.16. The horizontal bar shown in Figure 3.17 denotes the upstream shock transition region of the $M_A = 2$

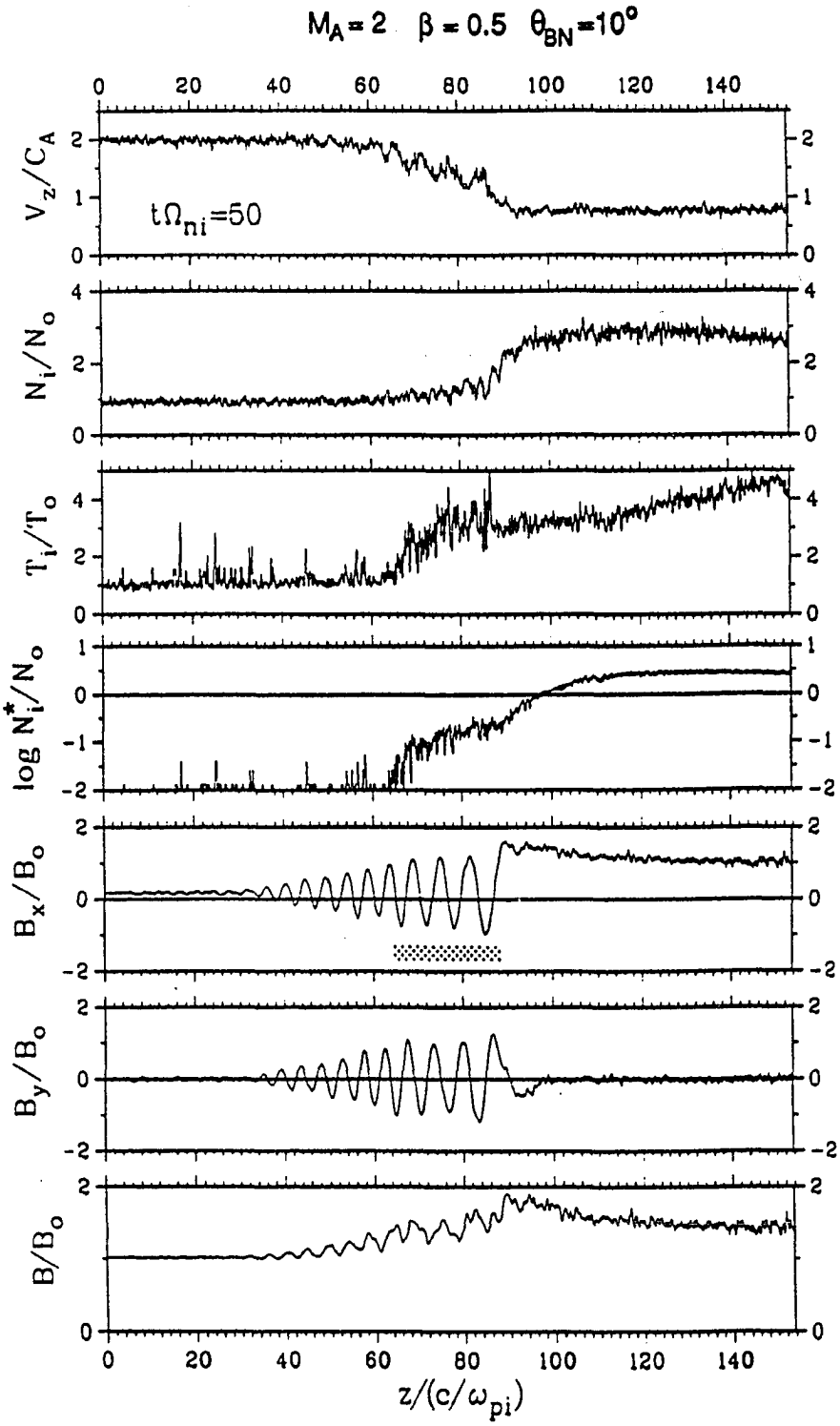

Figure 3.17 Spatial profiles of V_z, N_i, $\log N_i^*$, T_i, B_x, B_y, and B, obtained from the $M_A = 2$ shock simulation at $t\Omega_{ni} = 50$, where N_i^* is the ion density measured from ions shown in panels (*b*) and (*c*) of Figures 3.14–3.16. See text for further discussion in detail.

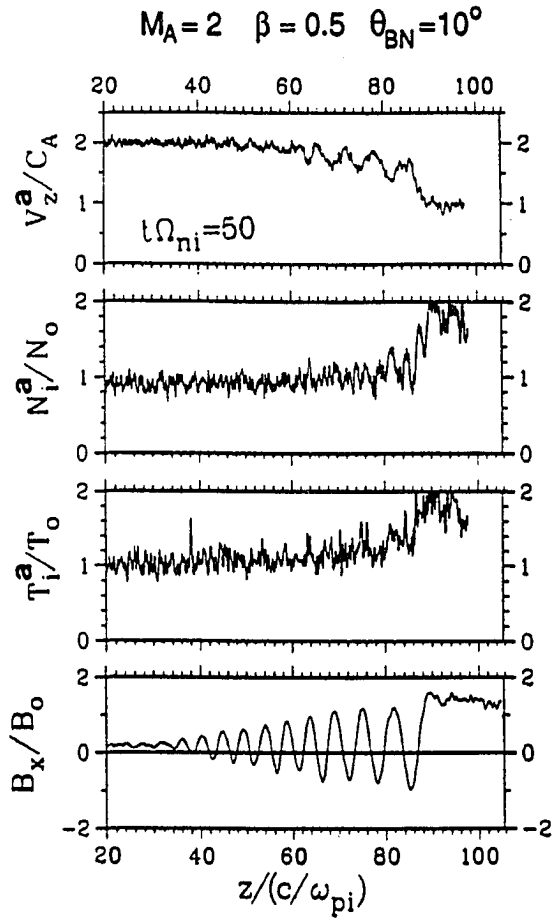

Figure 3.18 Spatial profiles of incoming upstream ion normal flow velocity V_z^a, number density N_i^a, temperature T_i^a, and the x-component magnetic field B_x obtained from the $M_A = 2$ shock simulation at $t\Omega_{ni} = 50$, where the incoming upstream ions are ions shown in panel (a) of Figures 3.14–3.16. A well-defined principal jump in density, temperature, and flow velocity appear at the same location — the shock front. Pre-deceleration and slightly pre-heating can also be found in the upstream shock transition region.

shock, which is defined by the region between shock front and the principal jump of Ti profile in the $M_A = 2$ shock simulation.

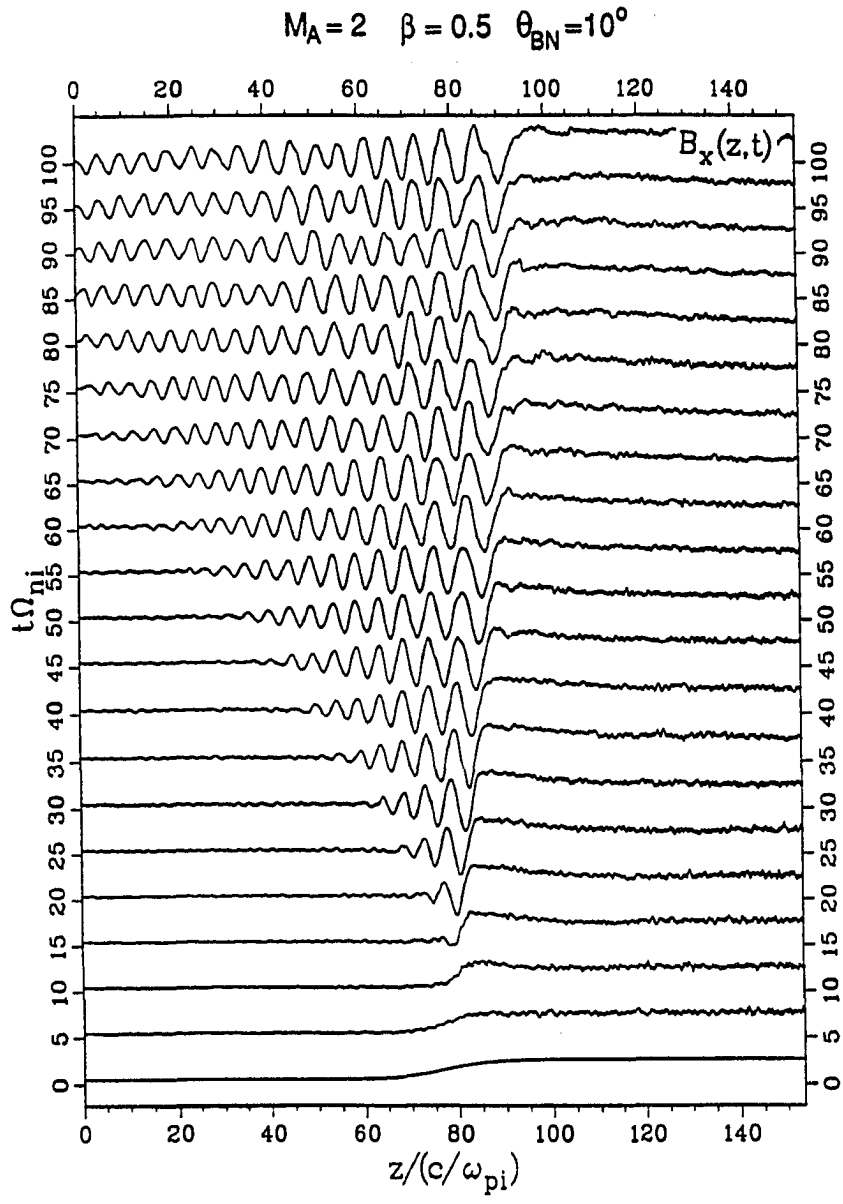

Figure 3.19 Spatial profiles of B_x plotted at successive times obtained from the $M_A = 2$ shock simulation. Large amplitude whistler waves in the upstream shock transition region are phase standing upstream from the shock front.

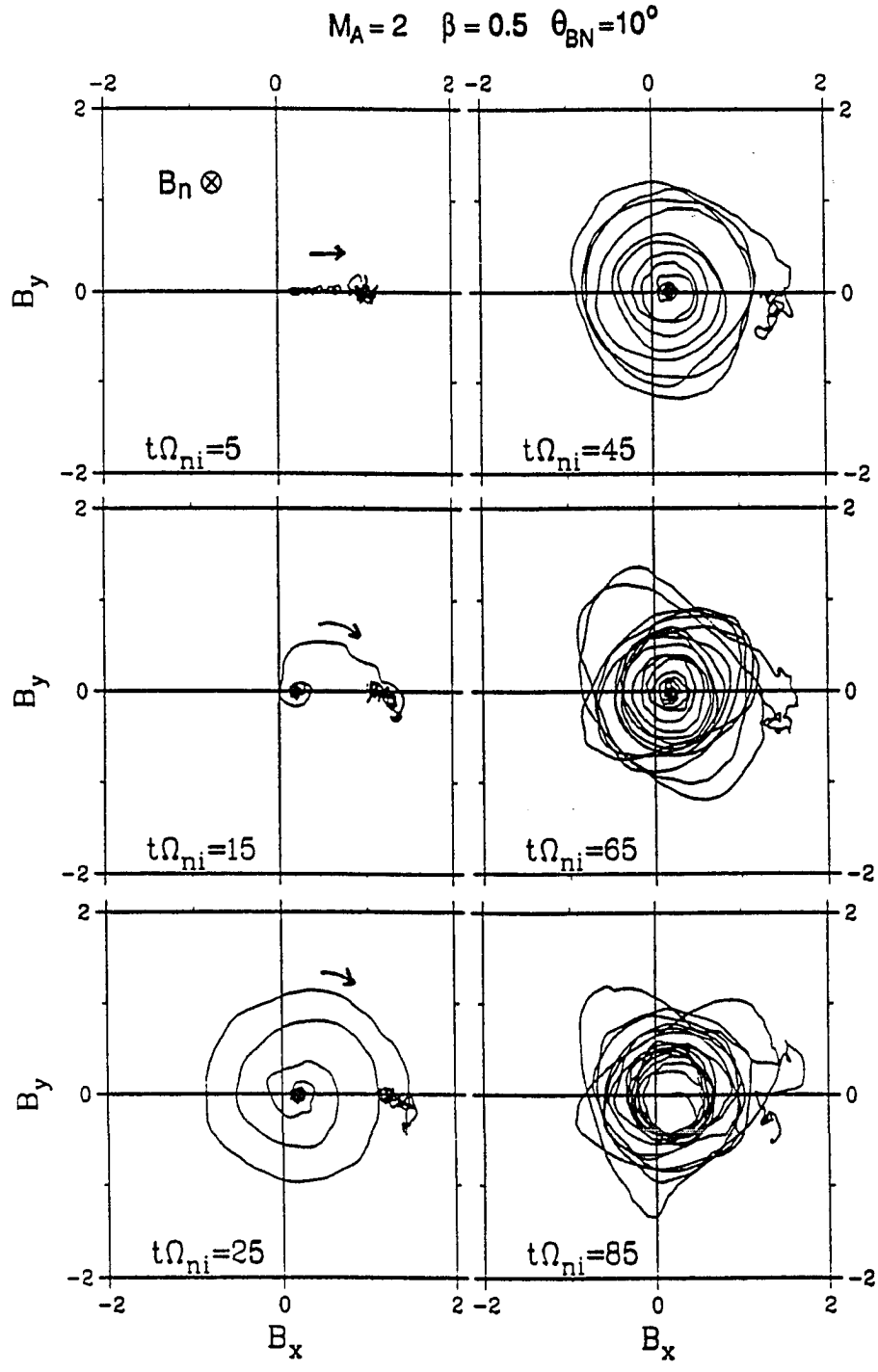

Figure 3.20 Magnetic hodograms obtained from the $M_A = 2$ shock simulation at different times as indicated. Arrows are going in downstream direction. See text for further discussion in detail.

According to the results shown in Figures 3.14–3.17, the plasma behavior and wave magnetic field characteristics inside the upstream shock transition region (USTR) can be summarized as follows. More of them will be discussed later in this section.

(1) Large amplitude whistler wave can be found in USTR in Figure 3.17. The wave amplitude in USTR is nearly constant and is almost as large as the amplitude of the jump of tangential magnetic field across the shock ramp. The amplitude of the upstream whistler waves gradually diminishes upstream from USTR.

(2) Due to nonlinear scattering by the large amplitude waves in USTR, the back-streaming leakage ions cannot move freely to the far upstream side. As a result, the leakage ion density is high and nearly constant in USTR (about 10%–15% N_o), but drops to less than 1% N_o upstream from USTR. The pitch angle distribution shown in Figure 3.16 indicates that the average pitch angle of leakage ions upstream from USTR is much less than the average pitch angle of leakage ions inside USTR. Namely, leakage ions upstream from USTR can move more freely toward the upstream boundary.

(3) Incoming ions in Figure 3.14*a* slow down slightly in USTR. Nonlinear wave-particle interaction between the incoming ions and the large amplitude waves in USTR is responsible for the pre-deceleration of the incoming upstream ions.

(4) The amplification of whistler waves in USTR is not very clear. The possible cause may be the nonlinear feedback effect of wave-particle interactions discussed in (2) and (3).

Figure 3.18 shows the spatial profiles of V_z^a, N_i^a, T_i^a, and B_x^a obtained from the $M_A = 2$ shock simulation at $t\Omega_{ni} = 50$, where V_z^a, N_i^a, and T_i^a, are the normal flow velocity, ion number density, and ion temperature measured from the upstream incoming ions shown in panel (*a*) of Figures 3.14–3.16. As we can see, principal

jumps of V_z^a, N_i^a, and T_i^a profiles are located at the same place — the shock front. Pre-deceleration and slightly pre-heating can be seen in the upstream shock transition region from the V_z^a and T_i^a profiles. The major ion heating takes place at the shock front. Apparently, for incoming upstream ions, pitch-angle scatterings due to sharp changes of nonlinear wave profile across the shock front are stronger than the pitch-angle scatterings by the nonlinear whistler waves in the upstream shock transition region. The result of increasing T_i^a across the shock front is different from the conclusion given in a previous simulation study by *Omidi et al.* [1990]. In their study, ion distribution functions in the velocity space are obtained by averaging the velocity distribution of simulated ion particles over a finite spatial extent. Using an eyeball estimation of thermal speed and mean flow velocity from these distribution function profiles, *Omidi et al.* [1990] argued that there is no real heating nor slowing down in the incoming upstream ions of the low Mach number quasi-parallel shocks at this stage. Note that longer wavelength nonlinear waves appeared in their simulation study in the later time, which can lead to noticeable ion heating, do not appear in our simulations. The change of shock characteristics in their simulation may be explained by the proposed three critical Mach numbers later in Section 3.5. Namely, the simulated shock chosen in their study may happen to be a shock with Mach number approximately equal to the second critical Mach number to be discussed in Section 3.5.

Figure 3.19 shows spatial profiles of B_x at successive times obtained from the $M_A = 2$ shock simulation. Large amplitude whistler waves in the upstream shock transition region are phase standing upstream from the shock front. This result is consistent with the previous simulation results obtained by *Kan and Swift* [1983] and by *Mandt and Kan* [1985], but is different from the conclusion of group standing

waves obtained by *Quest* [1988]. Note that our conclusion of phase-standing nonlinear whistler waves is obtained based on the plot shown in Figure 3.19. We did not compare the wavelength and wave speed of these nonlinear waves with the linear wave dispersion due to the nonlinearity of these phase-standing waves.

Figure 3.20 shows magnetic hodograms obtained from the $M_A = 2$ shock simulation at different times as indicated. The magnetic hodogram at $t\Omega_{ni} = 15$ indicates that the ramp field has an overshoot B_x on the downstream side during the initial development of shock ramp, which is different from the one shown in Figure 3.9 for the $M_A = 1.2$ fast shock. A spiral-type hodogram shown at $t\Omega_{ni} = 25$ indicates that large amplitude whistler waves are emitted to the upstream side. Note that only waves with group speed slightly greater than the upstream flow speed can leave the shock front and propagate further upstream. The magnetic hodogram at $t\Omega_{ni} = 45$ consists of a spiral-type hodogram on the far upstream side and four periods of highly circularly polarized whistler waves with similar amplitude next to the shock ramp. According to Figure 3.17, these four periods of whistler waves are waves in the upstream shock transition region. The wave polarization in the upstream shock transition region is nearly circular at $t\Omega_{ni} = 45$, but becomes noncircular at $t\Omega_{ni} = 65$. The upstream wave becomes chaotic at $t\Omega_{ni} = 85$ due to the reflection of nonlinear waves from upstream boundary as can be seen from Figure 3.19. Since nonlinear wave reflection at upstream boundary occurs after $t\Omega_{ni} = 70$, the noncircular, weak chaotic upstream wave hodogram shown at $t\Omega_{ni} = 65$ should be part of the shock evolution process. The weak chaotic behavior of the nonlinear waves in the upstream shock transition region may be explained by the increasing of shock heated leakage ions in that region. By carefully examining the ion distributions in the ϕ-z space as shown in Figure 3.16, we can see that pitch angles of shock heated diffuse ions are mostly around 90°. As

a result, the nicely coherent wavy structures of leakage ion distribution in the v_x-z space shown in Figure 3.15*c* are hardly seen in Figure 3.15*b* for the shock heated leakage ions. It is possible that nonlinear whistler waves in the upstream shock transition region will lose their circularly polarized characteristic through the increasing interactions with ions of nearly 90° pitch angle. Further theoretical study on this issue is needed to show whether the proposed idea is adequate or not.

3.3.3 $M_A = 4$ Shock

Simulation results shown in this section are obtained from the $M_A = 4$ shock simulation with initial ramp thickness $D_W = 3\ c/\omega_{pi}$.

Figures 3.21 and 3.22 plot spatial profiles of N_i, T_i, V_z, B_x, B_y, and B obtained from $M_A = 4$ shock simulation at $t\Omega_{ni} = 54$ and 83, respectively. The principal jump of V_z profile, which is well-defined at all times, will be denoted as the shock front for the $M_A = 4$ shock simulation. The shock ramp of total magnetic field B shows different shape at different time. A sharp jump on B can be seen across the shock front at $t\Omega_{ni} = 54$. A turbulent total magnetic field profile can be seen across the shock ramp at $t\Omega_{ni} = 83$. The changes of the shape of total magnetic field profile across the shock ramp were first reported by *Burgess* [1989], which initiate the study of shock front reformation process in high Mach number quasi-parallel shocks in current researches. Ion heating and flow slowing down can be found at shock front as well as in the extended shock transition region. The shock transition region of the $M_A = 4$ shock can be classified into three parts, based on the nonlinear wave characteristics, as denoted by the three horizontal bars in Figures 3.21 and 3.22. They are, from left to right, the upstream shock transition region, the downstream shock transition region, and the secondary downstream shock transition region. Short-wavelength nonlinear

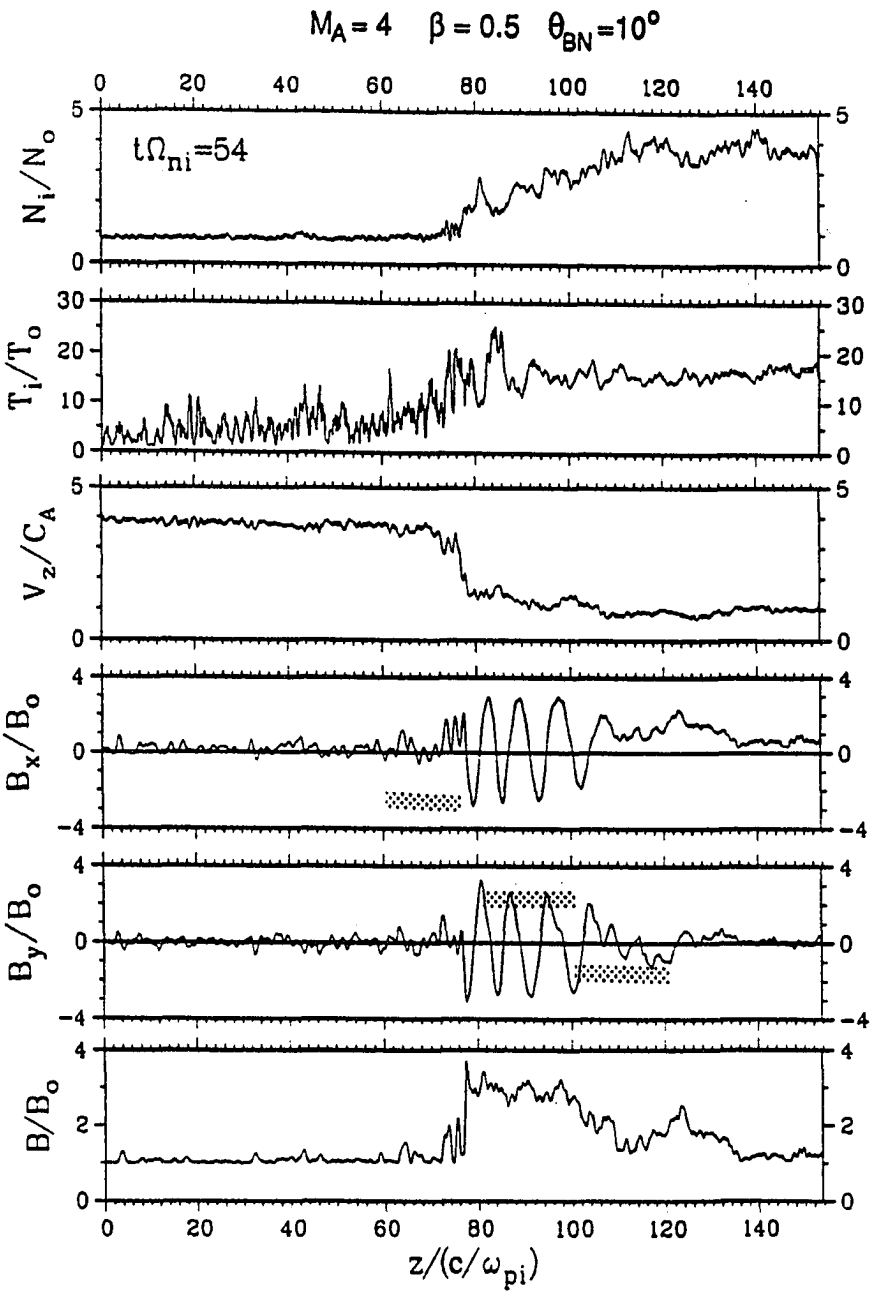

Figure 3.21 Spatial profiles of N_i, T_i, V_z, B_x, B_y, and B obtained from the $M_A = 4$ shock simulation at $t\Omega_{ni} = 54$. The principal jump of V_z profile will be denoted as the shock front for the $M_A = 4$ shock. Based on the characteristics of nonlinear wave structures, the shock transition region of the $M_A = 4$ shock is classified into three parts as denoted by the three horizontal bars. They are, from left to right, the upstream shock transition region, the downstream shock transition region, and the secondary downstream shock transition region.

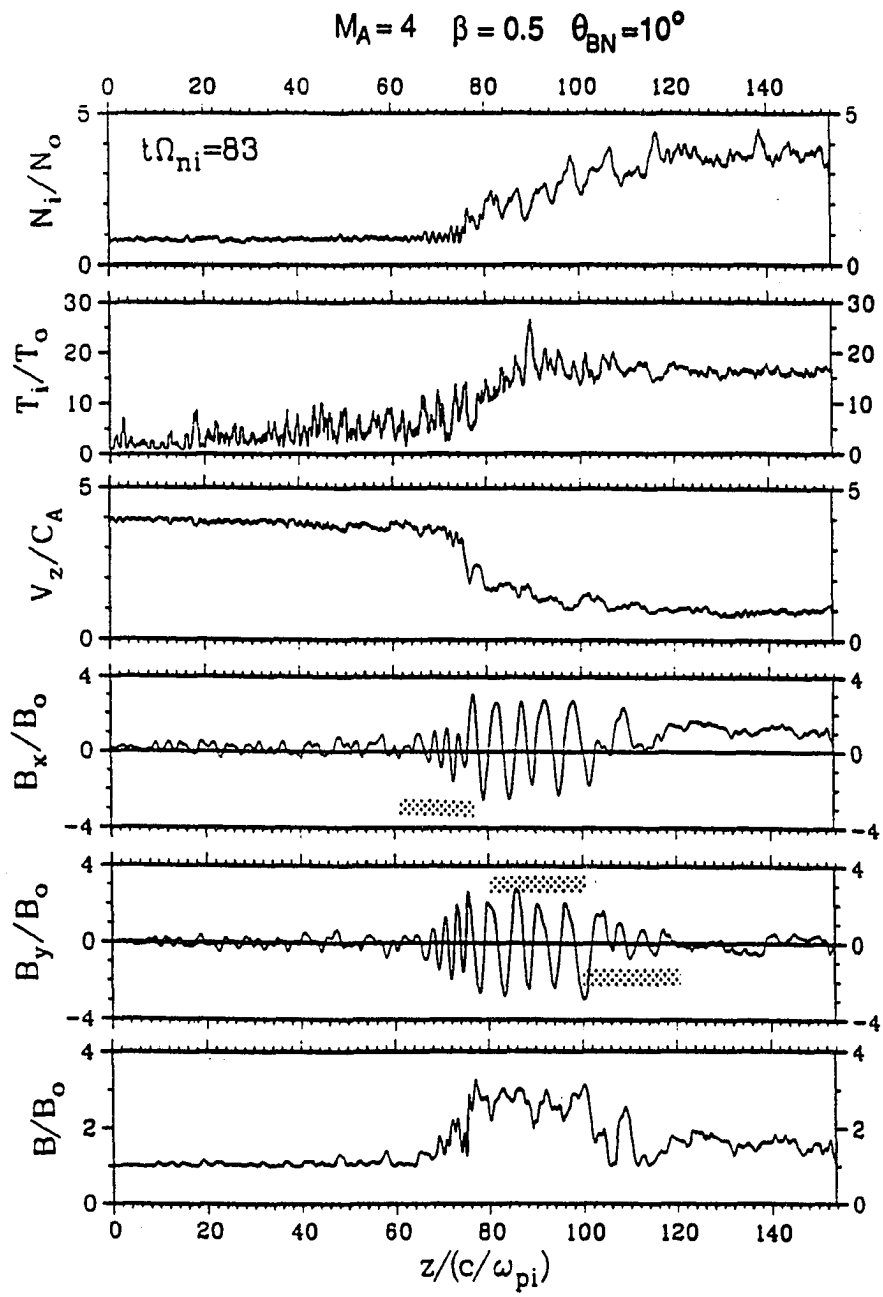

Figure 3.22 Spatial profiles of N_i, T_i, V_z, B_x, B_y, and B obtained from the $M_A = 4$ shock simulation at $t\Omega_{ni} = 83$, in the same format as shown in Figure 3.21. The B profile shows a turbulent ramp structure due to the presence of large amplitude whistler waves in the upstream shock transition region. The ramp thickness of the B profile is much thicker than it shown in Figure 3.21. However, the ramp thickness of the V_z profile is about the same in the two plots shown in Figures 3.21 and 3.22.

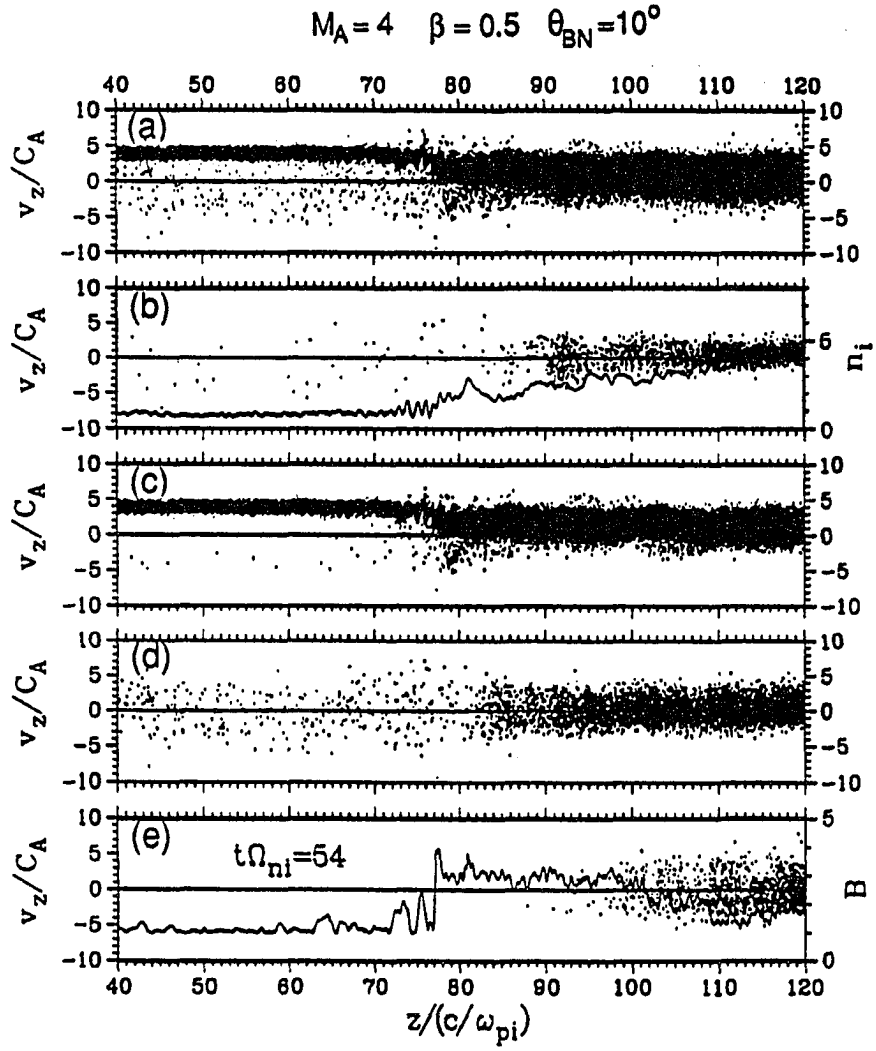

Figure 3.23 Scatter plots of ion distribution in the v_z-z space obtained from the $M_A = 4$ shock simulation at $t\Omega_{ni} = 54$. Ions shown in each panel are (*a*) the total ions, (*b*) the initial loaded upstream ions, (*c*) the incoming ions from upstream boundary after $t = 0$, (*d*) the initial loaded downstream ions, and (*e*) the incoming ions from downstream boundary after $t = 0$. The curves superimposed on panels (*b*) and (*e*) are the spatial profiles of ion density and total magnetic field. An ion reflection beam can be seen near the shock front at $z \approx 80\ c/\omega_{pi}$.

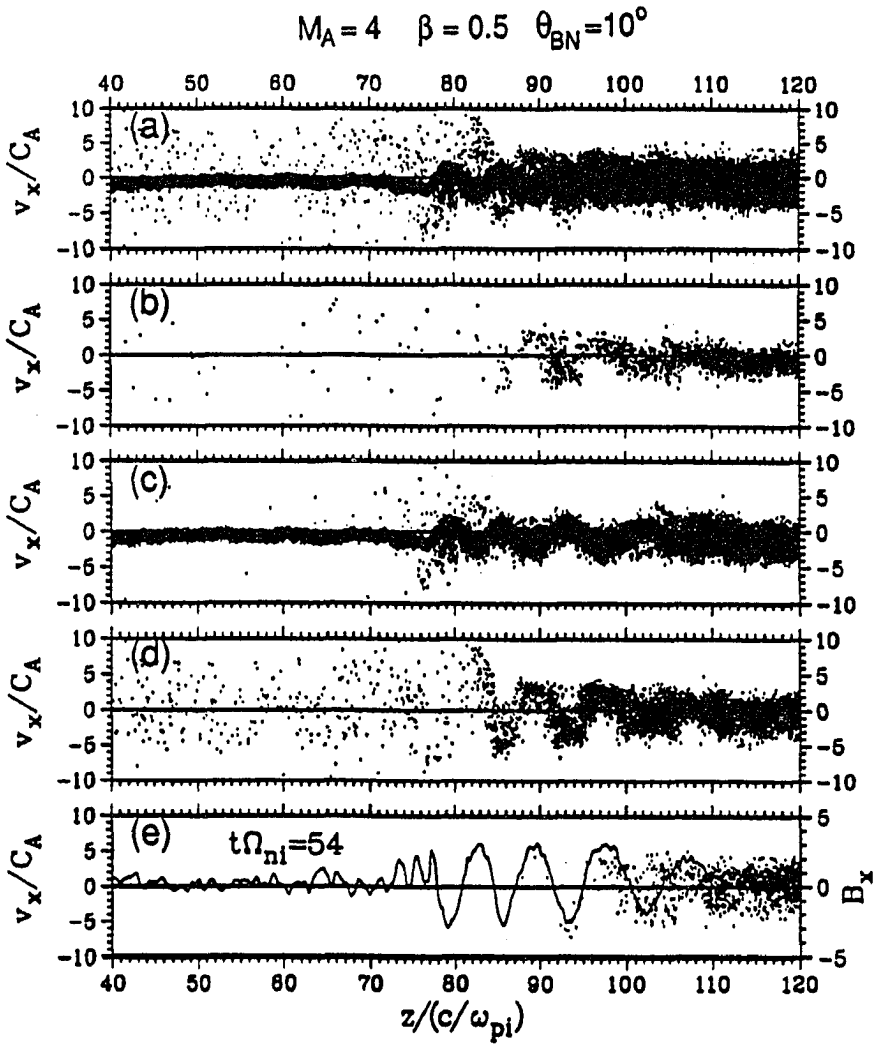

Figure 3.24 Scatter plots of ion distribution in the v_x-z space obtained from the $M_A = 4$ shock simulation at $t\Omega_{ni} = 54$. Ions shown in each panel are the same as those shown in Figure 3.23. The curve superimposed on panel (*e*) is the spatial profile of x-component of magnetic field. See text for further discussion in detail.

whistler waves can be found in the upstream shock transition region. The amplitude of these nonlinear whistler waves varies with time. Large amplitude whistler waves in the upstream shock transition region can lead to a turbulent shock ramp on the total magnetic field profile as shown in Figure 3.22. The downstream shock transition region consists of large-amplitude, long-wavelength hydromagnetic waves, which are

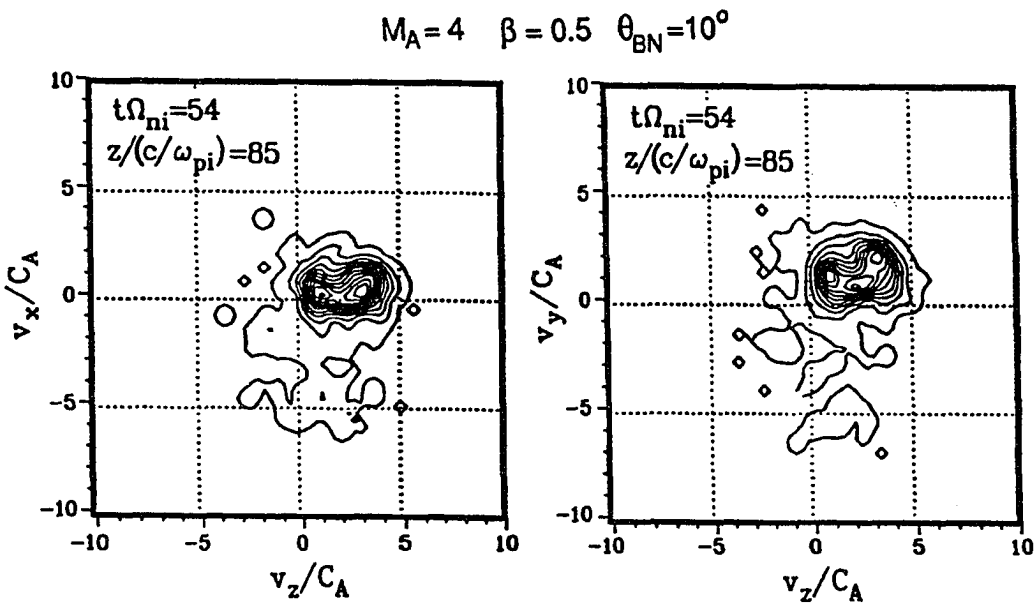

Figure 3.25 Contour plots of ion velocity distribution downstream from the shock front in the v_x-v_z space and v_y-v_z space obtained from the $M_A = 4$ shock simulation at $z = 85\ c/\omega_{pi}$ and $t\Omega_{ni} = 54$. Two-beam structure can be seen in the plot in the v_x-v_z space. Three-beam structure can be seen in the plot in the v_y-v_z space. This simulation result is similar to the observed multiple-ion-bunches distribution as shown in Figure 3.3.

the body of the overshoot magnetic field in the high Mach number quasi-parallel shocks. Small but finite amplitude, long-wavelength hydromagnetic waves can be seen in the secondary downstream shock transition region. Owing to the decreasing on total magnetic field and continuously increasing on ion density, the nonlinear waves in the secondary downstream shock transition region may be identified with nonlinear slow-mode waves. It may be noted that the spiky structures shown upstream from the shock front in the T_i profile in Figures 3.21 and 3.22 are due to the presence of suprathermal backstreaming ions, which will be discussed in Figures 3.23 and 3.24.

Figures 3.23 and 3.24 show scatter plots of ion distribution in the v_z-z space and v_x-z space from $z = 40$ to $120\ c/\omega_{pi}$ at $t\Omega_{ni} = 54$ obtained from the $M_A = 4$ shock

simulation, where ions shown in each panel are (*a*) the total ions, (*b*) the initially loaded upstream ions, (*c*) the incoming ions from upstream boundary after $t = 0$, (*d*) the initially loaded downstream ions, and (*e*) the incoming ions from downstream boundary after $t = 0$. The curves superimposed on panels (*b*) and (*e*) of Figure 3.23 are the ion density and total magnetic field profiles. The curves superimposed on panel (*e*) of Figure 3.24 is the x-component of magnetic field profile. A weak ion reflection beam can be seen slightly downstream from the shock front at $z \approx 80\, c/\omega_{pi}$ in Figure 3.23. The suprathermal ions on the upstream side are mostly from the downstream hot ions as shown in panel (*d*) of Figures 3.23 and 3.24. The scatter plot shown in Figure 3.24*d* indicates that the temperature of the upstream suprathermal leakage ions is greater than the temperature of downstream ions. Apparently, the leakage ions gain tangential component streaming kinetic energy as they backstream through the downstream shock transition region and then convert the streaming kinetic energy into thermal energy when they leak across the shock front. As a result, hot downstream ions with temperatures equal to $\sim 10\, T_o$ are able to produce suprathermal diffuse ions upstream from the shock front with temperatures equal to $\sim 100\, T_o$. Since the tangential electric field is nonzero in the shock transition regions, the downstream leakage ions may gain the streaming kinetic energy from the tangential electric field by drifting along the x-y plane. Note that the average normal velocity of ions in the downstream shock transition region is very small (much smaller than the thermal speed along the shock normal direction in that region). It is difficult to determine the flow direction from the scatter plot in the v_z-z space shown in Figure 3.23. The flow direction can be easily determined from the phase relationship between tangential magnetic field and the average tangential velocity of each group of ions. The B_x profile and the average v_x in the downstream shock transition region is out-of-phase

for ions shown in Figure 3.24*c* but in-phase for ions shown in Figures 3.24*b*, 3.24*d*, and 3.24*e*. For normal magnetic field $B_z < 0$, the above relationships indicate that the average normal flow direction of the ions in the downstream shock transition region directs to the downstream boundary in Figure 3.24*c*, but directs to the shock front in Figures 3.24*b*, 3.24*d*, and 3.24*e*. Thus, we may conclude that shock heated ions in Figure 3.24*b* can also contribute to the diffuse backstreaming ions on the upstream side. Note that a similar method, based on the phase-relationship between tangential field and velocity, has been introduced by *Neugebauer and Buti* [1990] to determine the normal flow direction across the observed rotational discontinuities for the first time. We suggest that the Neugebauer-Buti method should be commonly used in all the low Mach number nonlinear wave observations in the future. The scatter plot in the ϕ-z space as introduced in Sections 3.3.1 and 3.3.2 can provide similar information as the method we used above. The disadvantages of these two methods are that (1) the pitch-angle method can only be used in the de Hoffman-Teller frame and (2) the tangential phase-relationship method cannot be applied to a region with spatial extent much less than one half of a wavelength.

The simulation results are obtained earlier with a four-group labeling diagnostic which is not good enough to trace the ion reflection processes at the shock front. It is not clear therefore from this simulation study whether the reflected ions can directly contribute to the upstream backstreaming ions or not. The improved multi-group diagnostic discussed in Section 3.2.2 will be used later in the $M_A = 6$ shock study, which will enable us to see the dynamics of ion reflection in greater detail.

Figure 3.25 shows contour plots of ion velocity distribution in the v_x-v_z space and v_y-v_z space, at $z = 85\ c/\omega_{pi}$ and $t\Omega_{ni} = 54$ obtained from the $M_A = 4$ shock simulation. Two-beam structure can be seen in the contour plot in the v_x-v_z space.

Three-beam structure can be seen in the contour plot in the v_y-v_z space. The formation of the multiple ion beam structures can be explained as a consequence of reflected ion beam reentering the shock ramp before completely mixing with the directly transmitted ion beam. The multiple ion beam structures have been observed in the quasi-parallel bow shock crossing [*Gosling et al.*, 1989*b*] as shown in Figure 3.3. The multiple ion beam structure is often associated with high ion temperature and low ion density as one can see from Figure 3.21 at $z \approx 85\ c/\omega_{pi}$. The opposite variation in the ion temperature profile and ion density profile has been observed by *Thomsen et al.* [1990] at several quasi-parallel bow shock crossings.

Figure 3.26 shows scatter plots of ion distribution in the v_z-z space at different times obtained in the $M_A = 4$ shock simulation, where only ions entering from upstream boundary after $t = 0$ are plotted. Strong ion reflection beams can be seen at the shock front at $t\Omega_{ni} = 68$ and 83, which represent the beginning of two strong ion reflection events. A weak ion reflection beam can be seen downstream from the shock front at $t\Omega_{ni} = 82$, which is similar to the one shown in Figure 3.23. The normal velocity of the weak reflection beam is usually more negative than the normal velocity of the strong reflection beam.

Figure 3.27 shows spatial profiles of B_x at different times corresponding to each scatter plot shown in Figure 3.26. Large-amplitude, short-wavelength whistler waves in the upstream shock transition region can be seen at $t\Omega_{ni} = 66$–68 and 82–83. The amplitude of these whistler waves diminishes after the strong ion reflection events. A long-wavelength nonlinear wave pulse is formed at the shock front by the end of the strong ion reflection events at $t\Omega_{ni} = 75$ and 86.

Figure 3.28 shows magnetic hodograms obtained in the $M_A = 4$ shock simulation before, during, and after the two strong ion reflection events discussed in Figures

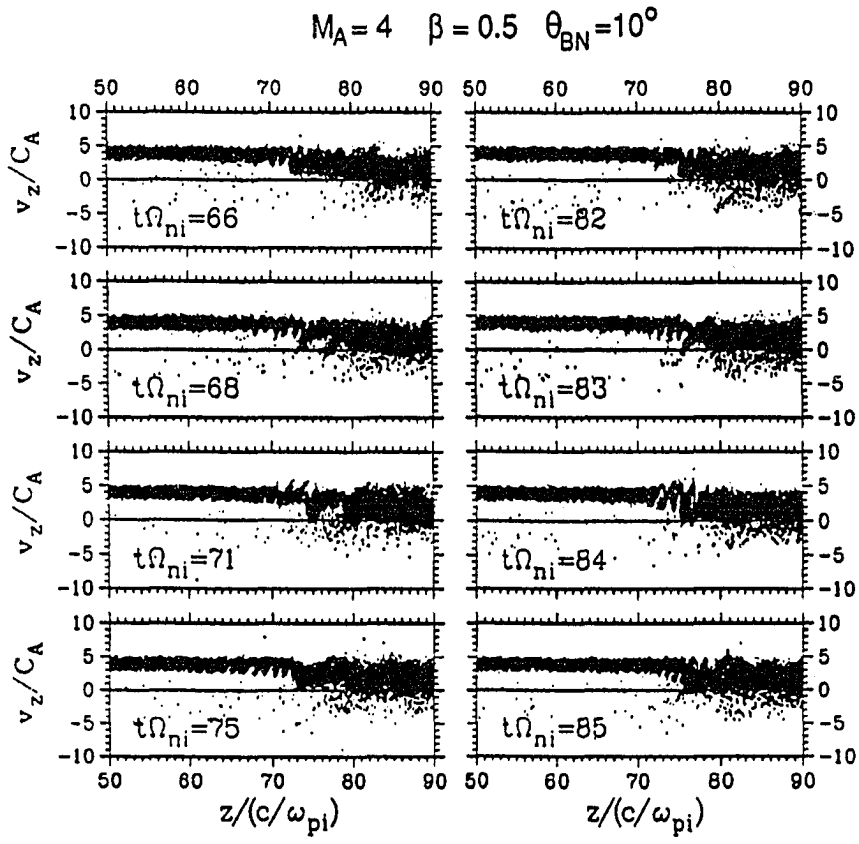

Figure 3.26 Scatter plots of incoming ions, entering from upstream boundary after $t = 0$, in the v_z-z phase space at different times during the period of $t\Omega_{ni} = 66$–85 obtained in the $M_A = 4$ shock simulation. Strong ion reflections can be seen at $t\Omega_{ni} = 68$ and 83. A weak ion reflection can be seen downstream from the shock front at $t\Omega_{ni} = 82$.

3.26 and 3.27. The hodograms are plotted from $z = 60$–$80\ c/\omega_{pi}$ which include the upstream, shock transition region and the shock front. The thick solid curves are approximately the magnetic hodogram across the shock ramp. The thick solid curves in panels (*a*), (*b*), and (*c*) are plotted from $z = 72$–$75\ c/\omega_{pi}$. The thick solid curves in panels (*d*), (*e*), and (*f*) are plotted from $z = 73$–$77\ c/\omega_{pi}$. The thick dashed curve in panel (*b*) is approximately the region of the second ion reflection beam from the upstream shown at $t\Omega_{ni} = 68$ in Figure 3.26. Spiral-type whistler-mode

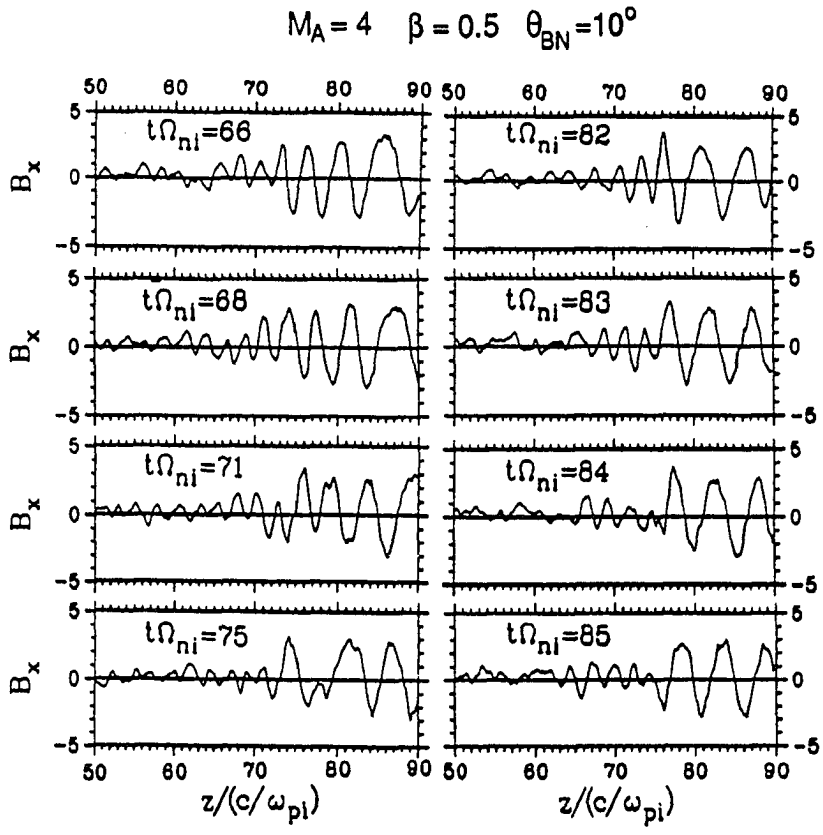

Figure 3.27 Spatial profiles of B_x obtained from the $M_A = 4$ shock simulation at different times corresponding to each scatter plot shown in Figure 3.26. Large-amplitude, short-wavelength whistler waves in the upstream shock transition region can be seen at $t\Omega_{ni} = 66$–68 and 82–83. The amplitude of these whistler waves diminishes after the strong ion reflection events started at $t\Omega_{ni} = 68$ and 83. A long-wavelength nonlinear wave pulse is formed at the shock front at the end of the strong ion reflection events at $t\Omega_{ni} = 75$ and 86.

magnetic hodograms can be found upstream from shock front in Figures 3.28*a* and 3.28*c* before the strong ion reflections at $t\Omega_{ni} = 68$ and 83. Highly irregular, chaotic magnetic hodograms appear in the shock ramp in Figures 3.28*d* and 3.28*f* after the strong ion reflections.

Figure 3.29 shows magnetic hodogram from $z = 80$–$100\ c/\omega_{pi}$ at $t\Omega_{ni} = 66$ obtained in the $M_A = 4$ shock simulation. As we can see, the hydromagnetic waves in

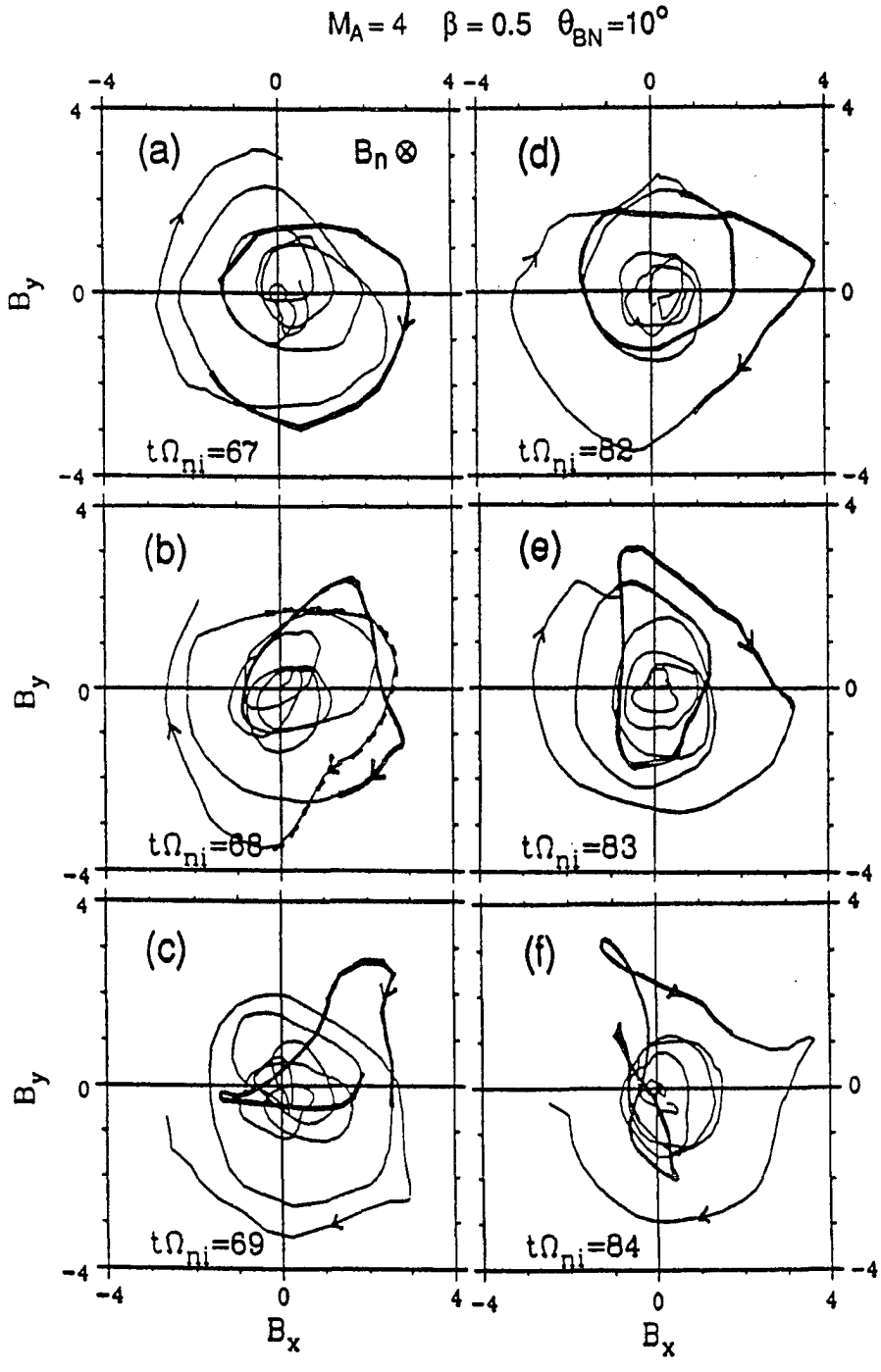

Figure 3.28 Magnetic hodograms obtained from the $M_A = 4$ shock simulation before, during, and after the two strong ion reflection events discussed in Figures 3.26 and 3.27. Arrows are going in downstream direction. See text for discussion in detail.

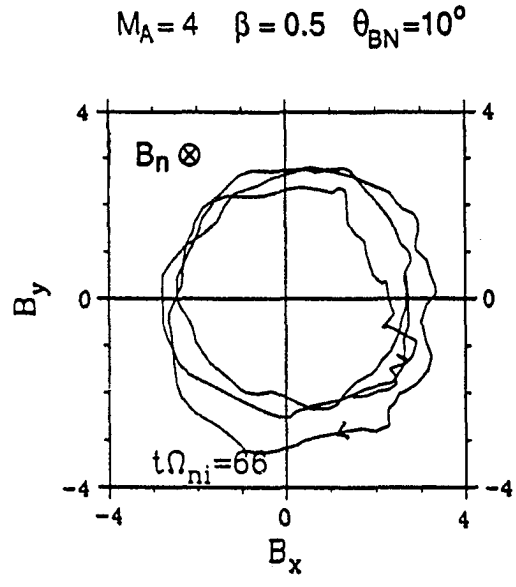

Figure 3.29 Magnetic hodogram in the downstream shock transition region obtained from the $M_A = 4$ shock simulation at $t\Omega_{ni} = 66$, where the hodogram is plotted from $z = 80$–$100\ c/\omega_{pi}$. The arrow is going in downstream direction.

the downstream shock transition region are right-handed and nearly circularly polarized nonlinear waves.

Figure 3.30 shows spatial profiles of (*a*) B_x and (*b*) B at successive times during the period of $t\Omega_{ni} = 54$–85 in the $M_A = 4$ shock simulation. As we can see, large-amplitude waves in the downstream shock transition region are generated at the shock front and then been swept downstream. Short-wavelength, large-amplitude whistler waves appear intermittently in the upstream shock transition region as one can see during the period of $t\Omega_{ni} = 65$–71 and the period of $t\Omega_{ni} = 79$–84 in Figure 3.30*a*. According to the results shown in Figures 3.26–3.27, the disappearance of large-amplitude whistler waves in the upstream shock transition region is strongly associated with the strong ion reflection event at the shock front. The disappearance of these large-amplitude whistler waves and the ending of strong ion reflection events are also closely

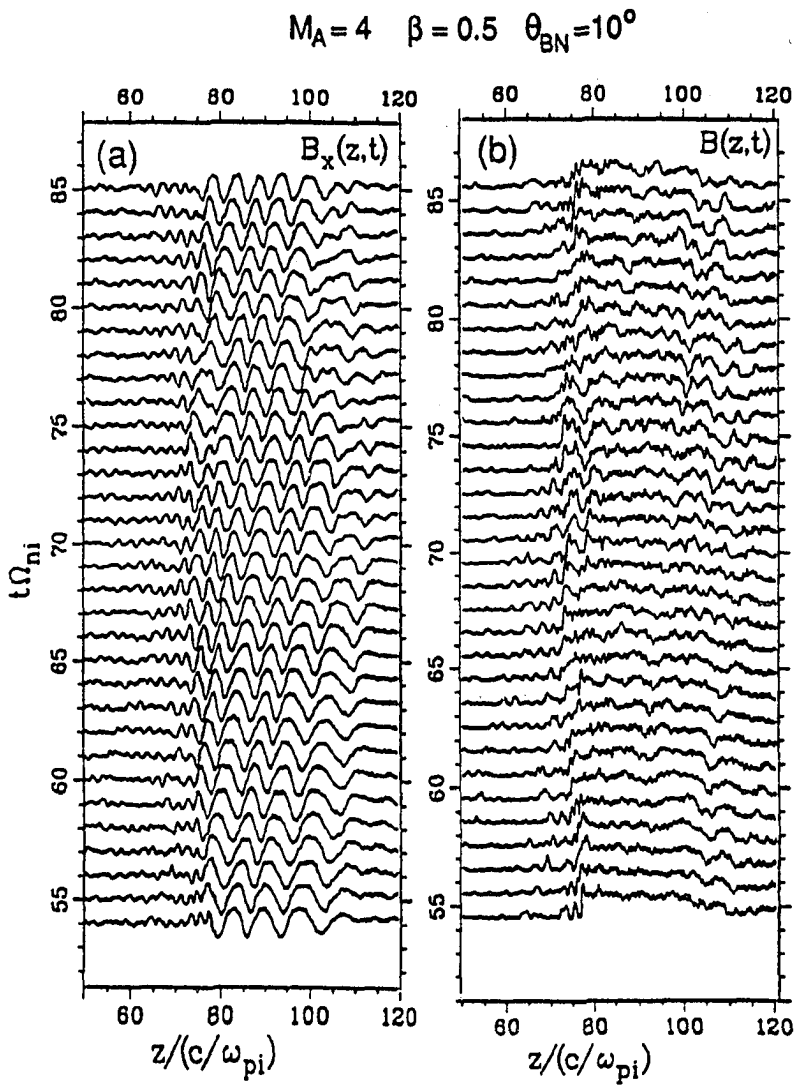

Figure 3.30 Spatial profiles of (*a*) B_x and (*b*) B at successive times obtained from the $M_A = 4$ shock simulation. Large amplitude waves in the downstream shock-transition region are generated at the shock front and then propagate toward the downstream side. Short-wavelength, large-amplitude whistler waves appear intermittently upstream of the shock front during the interval of $t\Omega_{ni} = 65$–71 and the interval of $t\Omega_{ni} = 79$–84 in panel (*a*).

associated with the formation of a new period of nonlinear waves in the downstream shock transition region. The alternate appearance of these large-amplitude whistler waves is one of the many cyclic behaviors found in the shock-transition region of the high Mach number quasi-parallel shocks. The steepness of the principal jump of total magnetic field profiles varies with time, which has been denoted as the reformation of shock front by *Burgess* [1989]. To fully understand the reformation process, we have to study all the cyclic variations occurring near the shock front. The cyclic variations include (1) generation of downstream waves at the shock front [*Winske et al*, 1990], (2) the appearance and disappearance of large-amplitude whistler waves in the upstream shock transition region [*Lyu and Kan*, 1990], (3) strong ion reflection events at the shock front [*Lyu and Kan*, 1990], and (4) variations of density profile and total magnetic field profile near the shock ramp [*Burgess*, 1989; *Lyu and Kan*, 1990].

3.3.4 $M_A = 6$ Shock

Simulation results shown in this section are obtained from the $M_A = 6$ shock simulation with initial ramp thickness $D_W = 30\ c/\omega_{pi}$.

Figures 3.31 and 3.32 plot spatial profiles of N_i, T_i, V_z, B_x, B_y, and B obtained from $M_A = 6$ shock simulation at $t\Omega_{ni} = 39$ and 44, respectively. We define the shock front based on the principal jump of V_z for the $M_A = 6$ shock simulation. The principal jump of V_z is gentle at $t\Omega_{ni} = 39$, but steep at $t\Omega_{ni} = 44$. The variation of shock-front thickness is the signature of shock front reformation process in the $M_A = 6$ shock simulation. A well-defined N_i jump can be found at the shock front in the $M_A = 6$ shock simulation. Apparently, the compression of N_i at the shock front in the $M_A = 6$ shock simulation is stronger than it in the $M_A = 4$ shock simulation

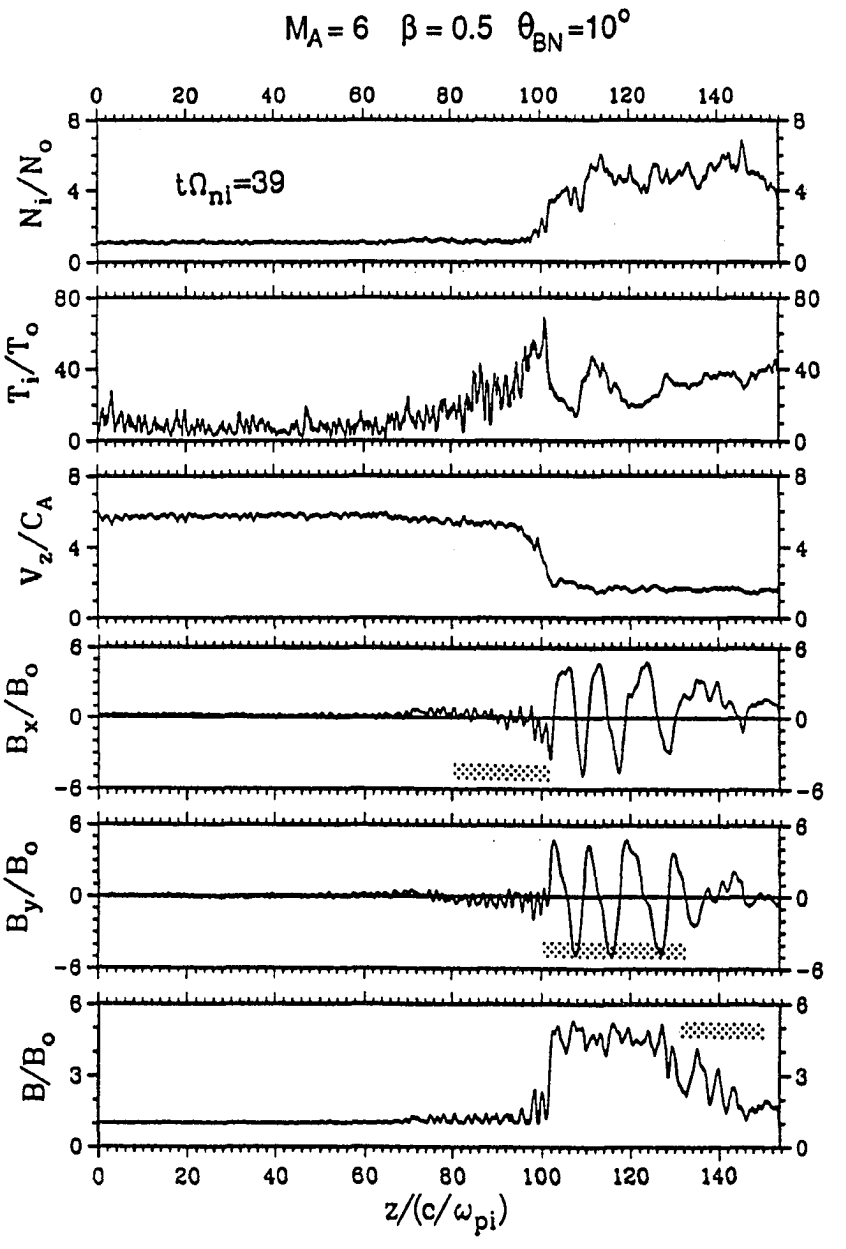

Figure 3.31 Spatial profiles of N_i, T_i, V_z, B_x, B_y, and B obtained from $M_A = 6$ shock simulation at $t\Omega_{ni} = 39$. The shock front will be defined based on the principal jump of V_z for the $M_A = 6$ shock simulation, which shows a gentle slope at this time. The shock transition region of the $M_A = 6$ shock is classified into three parts as denoted by the three horizontal bars. They are, from left to right, the upstream shock transition region, the downstream shock transition region, and the secondary downstream shock transition region. See text for further discussion in detail.

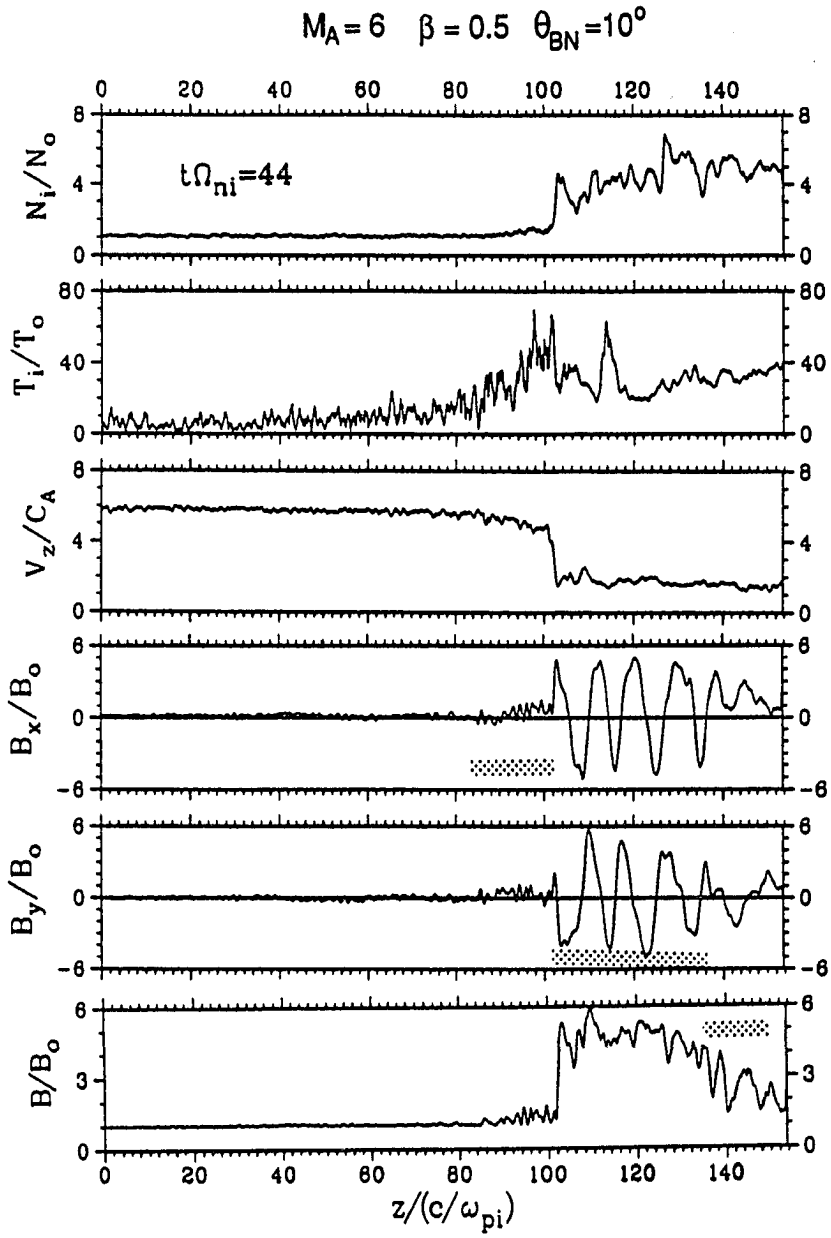

Figure 3.32 Spatial profiles of N_i, T_i, V_z, B_x, B_y, and B obtained from $M_A = 6$ shock simulation at $t\Omega_{ni} = 44$, in the same format as shown in Figure 3.31. The principal jump of V_z is steep at this time in comparison with the principal jump of V_z at $t\Omega_{ni} = 39$ as shown in Figure 3.31.

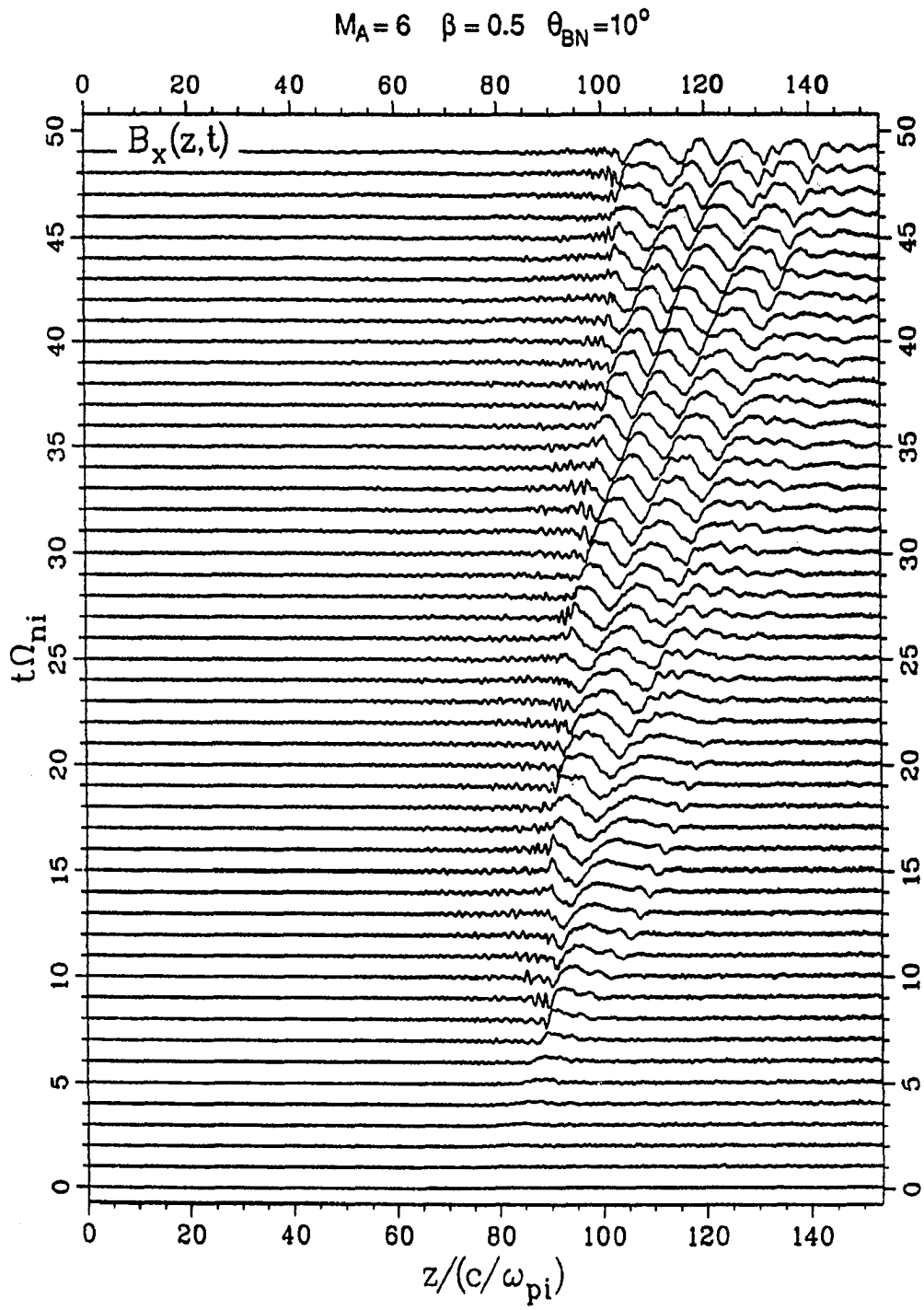

Figure 3.33 Spatial profiles of B_x plotted at successive times obtained in the $M_A = 6$ shock simulation. See text for discussion in detail.

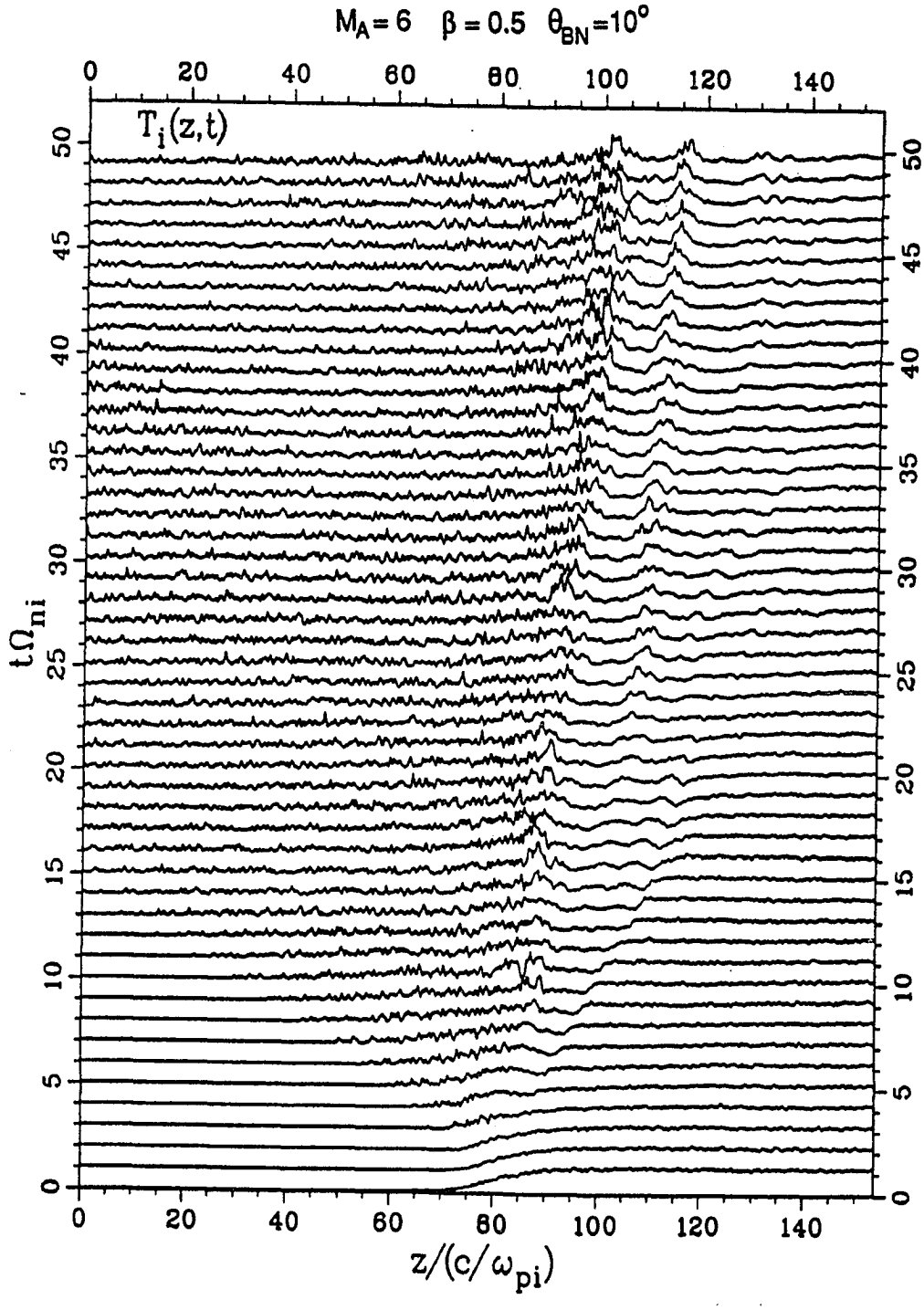

Figure 3.34 Spatial profiles of T_i plotted at successive times obtained in the $M_A = 6$ shock simulation. See text for discussion in detail.

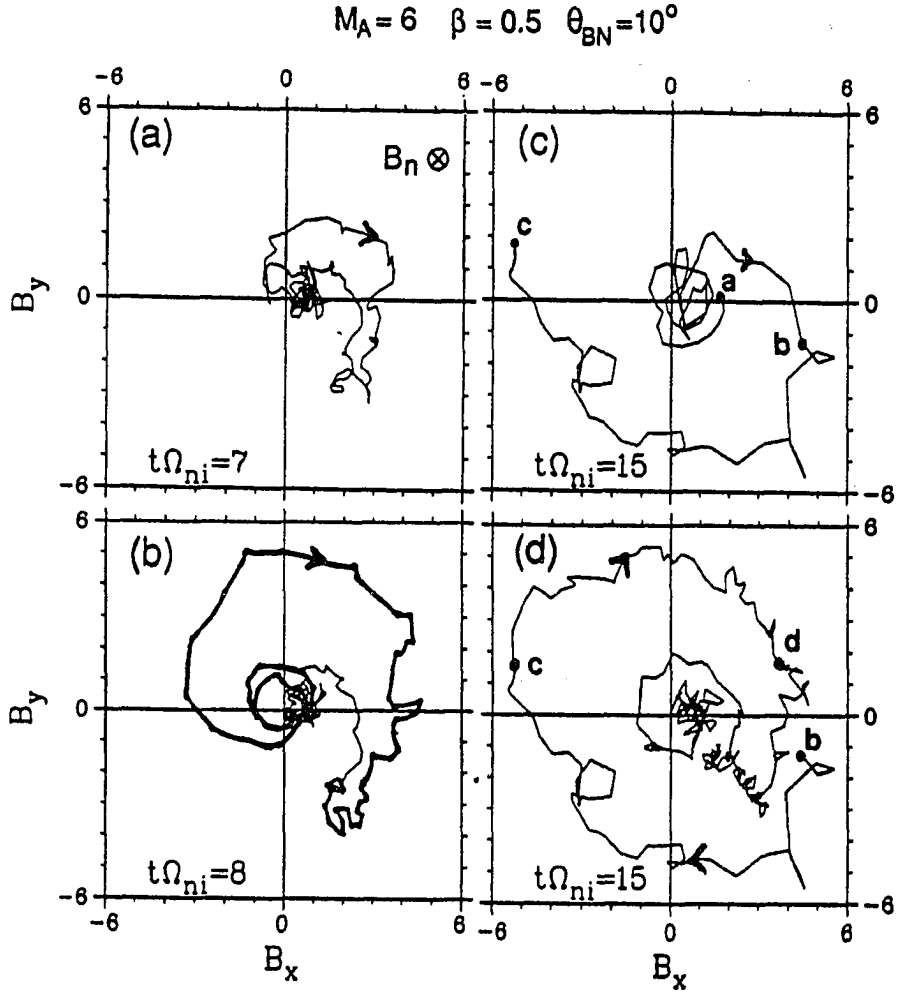

Figure 3.35 Magnetic hodograms in the shock transition regions during the formation of shock ramp at $t\Omega_{ni} = 7$, 8, and 15, obtained from the $M_A = 6$ shock simulation. Arrows are going in downstream direction. Magnetic hodograms shown in panels (*a*) and (*b*) are plotted from $z = 85$–$105\ c/\omega_{pi}$. The thick curve in (*b*) is plotted from $z = 85$–$95\ c/\omega_{pi}$. Magnetic hodogram shown in panel (*c*) is plotted from $z = 85$–$95\ c/\omega_{pi}$. Magnetic hodogram shown in panel (*d*) is plotted from $z = 90$–$120\ c/\omega_{pi}$. Points *a*, *b*, *c*, and *d* in panels (*c*) and (*d*) are corresponding to $z = 85$, 90, 95, and $100\ c/\omega_{pi}$, respectively. See text for discussion in detail.

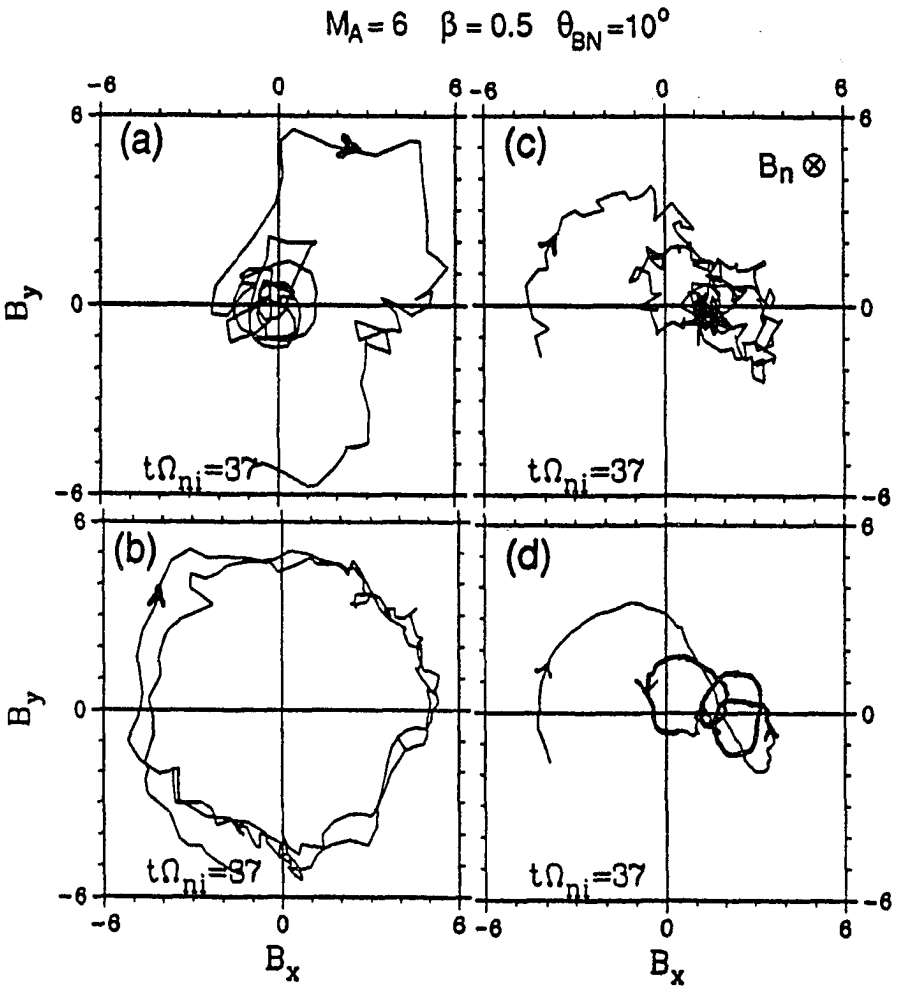

Figure 3.36 Magnetic hodograms in a fully developed shock transition region at $t\Omega_{ni} = 37$ obtained in the $M_A = 6$ shock simulation. Arrows are going in downstream direction. Panel (*a*) shows magnetic hodogram in the upstream shock transition region and across the shock ramp at $z = 90$–$105\ c/\omega_{pi}$. Panel (*b*) shows the circularly polarized magnetic hodogram in the downstream shock transition region at $z = 105$–$125\ c/\omega_{pi}$. Panels (*c*) and (*d*) show magnetic hodogram in the secondary downstream shock transition region at $z = 125$–$150\ c/\omega_{pi}$, where the hodogram curve in (*d*) is plotted over smoothed data to reveal the left-hand polarized nonlinear slow-mode wave as highlighted by the thick curve.

shown in Section 3.3.3. The shock transition region of the $M_A = 6$ shock is classified into three parts as denoted by the three horizontal bars. They are, from left to right, the upstream shock transition region, the downstream shock transition region, and the secondary downstream shock transition region. The general characteristics of nonlinear waves in the three shock transition regions are similar to those shown in the $M_A = 4$ shock, except that the amplitude and the wavelength of the upstream whistler waves are relatively small in comparison with the nonlinear hydromagnetic waves in the downstream shock transition region in the $M_A = 6$ shock simulation. A secondary peak on the ion temperature profile can be seen in the downstream shock transition region. The formation on the secondary peak on the T_i profile is not well-understood, but it is a common characteristic for all high Mach number shocks with $M_A \geq 6$. Additional peaks on the T_i profile in the downstream shock transition region may be formed with increasing Mach number. The spiky structures shown upstream from the shock front in the T_i profile are due to the presence of suprathermal backstreaming ions. Similar results have been obtained in the $M_A = 4$ shock simulation. The formation of these suprathermal backstreaming ions in the $M_A = 6$ shock will be discussed later in Figures 3.46–3.49.

Figure 3.33 shows spatial profiles of B_x at successive times obtained in the $M_A = 6$ shock simulation. Large-amplitude hydromagnetic waves are generated at the shock front and then been swept downstream to form the downstream shock-transition region. Short-wavelength nonlinear waves appear intermittently upstream from the shock front. The shock front gradually moves downstream especially during the period when the ramp field B_x is negative. Both ion leakages and ion reflections are responsible for the decreasing of shock speed. It will be shown later that a nearly field-aligned ion reflection can be found when the ramp field B_x is negative, which leads to over

dissipation at the shock front. By nonlinear steepening, the shock front will reform at slightly downstream from it previous position. The location of shock front is relatively stationary in the simulation frame when the ramp field B_x is positive. Although the average Mach number is apparently slightly less than 6, we shall still call it "the $M_A = 6$ shock simulation" for convenience.

Figure 3.34 shows spatial profiles of T_i at successive times obtained in the $M_A = 6$ shock simulation. As discussed in Figures 3.31 and 3.32, the spiky structures appeared upstream from the shock front in the T_i profiles are due to the presence of suprathermal backstreaming ions in that region. A secondary peak on the ion temperature profiles can be seen in the downstream shock transition region, which is phase standing in the average shock frame. Apparently, a slow-mode nonlinear waves is generated, when the downstream large-amplitude hydromagnetic waves interact with the phase-standing, high-temperature structure in the downstream shock transition region. Since the phase speed of this slow-mode nonlinear waves is less than the large-amplitude Alfvénic hydromagnetic waves in the downstream shock transition region, the slow-mode nonlinear waves were blown back to the far downstream side and form the secondary downstream shock transition region as shown in Figures 3.31 and 3.32.

Figure 3.35 shows magnetic hodograms in the shock transition regions during the formation of shock ramp at $t\Omega_{ni} = 7$, 8, and 15, obtained from the $M_A = 6$ shock simulation. Magnetic hodograms shown at $t\Omega_{ni} = 7$ and 8 ($z = 85$–$105\ c/\omega_{pi}$) consist of (1) a right-hand polarized nonlinear wave in the upstream shock transition region and across the shock ramp; and (2) a left-hand polarized nonlinear wave downstream from the shock front. Nonlinear whistler wave with a spiral-type magnetic hodogram is formed upstream from the shock front at $t\Omega_{ni} = 8$ as denoted by the thick curve (plotted from $z = 85$–$95\ c/\omega_{pi}$) shown in panel (*b*). Magnetic hodogram shown at

$t\Omega_{ni} = 15$ consists of (1) a right-hand polarized nonlinear wave in the upstream shock transition region and across the shock ramp as denoted by curve *a-b*; (2) a circularly right-hand polarized nonlinear Alfvén wave in the downstream shock transition region as denoted by curve *b-c-d*; and (3) nonlinear slow-mode waves in the secondary downstream shock transition region as denoted by a curve downstream from point *d*, where points *a*, *b*, *c*, and *d* in panels (*c*) and (*d*) are corresponding to $z = 85$, 90, 95, and 100 c/ω_{pi}, respectively. The nonlinear slow-mode waves in the secondary downstream shock transition region at $t\Omega_{ni} = 15$ consist of two parts: a linearly polarized nonlinear slow mode wave followed by a left-hand-polarized nonlinear slow-mode wavetrain structure.

Figure 3.36 shows magnetic hodogram in a fully developed shock transition region at $t\Omega_{ni} = 37$ obtained in the $M_A = 6$ shock simulation. Panel (*a*) shows the magnetic hodogram in the upstream shock transition region and across the shock ramp at $z =$ 90–105 c/ω_{pi}. Panel (*b*) shows the circularly polarized magnetic hodogram in the downstream shock transition region at $z =$ 105–125 c/ω_{pi}. Panels (*c*) and (*d*) show the magnetic hodogram in the secondary downstream shock transition region at $z =$ 125–150 c/ω_{pi}, where the hodogram curve in (*d*) is plotted over smoothed data to reveal the left-hand polarized nonlinear slow-mode wave as highlighted by the thick curve.

Figure 3.37 shows scatter plots of ion distributions in the v_z-z space and the spatial profiles of magnetic field B_x, B_y, and B, obtained from the $M_A = 6$ shock simulation at $t\Omega_{ni} =$ 20–31. The number encircled, shown in each scatter plot, is the group number of the ions shown in that panel. The classification of ion groups used in this section is given in Table 3.1. Several ion reflection events occur during the period of $t\Omega_{ni} =$ 20–31. The reflection events are strongly dependent on the orientation of the ramp

Table 3.1 Ion grouping diagnostic

Group Number	Descriptions
1	Initially loaded upstream ions
2	Incoming ions entering simulation box from the upstream boundary at $t\Omega_{ni} = 0 \sim 2$
3	Incoming ions entering simulation box from the upstream boundary at $t\Omega_{ni} = 2 \sim 4$
4	Incoming ions entering simulation box from the upstream boundary at $t\Omega_{ni} = 4 \sim 6$
•	•
•	•
•	•
•	•
n	Incoming ions entering simulation box from the upstream boundary at $t\Omega_{ni} = 2\cdot(n-2) \sim 2\cdot(n-1)$

field. The right-hand polarized nonlinear waves in the downstream shock transition region are generated at the shock ramp and then blown back to the downstream. Thus, the temporal variation of the ramp field must be left-hand polarized with respective to the normal magnetic field. For convenience, we shall use phase angle α in the following discussion, to denote the rotation angle of the left-hand polarized tangential ramp field with respect to the upstream tangential magnetic field. For instance, the upstream tangential magnetic field used in this study is in the positive-x direction and the normal magnetic field $B_z < 0$, thus a positive-B_x ramp field means $\alpha \approx 0$; a positive-B_y ramp field indicates $\alpha \approx 90°$; and so on. Ion reflection events occur during the period of $t\Omega_{ni} = 20$–31 are described below:

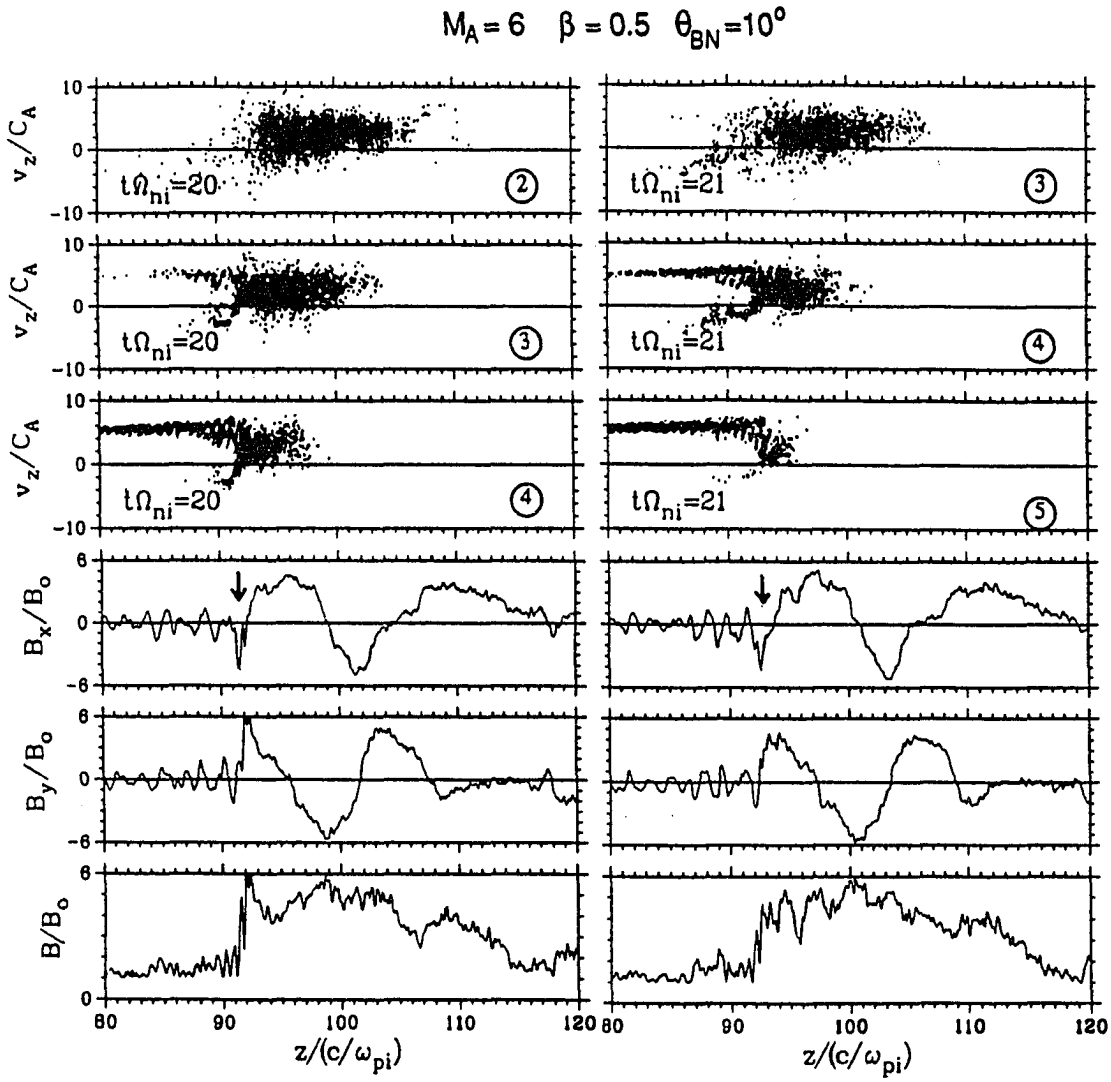

Figure 3.37 Scatter plots of ion distribution in the v_z-z space and the spatial profiles of B_x, B_y, and B at $t\Omega_{ni} = 20$–31 obtained in the $M_A = 6$ shock simulation. The number encircled, shown in each scatter plot, is the group number of the ions shown in that panel. The classification of ion groups used in this section is given in Table 3.1. Ion reflection events shown in this figure can be summarized as follows: (1) A strong highly field-aligned ion reflection event at $t\Omega_{ni} = 20$–23 with $B_x < 0$ ($\alpha \approx 180°$) followed by a week ion reflection event at $t\Omega_{ni} = 23$–24 with $B_y < 0$ ($\alpha \approx 270°$). (2) A reflect-reentering ion reflection event at $t\Omega_{ni} = 26$–27, with $B_x > 0$ ($\alpha \approx 0°$). (3) An ion reflection event at $t\Omega_{ni} = 28$–29, with $B_y > 0$ ($\alpha \approx 90°$). (4) A highly field-aligned ion reflection event at $t\Omega_{ni} = 30$–31, with $B_x < 0$ ($\alpha \approx 180°$). See text for further discussion in detail.

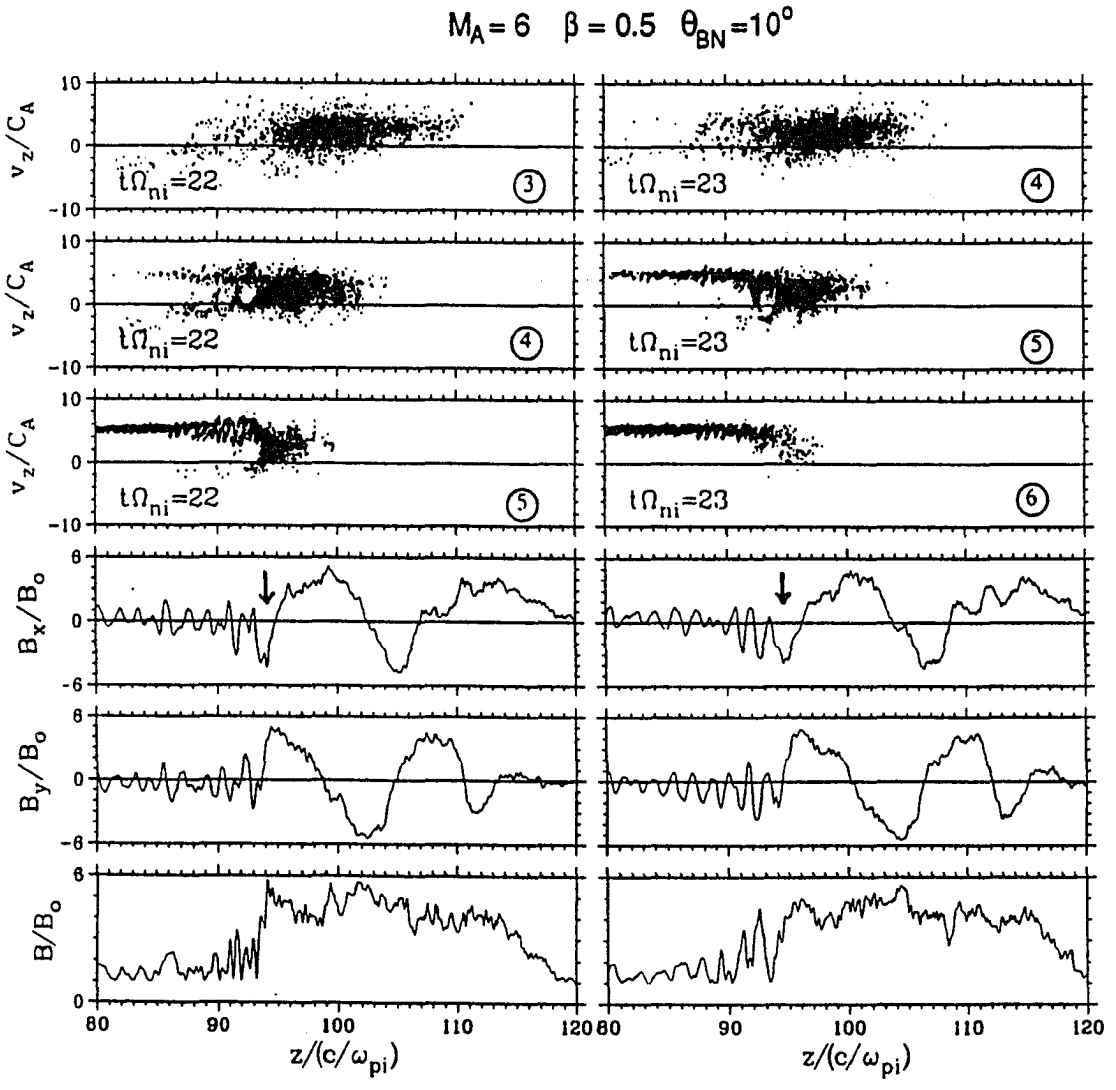

Figure 3.37 (Continued)

(1) *A strong ion reflection event at $t\Omega_{ni} = 20$–23, with $B_x < 0$ ($\alpha \approx 180°$), followed by a weak ion reflection event at $t\Omega_{ni} = 23$–24, with $B_y < 0$ ($\alpha \approx 270°$).* Ion reflection event shown at $t\Omega_{ni} = 20$–23 is characterized by a lengthy reflection beam distribution in the v_z-z space, and a negative-B_x ($\alpha \approx 180°$) ramp field. The lengthy reflection beam indicates that these reflected ions are highly field-aligned. For convenience, we shall call this type of ion reflection event as a highly field-aligned ion reflection event.

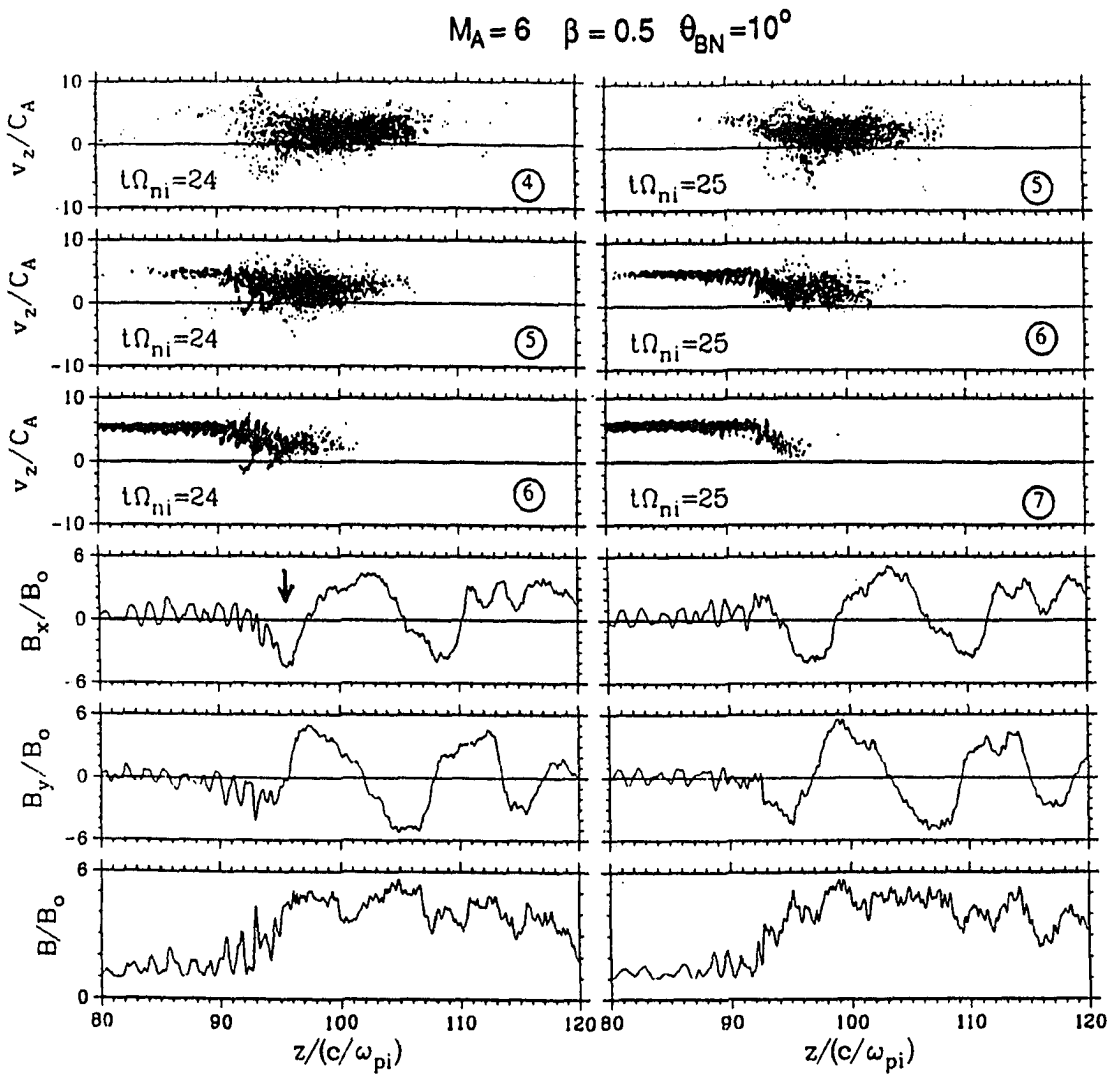

Figure 3.37 (Continued)

Gyrating ions are formed immediately upstream from the shock front. Interactions between the incoming ion beam and the reflected ion beam lead to short wavelength nonlinear waves in the upstream shock transition region. The short-wavelength nonlinear waves can lead to multiple ion reflections. They can also scatter the initially reflected ion beam back to the shock ramp, which will be shown later in detail. The negative-B_x pulse at the shock front intensifies, widens, and propagates downstream as

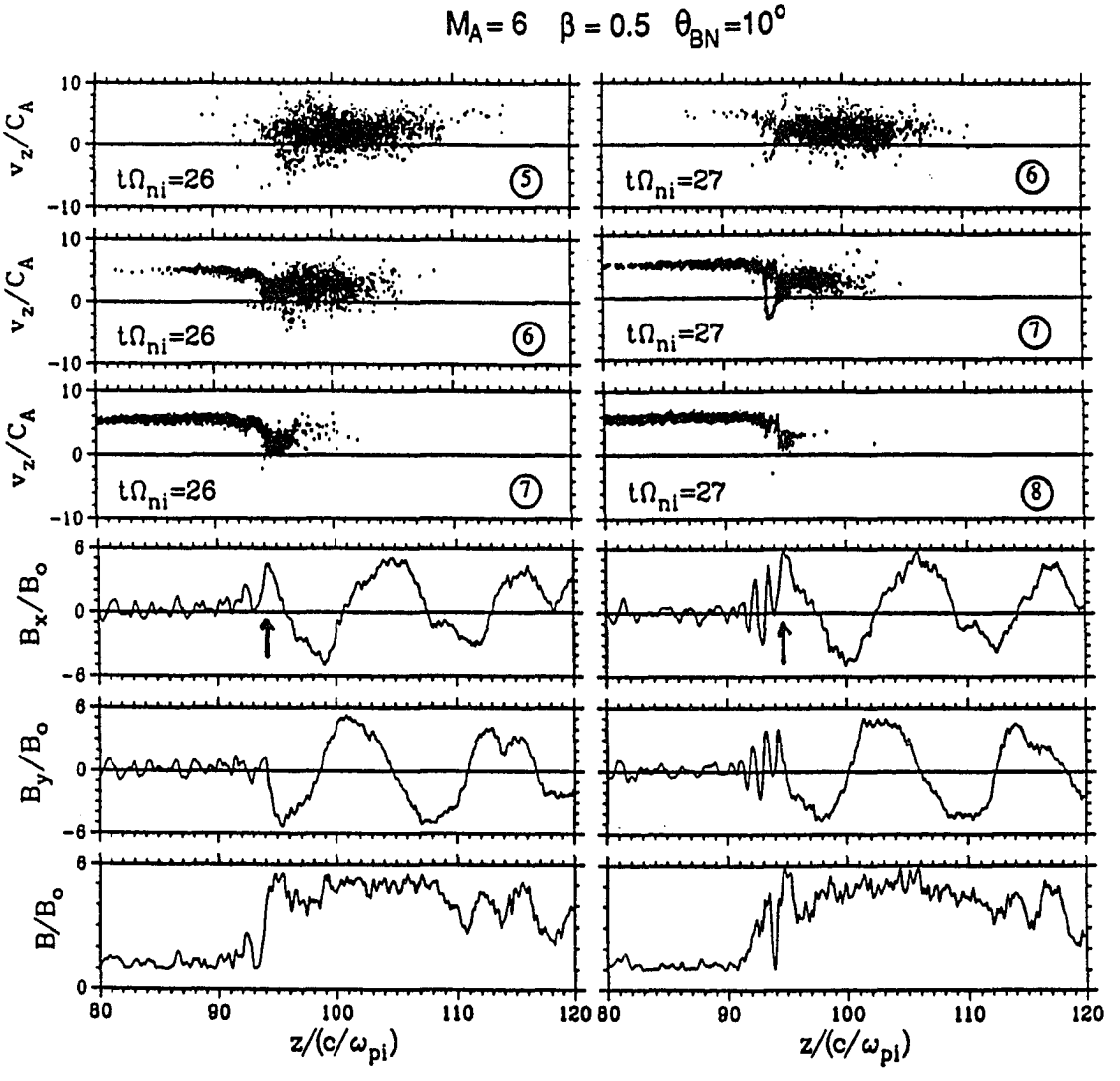

Figure 3.37 (Continued)

the reflection event proceeds. Due to the widening of the shock ramp, ion reflection event occurred at $t\Omega_{ni} = 24$, with a negative-B_y ($\alpha \approx 270°$) ramp field, is much weaker than the ion reflection at $t\Omega_{ni} = 20$–22. The shock ramp is too wide to reflect the incoming ions at $t\Omega_{ni} = 25$. No reflection beam can be found at $t\Omega_{ni} = 25$.

(2) *Ion reflection event at* $t\Omega_{ni} = 26$–27, *with* $B_x > 0$ ($\alpha \approx 0°$). Ion reflection shown at $t\Omega_{ni} = 27$ is characterized by a short ion reflection beam at the shock front. The

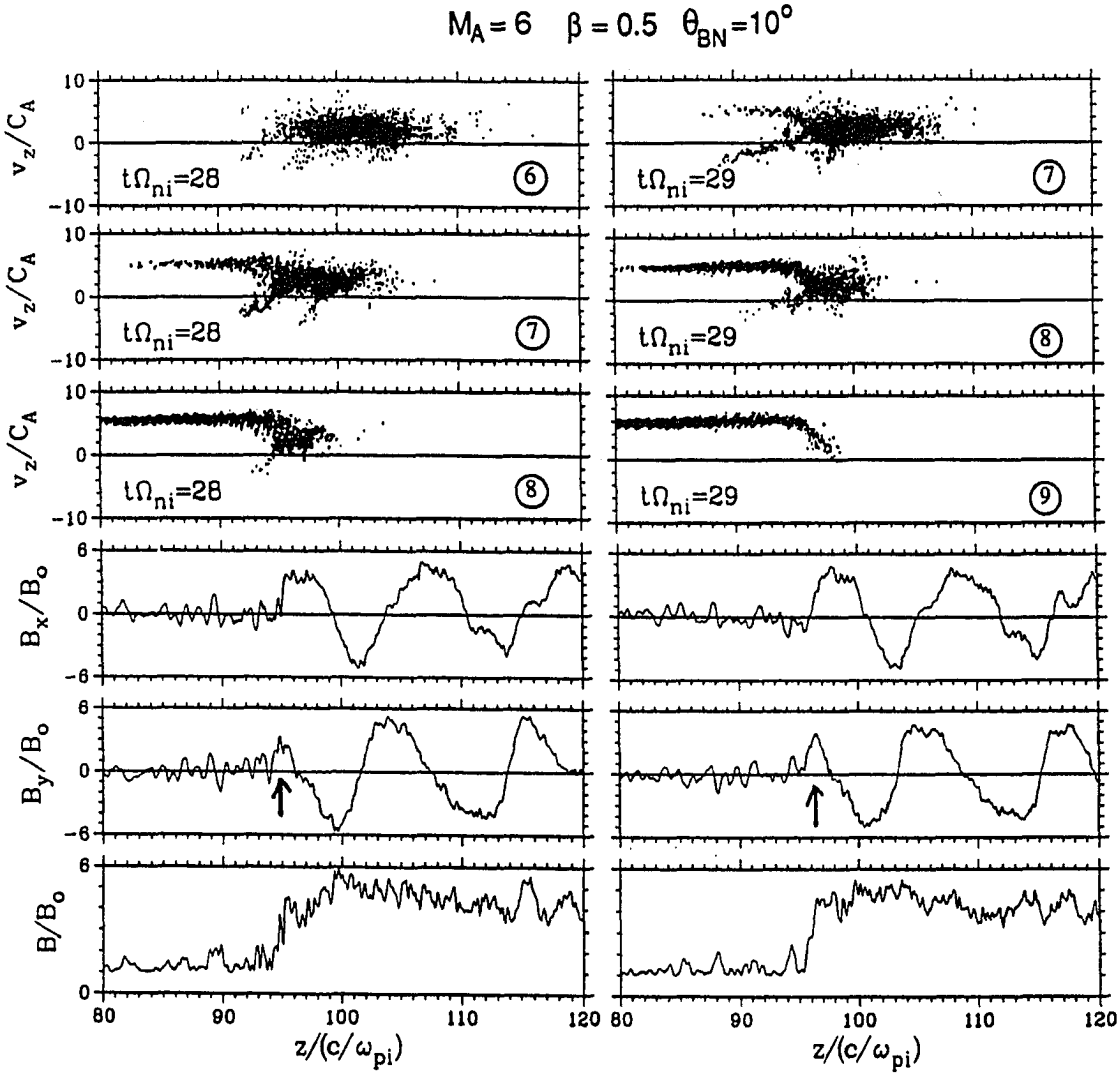

Figure 3.37 (Continued)

reflected ions reenter the shock front right after the reflection. For convenience, we shall call this type of ion reflection event a reflect-reentering ion reflection event. The magnetic field structure at the shock ramp and in the upstream shock transition region during this ion reflection event is similar to those shown in the $M_A = 4$ shock simulation. Namely, a positive B_x ramp field is formed at $t\Omega_{ni} = 26$. Large amplitude whistler waves are emitted from the over-steep positive B_x ramp field at $t\Omega_{ni} = 27$. At

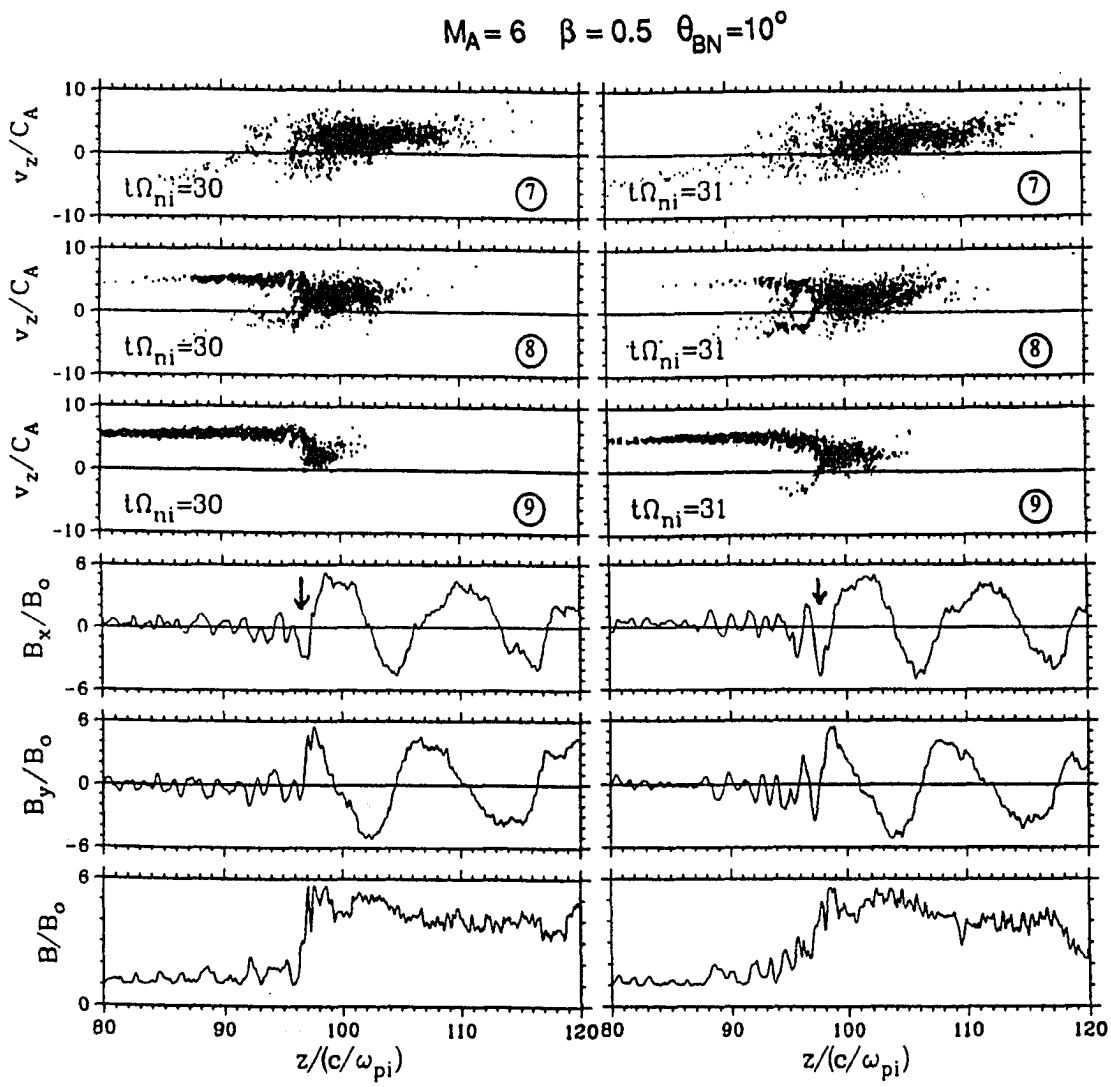

Figure 3.37 (Continued)

the mean time, the reflect-reentering ion reflection event occurred at the shock front. The amplitude of the whistler wave diminished after the reflection event.

(3) *Ion reflection event at* $t\Omega_{ni} = 28$–29, *with* $B_y > 0$ ($\alpha \approx 90°$). The ion reflection event at $t\Omega_{ni} = 28$–29 shows two different characteristics. Half of the reflected ions apparently gyrate back to the shock front, while the other half of the reflected ions form a lengthy but relatively low density reflected ion beam on the upstream side. No large

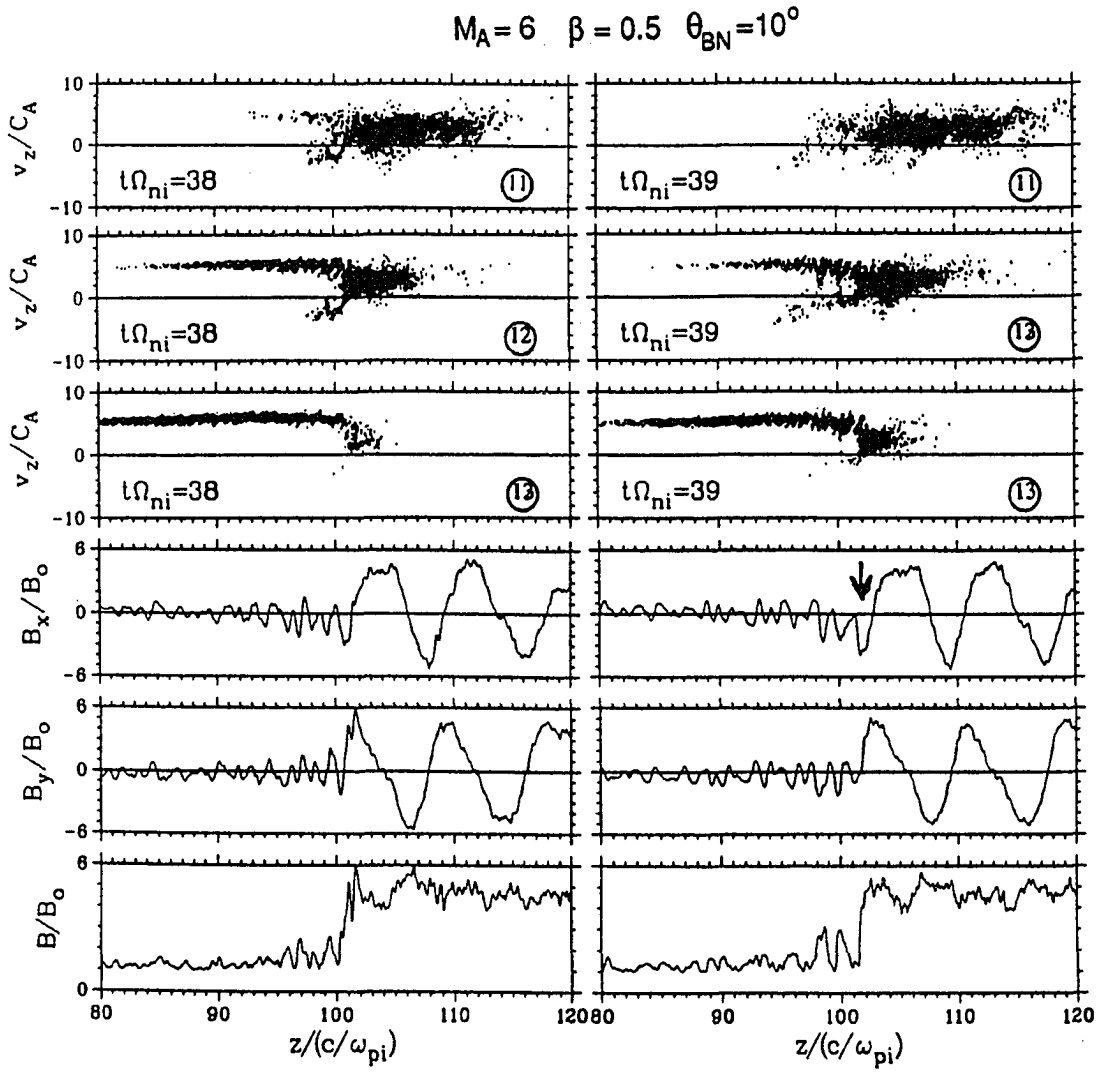

Figure 3.38 An example of highly field-aligned ion reflection event occurred during a negative-B_x ramp field ($\alpha \approx 180°$) obtained in the $M_A = 6$ shock simulation at $t\Omega_{ni} = 38$–39 under the same format as shown in Figure 3.37. Both field configuration and the reflected ion distributions shown in this reflection event are very similar to those shown in the reflection events at $t\Omega_{ni} = 20$–22 and at $t\Omega_{ni} = 30$–31 in Figure 3.37.

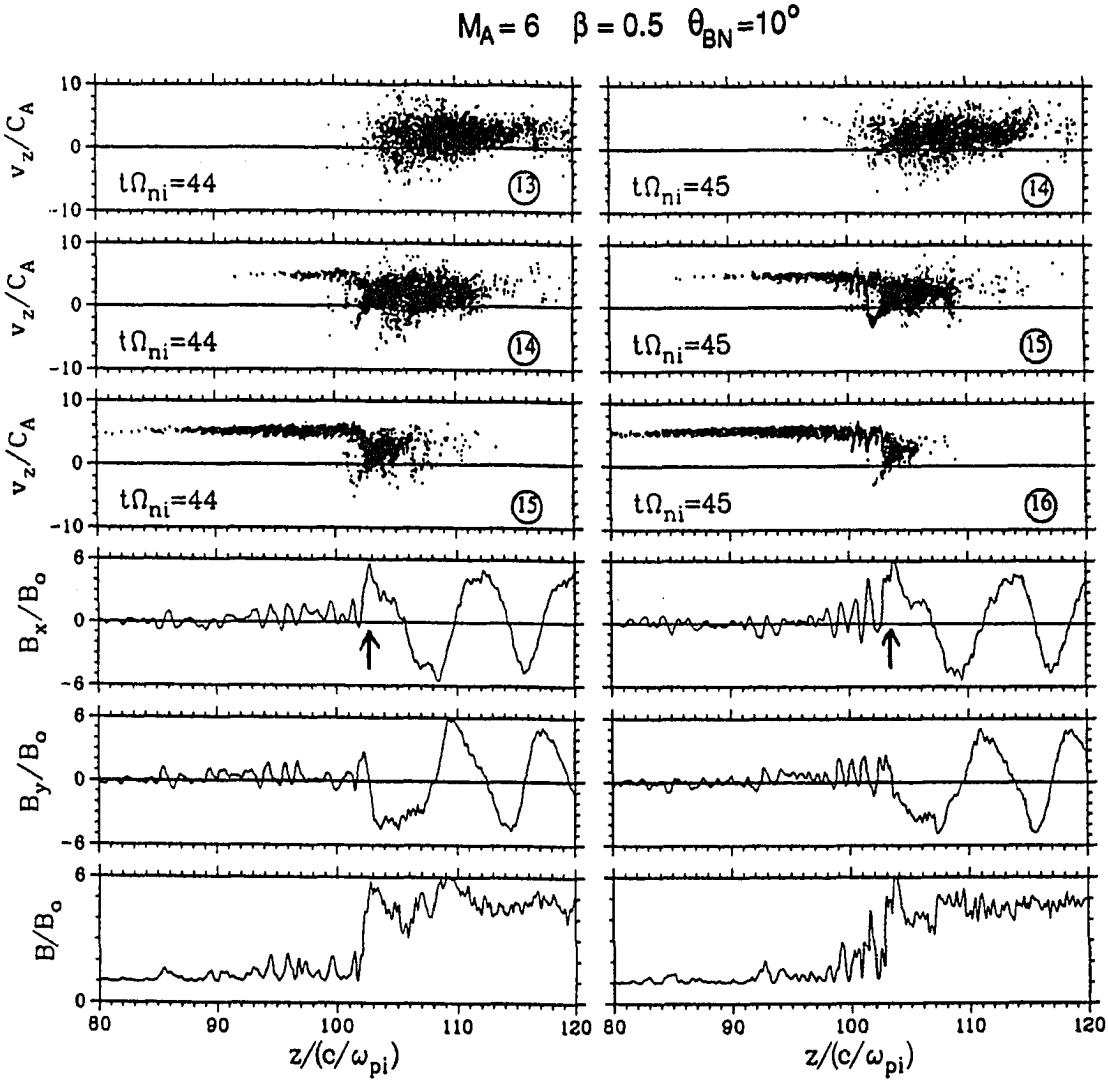

Figure 3.39 An example of reflect-reentering ion reflection event occurred during a positive-B_x ramp field ($\alpha \approx 0°$) obtained in the $M_A = 6$ shock simulation at $t\Omega_{ni} =$ 44–45 under the same format as shown in Figure 3.37. Both field configuration and the reflected ion distributions shown in this reflection event are very similar to those shown in the reflection event at $t\Omega_{ni} = 26$–27 in Figure 3.37.

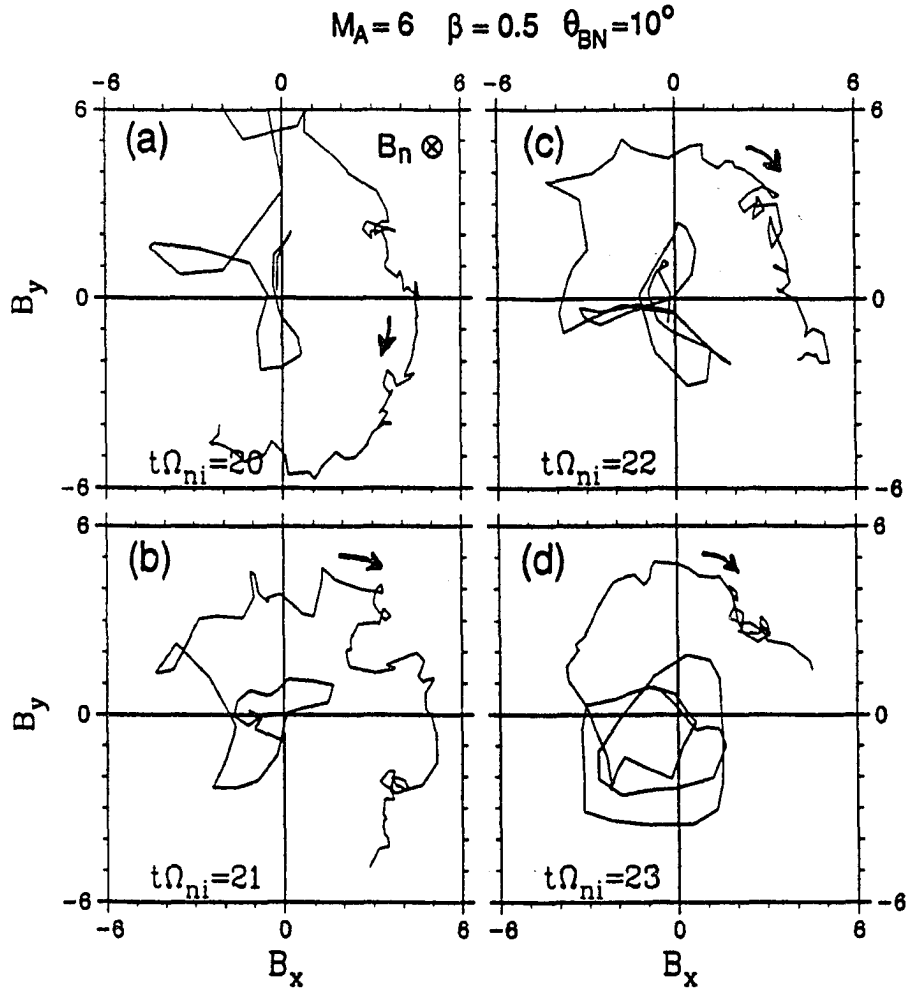

Figure 3.40 Magnetic field hodograms during a highly field-aligned ion reflection event in the $M_A = 6$ shock simulation at $t\Omega_{ni} = 20$–23. Arrows are going in downstream direction. See text for discussion in detail.

amplitude upstream waves have been generated by the lengthy but low density reflect ion beam at this time. The ramp field during this ion reflection event is characterized by a $B_y > 0$, i.e., $\alpha \approx 90°$.

(4) *Ion reflection event at $t\Omega_{ni} = 30$–31, with $B_x < 0$ ($\alpha \approx 180°$).* A highly field-aligned ion reflection can be found at $t\Omega_{ni} = 30$–31. Both ion distribution and

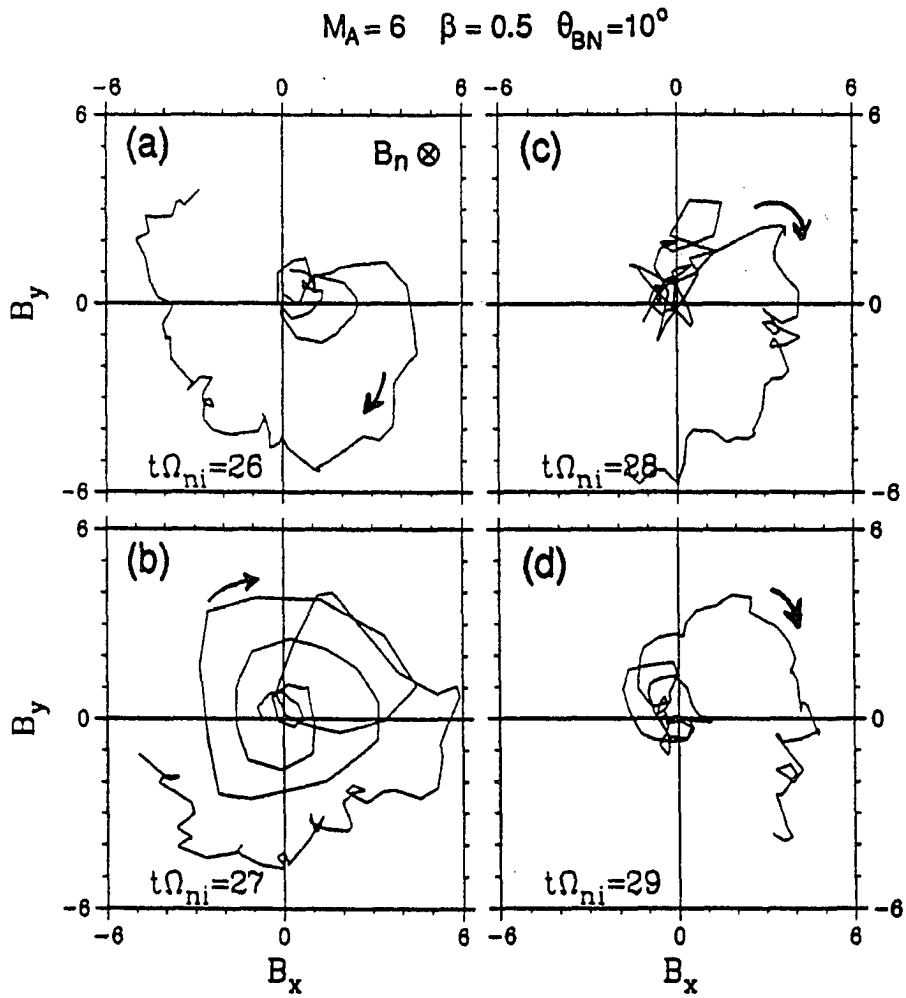

Figure 3.41 Magnetic field hodograms during a reflect-reentering ion reflection event obtained from the $M_A = 6$ shock simulation at $t\Omega_{ni} = 26$–29. Arrows are going in downstream direction. See text for discussion in detail.

magnetic field configuration shown in this ion reflection event are similar to those shown in the ion reflection event at $t\Omega_{ni} = 20$–22.

Figure 3.38 shows another example of a highly field-aligned ion reflection event that occurred during a negative-B_x ramp field ($\alpha \approx 180°$) obtained in the $M_A = 6$ shock simulation at $t\Omega_{ni} = 38$–39. Both field configuration and the reflected ion

distributions shown in this reflection event are very similar to those shown in the reflection events at $t\Omega_{ni} = 20$–22 and at $t\Omega_{ni} = 30$–31 in Figure 3.37.

Figure 3.39 shows another example of a reflect-reentering ion reflection event which occurred during a positive-B_x ramp field ($\alpha \approx 0°$) obtained in the $M_A = 6$ shock simulation at $t\Omega_{ni} = 44$–45. Both field configuration and the reflected ion distributions shown in this reflection event are very similar to those shown in the reflection event at $t\Omega_{ni} = 26$–27 in Figure 3.37.

In summary, two basic types of strong ion reflection events can be found in the $M_A = 6$ shock simulation. A strong reflect-reentering ion reflection event can be found during the ramp field phase angle $\alpha \approx 0°$. A strong, highly field-aligned ion reflection event can be found with ramp field phase angle $\alpha \approx 180°$, which can lead to broadening of the shock front. The shock front drifts backward during this type of ion reflection event. The strong reflected-reentering ion reflection events and highly field-aligned ion reflection events appear alternately at the shock front. Weak or mixing types of ion reflection events can be found when the ramp field phase angle $\alpha \approx 90°$ or $\alpha \approx 270°$, unless the shock front is too wide to reflect the incoming ions. Based on the simulation results shown in Figures 3.37–3.39, an gyro-reflection model will be proposed in Section 3.4 to describe the governing physical process of ion reflections in the high Mach number quasi-parallel shocks.

Two types of large-amplitude, short-wavelength nonlinear waves can be found in the upstream shock transition region associated with the two types of ion reflection events in the $M_A = 6$ shock simulation. One of them is generated by a two-stream instability due to the presence of a high-density ion reflection beam which extends far upstream from the shock front; the other is generated by nonlinear dispersion from a steep ramp field with phase angle $\alpha \approx 0°$.

Figure 3.40 shows magnetic hodogram in the upstream shock transition region and across the shock ramp at $z = 90$–$100\ c/\omega_{pi}$ during the strong field-aligned ion reflection event at $t\Omega_{ni} = 20$–23 obtained in the $M_A = 6$ shock simulation. The magnetic hodogram in the shock ramp is characterized by highly irregular structures. Right-hand polarized nonlinear waves are formed at $t\Omega_{ni} = 23$, due to the ion two-beam interactions in the upstream shock transition region.

Figure 3.41 shows magnetic hodogram in the upstream shock transition region and across the shock ramp at $z = 90$–$100\ c/\omega_{pi}$; before, during, and after the reflect-reentering ion reflection event at $t\Omega_{ni} \approx 27$, obtained in the $M_A = 6$ shock simulation. Before the ion reflection event, a large-amplitude positive-B_x ramp field can be seen. Large amplitude whistler waves are dispersed from the over-steepened positive-B_x ramp field and result in a spiral-type of magnetic hodogram at $t\Omega_{ni} = 27$. After the reflection event, the amplitude of the nonlinear whistler wave was diminished. No large-amplitude spiral-type magnetic hodogram can be found at $t\Omega_{ni} = 28$ and 29. Note that large amplitude nonlinear waves can be found in the upstream shock transition region at $t\Omega_{ni} = 23$ and $t\Omega_{ni} = 27$ as shown in Figure 3.40*d* and Figure 3.41*b*, respectively. However, the spiral-type magnetic hodogram can only be found when the upstream nonlinear waves are nonlinear whistler waves generated by dispersion from an over-steepened shock front as shown in Figure 3.41*b*. When the nonlinear waves are generated by ion two-beam interactions, the magnetic hodogram of these waves is characterized by an elliptically polarized chaotic hodogram as shown in Figure 3.40*d*.

The ion heating process of the reflected ions and transmitted ions in the shock transition region can be studied by tracing a group of ions during and after their first encounter with the shock front.

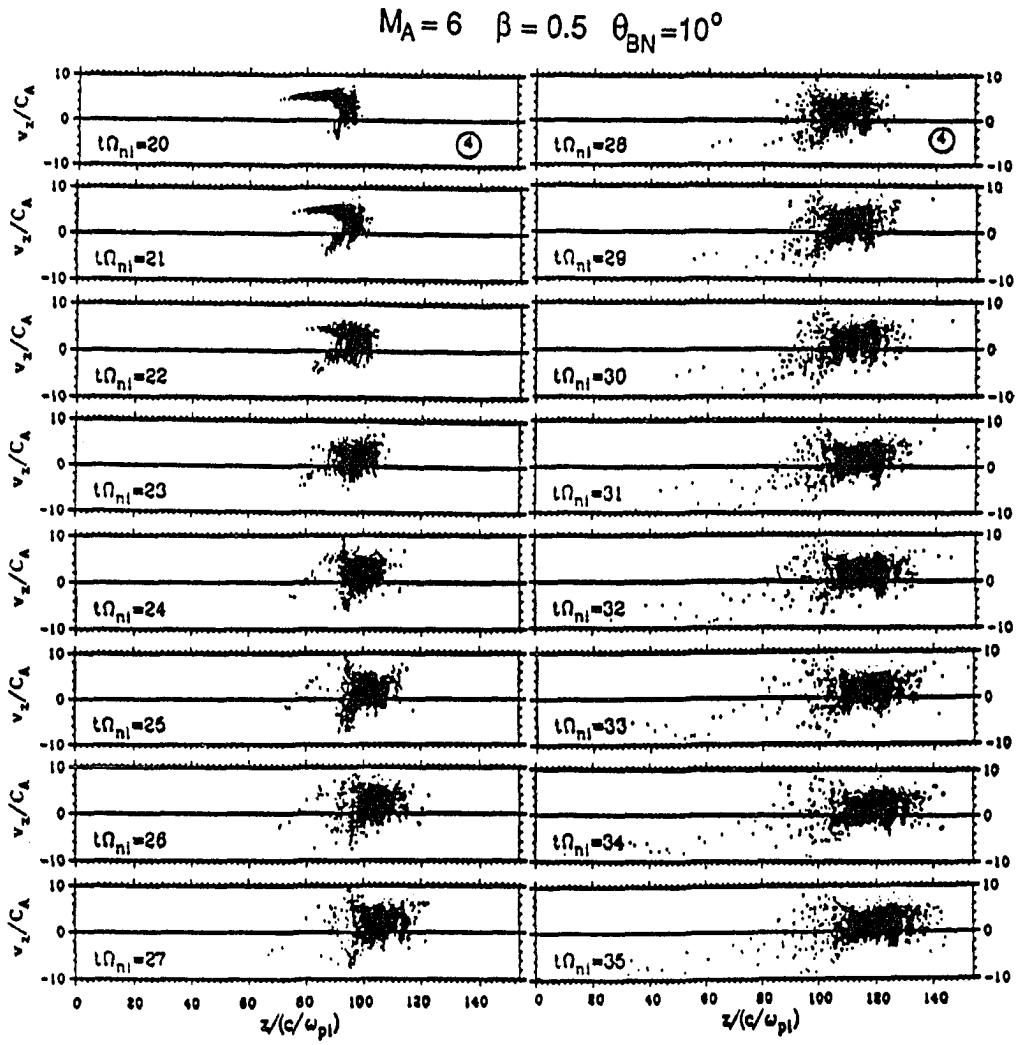

Figure 3.42 Scatter plots of group 4 ion distribution in the v_z-z space at successive times during the period of $t\Omega_{ni} = 20$–35.

Figure 3.42 shows scatter plots of group 4 ion distribution in the v_z-z space at successive times during the period of $t\Omega_{ni} = 20$–35. Most of the group 4 ions undergo a highly field-aligned reflection at the shock front at $t\Omega_{ni} \approx 20$–22 by a ramp field of $\alpha \approx 180°$. It can be seen that the reflected ions are first direct to the upstream but later gyrate back to the shock front. A strong ion heating at the shock ramp can be

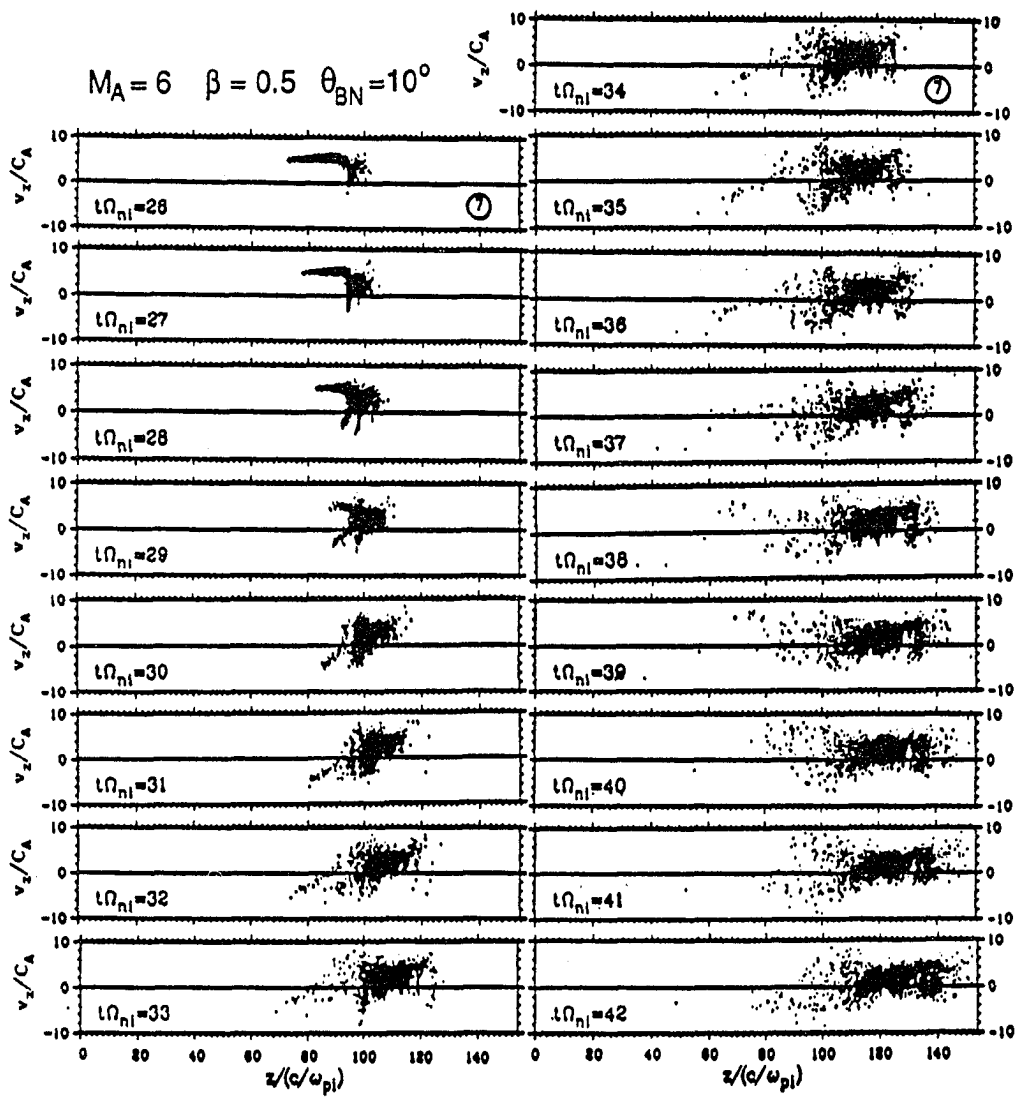

Figure 3.43 Scatter plots of group 7 ion distribution in the v_z-z space at successive times during the period of $t\Omega_{ni} = 26$–42.

seen at $t\Omega_{ni} = 24$–29. Some of the super-heated ions start to leak upstream without turning back to the shock front after $t\Omega_{ni} \approx 29$.

Figure 3.43 shows scatter plots of group 7 ion distribution in the v_z-z space at successive times during the period of $t\Omega_{ni} = 26$–42. The first part of group 7 ions reflected at the shock front at $t\Omega_{ni} \approx 26$–27 in a reflect-reentering manner by a ramp

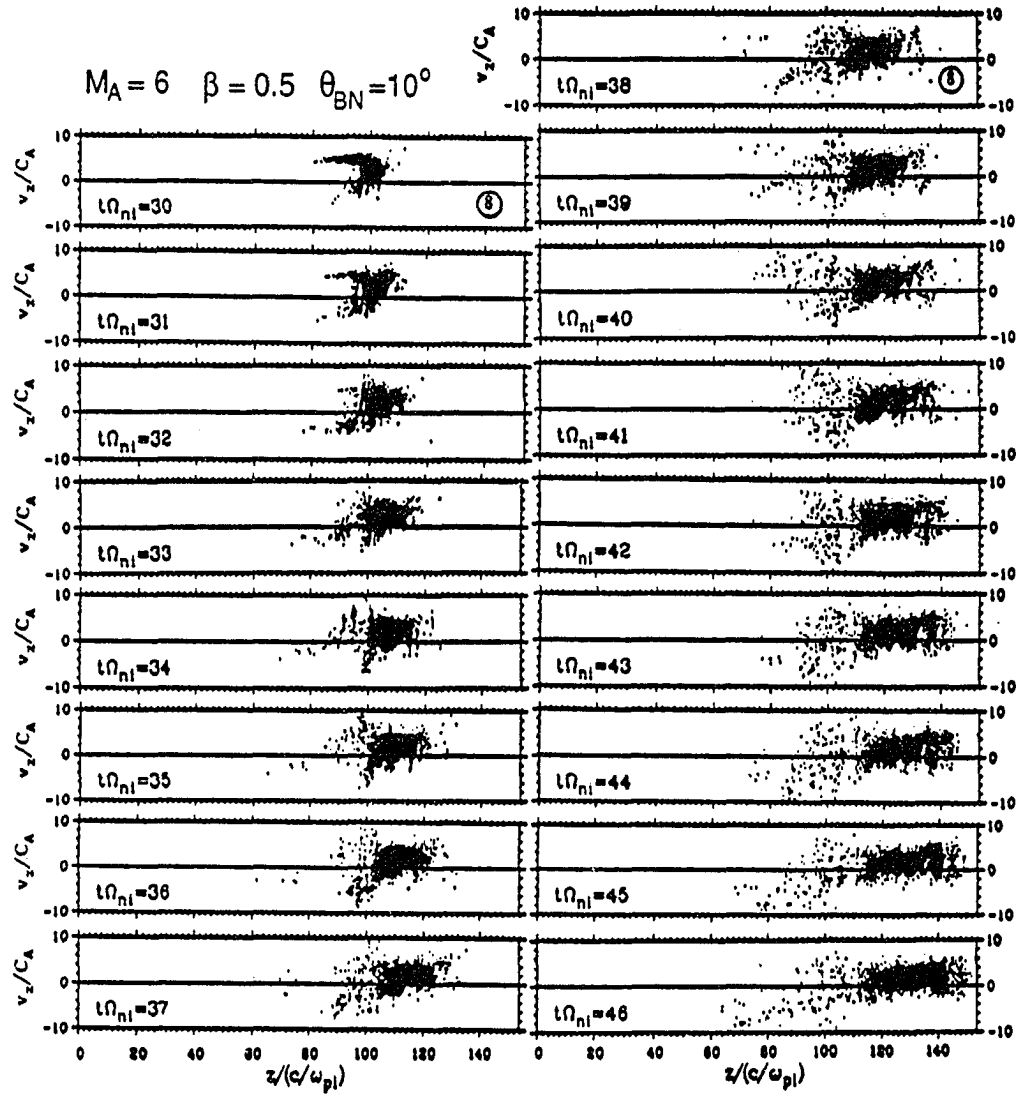

Figure 3.44 Scatter plots of group 8 ion distribution in the v_z-z space at successive times during the period of $t\Omega_{ni} = 30$–46.

field of $\alpha \approx 0°$; whereas, a mixed type of ion reflection event can be found at the shock front at $t\Omega_{ni} \approx 28$–29 by a ramp field of $\alpha \approx 90°$ as discussed in Figure 3.37. A strong ion heating at shock ramp can be seen at $t\Omega_{ni} \approx 31$–35. No shock-heated leakage ions can be found by the end of the scatter plot at $t\Omega_{ni} = 42$. Thus, we can

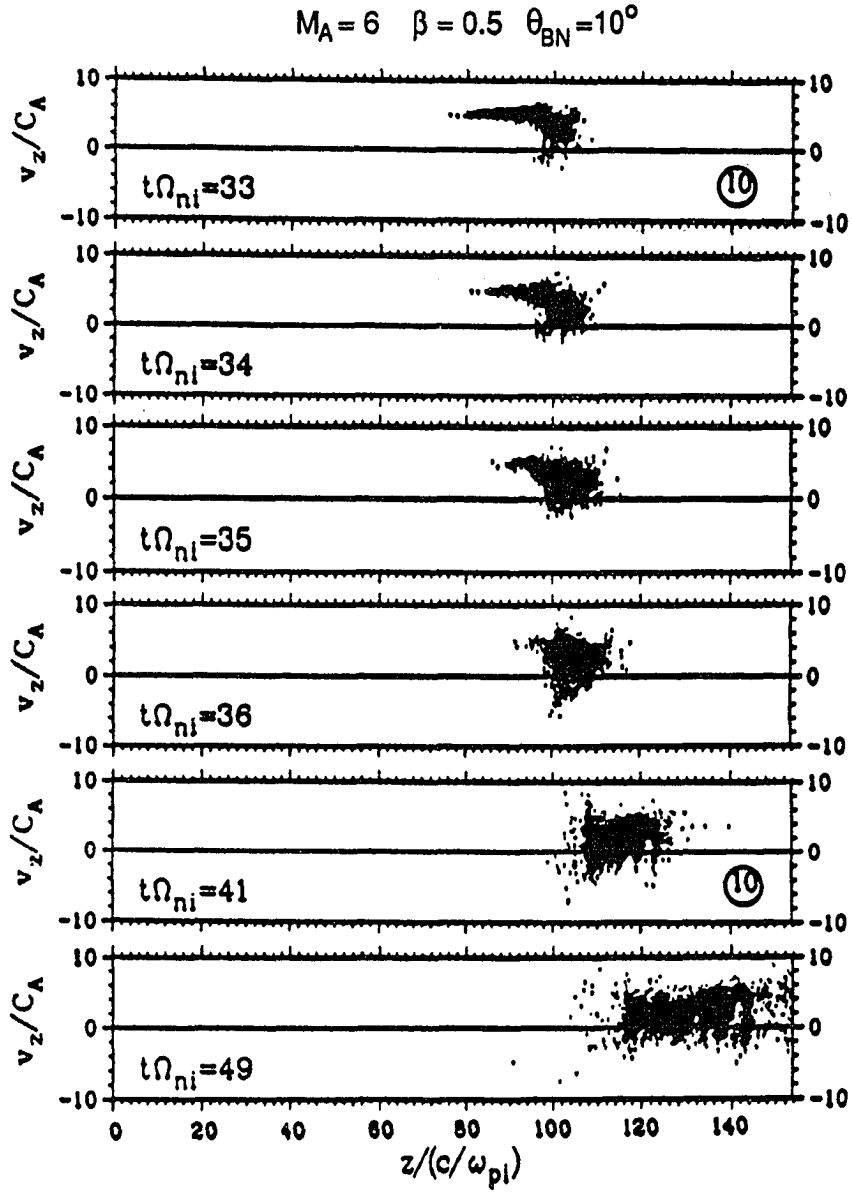

Figure 3.45 Scatter plots of group 10 ion distribution in the v_z-z space at successive times during the period of $t\Omega_{ni} = 33$–49. No strong heating can be found in the shock ramp, but a significant amount of ion heating can be found in the downstream shock transition region.

conclude that not all the highly field-aligned reflected ions can form shock front-heated leakage ions during a short period of time after reflection as shown in Figure 3.42.

Figure 3.44 shows scatter plots of group 8 ion distribution in the v_z-z space at successive times during the period of $t\Omega_{ni} = 30$–46. A highly field-aligned ion reflection event can be found at the shock front at $t\Omega_{ni} \approx 29$–31 by a ramp field of $\alpha \approx 180°$. A strong ion heating at shock front can be seen at $t\Omega_{ni} \approx 31$–35. No shock-heated leakage ions can be found until the end of the scatter plot at $t\Omega_{ni} = 46$.

Figure 3.45 shows scatter plots of group 10 ion distribution in the v_z-z space at successive times during the period of $t\Omega_{ni} = 33$–49. The group 10 ions enter the shock front after a strong highly field-aligned ion reflection event (occurred at $t\Omega_{ni} =$ 30–31 as can be seen in Figure 3.37). The shock front is not very steep at the time when they reach the shock front, but some of the ions in the group 10 still undergo reflection by a ramp field of $\alpha \approx 320°$ at $t\Omega_{ni} = 33$–35. The reflection is so weak that those reflected ions can only reach to a very small negative-v_z component during the reflection. In this case, no strong heating can be found in the shock ramp. But a significant amount of ion heating can be found in the downstream shock transition region.

In our simulation studies, we have not found a single ion reflection event in which reflected ions directly contribute to the suprathermal ions without returning back to the shock front. However, we also recognized that our simulation results may not be exclusively for all the quasi-parallel shocks. Thus, the model for the formation of suprathermal backstreaming ions observed upstream from the shock front as proposed by *Paschmann et al.* [1981] and *Gosling et al.* [1982] are still considered as an open issue for future study. Nevertheless, if we carefully examine the contour plots of observed gyrating ion distributions shown in Figure 3.2, we can see that the gyrating ions are hotter near the shock front in Figure 3.2*a* but cooler further upstream in Figure

3.2*b*. Thus, one may suspect that these observed gyrating ions were indeed turned around and headed back to the shocks front as those shown in Figures 3.42–3.44.

For those transmitted ions and reflected ions reentering the shock front, the ion heating processes continues to take place in the downstream shock transition region. Both downstream hot ions and shock-heated ions can contribute to backstreaming ions in the downstream shock transition region. The dynamics of these backstreaming ions and those forward ions in the downstream shock transition region are similar to those shown in the $M_A = 4$ shock simulations.

Figures 3.46, 3.47, 3.48, and 3.49 show scatter plots of ion distribution in the v_z-z space, v_x-z space, ϕ-z space, and v-z space, respectively, for different groups of ions obtained from the $M_A = 6$ shock simulation at $t\Omega_{ni} = 49$. The corresponding spatial profiles of N_i, T_i, B_x, B_y, and B obtained from the $M_A = 6$ shock simulation at $t\Omega_{ni} = 49$ are shown in Figure 3.50. Ions shown in panels (*a*)–(*e*) of Figures 3.46–3.49 are incoming ions from the upstream boundary during the time interval of (*a*) $t\Omega_{ni} \geq 30$, (*b*) $t\Omega_{ni} = 26$–30, (*c*) $t\Omega_{ni} = 20$–26, (*d*) $t\Omega_{ni} = 10$–20, and (*e*) $t\Omega_{ni} = 0$–10. Ions shown in panels (*f*)–(*h*) of Figures 3.46–3.49 are: (*f*) initial loaded upstream ions, (*g*) initial loaded downstream ions, and (*h*) incoming ions entering from the downstream boundary after $t = 0$. One can distinguish the backstreaming ions in the downstream shock transition region from either the phase angle distribution in the ϕ-z space or the phase relationship between B_x and average v_x as discussed in Figure 3.24. Backstreaming downstream hot ions can be seen in panels (*g*) and (*h*). Backstreaming shock-heated ions can be seen in panels (*e*) and (*f*), and upstream from the secondary peak of ion temperature profile in panels (*c*) and (*d*). These backstreaming ions gain tangential component streaming kinetic energy from the tangential electric field as they backstream across the downstream shock transition region. The streaming kinetic

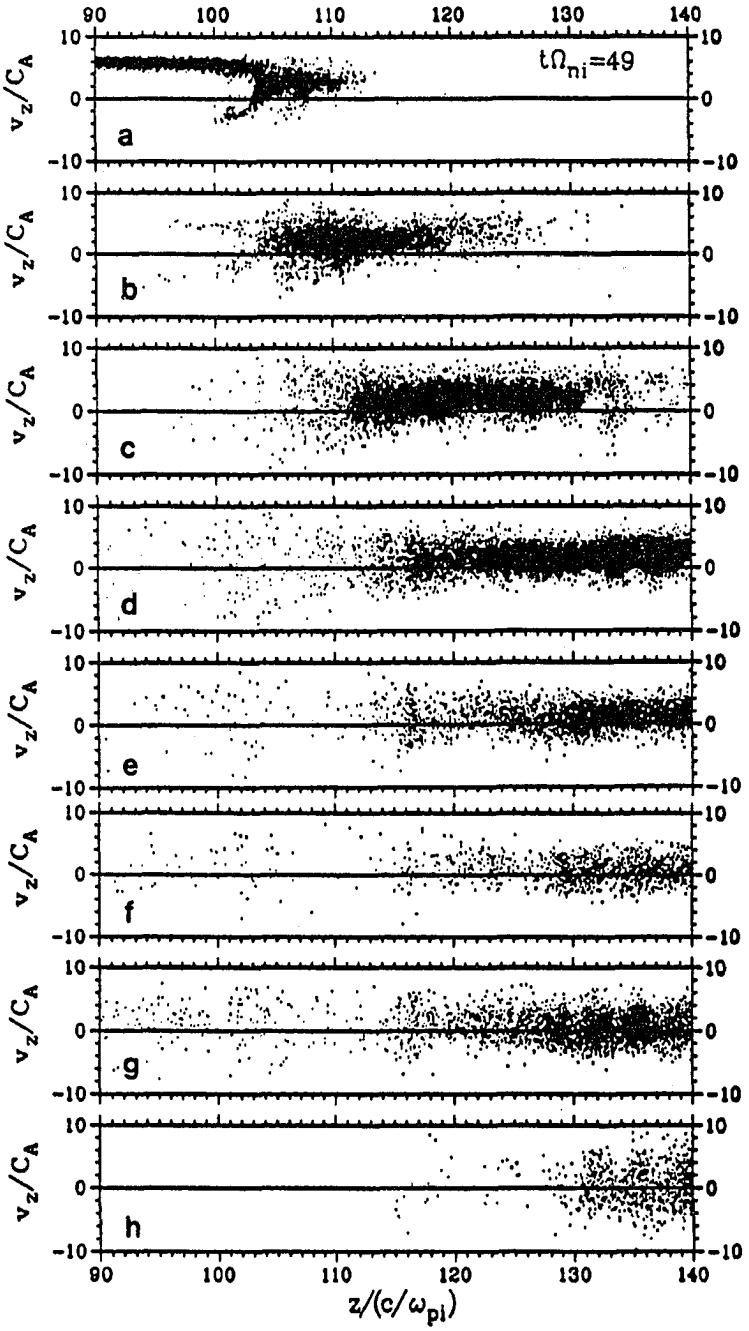

Figure 3.46 Scatter plots of ion distribution in the v_z-z space obtained from the $M_A = 6$ shock simulation at $t\Omega_{ni} = 49$. Ions shown in panels (*a*)–(*e*) are incoming ions from the upstream boundary during the time interval of (*a*) $t\Omega_{ni} \geq 30$, (*b*) $t\Omega_{ni} = 26$–30, (*c*) $t\Omega_{ni} = 20$–26, (*d*) $t\Omega_{ni} = 10$–20, and (*e*) $t\Omega_{ni} = 0$–10. Ions shown in panels (*f*)–(*h*) are: (*f*) initial loaded upstream ions, (*g*) initial loaded downstream ions, and (*h*) incoming ions entering from the downstream boundary after $t = 0$. Corresponding field structures are given in Figure 3.50.

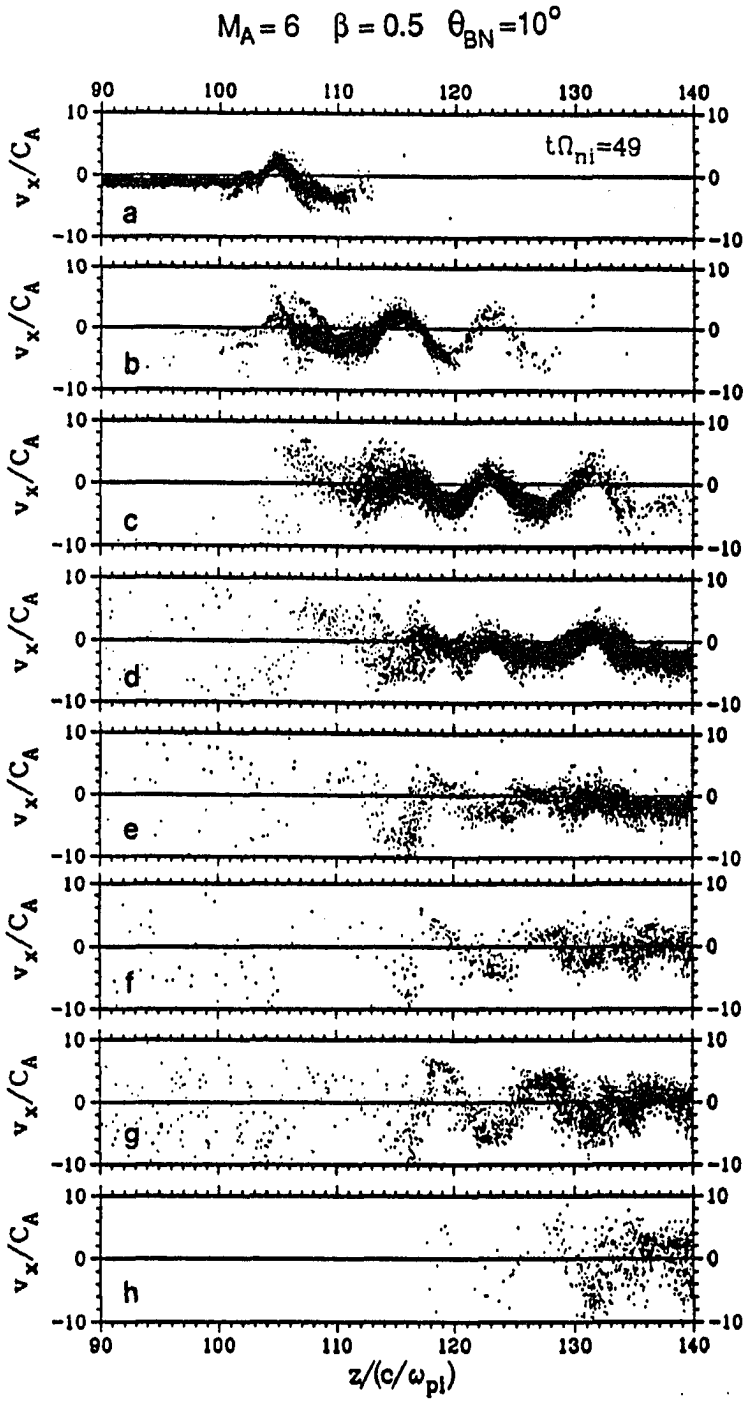

Figure 3.47 Scatter plots of ion distribution in the v_x-z space obtained from the $M_A = 6$ shock simulation at $t\Omega_{ni} = 49$. Ions shown in each panel are the same as the ions shown in Figure 3.46.

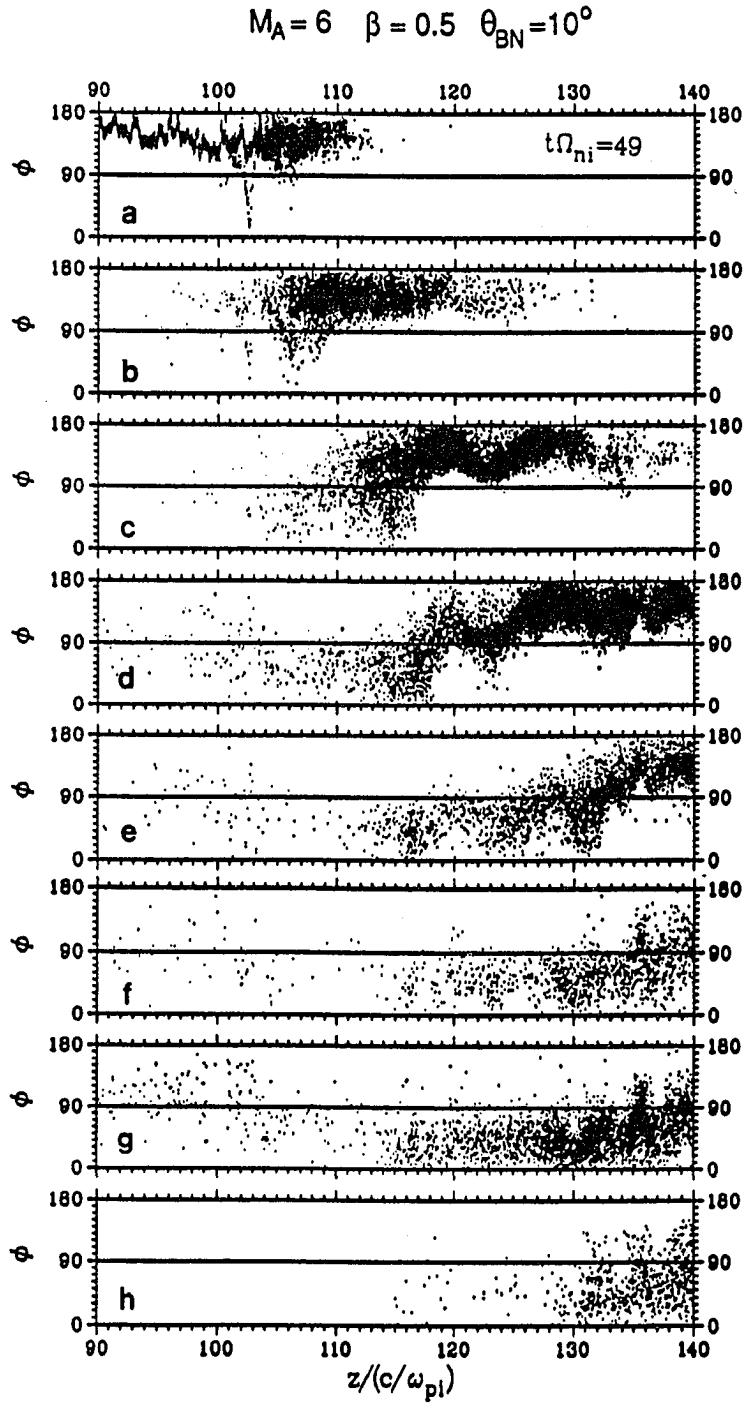

Figure 3.48 Scatter plots of ion distribution in the ϕ-z space obtained from the $M_A = 6$ shock simulation at $t\Omega_{ni} = 49$. Ions shown in each panel are the same as the ions shown in Figure 3.46.

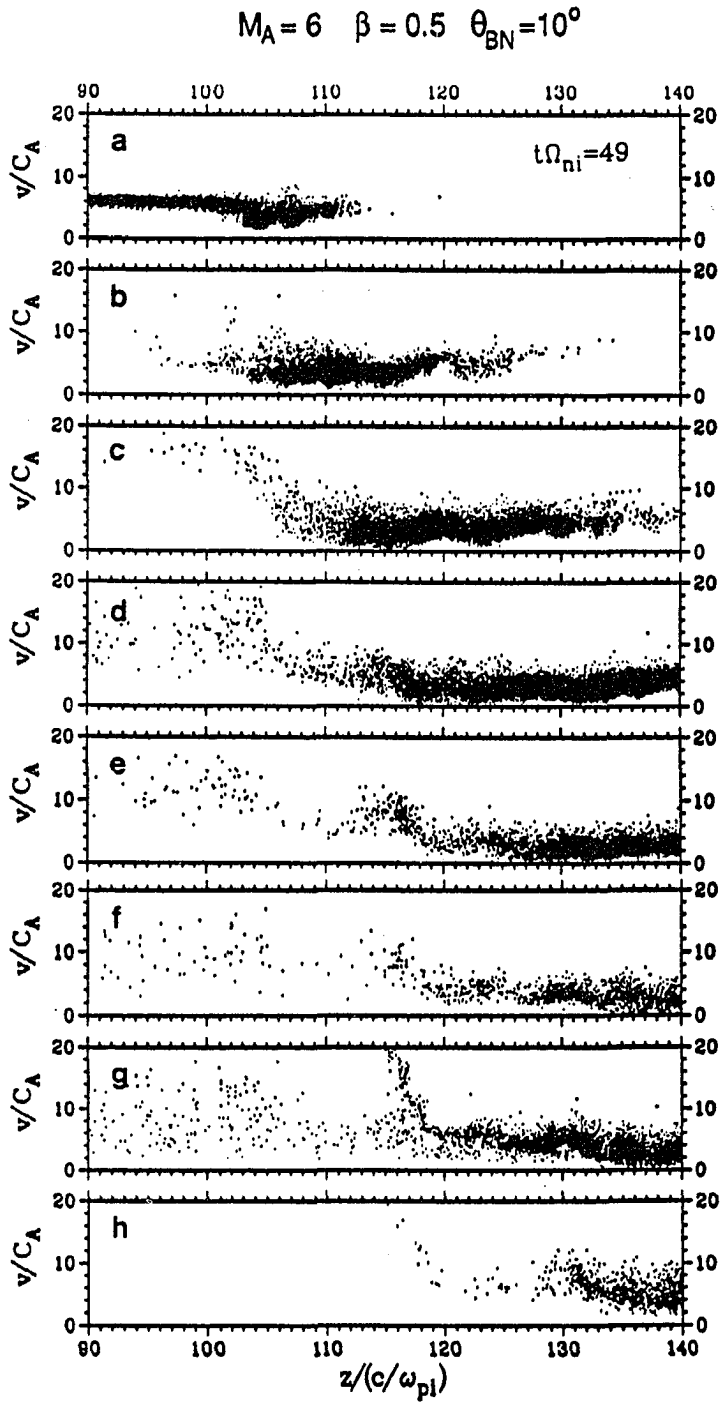

Figure 3.49 Scatter plots of ion distribution in v-z space for different groups of ions obtained from the $M_A = 6$ shock simulation at $t\Omega_{ni} = 49$. Ions shown in each panel are the same as the ions shown in Figure 3.46.

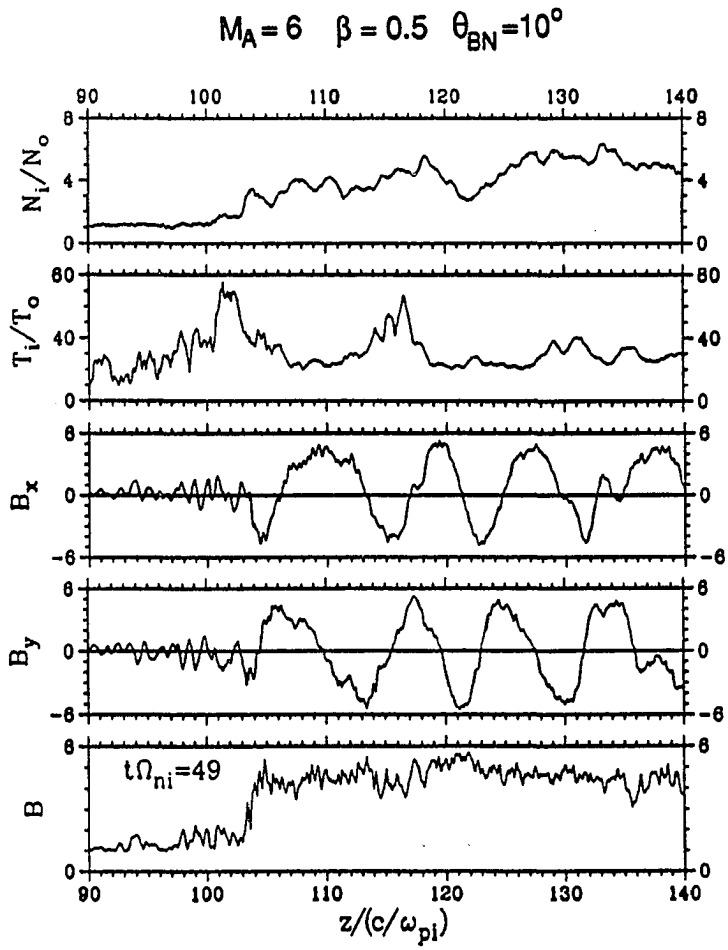

Figure 3.50 Spatial profiles of N_i, T_i, B_x, B_y, and B obtained from the $M_A = 6$ shock simulation at $t\Omega_{ni} = 49$.

energy was turned into thermal energy as these ions leak across the shock front. The heating of the transmitted ions are characterized by hook-shaped ion distributions in the v_z-z space as can be seen in panel (c). These hook-shaped gyrating ion distributions in the downstream shock transition region becomes even more clear when we plot one group of ions at a time as shown in Figures 3.42–3.45.

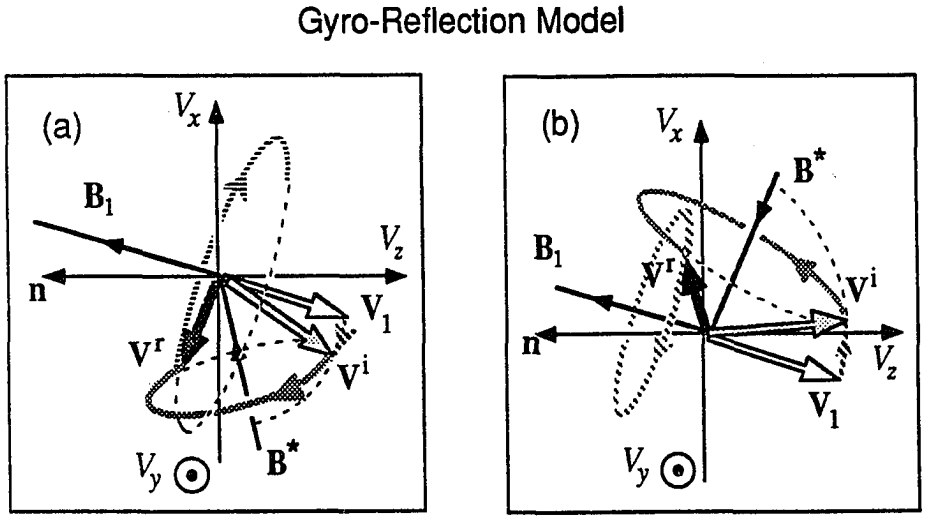

Figure 3.51 Sketches of the variation of velocity vectors of reflected ions during gyro-reflection processes in the velocity space, where $\mathbf{V}_1$ is the upstream velocity of incoming ions before entering the shock ramp, $\mathbf{V}^i$ is the incident velocity of the upstream ions measured in the shock ramp, $\mathbf{V}^r$ is the reflected velocity of reflected ions measured after they gyro-reflecting across the shock front. For convenience, the direction of upstream magnetic field $\mathbf{B}_1$, and the direction of ramp magnetic field $\mathbf{B}^*$ are also indicated in the velocity-space plot. The non-zero, cross-shock-front, tangential electric field will be ignored in the discussion given in this figure. The phase angle a of the ramp field $\mathbf{B}^*$ is 0° in panel (*a*), but 180° in panel (*b*).

3.4 A Gyro-Reflection Model

To explain the two types of ion reflection events obtained in the $M_A = 6$ shock simulation, a gyro-reflection model is proposed in this section.

Figure 3.51 sketches the variation of velocity vectors of reflected ions during gyro-reflection processes in the velocity space, where $\mathbf{V}_1$ is the upstream velocity of incoming ions before entering the shock ramp, $\mathbf{V}^i$ is the incident velocity of the upstream ions measured in the shock ramp, $\mathbf{V}^r$ is the reflected velocity of reflected ions measured after they gyro-reflecting across the shock front. For convenience, the direction of upstream magnetic field $\mathbf{B}_1$, and the direction of ramp magnetic field $\mathbf{B}^*$

are also indicated in the velocity-space plot. For simplicity, we shall ignore the non-zero, cross-shock-front, tangential electric field in our discussion, which can be easily added into the gyro-reflection model after the basic steps of constant-energy, gyro-reflection process is understood. The phase angle α of the ramp field $\mathbf{B}^\star$ is 0° in panel (*a*), but 180° in panel (*b*). Ion reflections at a ramp field with different phase angle can be obtained by the same method as discussed below. The ion reflection process governed by the gyro-reflection model shown in Figure 3.51 can be decomposed into three steps as described in follows:

(1) The first step of the gyro-reflection process is a pitch-angle scattering due to an abrupt change of magnetic field from $\mathbf{B}_1$ to $\mathbf{B}^\star$. The pitch-angle scattering is characterized by the change of ion velocity from $\mathbf{V}_1$ to $\mathbf{V}^i$. The amount of pitch-angle scattering depends on the radius of curvature of the magnetic field line across the shock front (R_B) and the gyro radius of the incoming ions (r_g). For $R_B \ll r_g$, the $\mathbf{V}^i$ should be approximately in the same direction as the $\mathbf{V}_1$, which is the largest pitch-angle scattering. For $R_B \gg r_g$, the $\mathbf{V}^i$ should align with the $\mathbf{B}^\star$. Namely, there will be no pitch-angle scattering if $R_B \gg r_g$. For high Mach number quasi-parallel shocks, we have $R_B \approx r_g$. Thus, a pitch-angle scattering with $\mathbf{V}^i \neq \mathbf{V}_1$ can be found across the shock front as illustrated in Figure 3.51.

(2) The second step of the gyro-reflection process is modeled by an incomplete gyro-motion with initial velocity $\mathbf{V}^i$ gyrating around the ramp field $\mathbf{B}^\star$ and is ended when the reflected ion reaches to the upstream side. The incomplete gyro-motion is characterized by the motion from $\mathbf{V}^i$ to $\mathbf{V}^r$ as shown in Figure 3.51. Since Figure 3.51 is plotted in the velocity space, the ion may reach to the upstream side after it has picked up a negative V_z component for a period of time. Namely, the gyro-motion may last for a half period or more than a half period before ions can reach

to the shock front and become reflected ions. As a result, there is an uncertainty on the reflected velocity $\mathbf{V}^r$ shown in Figure 3.51. Due to the thermal spread and the temporal variation of the ramp field, some of the incident ions may never reach to the upstream to become reflected ions. Note that there should be another pitch-angle scattering, which is similar to the change from $\mathbf{V}_1$ to $\mathbf{V}^i$, as reflected ions across the shock front to the upstream side. However, since there are enough uncertainties on the orientation of $\mathbf{V}^r$ as described above, further detail modeling on the changes of $\mathbf{V}^r$ seems unnecessary. Thus, for simplicity, the final pitch-angle scattering on $\mathbf{V}^r$ has been ignored in the above discussion and in Figure 3.51.

(3) The third step of the gyro-reflection process is characterized by a motion with initial velocity $\mathbf{V}^r$ gyrating around the upstream magnetic field $\mathbf{B}_1$. The final distribution of the reflected ions strongly depends on the orientation of $\mathbf{V}^r$ with respect to $\mathbf{B}_1$. For the two cases shown in Figure 3.51, the angle between $\mathbf{V}^r$ and $\mathbf{B}_1$ is about 90° in panel (*a*), but much smaller than 90° in panel (*b*). As a result, most of the reflected ions in panel (*a*) will reenter the shock ramp before they can complete one period of gyration around $\mathbf{B}_1$. On the other hand, the large parallel field velocity component shown in panel (*b*) implies that most of the reflected ions will continuously gyrate around $\mathbf{B}_1$ for several periods before being scattered back by locally generated nonlinear waves, which will be shown later in detail. Thus, reflecting ions distribution along the shock normal will have a narrow spatial extent for the case shown in panel (*a*), but a very long spatial extent for the case shown in panel (*b*). One can also expect to observe a secondary ion beam or multiple ion beams [*Gosling et al.*, 1989*b*; *Lyu and Kan*, 1990] downstream from the shock front for the case shown in panel (*a*), but gyrating ion distributions [*Gosling et al.*, 1982] upstream from the shock front for the case shown in panel (*b*).

It may be noted that although $\alpha \approx 180°$ ramp field can be found in the $M_A = 4$ shock simulation, no highly field-aligned reflected ion distribution has been found upstream from the shock front in the $M_A = 4$ shock simulation. The absence of highly field-aligned ion reflections in $M_A = 4$ shock indicates that the pitch-angle scattering discussed in the first step of gyro-reflection model is weak in the $M_A = 4$ shock. A weak pitch-angle scattering lead to a smaller pitch angle between $\mathbf{V}^r$ and $\mathbf{B}^*$. As a result, for $\alpha \approx 180°$, the highly field aligned $\mathbf{V}^r$ will bring the incoming ions into deep shock ramp so that the ions cannot gyro-reflect back to the shock front during the second step of the gyro-reflection as discussed above. Thus, the amount of pitch angle scattering discussed in step one is very important to determine if an ion can be reflected by the ramp field or not.

The proposed gyro-reflection model has successfully provided an explanation on the simulation results shown in Figures 3.37–3.39. Further evidence of the gyro-reflection processes is given in Figure 3.52. Figure 3.52 shows scatter plots of ion distributions of reflected ions and incoming upstream ions in the v_x-v_z space (the upper panels) and v_y-v_z space (the lower panels) obtained in the $M_A = 6$ shock simulation at different times as indicated. The phase angle of the ramp field at $t\Omega_{ni} = 39$, 42, and 44 are approximately $\alpha \approx 180°$, 270° and 0°. As we can see, the velocity-space distribution of the reflected ion beam varies with the variation of α. The gyro-reflection model may be the only model which allowed the reflected ion velocity direction to depend on the ramp field direction as shown in Figure 3.52. Neither specular reflection model [*Gosling et al.*, 1982] nor the adiabatic reflection model [e.g., *Sonnerup*, 1969; *Paschmann et al.*, 1980] can explain the simulation results shown in Figure 3.52, or to explain the physical process of the reflect-reentering ion reflection event and the highly field-aligned ion reflection event at the same time. The ion reflection process

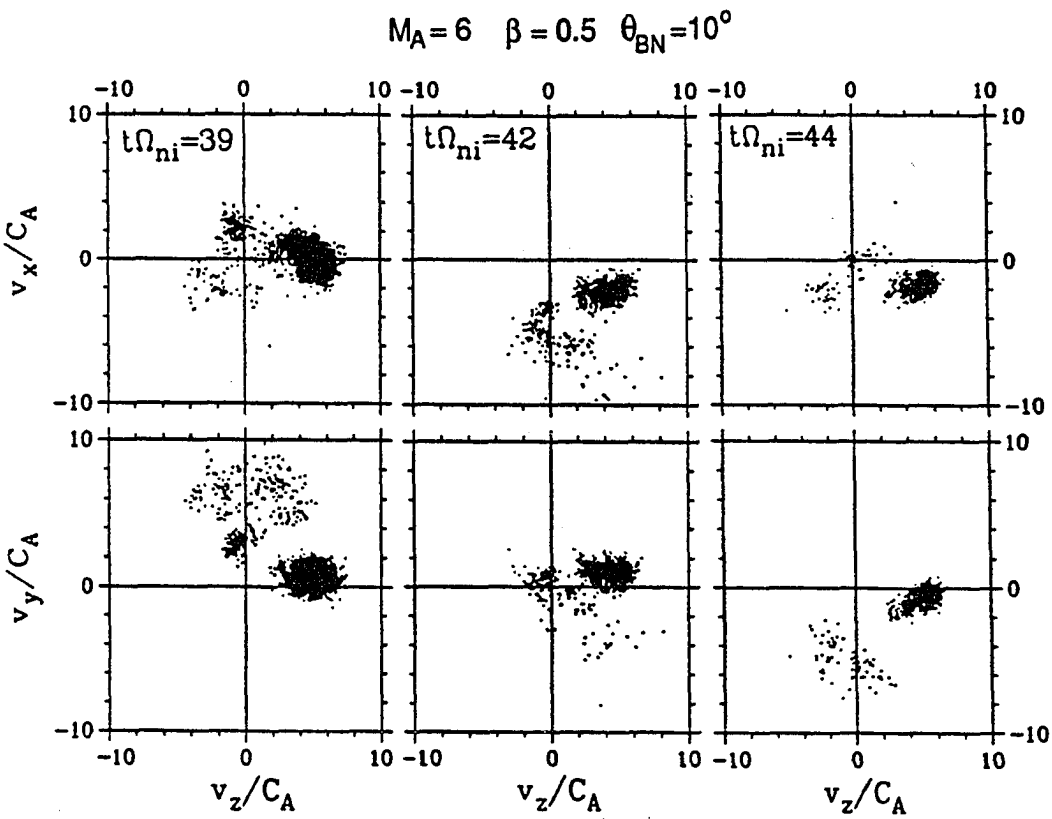

Figure 3.52 Scatter plots of ion distribution of reflected ions and incoming upstream ions in the v_x-v_z space (the upper panels) and v_y-v_z space (the lower panels) obtained in the $M_A = 6$ shock simulation at $t\Omega_{ni} = 39$, 42, and 44. Ions plotted at $t\Omega_{ni} = 39$ are groups 11–14 ions located at $z = 94$–$101.5\ c/\omega_{pi}$. Ions plotted at $t\Omega_{ni} = 42$ are groups 13–15 ions located at $z = 100$–$102\ c/\omega_{pi}$. Ions plotted at $t\Omega_{ni} = 44$ are groups 14–15 ions located at $z = 100$–$102.2\ c/\omega_{pi}$. The phase angle of the ramp field at $t\Omega_{ni} = 39$, 42, and 44 are approximately $\alpha \approx 180°$, 270° and 0°.

proposed by our model strongly depends on the orientation of the ramp field, the curvature of the magnetic field line across the shock front, and the gyro radius of the incoming upstream ions (which is about the same as the ion inertial length in the high Mach number fast shocks). Note that the importance of the magnetic force in the ion reflection process has also been discussed before in literature [*Leroy et*

al., 1981; *Leroy et al.*, 1982; *Leroy*, 1983] for ion reflections in quasi-perpendicular shocks. Unfortunately, the theoretical model proposed by *Leroy* [1983] is apparently not applicable to the ion reflection events observed in the quasi-parallel shocks, because there is no self-consistent "constant-profile" solution for the ramp field and the reflected ion distribution. The ramp-field and the ion reflection events in the quasi-parallel shock have never reached to a "time-independent" steady state. The entire shock transition region of the high Mach number quasi-parallel shock is in a dynamic equilibrium state. Indeed, even for perpendicular and quasi-perpendicular shocks, a dynamic equilibrium state has been found between the shock ramp and foot region by simulation studies of *Lembege and Dawson* [1986, 1987] and recently reported by *Liu and Quest* [1990]. Thus, the gyro-reflection model may be applicable to all the ion reflections observed in various collisionless shocks and discontinuities.

3.5 Summary — Three Critical Mach Numbers for Quasi-Parallel Shocks

Three critical Mach numbers will be proposed in this section to synthesize the Mach number dependence in quasi-parallel collisionless fast shocks.

Various types of critical Mach numbers have been introduced theoretically and experimentally to show the Mach number dependence on the shock wave structures. Ion-reflection critical Mach number defined based on the presence of ion reflections is the most commonly used critical Mach number in collisionless shock studies. For quasi-perpendicular shocks, a laminar shock structure can be found when an upstream Mach number is less than the ion-reflection critical Mach number; whereas a turbulent shock with foot and overshoot structures can be found when an upstream Mach number is greater than the ion-reflection critical Mach number. Critical Mach numbers obtained

from various theoretical models have been reviewed by *Kennel et al.* [1985]. For instance, using a dissipative MHD model, *Coroniti* [1970] showed that theoretically there is a critical Mach number to distinguish resistive shocks from viscous shocks. Above the critical Mach number the classical resistivity alone can no longer provide enough dissipation to balance the nonlinear steepening. A viscosity term in classical form is needed to add into his model to provide enough dissipation for a steady shock wave. If we consider ion reflection as a form of viscous dissipation, the critical Mach number defined by *Coroniti* [1970] may be comparable to the ion-reflection critical Mach number as defined in the conventional way. However, anomalous dissipations in collisionless shocks are different from the classical ones used by *Coroniti* [1970]. The critical Mach number obtained by *Coroniti* [1970] is consistently lower than the ion-reflection critical Mach number determined from the observations or hybrid simulations. Another well-known critical Mach number is the foreshock critical Mach number, which was introduced by *Kennel et al.* [1985]. The foreshock critical Mach number is obtained based on the ion leakage model proposed by *Edmiston et al.* [1982], in which large amplitude waves and the overshoot magnetic field in the shock transition region are ignored. Above the foreshock critical Mach number, leakages of downstream hot ions are expected to be found upstream from the shock front. For quasi-parallel shocks the foreshock critical Mach number is close to the critical Mach number introduced by *Coroniti* [1970]. Ion reflection in quasi-parallel shocks apparently has been ignored in the study of critical Mach numbers by *Kennel et al.* [1985], because there is no curve drawn for ion-reflection critical Mach number in the quasi-parallel shock region in Figure 16 in *Kennel et al.* [1985].

Table 3.2 Three critical Mach numbers for quasi-parallel shocks.

Critical Mach Number	Definition	
M_{C1}	$\left(\frac{V_{th}}{V_D}\right)_{\text{Downstream ion}} < 1$, if $M_A < M_{C1}$; $\gtrsim 1$, if $M_A \geq M_{C1}$	Ion-Leakage Critical Mach Number
M_{C2}	Absence / Presence of reflect-reentering ion reflection events, if $M_A < M_{C2}$ / if $M_A \geq M_{C2}$	Ion-Reflection Critical Mach Number
M_{C3}	Absence / Presence of highly field-aligned ion reflection events, if $M_A < M_{C3}$ / if $M_A \geq M_{C3}$	CSFRR Critical Mach Number

CSFRR: Cyclically Shock-Front Reformation-and-Retreat

V_{th} : Ion thermal velocity V_D : Ion drift velocity in the de Hoffman-Teller frame

From the simulation results shown in Section 3.3, we propose three critical Mach numbers for quasi-parallel fast shocks as listed in Table 3.2.

The first critical Mach number, M_{C1}, is determined based on the presence of a large number of leakage ions from the downstream side. Thus, the first critical Mach number will be called *ion-leakage critical Mach number*. The ion-leakage critical Mach number may be roughly estimated from the Rankine-Hugoniot jump conditions. Namely, when the downstream ion thermal speed is less than the downstream flow speed in the de Hoffman-Teller frame, the upstream Mach number is then less than the ion-leakage critical Mach number. The magnitude of the ion-leakage critical

Mach number is similar to the critical Mach number proposed by *Coroniti* [1970] and the foreshock critical Mach number proposed by *Kennel et al.* [1985] for quasi-parallel shocks. The difference between the foreshock critical Mach number and the ion-leakage critical Mach number is that for simplicity, the upstream magnetic field orientation has been ignored in determining the ion-leakage critical Mach number in our model.

The second critical Mach number, M_{C2}, is determined based on the presence of ion reflection at the shock front. Thus, it will be called *ion-reflection critical Mach number*. Above the second critical Mach number, ion reflection events can be found at the shock front, especially the reflected-reentering type of ion reflection events. Note that the second critical Mach number is determined based on simulation results or observations. The theoretical model which used to determine the ion-reflection critical Mach number in quasi-perpendicular shocks [e.g., *Kennel et al.*, 1985] is apparently not applicable to the quasi-parallel shocks.

The gyro-reflection model proposed in Section 3.4 indicates that highly field-aligned ion reflection events can only be found in very high Mach number quasi-parallel shocks. Thus, above the ion-reflection critical Mach number, there must be a third critical Mach number, M_{C3}, for quasi-parallel collisionless fast shocks, above which highly field-aligned ion reflections can occur at the shock front. Observed gyrating ion distributions just upstream from the shock front [*Gosling et al.*, 1982] are expected to be found when M_A is greater than M_{C3}. The highly field-aligned ion reflections can lead to reformation and retreat of the shock ramp on the spatial profiles of B_x, B_y, B, and V_z. Since the highly-field aligned ion reflection events and the reflected-reentering ion reflection events appear alternately at the shock front when the shock Mach number is greater than the third critical Mach number, cyclically shock

Table 3.3 Summary of simulation results.
Quasi-parallel shocks with upstream $\theta_{BN} = 10°$ and $\beta = 0.5$

Mach Number	$\left(\frac{V_{th}}{V_D}\right)$ Downstream ion	Ion Leakage	Ion Reflection	
$M_A = 1.2$ $M_A < M_{C1}$	~ 0.5	—	—	—
$M_A = 2$ $M_{C1} < M_A < M_{C2}$	~ 1	Shock Front v_z z	—	—
$M_A = 4$ $M_{C2} < M_A < M_{C3}$	~ 1.5	Leakage ion distribution in v_x-z space	Yes	—
$M_A = 6$ $M_{C3} < M_A$	~ 2	Shock Front	Yes	Yes

front reformation and retreat can be found when the shock Mach number is greater than M_{C3}. Thus, the third critical Mach number will be called *cyclically shock-front reformation-and-retreat critical Mach number.*

The Mach number dependence on nonlinear wave structures, leakage ion distributions, reflected ion behaviors, and ion heating processes in quasi-parallel collisionless fast shocks can be discussed based on the simulation results obtained in this chapter as summarized in Table 3.3.

Table 3.3 (Continued)

Mach Number	Magnetic Field Structure	Large-Amplitude Waves in		Cyclically Shock-Front		
				Reformation		Retreat
		USTR	DSTR	B	V_z	
$M_A = 1.2$	Shock Front 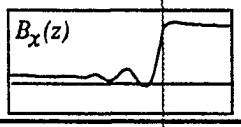	—	—	—	—	—
$M_A = 2$	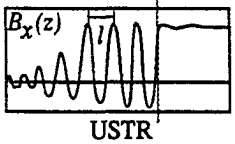	Phase-Standing $l \approx 6\ c/\omega_{pi}$ PPA$\approx 2B_0$	—	—	—	—
$M_A = 4$	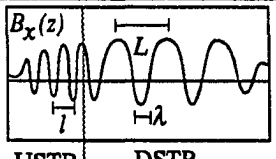	Intermittent $l \approx 3\ c/\omega_{pi}$ PPA $\approx 4\ B_0$	$\lambda \approx 2\ c/\omega_{pi}$ $L \approx 7\ c/\omega_{pi}$	Yes	—	—
$M_A = 6$	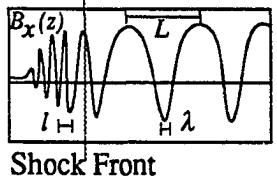	Intermittent $l \approx 1.5\ c/\omega_{pi}$ PPA $\approx 6\ B_0$	$\lambda \approx 1\ c/\omega_{pi}$ $L \approx 9\ c/\omega_{pi}$	Yes	Yes	Yes

USTR: Upstream Shock Transition Region

DSTR: Downstream Shock Transition Region

PPA: Peak-to-Peak Amplitude

For an upstream Mach number less than the first critical Mach number (i.e., the ion-leakage critical Mach number), the number of leakage ions upstream from shock front are so small that they can be ignored. No large-amplitude upstream waves can be found upstream from shock front with an amplitude as large as the shock ramp. As a result, shock waves with an upstream Mach number less than the first critical Mach

number are laminar shocks. The $M_A = 1.2$ fast shock studied in Section 3.3.1 is an example of this type of quasi-parallel shock.

For an upstream Mach number greater than the ion-leakage critical Mach number, such as the $M_A = 2$, 4, and 6 shocks, a large number of leakage ions can be found upstream from the shock front. The characteristics of the leakage ions depend on the nonlinear wave structures in the extended shock transition region; whereas the structure of nonlinear waves in the shock transition region strongly depend on the presence of ion reflections at the shock front. Thus, the distribution of leakage ions in a shock with an upstream Mach number less than the ion-reflection critical Mach number (such as the $M_A = 2$ shock) is different from the distribution of leakage ions in a shock with an upstream Mach number greater than the ion-reflection critical Mach number (such as the $M_A = 4$ and 6 shocks).

The $M_A = 2$ shock is an example of quasi-parallel shocks in which the upstream Mach number is greater than the ion-leakage critical Mach number but less than the ion-reflection critical Mach numbers. No ion reflections but a large number of leakage ions can be found upstream from shock front to form an upstream shock transition region. The large amplitude waves can confine most of the leakage ions in the upstream shock transition region. The leakage ion density is high (10%–15% of the upstream ion density) in the upstream shock transition region, but very low ($\sim$ 1% of the upstream ion density) upstream from the upstream shock transition region. Pitch angle scatterings by the large amplitude waves in the upstream shock transition region slow down the incoming upstream flow and slightly heat up the beam ion distribution. The major ion heating of the incoming upstream ions takes place at the shock front. As discussed in Figure 3.4*d*, a sharp turn on the magnetic field line can heat up the incoming ions efficiently if the incoming ions have been preheated slightly by other

mechanism. Thus, the slightly preheating and slowing down of upstream flow speed in the upstream shock transition region may play an important role for an efficient ion heating at the shock front.

For an upstream Mach number greater than the ion-reflection Mach number (e.g., the $M_A = 4$ and 6 shocks), cyclic ion reflection events at the shock front can generate large amplitude hydromagnetic waves with phase speed less than the local ion normal flow speed. These waves are blown back to the downstream and form a downstream shock transition region. The backstreaming downstream hot ions have to pass through the downstream shock transition region before they leak across the shock front. The scale length of these nonlinear waves in the downstream shock transition region varies from 1 c/ω_{pi} at $\alpha \approx 180°$ to 5 c/ω_{pi} at $\alpha \approx 0°$, where α is the phase angle of the nonlinear waves defined in Section 3.3.4. The equivalent scale lengths λ and L of these nonlinear waves in the downstream shock transition region in Table 3.3 satisfy the condition of $\lambda \ll L$ for ion heating due to nonadiabatically pitch-angle scattering as discussed in Figure 3.4*c*. Both incoming ions from upstream and backstreaming ions from downstream will interact with the nonlinear waves, especially in the region of $90° < \alpha < 270°$. The leakage ions gain tangential component streaming kinetic energy as they backstream through the downstream shock transition region and then convert the streaming kinetic energy into thermal energy when they leak across the shock front to result in a suprathermal backstreaming ions on the upstream side. Note that the temperature of the leakage ions in the upstream shock transition region in the $M_A = 2$ shock is about the same as the temperature of the downstream ions. However, the temperature of the upstream suprathermal backstreaming ions in the $M_A = 4$ and 6 shock simulations is about 10 times higher than the downstream ion temperature. There is no phase-standing whistler waves in the $M_A = 4$ and 6 shocks

to block the backstreaming motions of the leakage ions upstream from the shock front. No additional leakage ion density jump can be found in the of $M_A = 4$ and 6 shock simulations. However, the leakage ion density has already been reduced by the large amplitude waves in the downstream shock transition region. The leakage ion density upstream from the shock front is about 3% of the upstream ions density in the $M_A = 4$ shock which is much lower than the leakage ion density estimated based on the model proposed by *Edmiston et al.* [1982].

Ion reflection event in a reflect-reentering manner (e.g., ion reflection events shown in Figures 3.26 and 3.39) can be found when the upstream Mach number is greater than the ion-reflection critical Mach number (the second critical Mach number). The average shock front location remains unchanged during the reflected-reentering ion reflection event. Although the magnetic field structure at the shock front varies before, during, and after a reflect-reentering ion reflection event, the gradient of the normal velocity profile at the shock front apparently is not affected by the reflect-reentering ion reflection. The reflect-reentering ions can lead to multiple ion bunches downstream from the shock front. The heating (i.e., smear-out the multiple ion bunches) is complete by the nonlinear waves in the downstream shock transition region, where $\lambda \ll L$. A small number of the shock-heated ions can join the backstreaming downstream hot ions and then leak across the shock front to form suprathermal backstreaming ions on the upstream side.

The highly field-aligned ion reflection can be found when the upstream Mach number is greater than the third critical Mach number. The highly field-aligned ion reflection can lead to over dissipation at the shock front. The shock front drifts backward during each of the highly field-aligned ion reflection events. The interaction between the lengthy reflected ion beam and the incoming upstream ion beam can result

in two-stream instability. Nonlinear short wavelength waves (not a whistler mode) generated by the two-stream instability can lead to multiple ion reflection upstream from the shock front and bring the highly field-aligned reflected ions back to the shock front. Strong ion heating can be found at the shock ramp when the reflected ions gyrate back to the shock front. After heating up, some of the ions continue their journey to the downstream side, some of them reenter the upstream side and become suprathermal shock-front-heated leakage ions.

For an upstream Mach number in between the second and third critical Mach numbers, such as the $M_A = 4$ shock, only reflected-reentering type of ion reflections can be found at shock front. Cyclic magnetic shock-ramp reformation can be found in this type of shock, but the average position of the shock ramp remains unchanged. A small number of shock-heated leakage ions and a large number of downstream leakage ions are the source of the suprathermal backstreaming ions on the upstream side in the $M_A = 4$ shock simulation.

For an upstream Mach number greater than the third critical Mach number, such as the $M_A = 6$ shock, reflected-reentering ion reflection events and highly field-aligned ion reflection events appear alternately at the shock front. A large number of downstream leakage ions, shock-heated leakage ions and shock-front-heated leakage ions are the source of the suprathermal backstreaming ions on the upstream side in the $M_A = 6$ shock simulation, where the shock-heated ions are the transmitted and the reflected ions with heating complete in the downstream shock transition region. Strong shock front reformation can be found in both magnetic field profile and the normal flow velocity profile. The average position of the shocks front drifts backward during each of the highly field-aligned ion reflection events, but the average location of the shock front remain unchanged during the reflected-reentry reflection events. As a result,

a less steady shock front can be found when the upstream Mach number is greater than the third critical Mach number. The characteristics of super-third-critical Mach number quasi-parallel shocks can explain the simulation results obtained by Dr. Mark Mandt (private communication) in his Ph.D. thesis work that the average shock-front position always drift back to the downstream side in quasi-parallel shock simulations with $M_A \geq 6$. As a result, he has to put the initial shock front close to the upstream boundary in the very high Mach number shock simulation. On the other hand, with similar nonlinear wave structures in the shock transition region, the position of the shock front is almost unchanged after shock ramp is fully developed in the $M_A = 4$ shock simulation.

The structures of observed quasi-parallel shocks also shows Mach number dependence similar to the simulation results obtained in this chapter. Figures 3.53–3.55 show three low Mach number quasi-parallel shock observations. Figures 3.56 and 3.57 show two high Mach number quasi-parallel shock observations. As we can see, large amplitude whistler waves can be found upstream from the shock front in the observed low Mach number quasi-parallel shocks, whereas large amplitude nonlinear waves can be found downstream from the shock front in the observed high Mach number quasi-parallel shocks. The observed shock structure is consistent with the proposed Mach number dependence given in this section. Note that the large amplitude nonlinear waves structure in the downstream shock transition region may not be a plane wave if we consider the possibility that the occurrence of the intermittent ion reflection event may also be patchy on the shock front surface. As a result, the nonlinear waves will be generated at different locations on the shock front surface at different times. The patchy and intermittent generation of nonlinear waves will lead to a highly turbulent

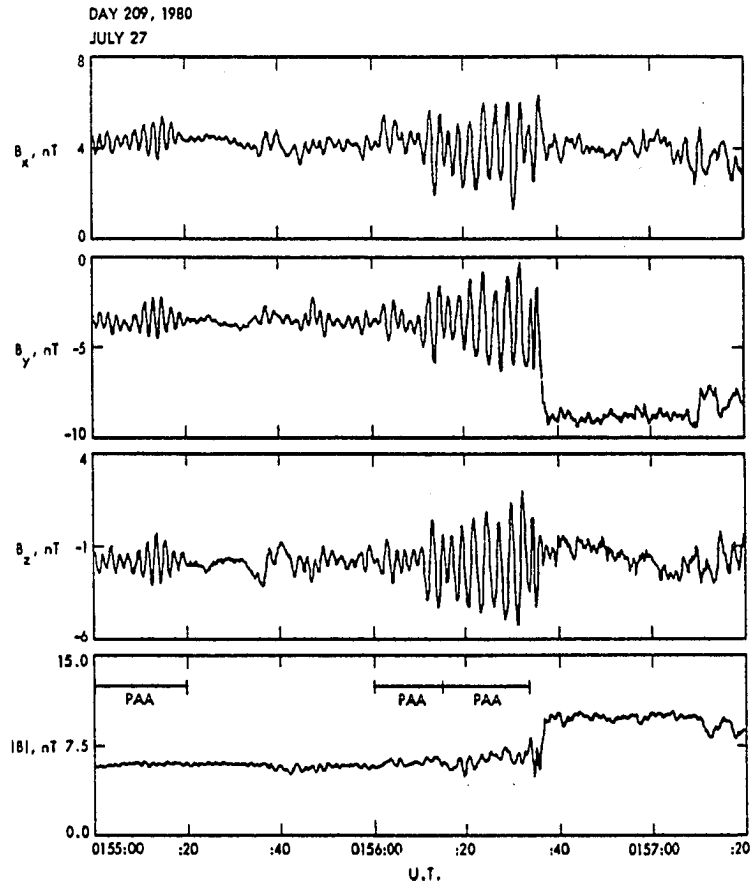

Figure 3.53 ISEE-3 observation of a low Mach number quasi-parallel shock. [after *Tsurutani et al.*, 1983].

chaotic wave structure as observed in the high Mach number shocks shown in Figures 3.56–3.57.

It may be noted that *Kennel et al.* [1985] also suggested that there might be a third critical Mach number ($\approx$ 12–13) for quasi-perpendicular shocks, above which ion reflection cannot provide all the needed dissipation and the shock will become an unsteady ion reflection shock [e.g., *Leroy et al.*, 1982]. The connection between the third critical Mach number of quasi-parallel shocks and the third critical Mach number

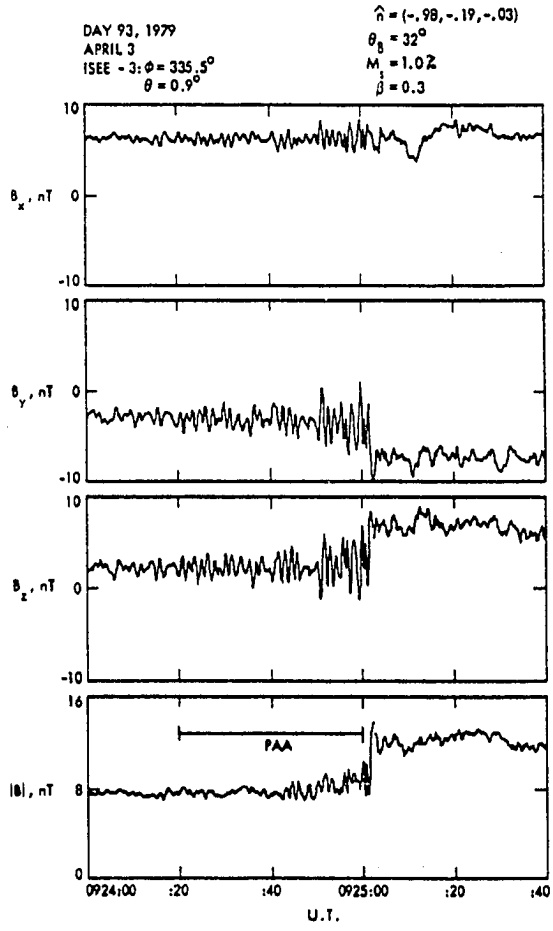

Figure 3.54 ISEE-3 observation of a low Mach number quasi-parallel shock. [after *Tsurutani et al.*, 1983].

of quasi-perpendicular shocks [*Kennel et al.*, 1985] is not clear and will not be studied in this thesis.

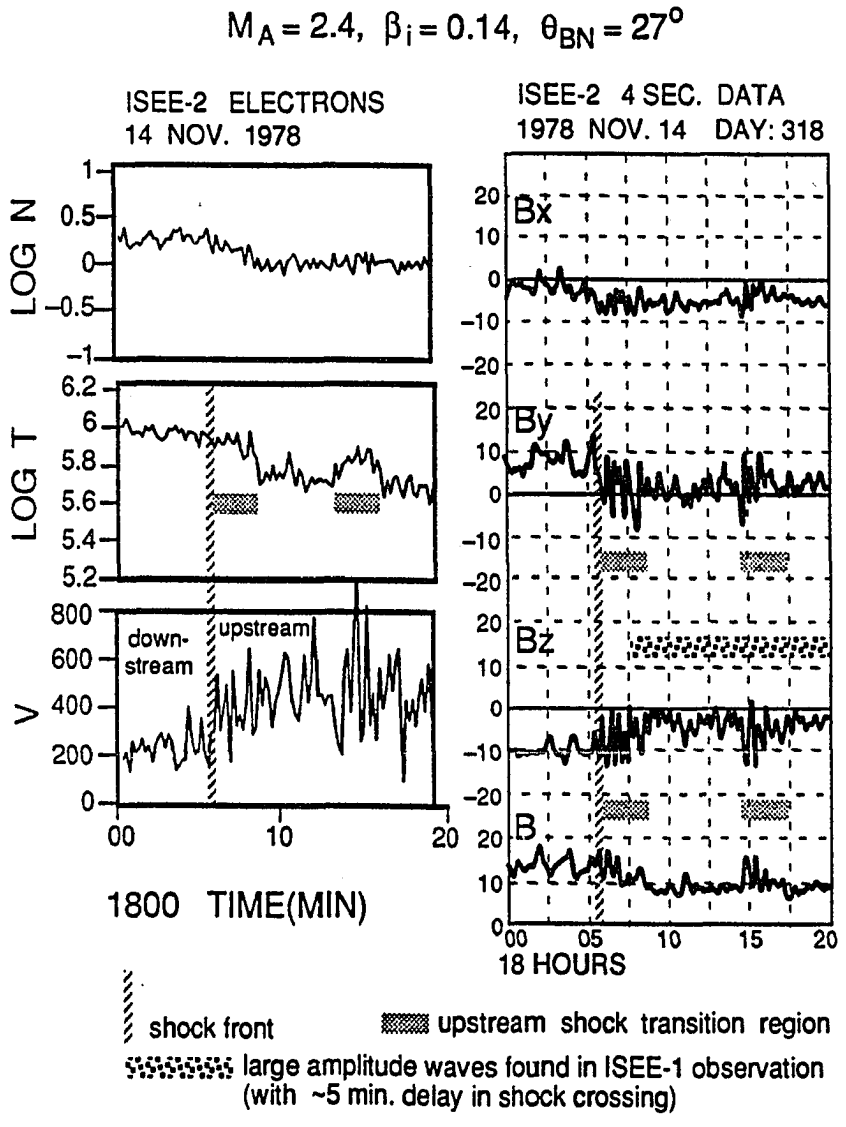

Figure 3.55 ISEE-2 observation of a low Mach number quasi-parallel shock. (Obtained from distributed observational data for the 1988 Los Alamos workshop on quasi-parallel shocks.)

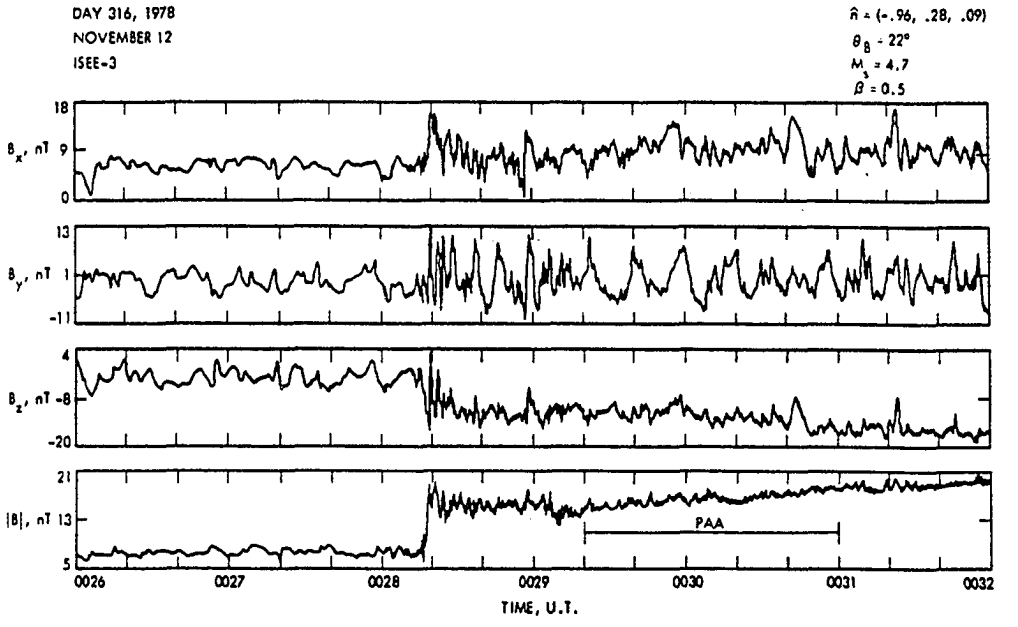

Figure 3.56 ISEE-3 observation of a high Mach number quasi-parallel shock. [after *Tsurutani et al.*, 1983].

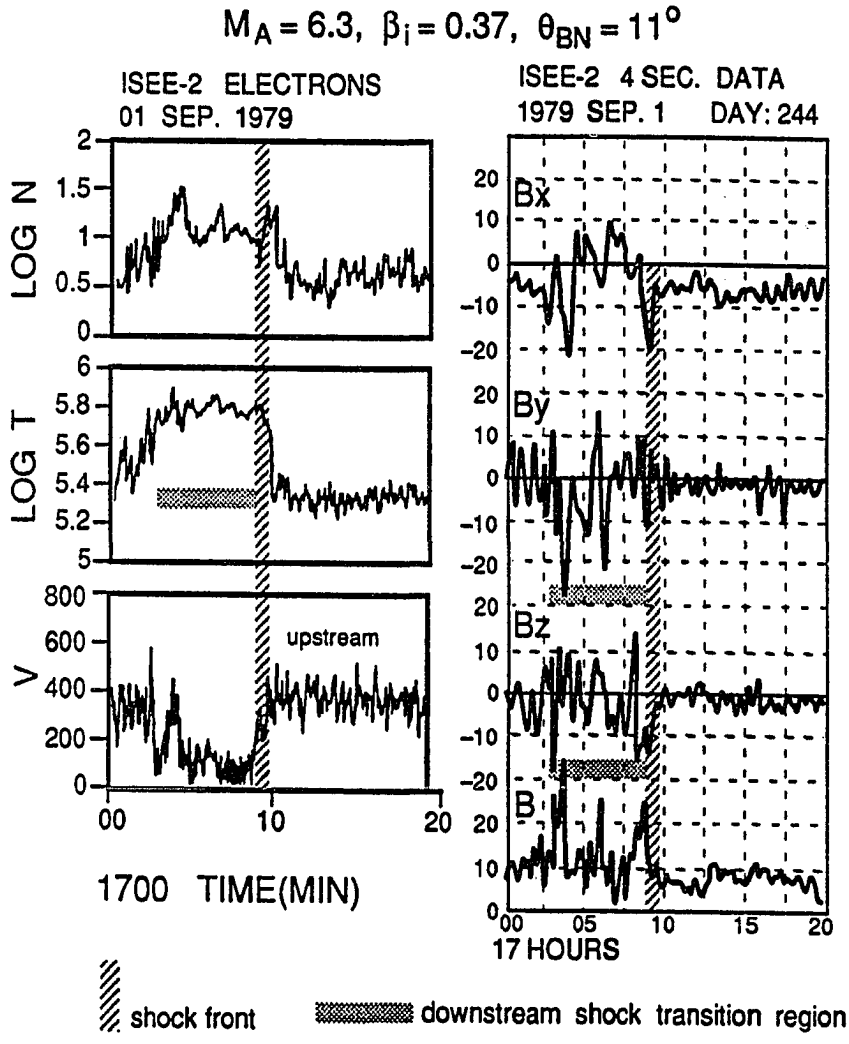

Figure 3.57 ISEE-2 observation of a high Mach number quasi-parallel shock. (Obtained from distributed observational data for the 1988 Los Alamos workshop on quasi-parallel shocks.)

Chapter 4

Simulation Study of Rotational Discontinuities, Switch-off Shocks, and Intermediate Shocks in Collisionless Plasmas

4.1 Introduction

Structures of rotational discontinuities, switch-off shocks, and intermediate shocks will be studied in this chapter by means of numerical simulations. According to the Rankine-Hugoniot jump conditions, the upstream normal flow speed of rotational discontinuities and switch-off shocks is equal to the upstream Alfvén mode speed; whereas the upstream normal flow speed of intermediate shocks is slightly greater than the Alfvén mode speed. Intermediate shock solution curves for upstream plasma $\beta = 0.5$, shock normal angle $\theta_{BN} = 0°$, 20°, and 45° have been shown Figure 1.4, where the shock normal angle θ_{BN} is the acute angle between the shock normal direction and the upstream magnetic field direction. According to Figures 1.4*b* and 1.4*c*, one end of the solution curve connects to the rotational discontinuity solution and the other end of the solution curve connects to the switch-off shock solution. The rotational discontinuity (RD) solution is a neighboring solution of the Alfvén shock solution, and a switch-off shock solution is a neighboring solution of the Alfvén-slow shock solution. Thus, by studying the behavior of RDs and switch-off shocks, it may help us to understand the behavior of intermediate shocks. This is the reason why we choose to study the three different subjects (RDs, switch-off shocks, and intermediate shocks) together in this chapter.

Rotational discontinuities have been studied analytically in Chapter 2 of this thesis, where various types of rotational structures are obtained analytically based on the pseudopotential method and the multiple pseudopotential method. However, analytical solutions obtained in Chapter 2 do not provide information about how these rotational structures are formed. Section 4.3 will explore the formation of several types of rotational structures obtained in Chapter 2 under different initial conditions.

Switch-off shock is the strongest slow shock for a given upstream shock normal angle and upstream plasma beta. Hybrid simulation studies of slow shocks have been carried out by *Swift* [1983], *Winske et al.* [1985], *Lee et al.* [1989*b*], *Omidi and Winske* [1989]. In early simulation studies [*Swift*, 1983; *Winske et al.*, 1985], large-amplitude, left-hand polarized nonlinear waves are found on the downstream side of the slow shock, which are consistent with the theoretical prediction of slow shock structures given by *Coroniti* [1971]. Since slow-mode shocks observed in the distant geomagnetic tail and in the plasma sheet boundary layer [e.g., *Feldman et al.*, 1984, 1985, 1987] do not show large amplitude rotational wavetrains on the downstream side as predicted by *Coroniti* [1971], simulation studies of slow shocks have been carried out to look for slow shocks without large amplitude wavetrains on the downstream side [e.g., *Lee et al.*, 1989*b*; *Omidi and Winske*, 1989]. *Lee et al.* [1989*b*] showed that by slightly reducing the upstream flow speed, a sub-Alfvénic, non-switch-off slow shock may appear with no large amplitude rotational wavetrains on the downstream side. *Omidi and Winske* [1989] showed that if the upstream flow speed is subsonic and the ratio of electron to ion temperature is large, a large amplitude wavetrain is observed. On the other hand if the flow is supersonic, or T_e/T_i is small, no wavetrain is associated with the shock. Switch-off shocks will be studied in Section 4.4 based on

hybrid simulations. This study will explore a different physical mechanism to explain the absence of downstream wavetrains in some of the observed switch-off shocks.

Intermediate shocks have been introduced and discussed in Table 1.1 and Section 1.1.3. Alfvén shocks are one type of intermediate shocks. Alfvén shocks have been studied based on MHD simulations [*Wu*, 1987, 1988*a*,*b*], two-fluid simulations [*Lyu and Kan*, 1989*a*], and hybrid simulations [*Lee et al.*, 1989*a*]. Both MHD simulations and two-fluid simulations show that Alfvén shocks can exist with a relatively stable structure. However, *Lee et al.* [1989*a*] found that Alfvén shocks are unstable in the hybrid code simulations. In this study, the Alfvén shock and other intermediate shocks will be reexamined based on hybrid simulations. To obtain a stable Alfvén shock, the simulation system length used in this study is much longer than the one used in previous study by *Lee et al.* [1989*a*]. The simulation system length used in our study is determined by the length of shock transition region obtained from two-fluid simulation studies. The simulation results obtained from the hybrid code simulations are similar to those obtained from the two-fluid simulations except for the shock-preheating due to leakage ions that occurs in the hybrid simulation but not in the two-fluid simulations. The structures of Alfvén shocks are found depending on the initial conditions of the shock ramp in the two-fluid simulations [*Lyu and Kan*, 1989*a*]. The evolution of intermediate shocks under different initial conditions will also be studied in Section 4.5.1 using hybrid simulations. Systematic changes among the intermediate shocks, switch-off shocks, and rotational discontinuities will all be discussed.

4.2 Simulation Model

Simulation results shown in this chapter are obtained based on the one-dimensional hybrid simulation code (particle ions and fluid electrons) as used in Chapter 3. Initial conditions and boundary conditions of the hybrid code simulations are similar to the one discussed in Chapter 3. The coordinate system used in the hybrid-code simulations is also the same as the one used in Chapter 3, where the shock normal is along the $-z$ direction. No dissipation term is added in the electron fluid equations in this hybrid code simulation study. Note that an additional dissipation term has been added in previous slow shock simulations by *Lee et al.* [1989*b*] (private communication with Yu Lin), and by *Omidi and Winske* [1989]. Particle labeling diagnostic introduced in Chapter 3 will be used to study the ion leakage and ion reflection processes in the simulated switch-off shocks.

4.3 Rotational Discontinuities

Theoretical study of rotational discontinuities given in Chapter 2 showed that for upstream $C_A > V_{AX}$ (or $\gamma\beta/2 > \cos^2\theta_{BN}$, where $\gamma = 5/3$) the magnetic hodogram is highly circularly polarized for a right-hand polarized RD, but relatively flat for a left-hand polarized RD. On the other hand, for upstream $C_A < V_{AX}$ (or $\gamma\beta/2 < \cos^2\theta_{BN}$) the magnetic hodogram is highly circularly polarized for a left-hand polarized RD, but relatively flat for a right-hand polarized RD.

Rotational discontinuities with upstream $\gamma\beta/2 > \cos^2\theta_{BN}$ have been studied comprehensively by *Swift and Lee* [1983] under different initial conditions. Figure 4.1 shows some of the simulation results obtained by *Swift and Lee* [1983]. The magnetic hodograms in Figure 4.1 are highly circularly polarized for the right-hand polarized

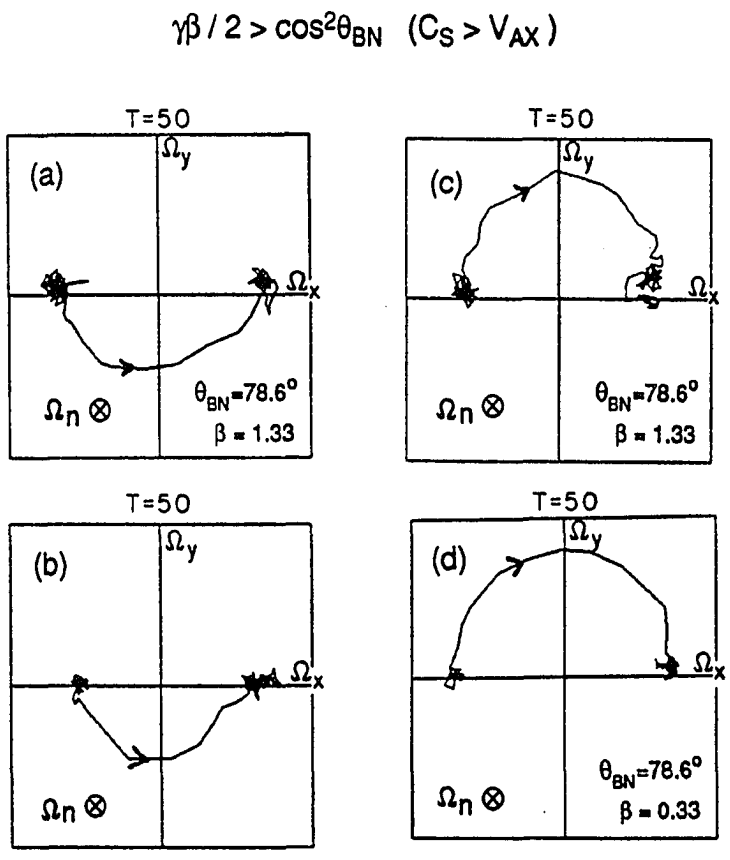

Figure 4.1 Magnetic hodograms of rotational discontinuities with upstream $\gamma\beta/2 > \cos^2\theta_{BN}$ obtained from hybrid simulation [after *Swift and Lee*, 1983]. Magnetic hodograms of the left-hand polarized RDs shown in panels (*a*) and (*b*) are flat. Magnetic hodograms of the right-hand polarized RDs shown in panels (*c*) and (*d*) are highly circular.

RDs in panels (*c*) and (*d*), but relatively flat for the left-hand polarized RDs in panels (*a*) and (*b*).

Rotational discontinuities with upstream $\gamma\beta/2 < \cos^2\theta_{BN}$ have been studied by *Richter and Scholer* [1989] and by *Goodrich and Cargill* [1991] with initial ramp thickness of a few ion inertial lengths (2–4 c/ω_{pi}). Rotational discontinuities with upstream $\gamma\beta/2 > \cos^2\theta_{BN}$ have also been studied by *Richter and Scholer* [1989] and by *Goodrich and Cargill* [1991]. The simulation results obtained by *Richter and*

Scholer [1989] indicate that rotational discontinuities with θ_{BN} greater than about 45° are relatively stable, whereas rotational discontinuities with $\theta_{BN} \leq 30°$ are unstable. These unstable rotational discontinuities disintegrate into waves, leading to an S-shaped magnetic hodogram. At late times of their simulation runs, the transition region of the rotational structure occurs over the entire length of simulation system, which is about 80 c/ω_{pi} [*Richter and Scholer*, 1989]. *Goodrich and Cargill* [1991] showed that by using longer simulation system length of $\sim$ 200 c/ω_{pi} and longer simulation times, the S-shaped magnetic hodogram with large amplitude upstream waves and downstream waves are relatively stable. In addition, when the initial ramp thickness is less than one ion inertial length ($\approx 0.6\ c/\omega_{pi}$), S-shaped RDs with large amplitude downstream waves can also be found in the RD simulations with large θ_{BN} and $\gamma\beta/2 > \cos^2\theta_{BN}$ [*Goodrich and Cargill*, 1991]. In summary, the simulation of rotational discontinuities with $\gamma\beta/2 < \cos^2\theta_{BN}$ obtained in these two studies [*Richter and Scholer*, 1989; *Goodrich and Cargill*, 1991] are characteristically S-shaped structures with large amplitude upstream waves and/or downstream waves. S-shaped rotational structures have also been obtained in the two-fluid simulation study of Alfvén shocks by *Lyu and Kan* [1989*a*]. The Alfvén shock simulation studies show that a highly circularly polarized magnetic hodogram can be found in Alfvén shocks with small θ_{BN} if the initial ramp thickness is wide enough. Since Alfvén shock solutions are neighboring solutions of rotational discontinuity solution as shown in Figure 1.4, similar characteristics shown in the Alfvén shock simulation can be found in the rotational discontinuities. Namely, non-S-shaped rotational discontinuities at small θ_{BN} as predicted in Chapter 2 can be expected to form when the initial ramp thickness is much thicker than the one used in previous simulation studies [e.g., *Richter and Scholer*, 1989; *Goodrich and Cargill*, 1991].

Table 4.1 Rotational Discontinuity Simulations

	Upstream			Initial Polarization		(c/ω_{pi})		
Case	θ_{BN}	β	M_A	B_t	V_t	D_W	L	Δ
G1	30°	0.5	cos30°	L.H.P.	L.H.P.	30	307.2	0.2
G2	30°	0.5	cos30°	R.H.P.	R.H.P.	30	307.2	0.2
G3	30°	0.5	cos30°	L.H.P.	Linear	30	307.2	0.2
G4	30°	0.5	cos30°	R.H.P.	Linear	30	307.2	0.2
G5	30°	0.5	cos30°	L.H.P.	L.H.P.	3	307.2	0.2

D_W: initial ramp thickness. L: simulation system length. Δ: grid size.

Rotational discontinuities with upstream $\gamma\beta/2 < \cos^2\theta_{BN}$ are reexamined in this section. Five examples of rotational discontinuities with upstream plasma $\beta = 0.5$, $\theta_{BN} = 30°$, and $M_A = \cos\theta_{BN}$ will be presented in this section under different initial conditions as listed in Table 4.1. Grid size used in this study is 0.2 c/ω_{pi}. Simulation system length is 307.2 c/ω_{pi}. Rotation angle of the tangential magnetic field across the shock ramp is 180° for all five cases.

Figure 4.2 shows the magnetic hodograms of Cases G1 and G2. The initial ramp thickness used in Cases G1 and G2 is about 30 c/ω_{pi}. A circularly polarized initial tangential magnetic field is used in both cases. The polarization of the tangential magnetic field is left-handed for Case G1, but right-handed for Case G2. The initial flow velocity is anti-parallel to the magnetic field everywhere including the shock transition region. As we can see, the simulation results of the these two cases are consistent with the predictions given in Chapter 2. Namely, a highly circularly left-hand polarized rotational discontinuity is formed in Case G1; whereas, a relatively flat and

right-hand polarized magnetic hodograms is formed in Case G2. Temporal evolution of the spatial profiles of tangential magnetic field, B_x and B_y, is shown in Figures 4.3 and 4.4 for Cases G1 and G2, respectively. The spatial profiles shown in Figure 4.3 and Figure 4.4 indicated that the structure of the two rotational discontinuities Case G1 and Case G2 are very stable with a final ramp thickness slightly less than 30 c/ω_{pi} in Case G1, but much wider than 30 c/ω_{pi} in Case G2.

Figure 4.5 shows the magnetic hodograms of Cases G3 and G4. Initial conditions of Cases G3 and G4 are similar to the initial conditions of Cases G1 and G2, respectively, except that the initial tangential velocity is linearly polarized (i.e., the average ion velocity is in the same plane) across the shock ramp in Cases G3 and G4. Namely, the initial conditions of Cases G3 and G4 are not purely Alfvénic. As a result, the initial tangential electric field is zero on the upstream side and downstream side of the RD, but non-zero at the initial ramp region. A nonlinear fast mode wave is generated at the ramp and propagates downstream as shown in Figures 4.6 and 4.7, where Figures 4.6 and 4.7 plot the spatial profiles of tangential magnetic field, B_x and B_y, at successive times for Cases G3 and G4, respectively. After the fast mode nonlinear wave is detached from the RD structure, which is located at the center of the simulation system, an S-shaped RD structure is formed in both Cases G3 and G4. The structure of the S-shaped RDs can be identified by a half of an inner-loop constant pseudopotential contour and another half of a banana-shaped constant pseudopotential contour as discussed in Chapter 2.

Figure 4.8 shows the magnetic hodograms of Case G5. Figure 4.9 shows tangential magnetic field profiles at successive times obtained in Case G5. Initial conditions of Case G5 are similar to the initial conditions of Case G1 except that a thinner initial ramp with thickness $D_W = 3\ c/\omega_{pi}$ is used in Case G5. The final structure of Case

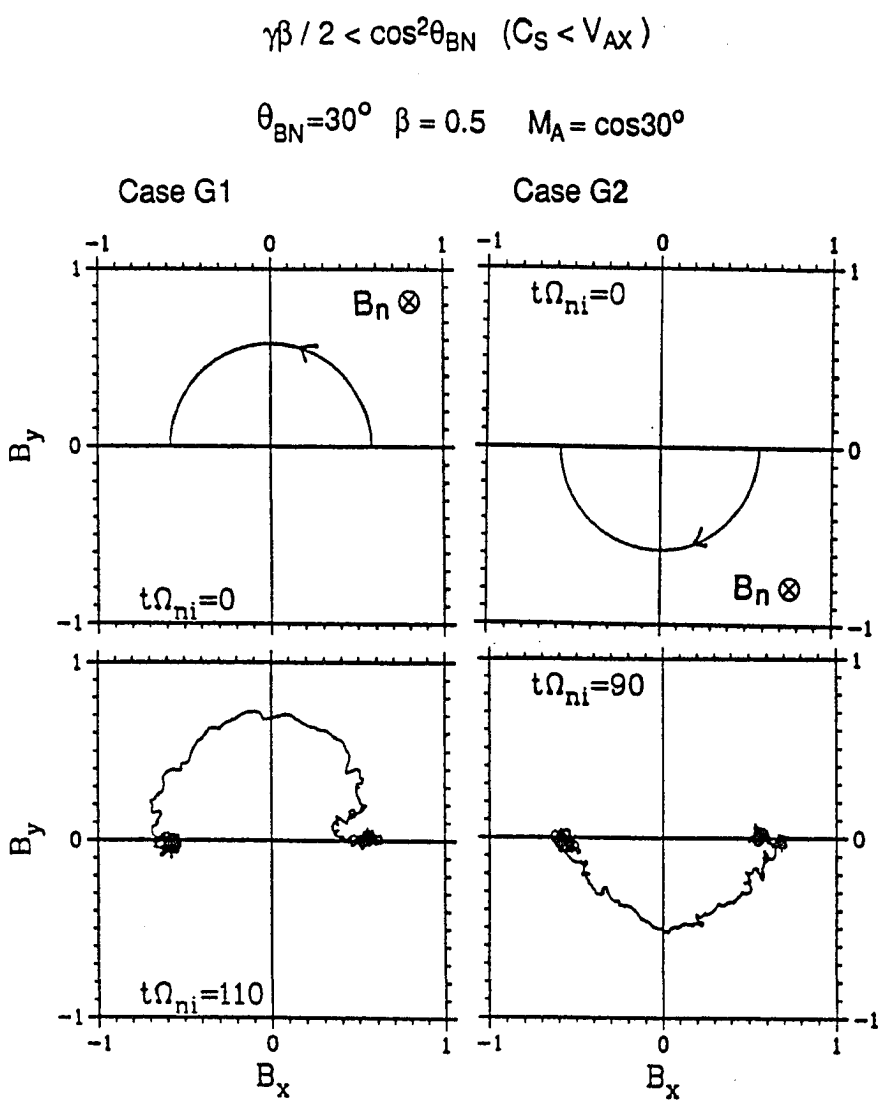

Figure 4.2 Magnetic hodograms of rotational discontinuities Cases G1 and G2 with upstream $\gamma\beta/2 < \cos^2\theta_{BN}$. Hodograms shown in this figure are plotted from $z = 80\ c/\omega_{pi}$ to $z = 240\ c/\omega_{pi}$. Magnetic hodogram of the left-hand polarized RD Case G1 is highly circular. Magnetic hodogram of the right-hand polarized RD Case G2 is relatively flat.

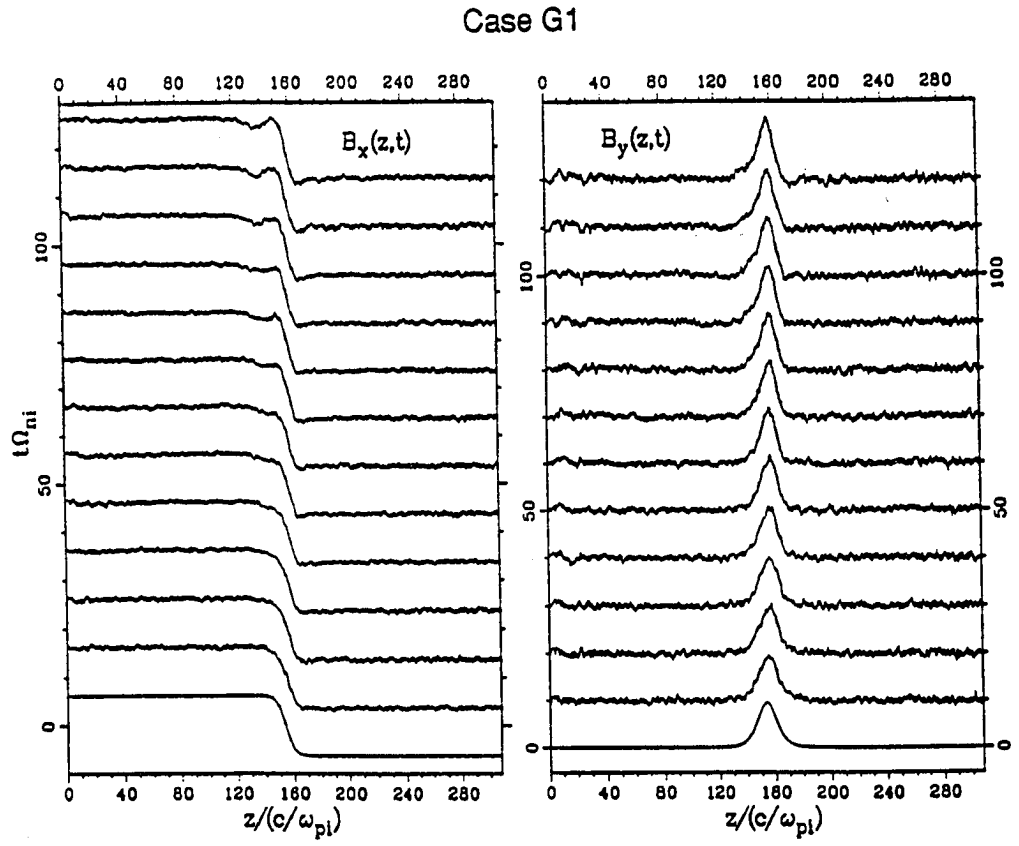

Figure 4.3 Spatial profiles of tangential magnetic field B_x and B_y obtained from Case G1 plotted at successive times. The final ramp thickness is slightly thinner than the initial ramp thickness (30 c/ω_{pi}) in this left-hand polarized RD simulation.

G5 is similar to the one shown in Case G3 but with additional left-hand polarized nonlinear wavetrain on the downstream side. The downstream wavetrain structure is similar to the banana-shaped wavetrain solution discussed in Chapter 2. The banana-shaped wavetrain is apparently dispersed from the over-steepened initial ramp field. Since the initial ramp thickness used in Case G5 is similar to the one used in previous simulation studies by *Richter and Scholer* [1989] and by *Goodrich and Cargill* [1991], simulation result of Case G5 is consistent with the previous simulation results [*Richter and Scholer*, 1989; *Goodrich and Cargill*, 1991].

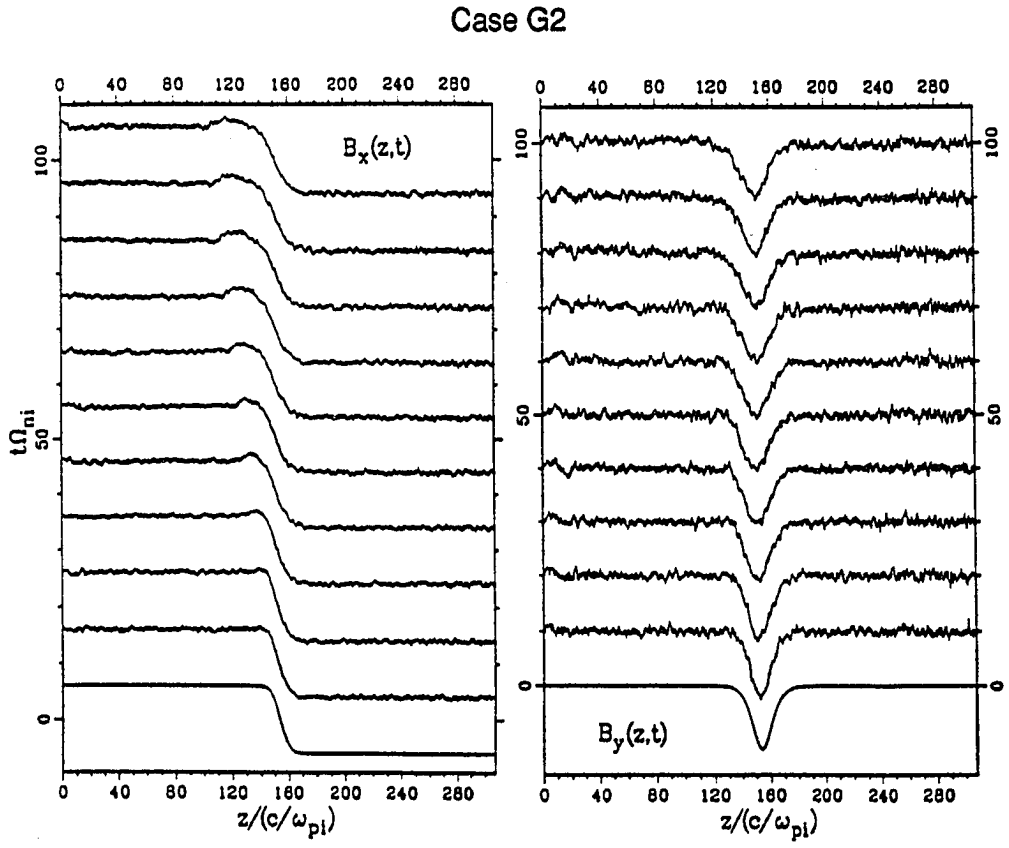

Figure 4.4 Spatial profiles of B_x and B_y obtained from Case G2 plotted at successive times. The final ramp thickness is much thicker than the initial ramp thickness (30 c/ω_{pi}) in this right-hand polarized RD simulation.

In summary, non-S-shaped RDs in plasmas of $C_A < V_{AX}$ (or $\gamma\beta/2 < \cos^2\theta_{BN}$) have been studied in this section using hybrid simulations with initial ramp thickness of a few tens of ion inertial lengths. The final ramp thickness of a right-hand polarized RD is also a few tens of ion inertial lengths, but a few ion inertial lengths for the left-hand polarized RDs. The magnetic hodogram of these RDs is highly circularly polarized for a left-hand polarized RD, but relatively flat for a right-hand polarized RD. These simulation results are consistent with the theoretical predictions given in Chapter 2.

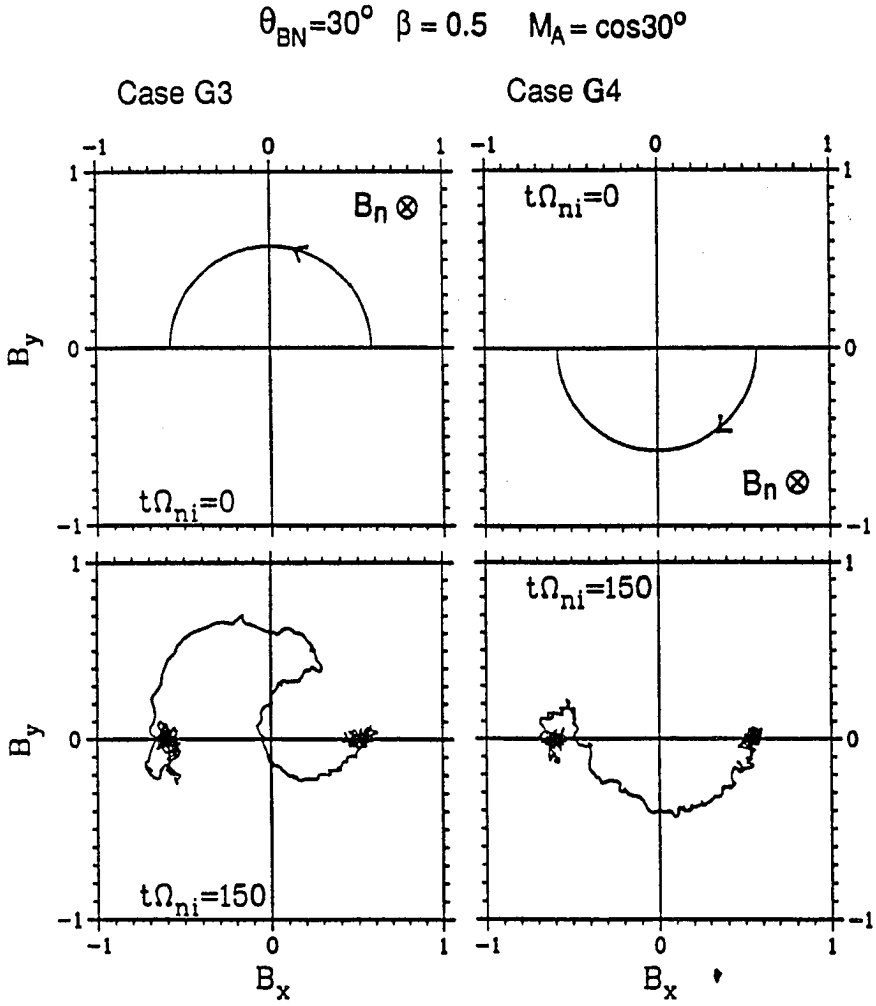

Figure 4.5 Magnetic hodograms of Cases G3 and G4 from $z = 80\, c/\omega_{pi}$ to $z = 240\, c/\omega_{pi}$. Non-Alfvénic initial conditions are used in these two cases, where the initial velocity profile are linearly polarized across the RD ramp. The S-shaped magnetic hodograms shown at $t\Omega_{ni} = 150$ is characterized by a right-hand polarized nonlinear wave profile followed by a left-hand polarized nonlinear wave profile.

S-shaped RDs accompanied by large amplitude upstream or downstream wave-trains can be formed if the initial ramp thickness is small enough (which is a few ion inertial lengths for the quasi-parallel RDs studied in this section). On the other hand, S-shaped RDs without large amplitude wavetrain structures can be formed by a wide (which is a few tens of ion inertial lengths for the 30° RDs studied in this section)

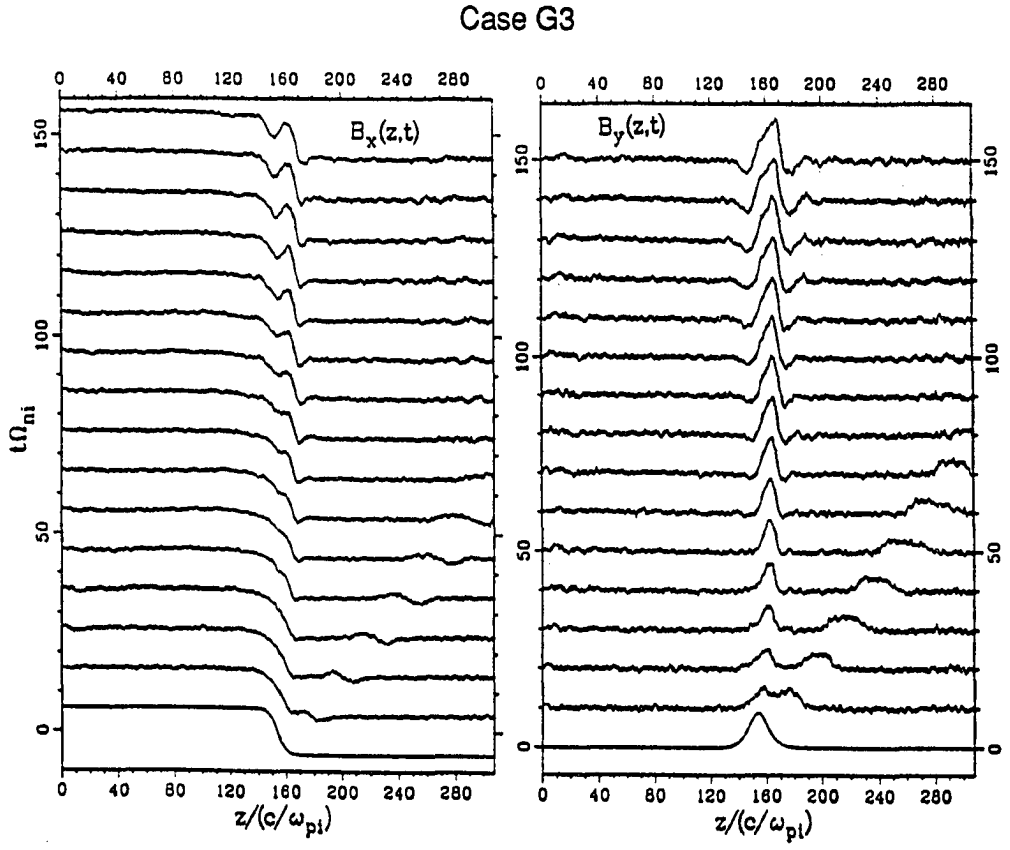

Figure 4.6 Spatial profiles of B_x and B_y obtained from simulation Case G3 plotted at successive times. A nonlinear wave is generated at the non-Alfvénic initial transition region and propagating downstream. After the nonlinear wave profile detached from the central ramp region, an S-shaped rotational structure is formed as shown in Figure 4.5. No large amplitude upstream wavetrain or downstream wavetrain can be found in this quasi-lamina S-shaped rotational structure.

and non-Alfvénic initial ramp field as shown in Cases G3 and G4 for the first time. The final ramp thickness of the S-shaped RDs is about a few ion inertial lengths.

Note that so far all the S-shaped RDs obtained in simulation studies are characterized by a right-hand polarized wave field followed by a left-hand polarized wave field. It has been shown in Chapter 2 that an S-shaped rotational structure with right-hand polarized nonlinear wave structure followed by a left-hand polarized structure may

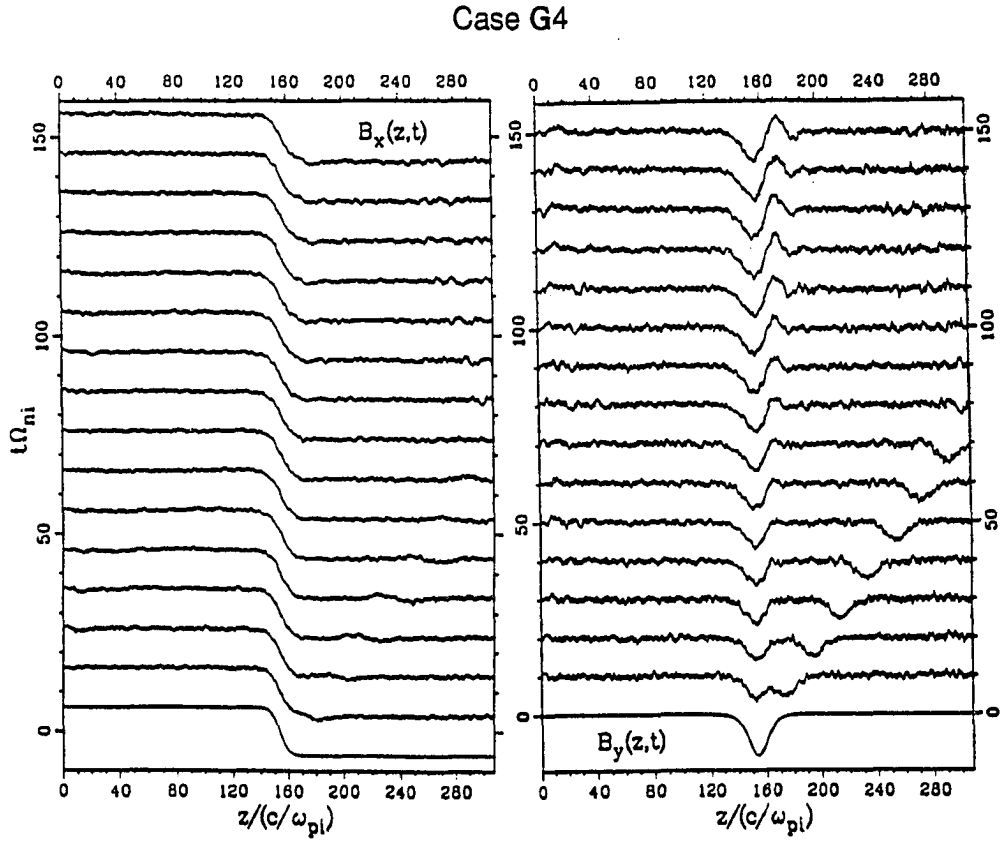

Figure 4.7 Spatial profiles of B_x and B_y obtained from simulation Case G4 plotted at successive times. A nonlinear wave is generated at the non-Alfvénic initial transition region and propagating downstream. After the nonlinear wave profile detached from the central ramp region, a quasi-lamina S-shaped rotational structure is formed as shown in Figure 4.5.

turn into an Alfvén shock. Figure 4.10 shows the spatial profile of $p\rho^{-\gamma}$ ($\gamma = 5/3$) obtained from the simulations of Cases G3–G5. As one can see, there is a net increase in the function of $p\rho^{-\gamma}$ across the ramp field. Note that the function $C_V \ln(p\rho^{-\gamma})$ may represent the local entropy of the plasma at the upstream and downstream sides of the rotational structure but not at the transition region, where C_V is the heat capacity at constant volume. The entropy may not be well defined when the plasma distribution

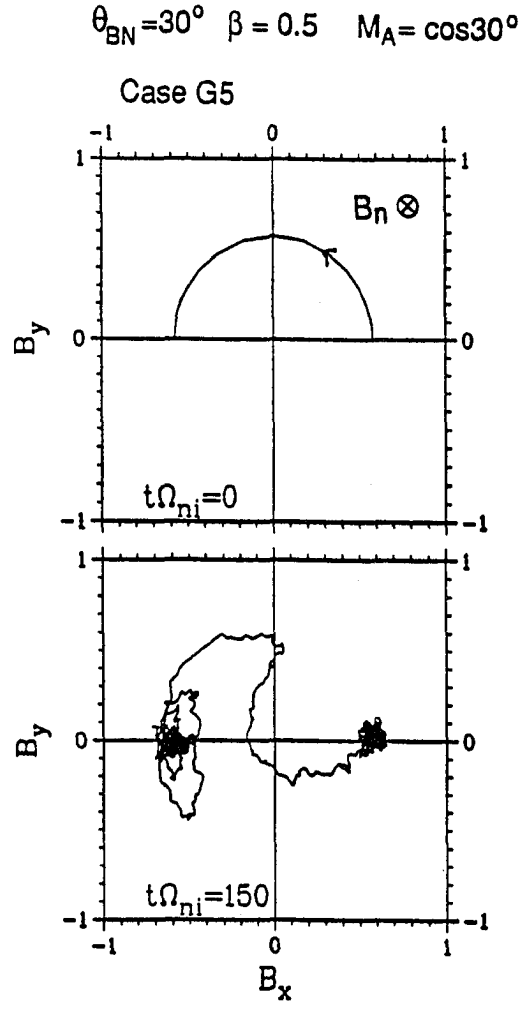

Figure 4.8 Magnetic hodograms of Case G5 from $z = 80\, c/\omega_{pi}$ to $z = 240\, c/\omega_{pi}$. The initial conditions of this case is similar to the one used in Case G1 but with a rather small initial ramp thickness of $3\, c/\omega_{pi}$. The magnetic hodogram shown at $t\Omega_{ni} = 150$ is similar to the one shown in Case G3 but with additional banana-shaped nonlinear wavetrain on the downstream side.

is non-Maxwellian such as at the shock transition regions. We may explain the simulation results as partially due to the choice of 180° rotation angle across the shock ramp. According to the Rankine-Hugoniot jump conditions, the tangential magnetic field across an Alfvén shock must rotate 180°. Thus, when the boundary conditions of the rotational discontinuities require a rotation of 180°, the final structure may turn

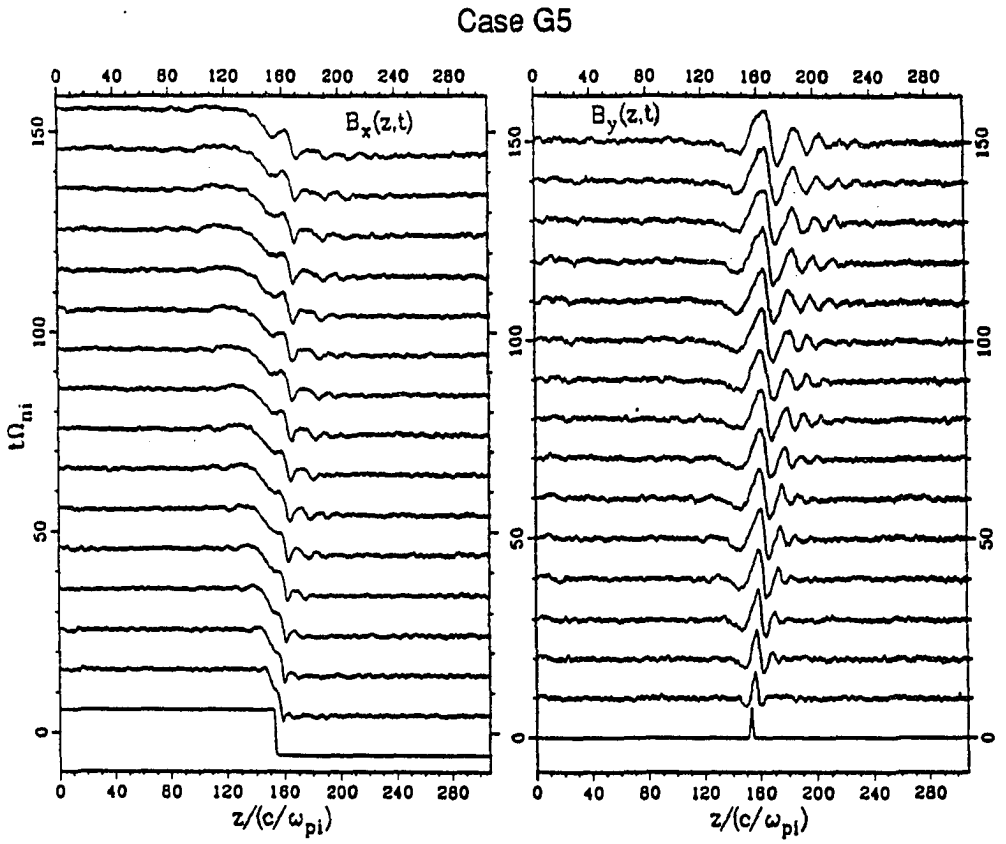

Figure 4.9 Spatial profiles of B_x and B_y obtained from simulation Case G5 plotted at successive times. A large amplitude downstream wavetrain is emitted from the over-steepened initial ramp field. The transition region disintegrated at beginning but steepened again after $t\Omega_{ni} \approx 100$.

into an Alfvén shock, which is a neighboring solution of the rotational discontinuity as shown in Figure 1.4. As a result, we suggest that the various types of RDs predicted in Chapter 2, such as the staple-shaped RDs, Ω-shaped RDs, and S-shaped RDs with left-hand polarized wave field followed by right-hand polarized wave field can occur when the rotation angle is not equal to 180°. For instance, staple-shaped rotational discontinuities discussed in Figures 2.25 and 2.26 in Chapter 2 are likely to form when the initial tangential magnetic field rotates less than 180° and the initial ramp is non-Alfvénic or the initial ramp thickness is too small. For initial rotation

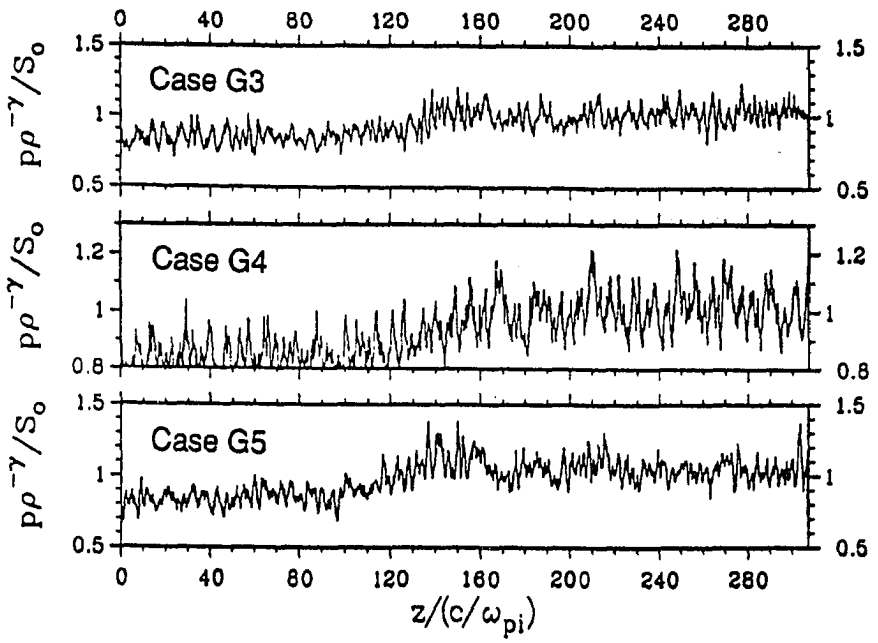

Figure 4.10 Spatial profiles of $p\rho^{-\gamma}$ ($\gamma = 5/3$) obtained from Cases G3–G5 simulations at $t\Omega_{ni} = 150$.

angle greater than 180°, the possible RD structures may be either an Ω-shaped RD (as obtained by *Swift and Lee* [1983]) or an S-shaped RD with left-hand polarized wave field followed by right-hand polarized wave field.

4.4 Switch-off Shocks

Three examples of switch-off shocks with upstream plasma $\beta = 0.5$, $\theta_{BN} = 80°$, and $M_A = \cos\theta_{BN}$ are studied under different initial conditions as listed in Table 4.2. They are Cases Z1, Z2, and Z3. According to the upstream conditions, one can show that C_A is greater than V_{AX} (or $\gamma\beta/2 > \cos^2\theta_{BN}$) on the upstream and downstream sides of the switch-off shocks. Thus, they are subcritical slow shocks as defined by *Coroniti* [1970, 1971]. Grid size used in this study is 0.1 c/ω_{pi}. Simulation system length is 153.6 c/ω_{pi}. Initial ramp thickness is chosen to be $D_W = 3\ c/\omega_{pi}$. Initial

Table 4.2 Switch-Off Shock Simulations

	Upstream			Initial Polarization		(c/ω_{pi})		
Case	θ_{BN}	β	M_A	B_t	V_t	D_W	L	Δ
Z1	80°	0.5	cos80°	L.H.P.	Linear	3	153.6	0.1
Z2	80°	0.5	cos80°	R.H.P.	Linear	3	153.6	0.1
Z3	80°	0.5	cos80°	Linear	Linear	3	153.6	0.1

D_W: initial ramp thickness. L: simulation system length. Δ: grid size.

tangential velocity is linearly polarized across the shock ramp. The polarization of the initial tangential magnetic field is left-handed in Case Z1, right-handed in Case Z2, and linear in Case Z3. Note that the initial tangential magnetic field is linearly polarized across the shock ramp in all the previous simulation studies of switch-off shocks [*Swift*, 1983; *Winske et al.*, 1985; *Lee et al.*, 1989*b*; *Omidi and Winske*, 1989].

Figure 4.11 shows the evolution of magnetic hodograms obtained from Case Z1 simulation. Figure 4.12 shows the spatial profiles of total magnetic field B and tangential magnetic field components B_x and B_y obtained from Case Z1 simulation. A relatively stable shock structure is formed after $t = 18\ \Omega_{ni}^{-1} \approx 103\ \Omega_i^{-1}$, which is characterized by a magnetic hodogram with a right-hand polarized hook-shaped structure followed by large amplitude left-hand polarized nonlinear slow-mode wavetrain. Although the initial condition used in Case Z1 is quite different from the one used in the previous simulation studies, the simulation result of Case Z1 is similar to the results obtained in previous studies [e.g., *Swift*, 1983] and consistent with the theoretical prediction of subcritical slow shock structures [*Coroniti*, 1970, 1971].

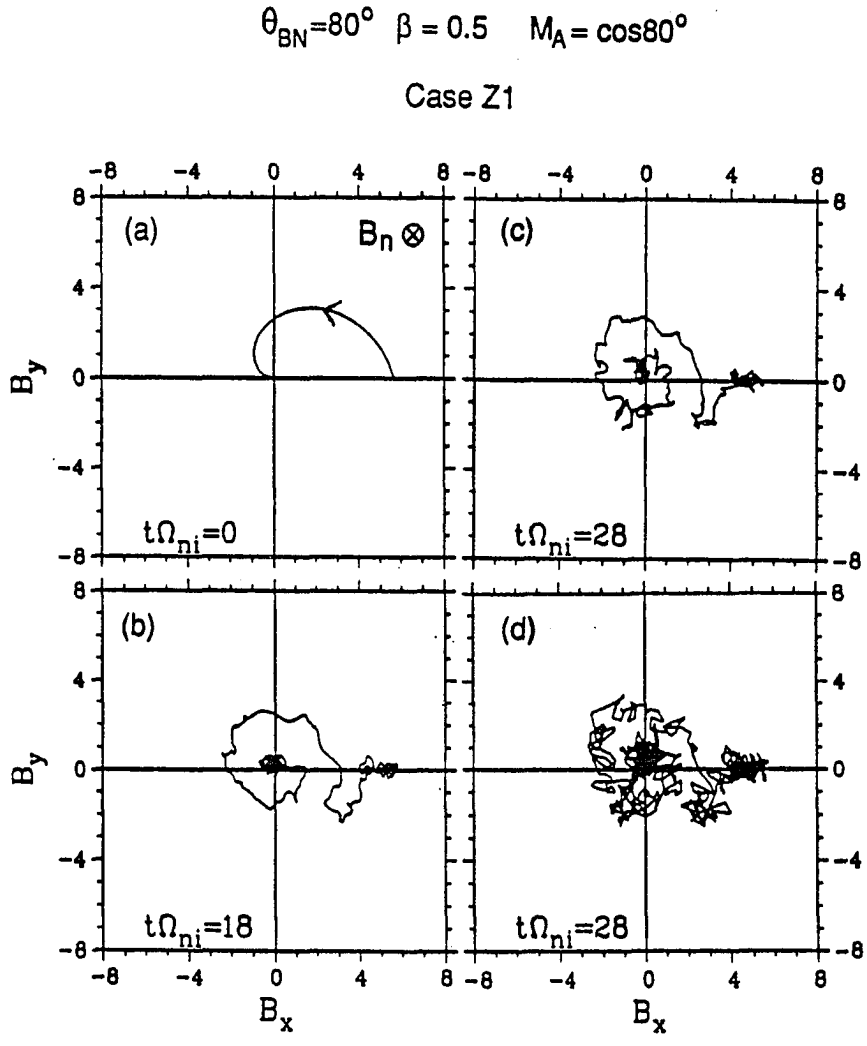

Figure 4.11 Magnetic hodograms of switch-off shock simulation Case Z1 from $z = 60\ c/\omega_{pi}$ to $z = 120\ c/\omega_{pi}$ and at different times as indicated. Hodograms shown in panels (*a*)–(*c*) are plotted with smoothed data over $0.7\ c/\omega_{pi}$. Hodogram shown in panel (*d*) is plotted with unsmoothed data. A quasi-stable magnetic hodogram is formed since $t \approx 18\ \Omega_{ni}^{-1} \approx 103\ \Omega_i^{-1}$, which can be characterized by a right-hand polarized hook-shaped nonlinear wave profile followed by a left-hand polarized nonlinear wavetrain structure on the downstream side.

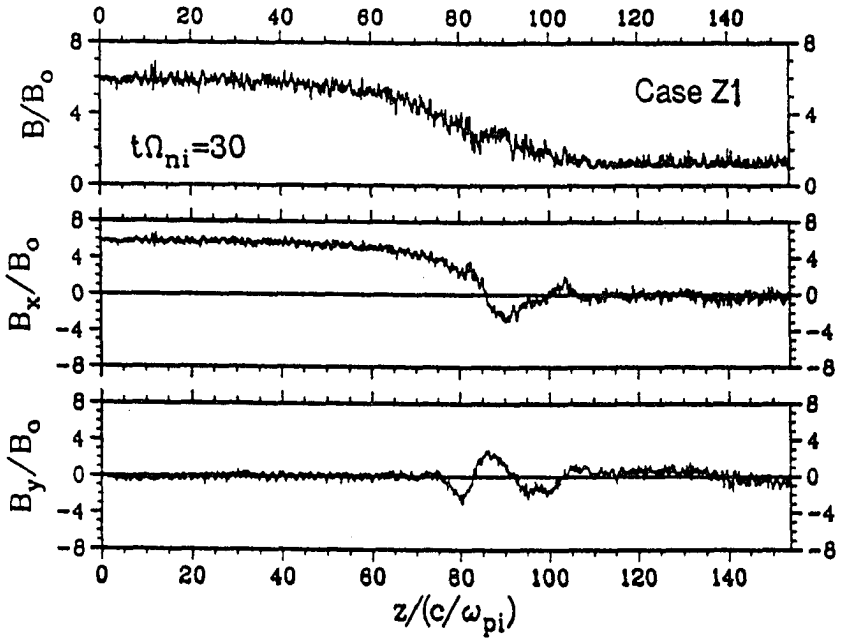

Figure 4.12 Spatial profiles of total magnetic field B, tangential magnetic field B_x and B_y at $t = 30\ \Omega_{ni}^{-1} \approx 173\ \Omega_i^{-1}$ obtained from switch-off simulation Case Z1, where the normalized constant B_o is the magnitude of the normal magnetic field components. Large-amplitude wavetrain structures can be seen on the downstream side.

Figure 4.13 shows the evolution of magnetic hodograms obtained from Case Z2 simulation. Figure 4.14 shows the spatial profiles of total magnetic field B and tangential magnetic field components B_x and B_y obtained from Case Z2 simulation. A relatively stable ramp field is formed since $t = 18\ \Omega_{ni}^{-1} \approx 103\ \Omega_i^{-1}$, which can be characterized by a linearly polarized ramp field followed by a right-handed polarized ramp field. No large-amplitude wavetrains can be found on the downstream of the shock front in Case Z2 simulation. The reason why large-amplitude downstream wavetrain is absent from Case Z2 simulation is not very clear yet. A possible explanation will be given at the end of this section based on the ion dynamics to be presented in Figures 4.19–4.22.

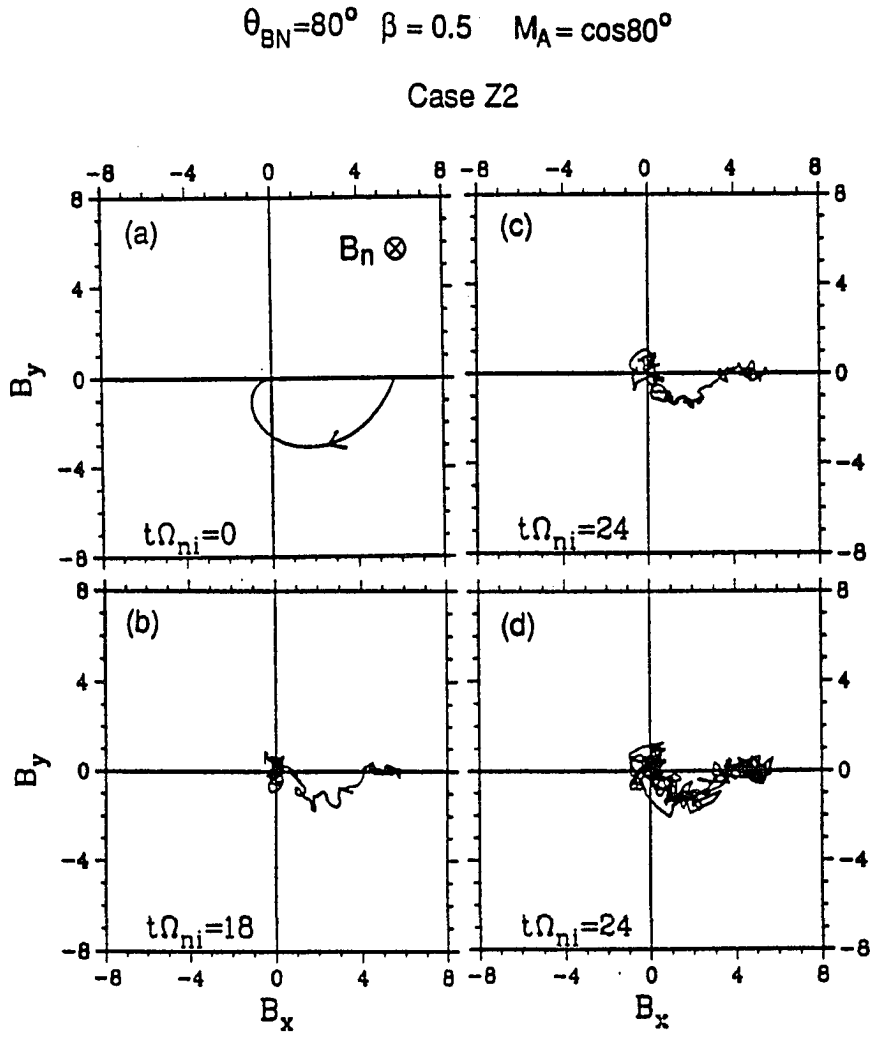

Figure 4.13 Magnetic hodograms of switch-off shock simulation Case Z2 from $z = 60\ c/\omega_{pi}$ to $z = 100\ c/\omega_{pi}$ and at different times as indicated. Hodograms shown in panels (*a*)–(*c*) are plotted with smoothed data over $0.7\ c/\omega_{pi}$. Hodogram shown in panel (*d*) is plotted with unsmoothed data. A stable magnetic hodogram is formed since $t \approx 18\ \Omega_{ni}^{-1} \approx 103\ \Omega_i^{-1}$, which can be characterized by a linearly polarized nonlinear wave followed by a right-hand polarized nonlinear wave profile.

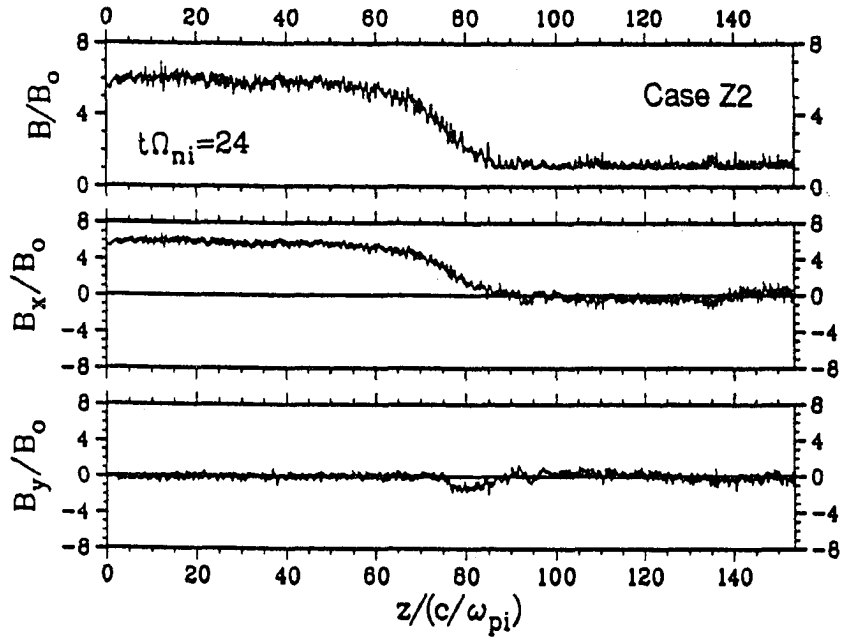

Figure 4.14 Spatial profiles of total magnetic field B, tangential magnetic field B_x and B_y at $t = 24\ \Omega_{ni}^{-1} \approx 138\ \Omega_i^{-1}$ obtained from switch-off simulation Case Z2. Case Z2 is a quasi-lamina subcritical switch-off shock since no large-amplitude downstream wavetrain structures can be found in this case.

Simulation results of Case Z3 are similar to the simulation results of Case Z1 as can be seen from the magnetic hodograms shown in the Figure 4.15. Since the initial condition of the ramp field in Case Z3 is similar to the previous simulation studies of switch-off shocks, it is no surprise that the result of Case Z3 is consistent with previous simulation results [*Swift*, 1983; *Winske et al.*, 1985; *Lee et al.*, 1989*b*; *Omidi and Winske*, 1989] and the theoretical prediction of subcritical slow shock structures [*Coroniti*, 1970, 1971].

The nonlinear interaction between ions and the large amplitude waves in the downstream shock transition regions have been considered as an important shock-heating mechanism for switch-off shocks [e.g., *Swift*, 1983]. Thus, it is interesting to study the shock-heating mechanism in the simulated shock Case Z2, in which no large

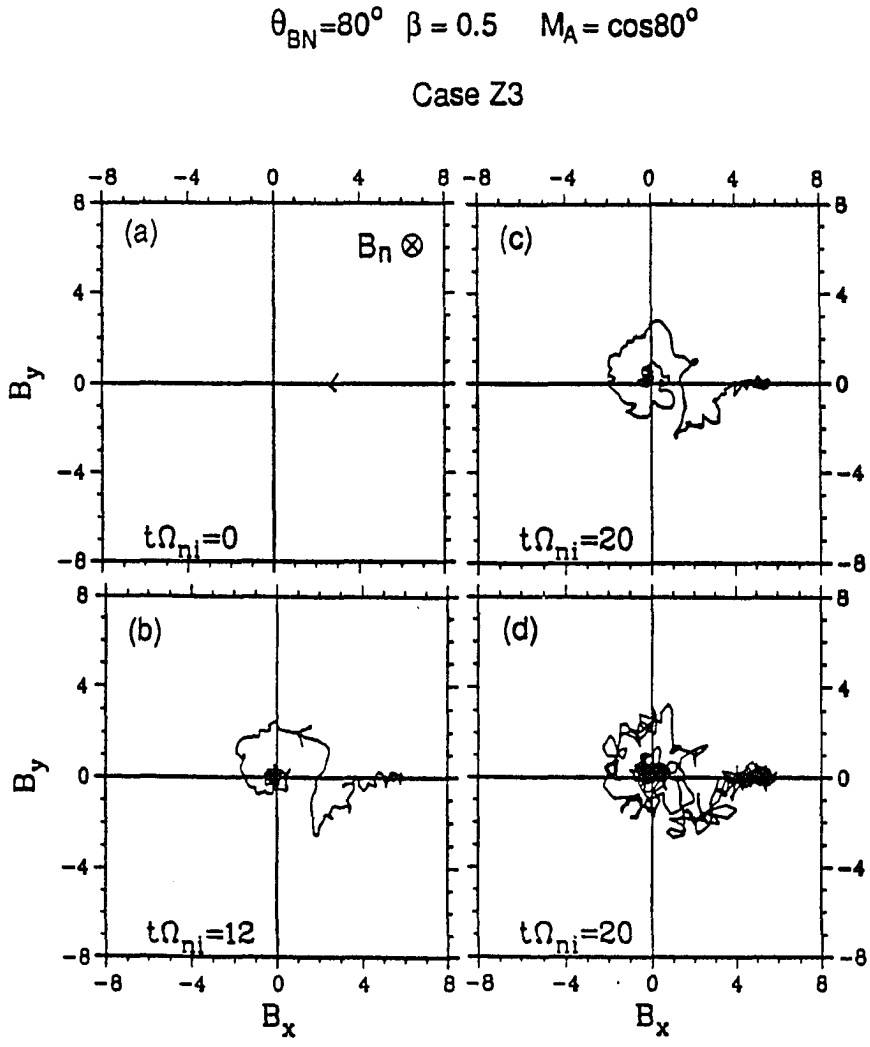

Figure 4.15 Magnetic hodograms of switch-off shock simulation Case Z3 from $z = 60\ c/\omega_{pi}$ to $z = 110\ c/\omega_{pi}$ and at different times as indicated. Hodograms shown in panels (*a*)–(*c*) are plotted with smoothed data over $0.7\ c/\omega_{pi}$. Hodogram shown in panel (*d*) is plotted with unsmoothed data. The hodogram structure of Case Z3 is similar to the hodogram structure of Case Z1 as shown in Figure 4.11.

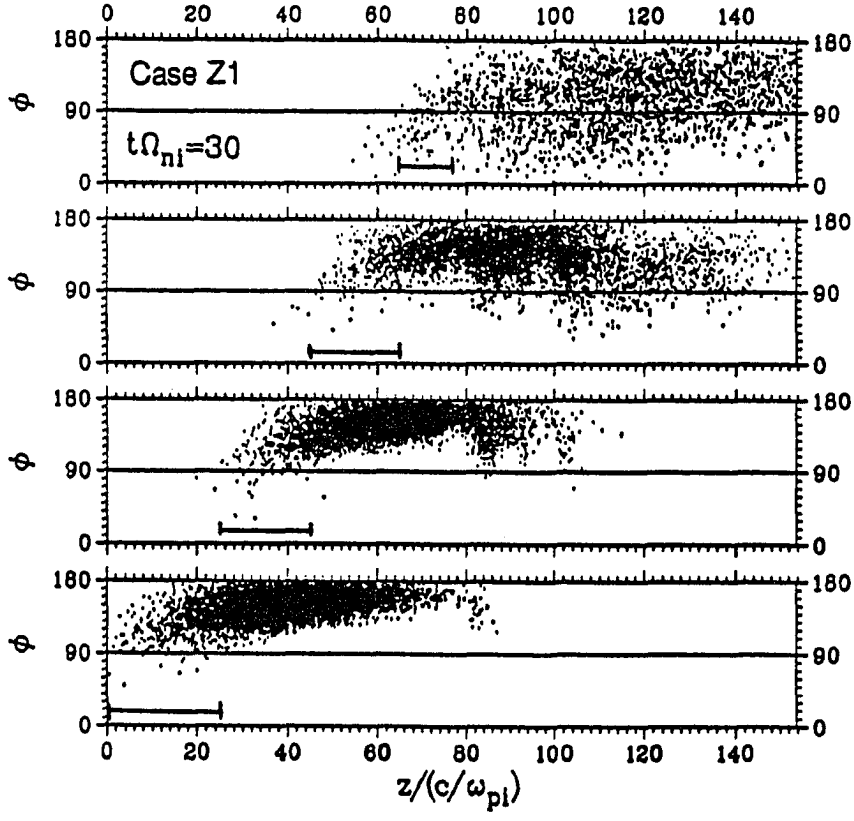

Figure 4.16 Scatter plots of ion pitch angle distributions in the ϕ-z space for all the initially loaded ions in Case Z1 at $t\Omega_{ni} = 30$. Ions plotted in different panels are initially loaded in the regions as denoted by the horizontal bars.

amplitude wavetrains can be found in the downstream shock transition region. To show the differences on shock-heating processes, ion dynamics in the shock transition regions of Case Z1 and Case Z2 simulations are examined below.

Scatter plots of ion pitch angle distributions in the ϕ-z space, and scatter plots of ion phase space distributions in v_z-z space and v_x-z space are shown in Figures 4.16–4.18 for all the initially loaded ions in Case Z1 at $t\Omega_{ni} = 30$, where ϕ is the ion pitch angle defined by the angle between ion velocity direction and local magnetic field direction. Useful informations provided by the scatter plots in the ϕ-z space

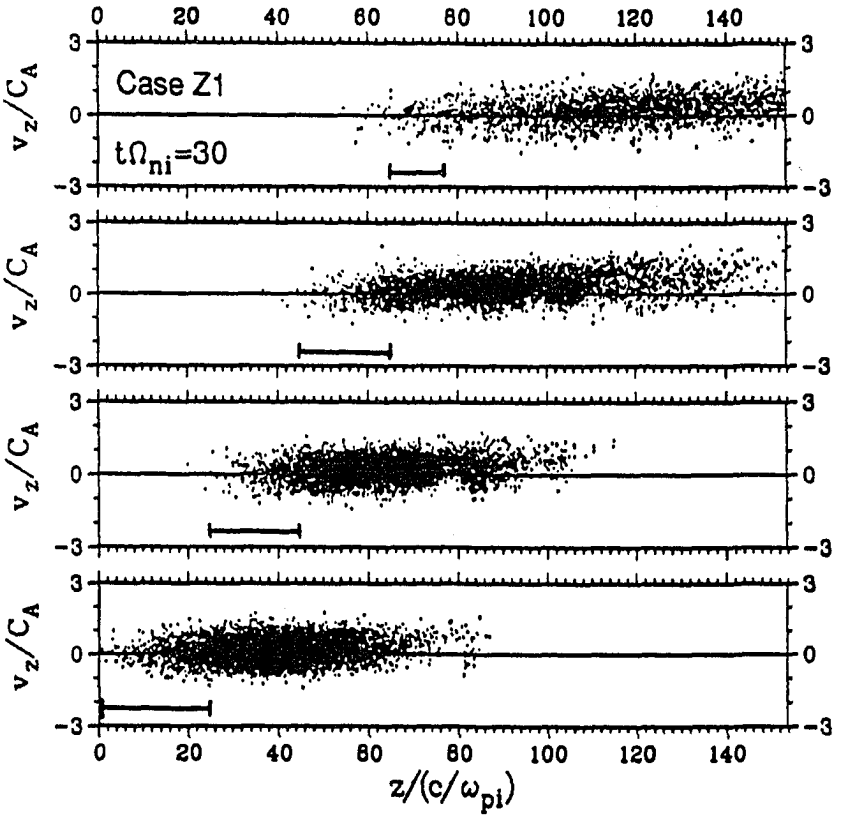

Figure 4.17 Scatter plots of ion phase space distributions in the v_z-z space for all the initially loaded ions in Case Z1 at $t\Omega_{ni} = 30$. Ions plotted in different panels are initially loaded in the regions as denoted by the horizontal bars.

have been discussed in Chapter 3. Ions plot in different panels are initially loaded in the regions as denoted by the horizontal bars. The incoming upstream ions are heated in the downstream shock transition regions due to pitch angle scattering by the large amplitude wavetrains. Similar results can be found in Case Z3. From the scatter plots shown in Figures 4.16–4.18, we may conclude that there are no coherent ion reflections at the shock front of the switch-off shocks in Cases Z1 and Z3.

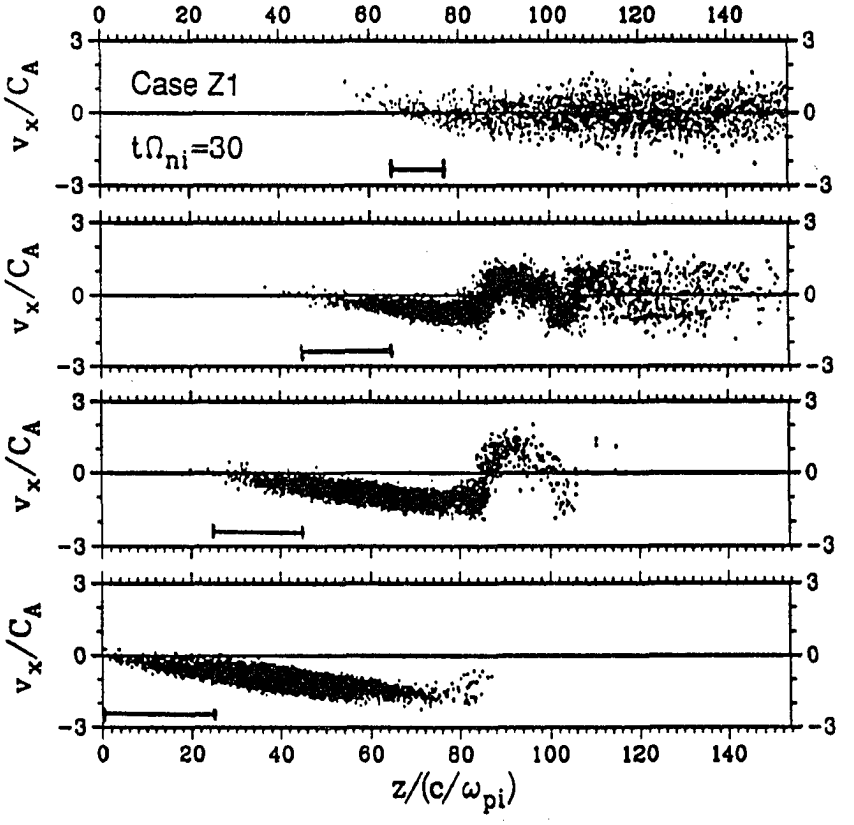

Figure 4.18 Scatter plots of ion phase space distributions in the v_x-z space for all the initially loaded ions in Case Z1 at $t\Omega_{ni} = 30$. Ions plotted in different panels are initially loaded in the regions as denoted by the horizontal bars.

Scatter plots of ion pitch angle distributions in the ϕ-z space, and scatter plots of ion phase space distributions in v_z-z space and v_x-z space are shown in Figures 4.19–4.21 for all the initially loaded ions in Case Z2 at $t\Omega_{ni} = 24$ under the same format as shown in Figure 4.16. Coherent ion reflections can be seen near the shock ramp in the second and the third panels of Figure 4.19 and Figure 4.20. A clearer picture of ion reflection process is shown in Figure 4.22. Figure 4.22 shows scatter plots of (*a*) ion pitch angle distributions in the ϕ-z space, (*b*) ion phase space distributions in the v_z-z space, and (*c*) v_x-z space for ions initially loaded in the regions as denoted by

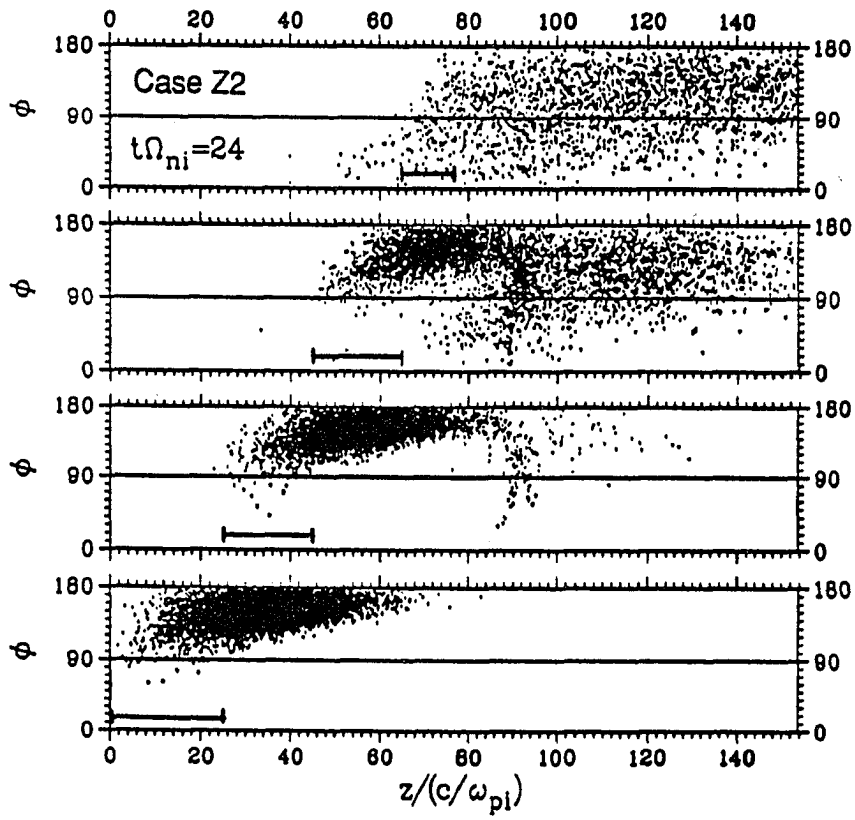

Figure 4.19 Scatter plots of ion pitch angle distributions in the ϕ-z space for all the initially loaded ions in Case Z2 at $t\Omega_{ni} = 24$. Ions plotted in different panels are initially loaded in the regions as denoted by the horizontal bars.

the horizontal bars in Case Z2 at $t\Omega_{ni} = 24$. No diffuse type leakage ions but a dense coherent reflection beam of ions can be found in Figure 4.22. A strong anomalous viscosity generated by ion reflection at the shock ramp can result in effective shock-heating without the help from large amplitude downstream waves. Thus, we may conclude that the ion reflection at the shock ramp may be responsible for the absence of downstream wavetrains in the switch-off shock Case Z2.

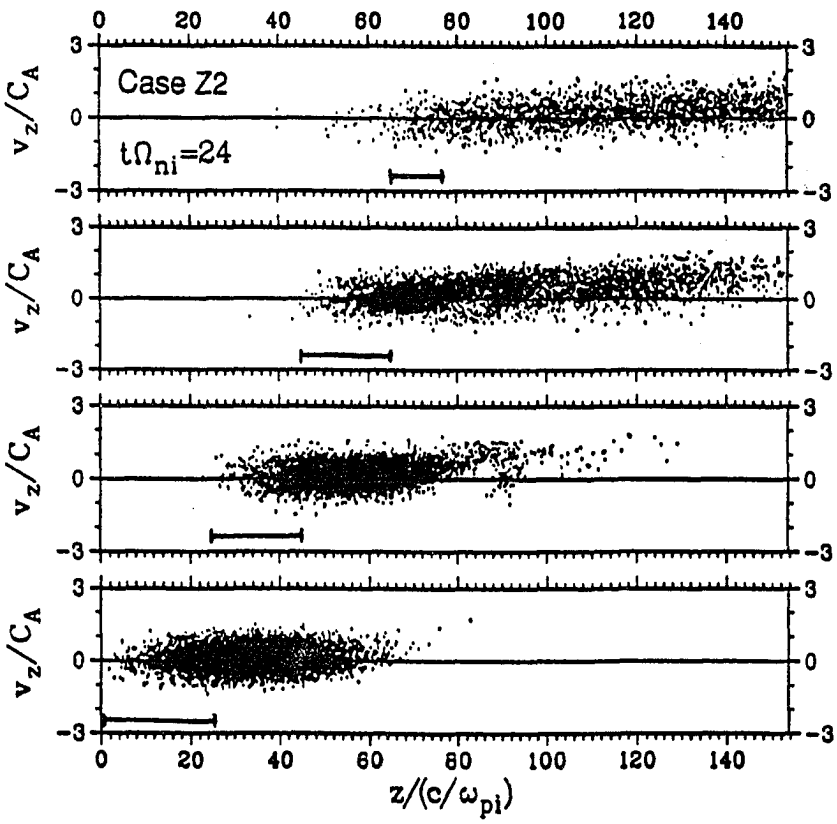

Figure 4.20 Scatter plots of ion phase space distributions in the v_z-z space for all the initially loaded ions in Case Z2 at $t\Omega_{ni} = 24$. Ions plotted in different panels are initially loaded in the regions as denoted by the horizontal bars.

4.5 Intermediate Shocks

Intermediate shocks consist of Alfvén shocks, Alfvén-slow shocks, fast-Alfvén shocks, and fast-Alfvén-slow shocks as discussed in Table 1.1 and Section 1.1.3 in Chapter 1 of this thesis. According to Figure 1.4, the fast-Alfvén shocks, and the fast-Alfvén-slow shocks can only be found in low β plasma with small θ_{BN}. Intermediate shocks with $\beta = 0.5$ and $\theta_{BN} = 80°$, 45° and 10° will be studied in this sections as listed in Table 4.3.

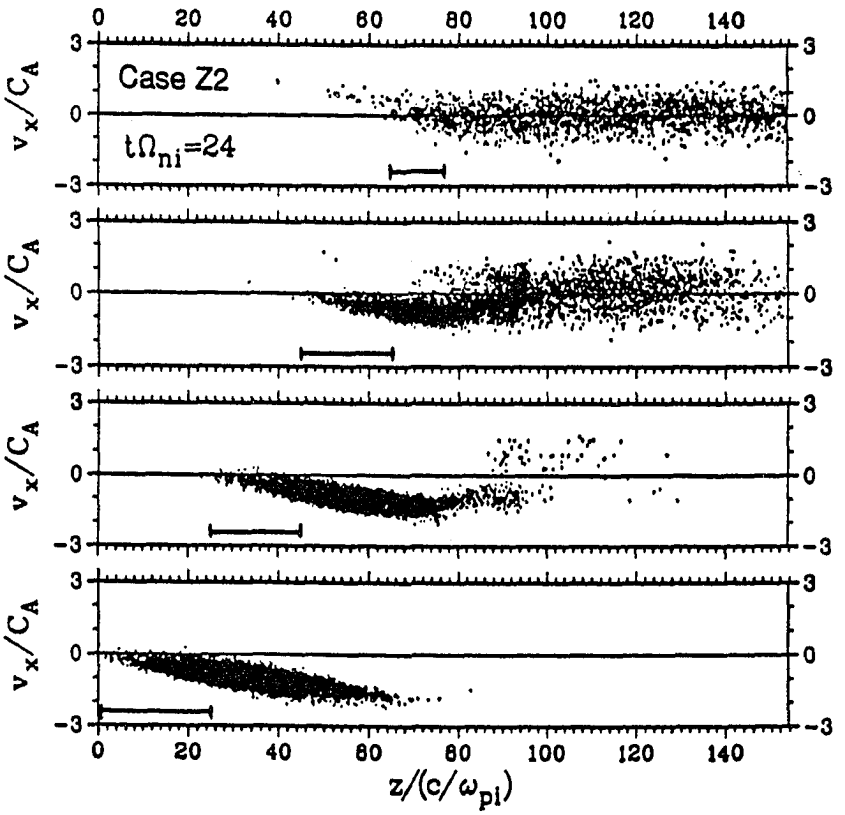

Figure 4.21 Scatter plots of ion phase space distributions in the v_x-z space for all the initially loaded ions in Case Z2 at $t\Omega_{ni} = 24$. Ions plotted in different panels are initially loaded in the regions as denoted by the horizontal bars.

4.5.1 Quasi-Perpendicular Intermediate Shocks With $\theta_{BN} = 80°$

For upstream plasma $\beta = 0.5$ and $\theta_{BN} = 80°$, only Alfvén shock and Alfvén-slow shock solutions can be found from the Rankine-Hugoniot jump conditions. Four examples with $M_A = 0.18$ (which is slightly greater than cos80° $\approx$ 0.173648...) are studied. Two of them are Alfvén-slow shocks and two of them are Alfvén shocks. The Alfvén-slow shocks are given by Cases $Z_{A\text{-}S}1$ and $Z_{A\text{-}S}2$. The Alfvén shocks are given by Cases Z_A1 and Z_A2. The initial ramp thickness is 3 c/ω_{pi} for all four cases. To keep the intermediate shock from turning into a rotational discontinuity, the

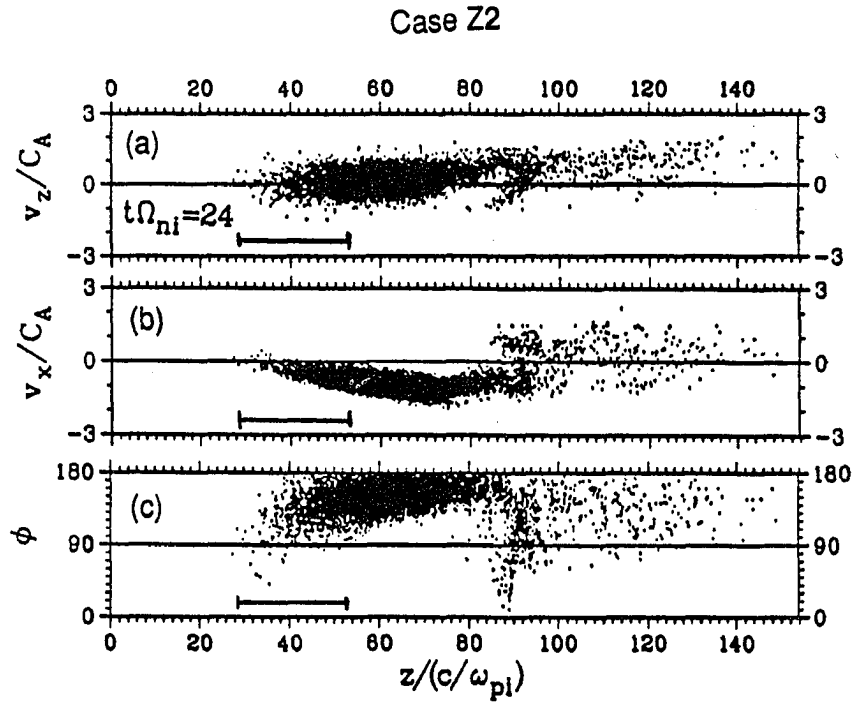

Figure 4.22 Scatter plots of (*a*) ion pitch angle distributions in the ϕ-z space, (*b*) ion phase space distributions in the v_z-z space, and (*c*) v_x-z space during ion reflection at shock front for ions initially loaded in the regions as denoted by the horizontal bars in Case Z2 at $t\Omega_{ni} = 24$.

initial velocity profile is linearly polarized across the shock ramp in all four cases. The initial tangential magnetic field is left-hand circularly polarized in Cases $Z_{A\cdot S}1$ and Z_A1 but right-hand circularly polarized in Cases $Z_{A\cdot S}2$ and Z_A2. As we can see, the polarizations of initial tangential magnetic field and velocity profiles across the shock ramp of Cases $Z_{A\cdot S}1$ and Z_A1 are similar to those in Case Z1. Likewise, the polarizations of initial tangential magnetic field and velocity profiles across the shock ramp of Cases $Z_{A\cdot S}2$ and Z_A2 are similar to those in Case Z2. It may be noted that an initial shock ramp with a linearly polarized tangential magnetic field as used in Case Z3 is not applicable to the intermediate shock simulations, especially the Alfvén shock

Table 4.3 Intermediate Shock Simulations

		Upstream			Initial Polarization		(c/ω_{pi})		
Case	Type	θ_{BN}	β	M_A	B_t	V_t	D_W	L	Δ
$Z_{A\cdot S}1$	2→3	80°	0.5	0.18	L.H.P.	Linear	3	153.6	0.1
$Z_{A\cdot S}2$	2→3	80°	0.5	0.18	R.H.P.	Linear	3	153.6	0.1
Z_A1	2→4	80°	0.5	0.18	L.H.P.	Linear	3	153.6	0.1
Z_A2	2→4	80°	0.5	0.18	R.H.P.	Linear	3	153.6	0.1
$S_{A\cdot S}$	2→3	45°	0.5	0.73	Linear	Linear	30	307.2	0.2
S_A	2→4	45°	0.5	0.73	Linear	Linear	30	307.2	0.2
$Q_{F\cdot A\cdot S}$	1→4	10°	0.5	1.2	Linear	Linear	30	307.2	0.2
$Q_{F\cdot A}$	1→3	10°	0.5	1.2	Linear	Linear	30	307.2	0.2
$Q_{A\cdot S}$	2→4	10°	0.5	1.0	Linear	Linear	30	307.2	0.2
Q_A	2→3	10°	0.5	1.0	Linear	Linear	30	307.2	0.2

D_W: initial ramp thickness. L: simulation system length. Δ: grid size.

Types: 1→3: Fast-Alfvén shock 1→4: Fast-Alfvén-Slow shock
2→3: Alfvén shock 2→4: Alfvén-Slow shock

simulations, at large θ_{BN}. A linearly polarized tangential magnetic field at $t = 0$ will lead to a minimum total pressure at the shock ramp in an intermediate shock simulation. Since the normal magnetic field component is very small for intermediate shocks with $\theta_{BN} = 80°$, there will be a large difference between the minimum total pressure at the shock ramp and the total pressure on the upstream and downstream sides. The very unbalanced initial state across the shock ramp will lead to a long wavelength large

disturbance at the shock ramp. Thus, one needs a very long simulation box to handle the large initial disturbance properly.

Figures 4.23–4.26 show the evolution of the tangential magnetic field hodogram of the simulation Cases $Z_{A\cdot S}1$, $Z_{A\cdot S}2$, Z_A1, and Z_A2. From the simulation results shown in Figures 4.23–4.26, we can conclude that each simulation has reached to a quasi-steady state during the period of $t\Omega_{ni} = 18$–24 (i.e., $t\Omega_i \approx 103$–138).

To show the systematic changes among the switch-off shocks studied in Section 4.4 and the intermediate shocks studied in this section, a summary of magnetic hodograms at the end of each simulation run is shown in Figures 4.27 and 4.28, where hodograms shown in Figure 4.27 are plotted over unsmoothed data and hodograms shown in Figure 4.28 are plotted over smoothed data. As one can see, there is a systematic change of shock structures from switch-off shocks, to Alfvén-slow shocks, and then to Alfvén shocks for each set of cases (i.e., simulation results shown in the left-hand column for Cases Z1, $Z_{A\cdot S}1$, and Z_A1; and simulation results shown in the right-hand column for Cases Z2, $Z_{A\cdot S}2$, and Z_A2). The flatness of the magnetic hodogram shown in Cases Z_A1 and Z_A2 is similar to the rotational discontinuities with $\beta = 0.5$ and $\theta_{BN} = 80°$ as predicted in Chapter 2 and simulated by *Swift and Lee* [1983]. The magnetic hodograms of Cases Z2 and $Z_{A\cdot S}2$ shows similar characteristics which can be used to compare with the observed Uranian magnetopause by Voyager-2.

Figure 4.29 shows hodogram of Voyager-2 magnetic field measurements across the Uranian magnetopause in the principal axis system [after *Russell et al.*, 1989], where the principal axis system is determined from the minimum variance method [*Sonnerup and Cahill*, 1967]. The structure of Uranian magnetopause differs from the typical terrestrial magnetopause due to high plasma beta in the Uranian magnetosheath [*Russell et al.*, 1989]. Similar magnetopause structures can be found occasionally at

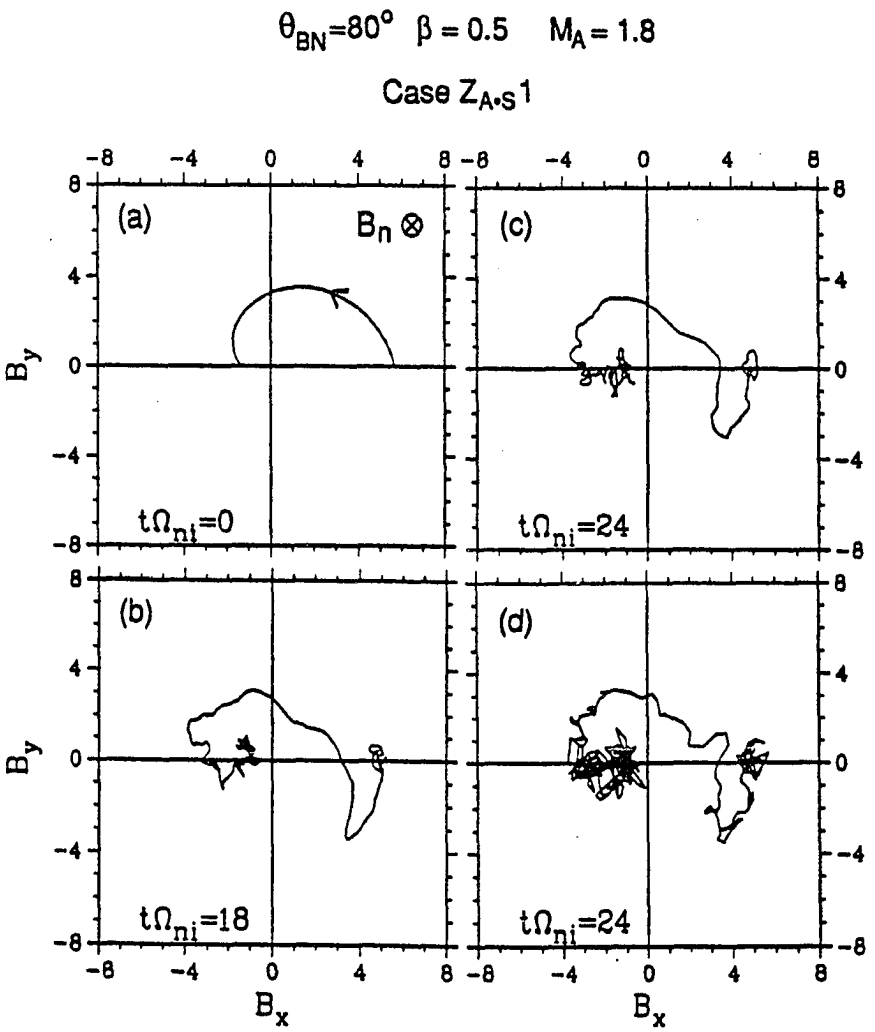

Figure 4.23 Magnetic hodograms of Alfvén-slow shock simulation Case $Z_{A\text{-}S}1$ from $z = 70\ c/\omega_{pi}$ to $z = 105\ c/\omega_{pi}$ and at different times as indicated. Hodograms shown in panels (*a*)–(*c*) are plotted with smoothed data over $0.7\ c/\omega_{pi}$. Hodogram shown in panel (*d*) is plotted with unsmoothed data.

Earth magnetopause when the plasma beta in the magnetosheath is high enough ($\sim$ 100) [*Russell et al.*, 1989]. The observed Uranian magnetopause may be a slow shock [*Russell et al.*, 1989], which implies flow from magnetosphere to magnetosheath. The magnetic hodogram from magnetosphere to magnetosheath is characterized by a linearly polarized nonlinear wave in the upstream shock transition region followed

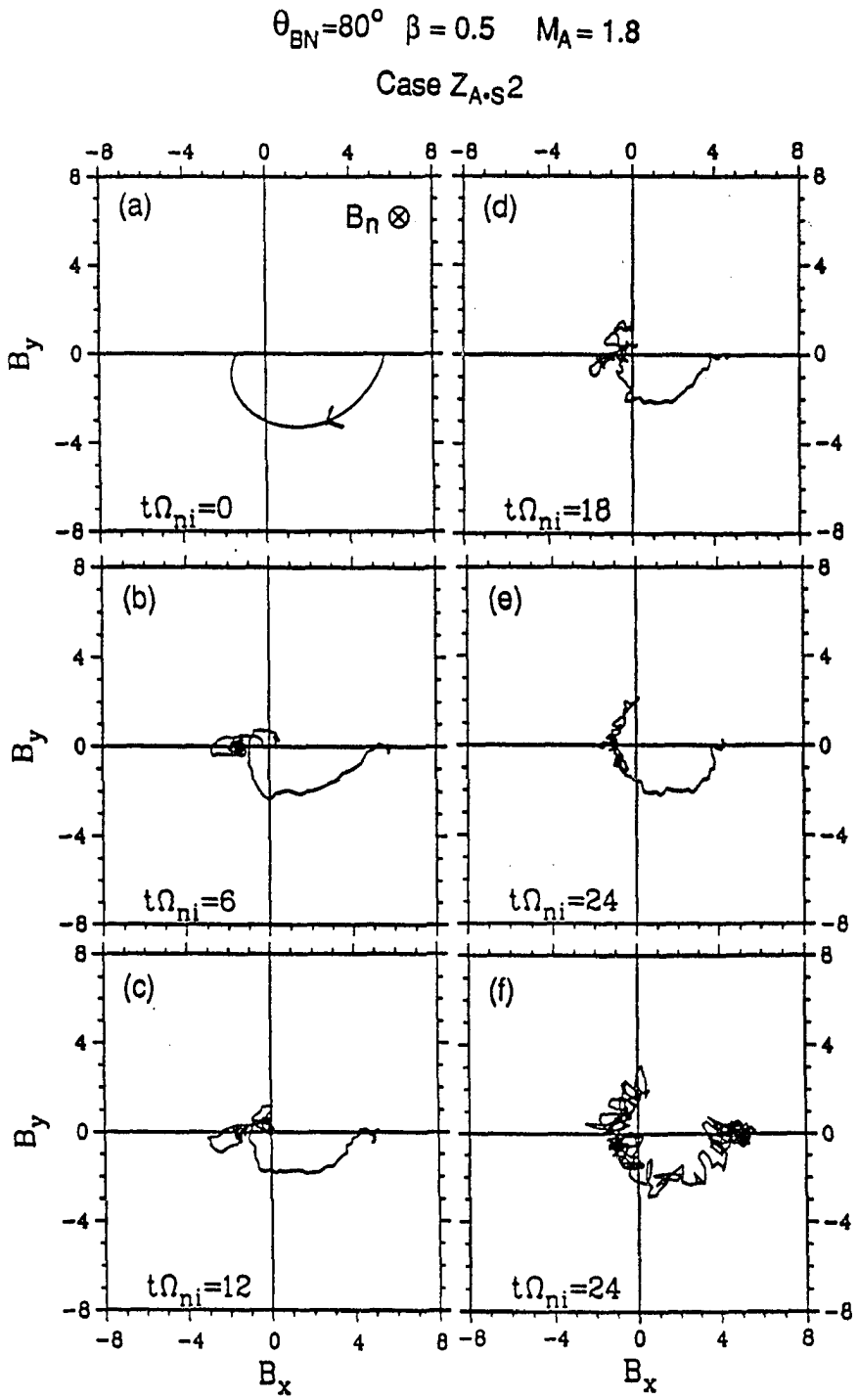

Figure 4.24 Magnetic hodograms of Alfvén-slow shock simulation Case $Z_{A\text{-}S}2$ from $z = 70\ c/\omega_{pi}$ to $z = 110\ c/\omega_{pi}$ and at different times as indicated. Hodograms shown in panels (*a*)–(*e*) are plotted with smoothed data over $1.1\ c/\omega_{pi}$. Hodogram shown in panel (*f*) is plotted with unsmoothed data.

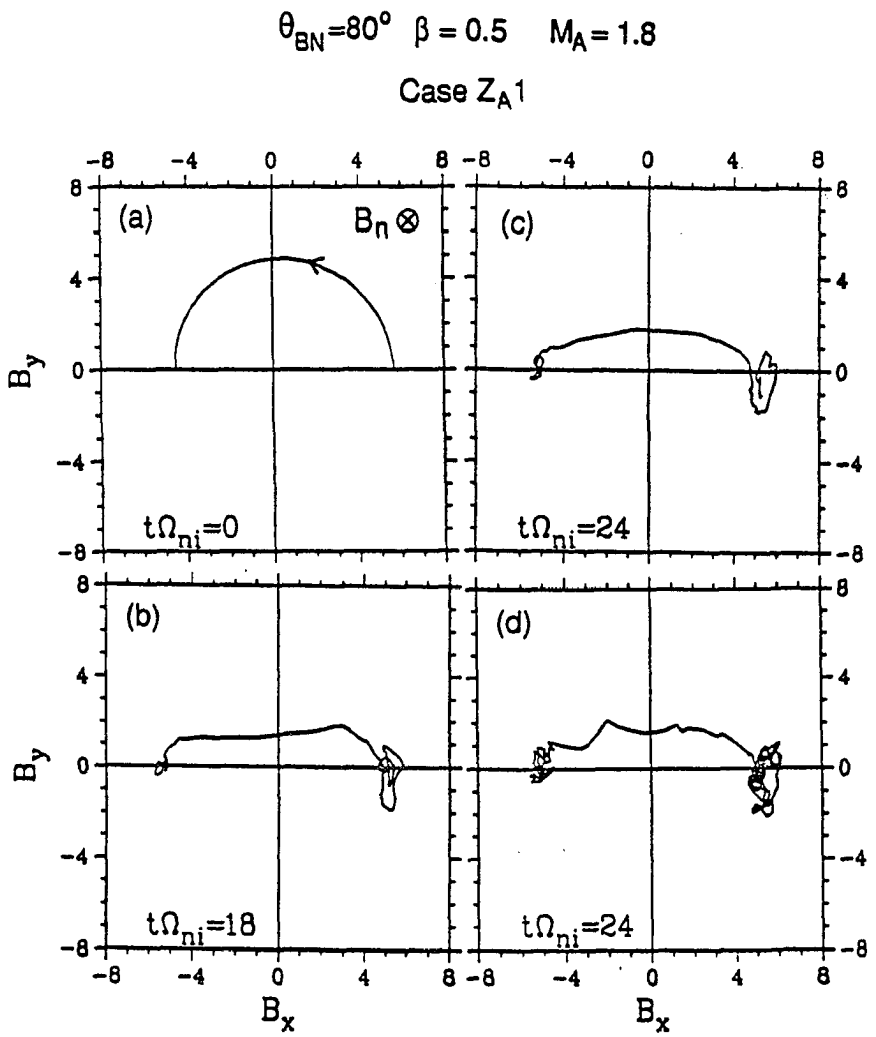

Figure 4.25 Magnetic hodograms of Alfvévn shock simulation Case Z_A1 from z = $z = 70\ c/\omega_{pi}$ to $z = 85\ c/\omega_{pi}$ and at different times as indicated. Hodograms shown in panels (*a*)–(*c*) are plotted with smoothed data over $0.7\ c/\omega_{pi}$. Hodogram shown in panel (*d*) is plotted with unsmoothed data.

by a right-hand polarized nonlinear wave in the downstream shock transition region. The magnetic hodogram observed at Uranian magnetopause crossing is similar to the magnetic hodogram obtained in the switch-off shock Case Z2 and the Alfvén-slow shock Case $Z_{A.S}2$ as shown in Figure 4.28.

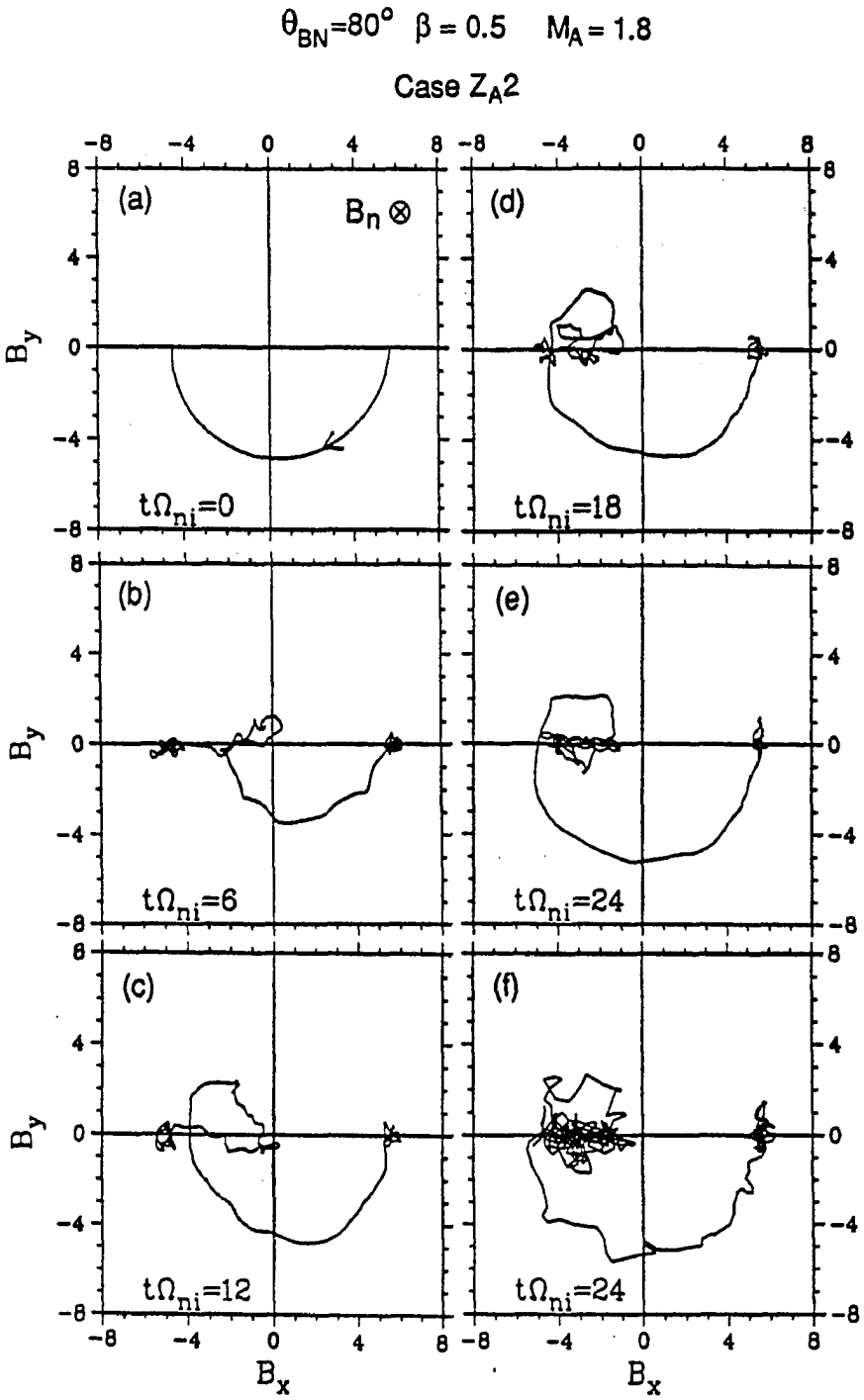

Figure 4.26 Magnetic hodograms of Alfvén-slow shock simulation Case Z_A2 from $z = 60\ c/\omega_{pi}$ to $z = 100\ c/\omega_{pi}$ and at different times as indicated. Hodograms shown in panels (*a*)–(*e*) are plotted with smoothed data over $0.7\ c/\omega_{pi}$. Hodogram shown in panel (*f*) is plotted with unsmoothed data.

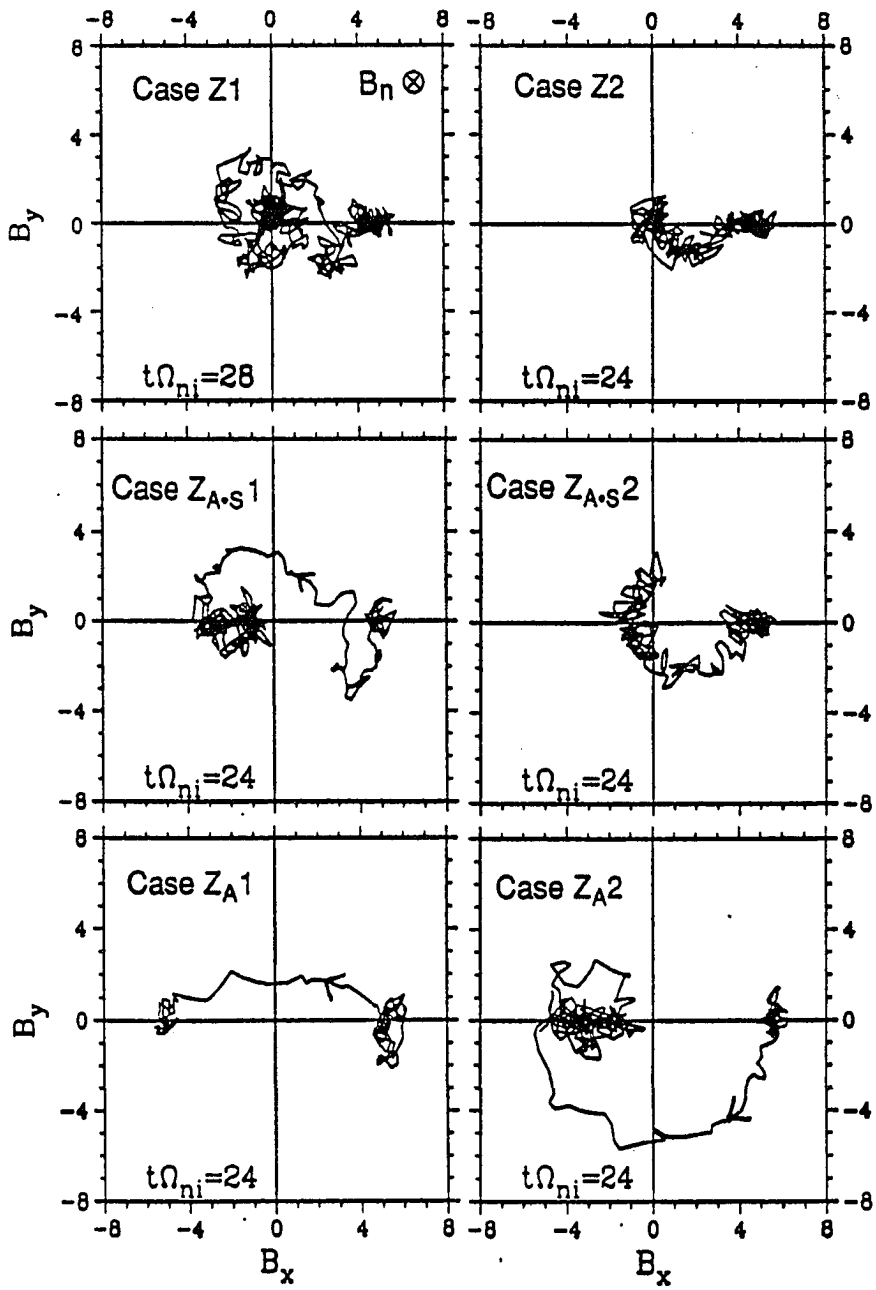

Figure 4.27 Summary of magnetic hodograms of Cases Z1, Z2, $Z_{A\cdot S}1$, $Z_{A\cdot S}2$, Z_A1, and Z_A2 plotted from unsmoothed data.

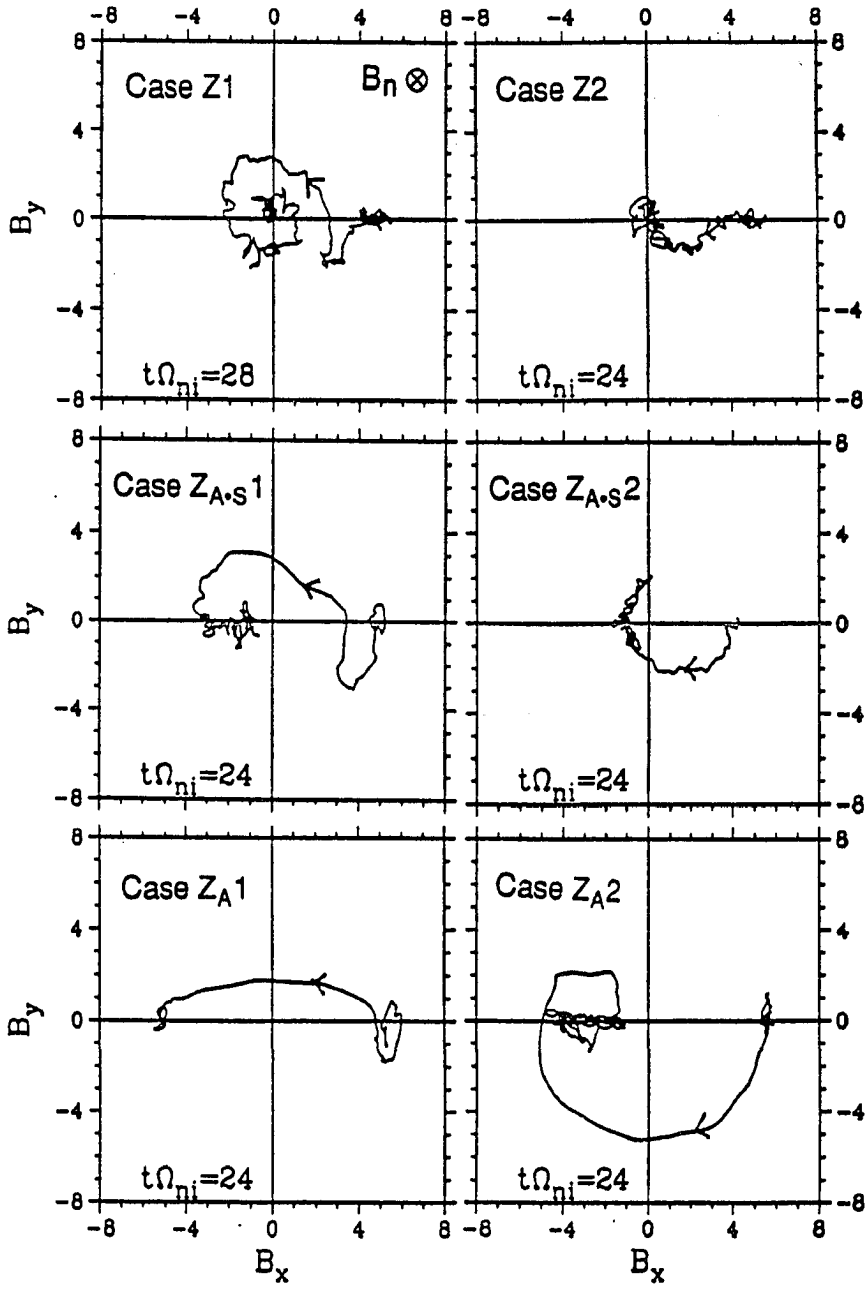

Figure 4.28 Summary of magnetic hodograms of Cases Z1, Z2, $Z_{A\cdot S}1$, $Z_{A\cdot S}2$, Z_A1, and Z_A2 plotted over smoothed data.

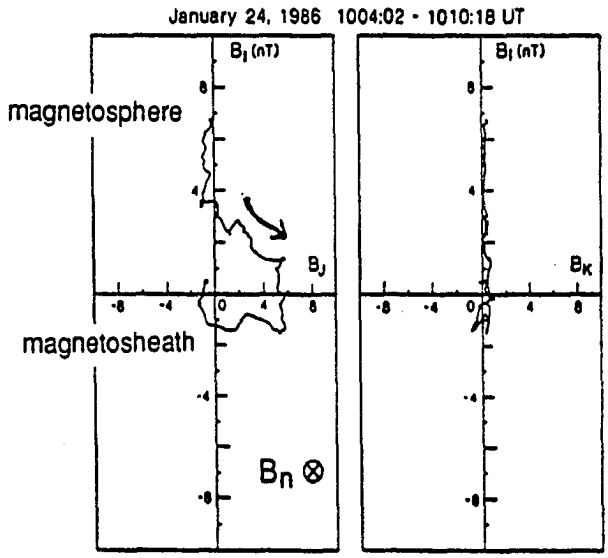

Figure 4.29 Hodogram of Voyager-2 magnetic field measurements across the Uranian magnetopause in the principal axis system [after *Russell et al.*, 1989]. The observed Uranian magnetopause may be a slow shock, which implies flow from magnetosphere to magnetosheath [*Russell et al.*, 1989]. The magnetic hodogram from magnetosphere to magnetosheath is characterized by a linearly polarized nonlinear wave followed by a right-hand polarized nonlinear wave, which is similar to the magnetic hodograms shown in the switch-off shock Case Z2 and the Alfvén-slow shock Case $Z_{A,S}2$ in Figure 4.28.

Lee et al. [1989*a*] called that the intermediate shock is unstable and will evolve into a rotational discontinuity with little jump in the magnetic field magnitude and plasma density. We disagree on their argument about the magnetic field structure evolve into a rotational discontinuity and we shall show that a stable density jump can always be found in our simulation results. We shall use Case Z_A2 as an example to demonstrate that the magnetic hodogram of Alfvén shock is similar but not identical to the magnetic hodogram of a rotational discontinuity. The magnetic hodogram of Case Z_A2 is similar the magnetic hodogram of intermediate shock Case F shown in Figure 10 in *Lee et al.* [1989*a*]. In both cases, the magnetic hodogram in the shock transition region consists of two parts, i.e., the upstream shock transition region with

a highly circularly polarized structure and the downstream shock transition region in which the magnetic field strength decreases toward the downstream side. Since the magnetic hodogram does not stop (or the magnetic field profile is not flat) at the connection between the upstream shock transition region and the downstream shock transition region, the two parts of magnetic hodogram cannot be treated as two separated nonlinear wave structures. It may be noted that highly circularly polarized magnetic hodograms can be found in the shock transition region of quasi-parallel fast shocks as discussed in Chapter 3 and in the switch-off shock Case Z1. However, no one ever doubts about the existence of switch-off shock and quasi-parallel fast shocks. Thus, the presence of a highly circularly polarized magnetic hodogram in the shock transition region should have nothing to do with the stability of the intermediate shock structures.

The evidence of compression and heating in the simulated Alfvén shocks is given in Figure 4.30 and 4.31 Figure 4.30 shows the spatial profiles of ion density and ion pressures (parallel pressure and perpendicular pressure) of the Alfvén shock Case Z_A1 at $t\Omega_{ni} = 0$ and 24. Figure 4.31 shows the spatial profiles of ion density and ion pressures of the Alfvén shock Case Z_A2 at $t\Omega_{ni} = 0$ and 24, where ion density profile shown in panel (c) is plotted with smoothed data over 10 c/ω_{pi}. An increase of the ion density and ion pressure across the shock ramp can be seen from both Figures 4.30 and 4.31. Thus, we can conclude that Alfvén shocks obtained in Case Z_A1 and Case Z_A2 do not turn into rotational discontinuities by the end of the simulations.

4.5.2 Intermediate Shocks With $\theta_{BN} = 45°$

For upstream plasma $\beta = 0.5$ and $\theta_{BN} = 45°$, only Alfvén shock and Alfvén-slow shock solutions can be found from the Rankine-Hugoniot jump conditions. Two

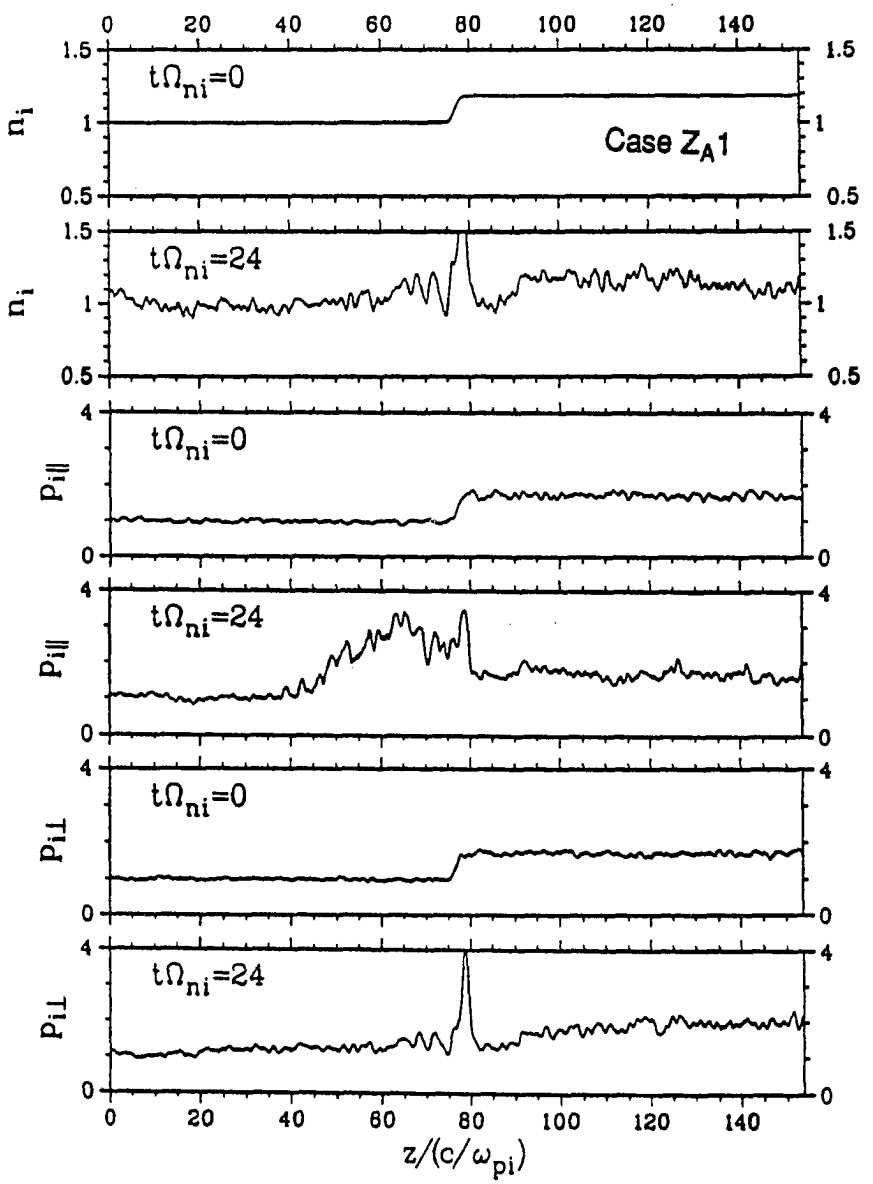

Figure 4.30 Spatial profiles of ion density and ion pressures (parallel pressure and perpendicular pressure) obtained from Alfvén shock simulation Case Z_A1 at $t\Omega_{ni} = 0$ and 24.

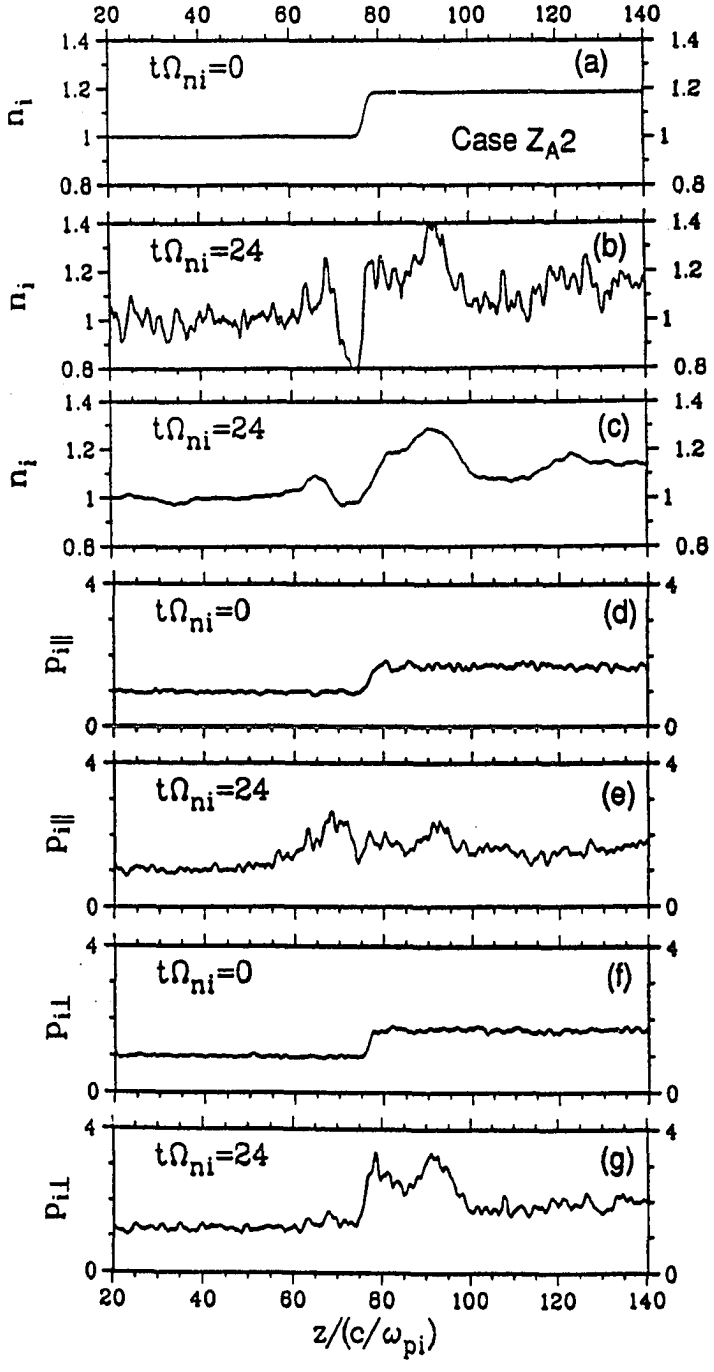

Figure 4.31 Spatial profiles of ion density and ion pressures obtained from Alfvén shock simulation Case Z_A2 at $t\Omega_{ni} = 0$ and 24, where ion density profile shown in panel (*c*) is plotted with smoothed data over 10 c/ω_{pi}.

examples with $M_A = 0.73$ (which is slightly greater than cos45° $\approx$ 0.7010...) are studied. One of them is Alfvén-slow shock as given by Case $S_{A\text{-}S}$ and the other is Alfvén shock as given by Case S_A. The initial ramp thickness of Cases $S_{A\text{-}S}$ and S_A is 30 c/ω_{pi}. The initial velocity profile is linearly polarized across the shock ramp in both cases. The initial tangential magnetic field is also linearly polarized across the shock ramp in both cases.

Simulation results of Case $S_{A\text{-}S}$ are given in Figures 4.32 and 4.33. Figure 4.32 shows the evolution of the tangential magnetic field hodogram of the simulation Case $S_{A\text{-}S}$. The hodogram of the Alfvén-slow shock Case $S_{A\text{-}S}$ is characterized by a linearly polarized nonlinear wave field followed by a left-hand polarized nonlinear wavetrain on the downstream side. Again, the left-hand polarized wavetrain structure is similar to the structure commonly found in simulation studies of switch-off shocks — the neighboring solutions of Alfvén-slow shock solutions. Note that in this case the upstream $\gamma\beta/2$ is slightly less than $\cos^2\theta_{BN}$. When the upstream $\gamma\beta/2$ is much less than the $\cos^2\theta_{BN}$, no large-amplitude downstream wavetrains are present in the switch-off shocks simulated by *Omidi and Winske* [1989] and the simulated Alfvén-slow shocks to be discussed in Section 4.5.3. Figure 4.33 shows the spatial profiles of tangential magnetic fields B_x and B_y at successive times for the Alfvén-slow shock Case $S_{A\text{-}S}$. As we can see, the transition region of this Alfvén-slow shock is about 50–100 c/ω_{pi}.

Simulation results of Case S_A are given in Figures 4.34 and 4.35. Figure 4.34 shows the evolution of tangential magnetic field hodogram of the simulation Case S_A. Hodograms in panels (*a*)–(*c*) are plotted from $z = 110\ c/\omega_{pi}$ to $z = 250\ c/\omega_{pi}$. Hodogram shown in panel (*d*) is plotted from $z = 130\ c/\omega_{pi}$ to $z = 250\ c/\omega_{pi}$. Figure 4.35 shows the spatial profiles of tangential magnetic fields B_x and B_y at

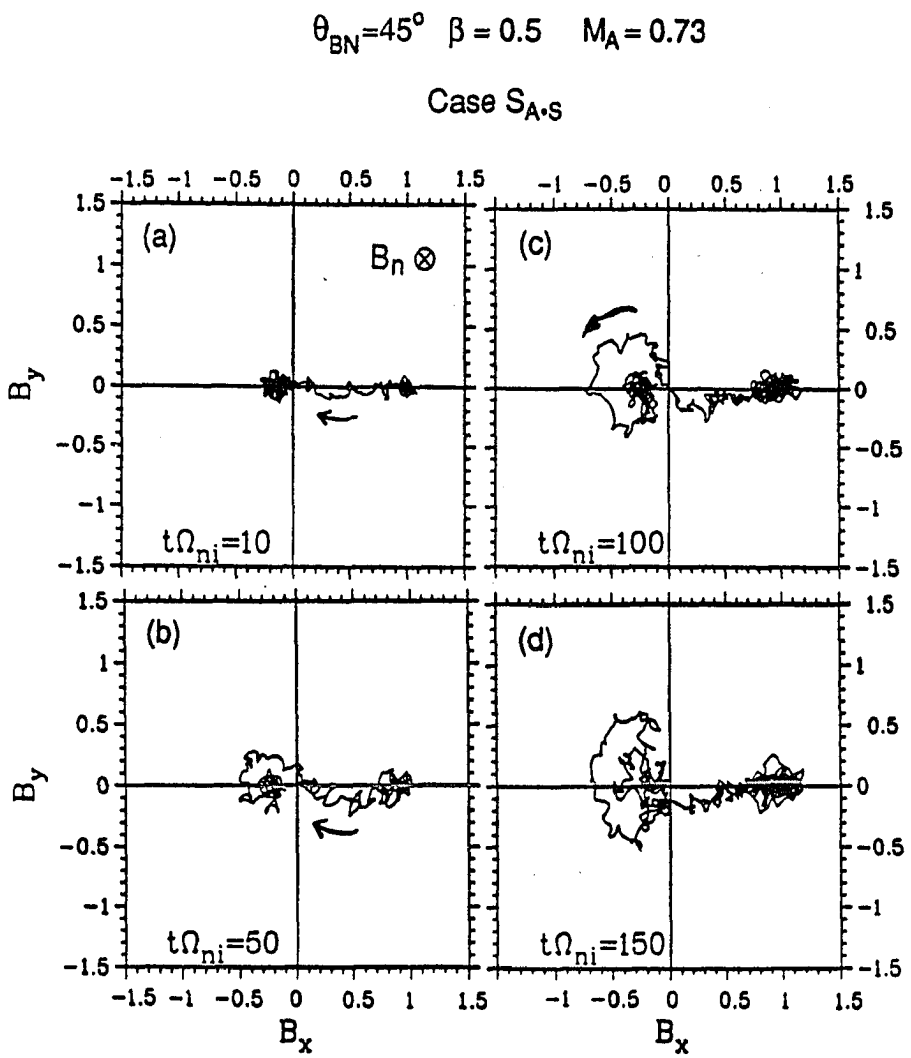

Figure 4.32 Magnetic hodogram of Alfvén-slow shock simulation Case $S_{A\text{-}S}$. The hodogram of Case $S_{A\text{-}S}$ can be characterized by a linearly polarized nonlinear wave field followed by a left-hand polarized nonlinear wavetrain downstream of the shock front.

successive times for the Alfvén shock Case S_A. The transition region of the Alfvén shock Case S_A shown in Figure 4.35 is about 30–50 c/ω_{pi}, which is much narrower than the transition regions of the Alfvén-slow shock Case $S_{A\text{-}S}$ shown in Figure 4.33. According to the spatial profiles shown in Figure 4.35, the nonlinear wave shown on the upstream side of the hodogram in panel (*c*) of Figures 4.34 does not belong

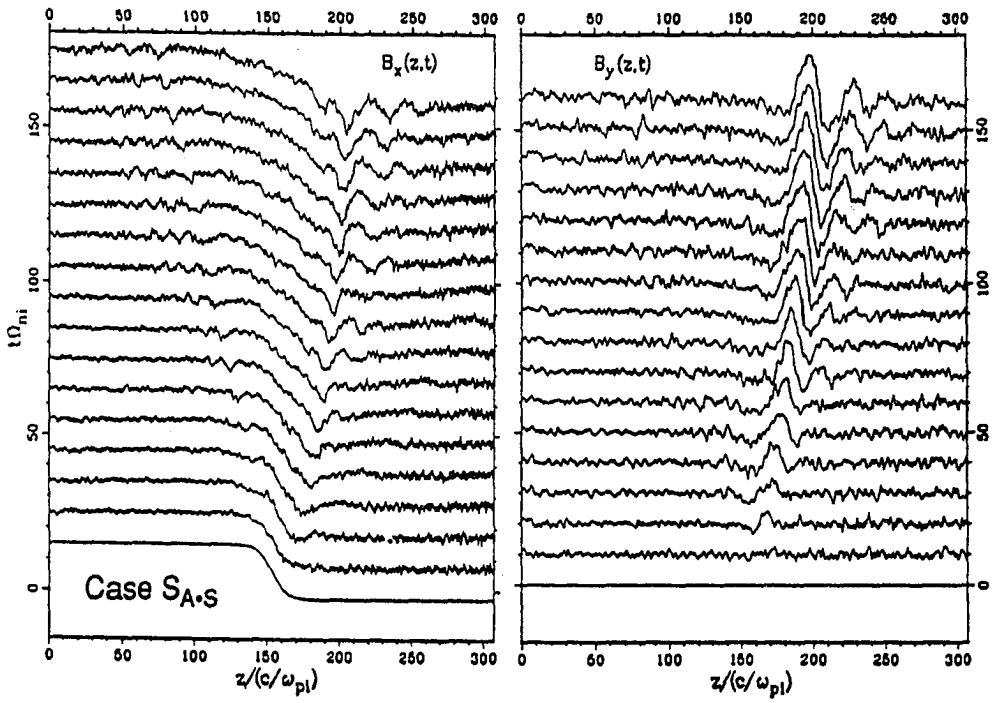

Figure 4.33 Spatial profiles of tangential magnetic fields B_x and B_y obtained from Alfvén-slow shock simulation Case $S_{A\cdot S}$ plotted at successive times.

to the Alfvén shock. From density profile (not shown) the upstream nonlinear wave is a fast-mode rarefaction soliton as discussed in Chapter 2. Thus, the hodograms shown in panel (*d*) of Figure 4.34 can represent the magnetic hodogram of the Alfvén shock Case S_A, which is characterized by a right-hand polarized nonlinear wave field followed by a left-hand polarized, banana-shaped (or hook-shaped) nonlinear wave structures on the downstream side. Note that the initially linearly polarized tangential magnetic field across the shock ramp is responsible for the generation of the upstream fast-mode rarefaction soliton structure. We are able to simulate the Alfvén shock Case S_A with a linearly polarized initial B field because both the amplitude and propagation speed of the fast-mode rarefaction soliton generated in the Alfvén shock with $\theta_{BN} = 45°$ is relatively smaller than the one generated in an Alfvén shock with $\theta_{BN} = 80°$

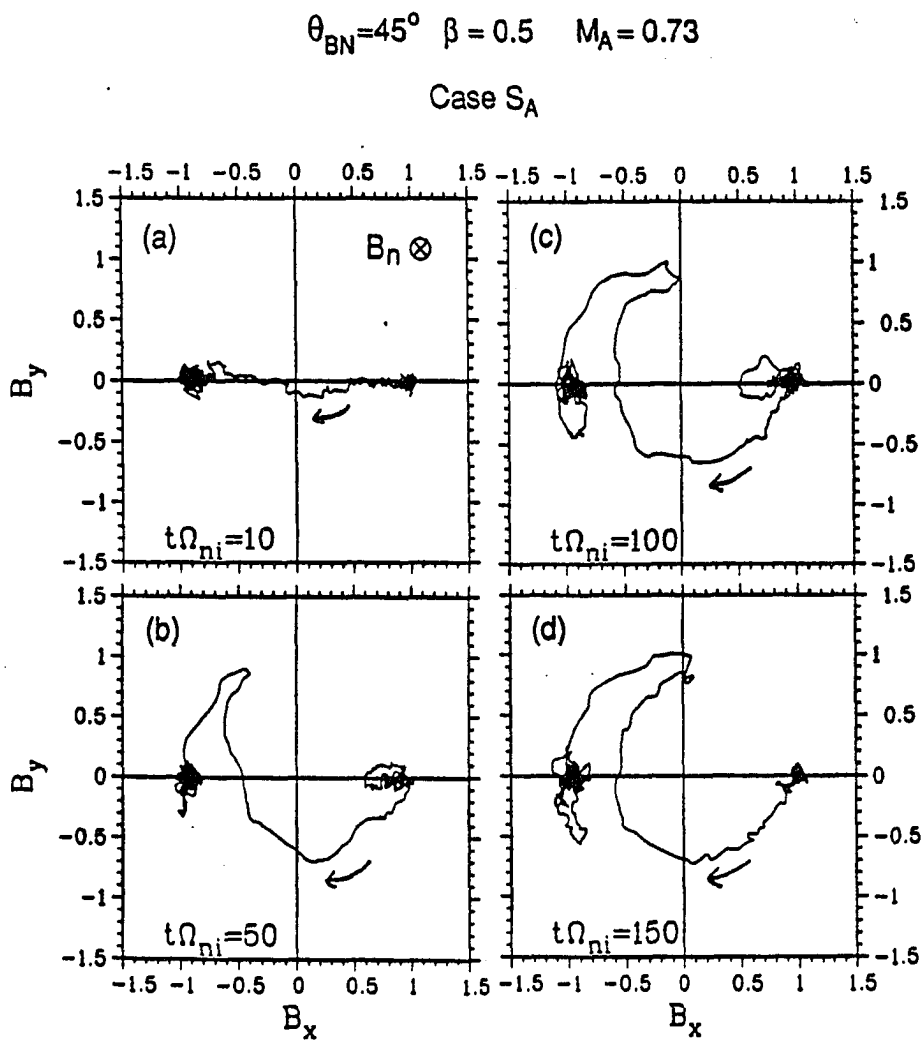

Figure 4.34 Magnetic hodogram of Alfvén shock simulation Case S_A, where panels (*a*)–(*c*) are plotted over unsmoothed data $z = 110\ c/\omega_{pi}$ to $z = 250\ c/\omega_{pi}$; and panel (*d*) is plotted over unsmoothed data from $z = 130\ c/\omega_{pi}$ to $z = 250\ c/\omega_{pi}$. The upstream close-loop magnetic hodogram shown in panel (*c*) belongs to a nonlinear fast-mode rarefaction soliton, which is not part of the S-shaped rotational structure. The fast mode soliton is located near $z = 100$–$110\ c/\omega_{pi}$ at $t\Omega_{ni} = 150$ (to be shown in Figure 4.35). Thus, the fast-mode rarefaction soliton is absent from the hodogram plot shown in panel (*d*).

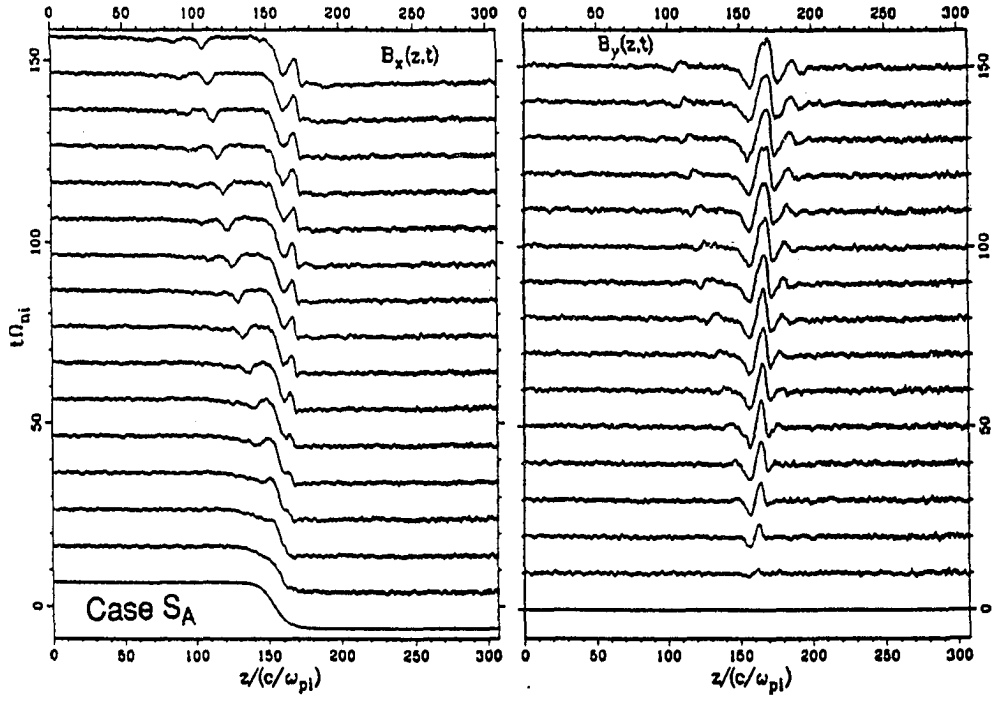

Figure 4.35 Spatial profiles of tangential magnetic fields B_x and B_y obtained from Alfvén shock simulation Case S_A plotted at successive times. A stable Alfvén shock is formed after the rarefaction fast-mode soliton structure is detached from the shock ramp.

as those studied in Section 4.5.1. In addition, the simulation system length used in this section is twice as long as the one used in Section 4.5.1.

Again, we shall show the evidence of compression and heating in the simulated Alfvén shock Case S_A. Figure 4.36 shows the spatial profiles of ion density and ion pressures (parallel pressure and perpendicular pressure) of the Alfvén shock Case S_A at $t\Omega_{ni} = 50$ and 100. As we can see, ion density and ion pressure have reached to a quasi-steady state during the period of $t\Omega_{ni} = 50$–100. An increase of the ion density and ion pressure across the shock ramp can be seen in Figure 4.36. Figure 4.37 shows the spatial profiles of $p\rho^{-\gamma}$ and ion temperature T_i of the Alfvén shock Case S_A at $t\Omega_{ni} = 100$. An increase of entropy and ion temperature across the Alfvén shock

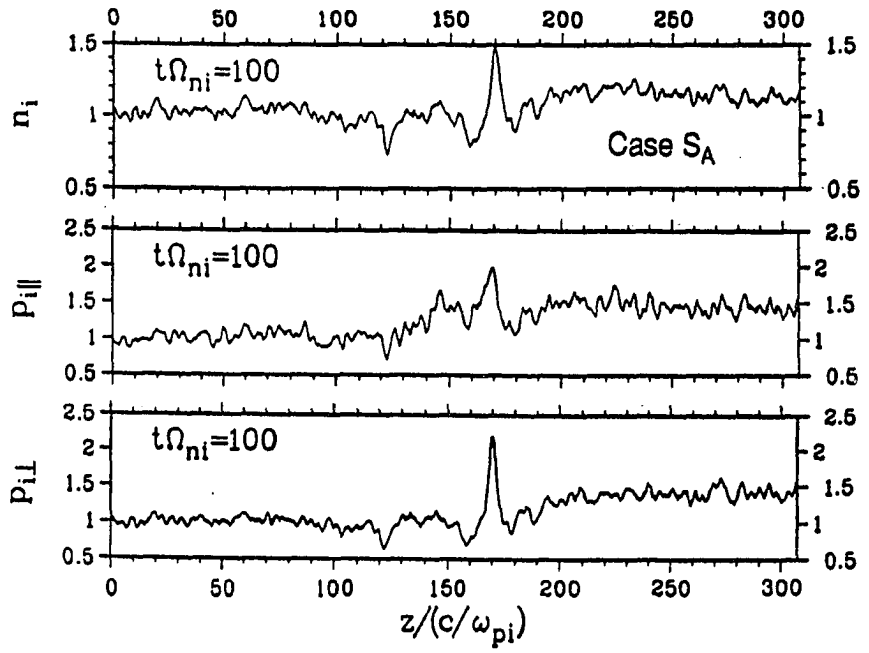

Figure 4.36 Spatial profiles of ion density and ion pressures (parallel pressure and perpendicular pressure) obtained from Alfvén shock simulation Case S_A at $t\Omega_{ni}$ = 100. A net increase on ion density and ion pressure can be seen across the shock ramp in this figure.

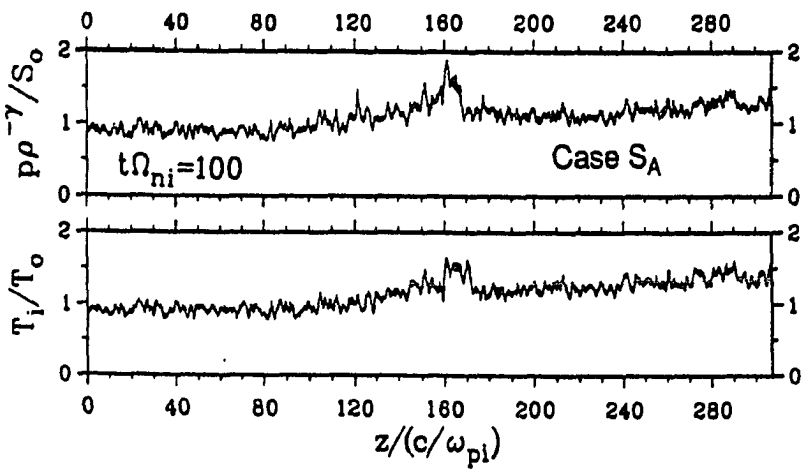

Figure 4.37 Spatial profiles of $p\rho^{-\gamma}$ and ion temperature T_i obtained from Alfvén shock simulation Case S_A at $t\Omega_{ni}$ = 100. An increase on entropy and ion temperature can be seen across the shock ramp in this figure.

ramp can also be seen in Figure 4.37. Thus, we can conclude that the Alfvén shock Case S_A does not turn into a rotational discontinuity by the end of the simulation.

4.5.3 Quasi-Parallel Intermediate Shocks With $\theta_{BN} = 10°$

For upstream plasma $\beta = 0.5$ and $\theta_{BN} = 10°$, all four types of intermediate shock solutions can be found from the Rankine-Hugoniot jump conditions. Four examples to be studied in this section are denoted on the intermediate shock solution curve as shown in Figure 4.38. They are Alfvén-slow shock Case $Q_{A\text{-}S}$, fast-Alfvén-slow shock Case $Q_{F\text{-}A\text{-}S}$, fast-Alfvén shock Case $Q_{F\text{-}A}$, and Alfvén shock Case Q_A. The Mach number of Cases $Q_{A\text{-}S}$ and Q_A is chosen to be $M_A = 1.0$ (which is slightly greater than $\cos 10° \approx 0.9848...$). The Mach number of Cases $Q_{F\text{-}A\text{-}S}$ and $Q_{F\text{-}A}$ is chosen to be $M_A = 1.2$, which is the same as the first example of quasi-parallel fast shock studied in Chapter 3. The initial ramp thickness of the four cases is 30 c/ω_{pi}. The initial velocity profile is linearly polarized across the shock ramp in all four cases. The initial tangential magnetic field is also chosen to be linearly polarized across the initial shock ramp in all four cases.

Figure 4.39 shows the magnetic hodograms of the fast-Alfvén shock Case $Q_{F\text{-}A}$ and the fast-Alfvén-slow shock Case $Q_{F\text{-}A\text{-}S}$. The magnetic hodograms of the neighboring solutions Case $Q_{F\text{-}A}$ and Case $Q_{F\text{-}A\text{-}S}$ are very similar to each other, which are characterized by S-shaped magnetic hodogram with large amplitude nonlinear wavetrains on the upstream and downstream side. Figure 4.40 shows the magnetic hodograms of the Alfvén shock Case Q_A and the Alfvén-slow shock Case $Q_{A\text{-}S}$. The S-shaped magnetic hodograms shown in Case Q_A and Case $Q_{A\text{-}S}$ are very flat. All the S-shaped magnetic hodograms shown in Figure 4.39 and 4.40 are characterized by right-hand polarized wave filed on the upstream side and then followed by left-hand

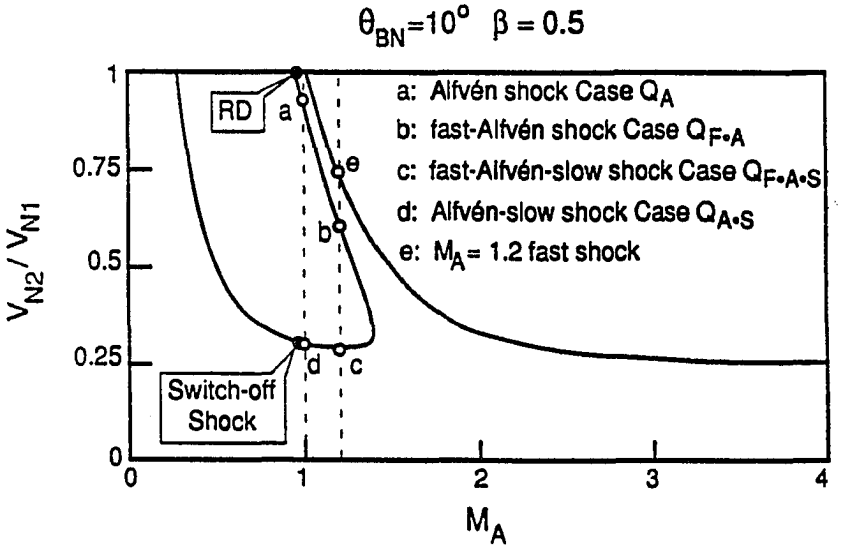

Figure 4.38 Rankine-Hugoniot jump conditions of fast shocks, intermediate shocks and slow shocks at $\theta_{BN} = 10°$ and $\beta = 0.5$. The jump conditions of intermediate shocks Cases Q_A, $Q_{F\text{-}A}$, $Q_{F\text{-}A\text{-}S}$, $Q_{A\text{-}S}$ and fast shock with $M_A = 1.2$ are denoted by points *a–e*.

polarized wave field on the downstream side. No large amplitude wavetrain structure can be found on the downstream side of the Alfvén-slow shock Case $Q_{A\text{-}S}$ in Figure 4.40. Simulation Case $Q_{A\text{-}S}$ is characterized by upstream $\gamma\beta/2$ much less than the $\cos^2\theta_{BN}$. For upstream $T_i = T_e$, we have $\gamma\beta_i < \cos^2\theta_{BN}$ for Case $Q_{A\text{-}S}$. Simulation results obtained by *Omidi and Winske* [1989] indicate that for $\gamma\beta_i < \cos^2\theta_{BN}$, no large amplitude downstream waves can be found in switch-off shock simulations. Again, the neighboring solutions, Alfvén-slow shocks and the switch-off shock, show a similar characteristic on the upstream parameter dependence.

Figure 4.41 plots the ion density profiles and total magnetic field profile of the Alfvén shock Case Q_A at successive times. The tick mark on the vertical axis not only denotes the time of each curve but also denotes the zero density or $B = 0$ with respect to each curve. Thus, we can obtain the percentage of ion density jump (or total

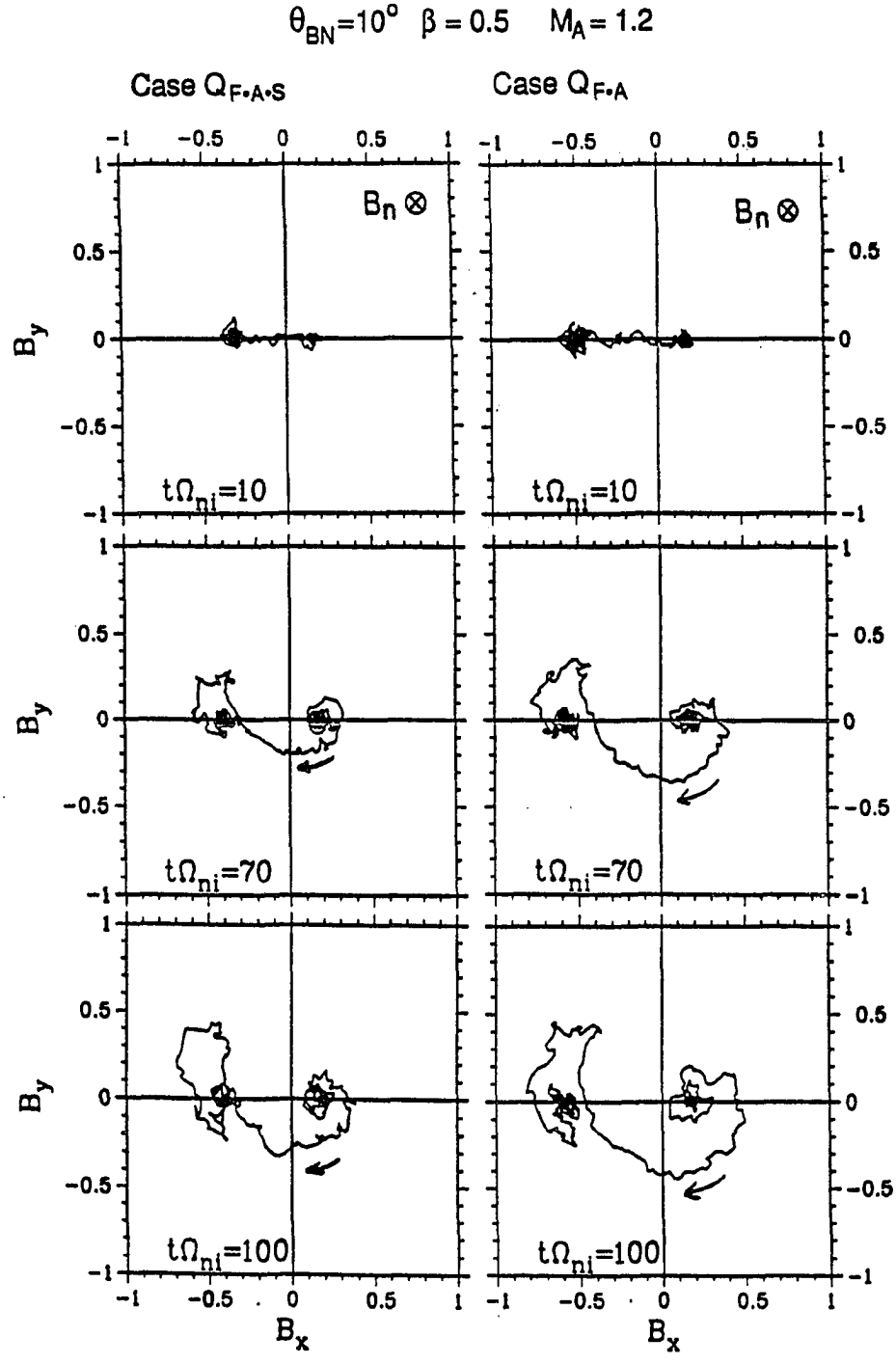

Figure 4.39 Magnetic hodograms obtained from hybrid simulations of fast-Alfvén-slow shock Case $Q_{F\cdot A\cdot S}$ and fast-Alfvén shock Case $Q_{F\cdot A}$.

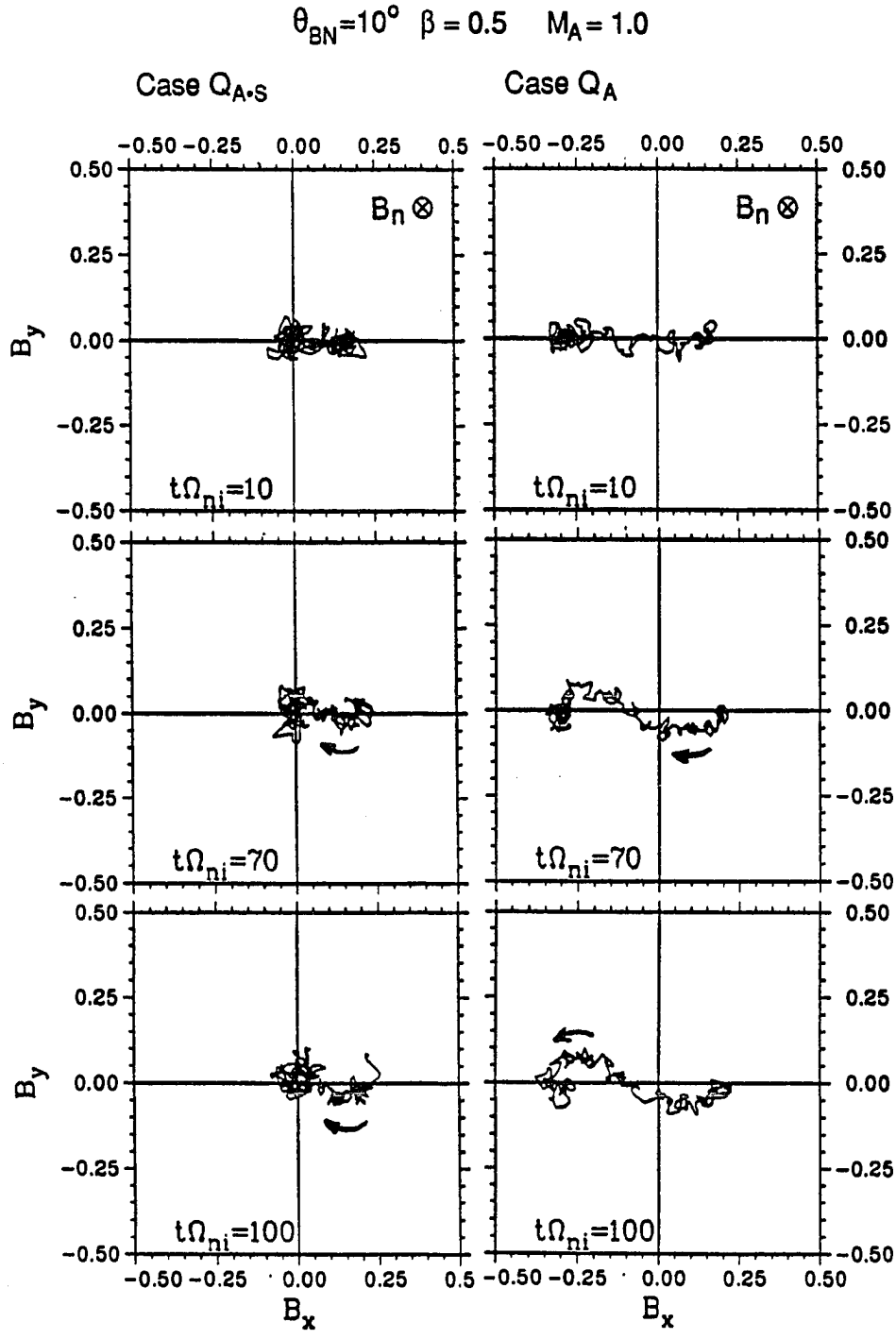

Figure 4.40 Magnetic hodograms obtained from hybrid simulations of Alfvén-slow shock Case $Q_{A\text{-}S}$ and Alfvén shock Case Q_A.

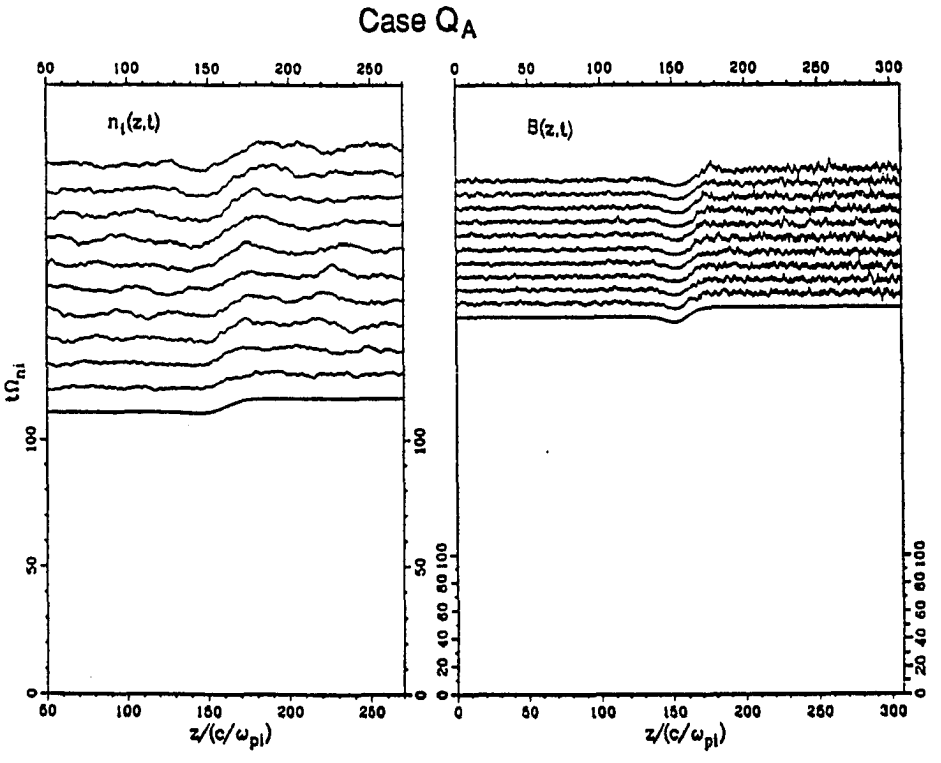

Figure 4.41 Spatial profiles of the ion density and total magnetic field obtained from Alfvén shock simulation Case Q_A plotted at successive times. The tick mark on the vertical axis denotes the time of each curve and also denotes the zero density or $B = 0$ with respect to each curve. Small but stable density jump and total magnetic field jump can be seen across the shock transition region.

magnetic field jump) across the shock ramp with respect to the upstream ion density (or upstream total magnetic field) from Figure 4.41. There are less than 3% density changes across the shock ramp in this case. To reveal the small density jump from numerical noise, the density profiles shown in Figure 4.41 are plotted with smoothed data over 10 c/ω_{pi}. Again, the evidence of compression shown in Figure 4.41 indicates that the Alfvén shock Case Q_A does not turn into rotational discontinuities by the end of the simulation.

Although the upstream boundary conditions of the fast-Alfvén shock Case $Q_{F\text{-}A}$ and the fast-Alfvén-slow shock Case $Q_{F\text{-}A\text{-}S}$ are the same as the $M_A = 1.2$ fast shock

studied in Chapter 3, the density jump and temperature jump across the shock ramp in Cases $Q_{F\cdot A}$ and $Q_{F\cdot A\cdot S}$ are stronger than the density jump and temperature jump across the $M_A = 1.2$ fast shock shown in Chapter 3. The $M_A = 1.2$ fast shock is laminar shock. No magnetic field overshoot, no large amplitude upstream waves, and no large numbers of leakage ions can be found in the $M_A = 1.2$ fast shock simulation, but all of them can be found in the fast-Alfvén shock Case $Q_{F\cdot A}$ and in the fast-Alfvén-slow shock Case $Q_{F\cdot A\cdot S}$. Figure 4.42 shows the spatial profiles of B_x, B_y, N_i, and B of the fast-Alfvén shock simulation Case $Q_{F\cdot A}$ at successive times. Large amplitude nonlinear waves can be seen in the B_y profiles. An overshoot structure can be seen on the profiles of total magnetic field B. Similar results can be found in the fast-Alfvén-slow shock simulation study of Case $Q_{F\cdot A\cdot S}$. Various types of spatial profiles for Case $Q_{F\cdot A\cdot S}$ are plotted in Figure 4.43. Figure 4.43 shows the spatial profiles of ion density N_i, ion temperature T_i, ion normal flow velocity V_z, ion heat flux q_{zi}, total magnetic field B, and tangential magnetic field B_x, B_y at $t\Omega_{ni} = 100$. The wide-spread negative q_{zi} signature upstream from the shock front indicates that large numbers of hot ions leak across the shock ramp. Ion temperature increases in the foreshock region due to presence of leakage ion populations. Similar spatial profiles can be found in the fast-Alfvén shock simulation of Case $Q_{F\cdot A}$. The simulation results of fast-Alfvén shock Case $Q_{F\cdot A}$ and fast-Alfvén-slow shock Case $Q_{F\cdot A\cdot S}$ can be used to explain nonlinear discrete wave packets observed upstream from quasi-parallel shocks.

Discrete wave packets or steepened magnetosonic waves have been observed upstream from Earth bow shocks associated with diffuse ion populations by ISEE 1 and 2 spacecraft [e.g., *Hoppe et al.*, 1981; *Le et al.*, 1989] and at comet Giacobini-Zinner by ICE spacecraft [e.g., *Tsurutani and Smith*, 1986; *Tsurutani et al.*, 1987; *Le et al.*, 1989]. Figure 4.44 shows an example of discrete wave packet observed by ISEE 1

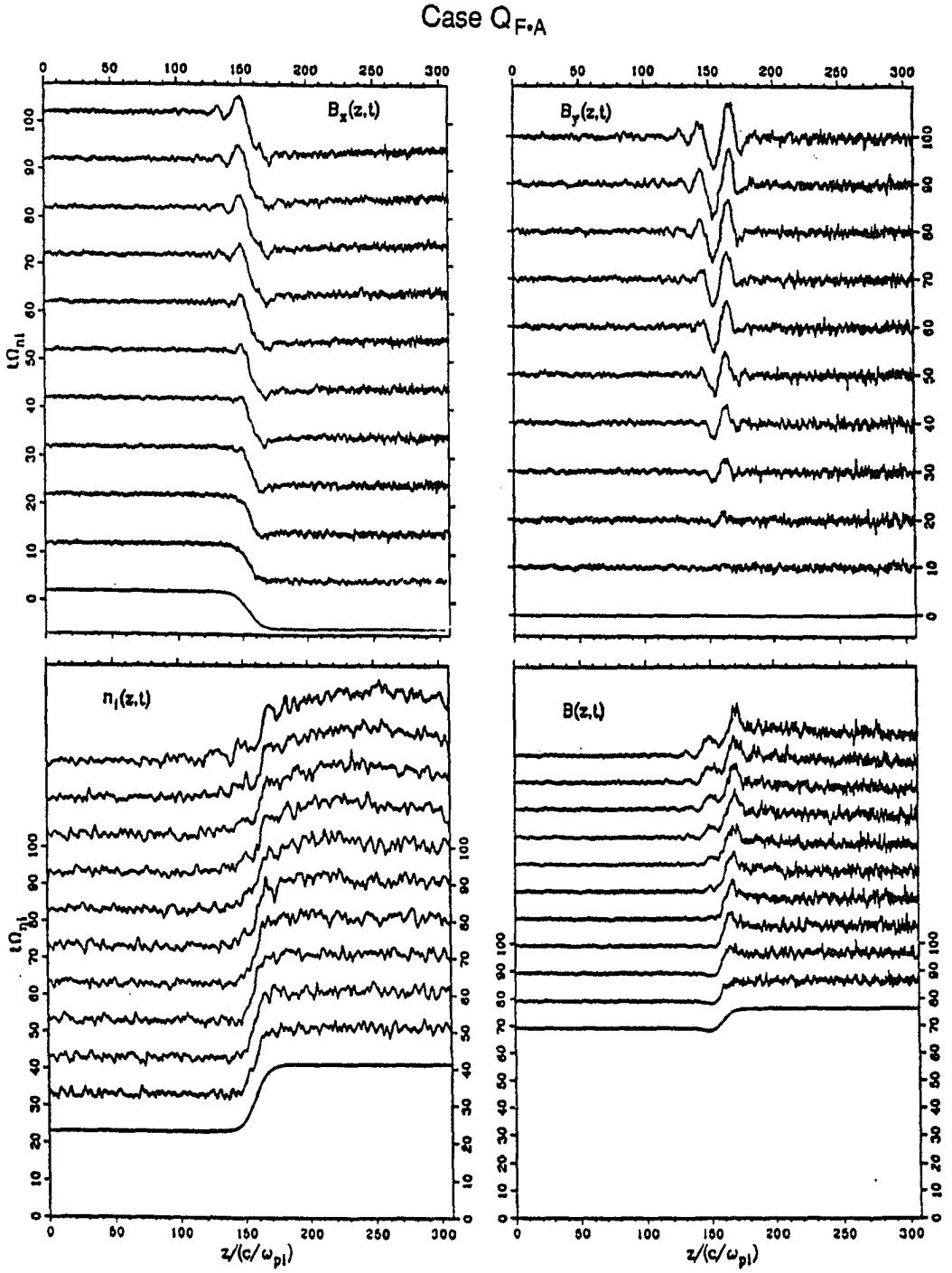

Figure 4.42 Spatial profiles of B_x, B_y, N_i and B obtained from fast-Alfvén shock simulation Case $Q_{F\cdot A}$ plotted at successive times.

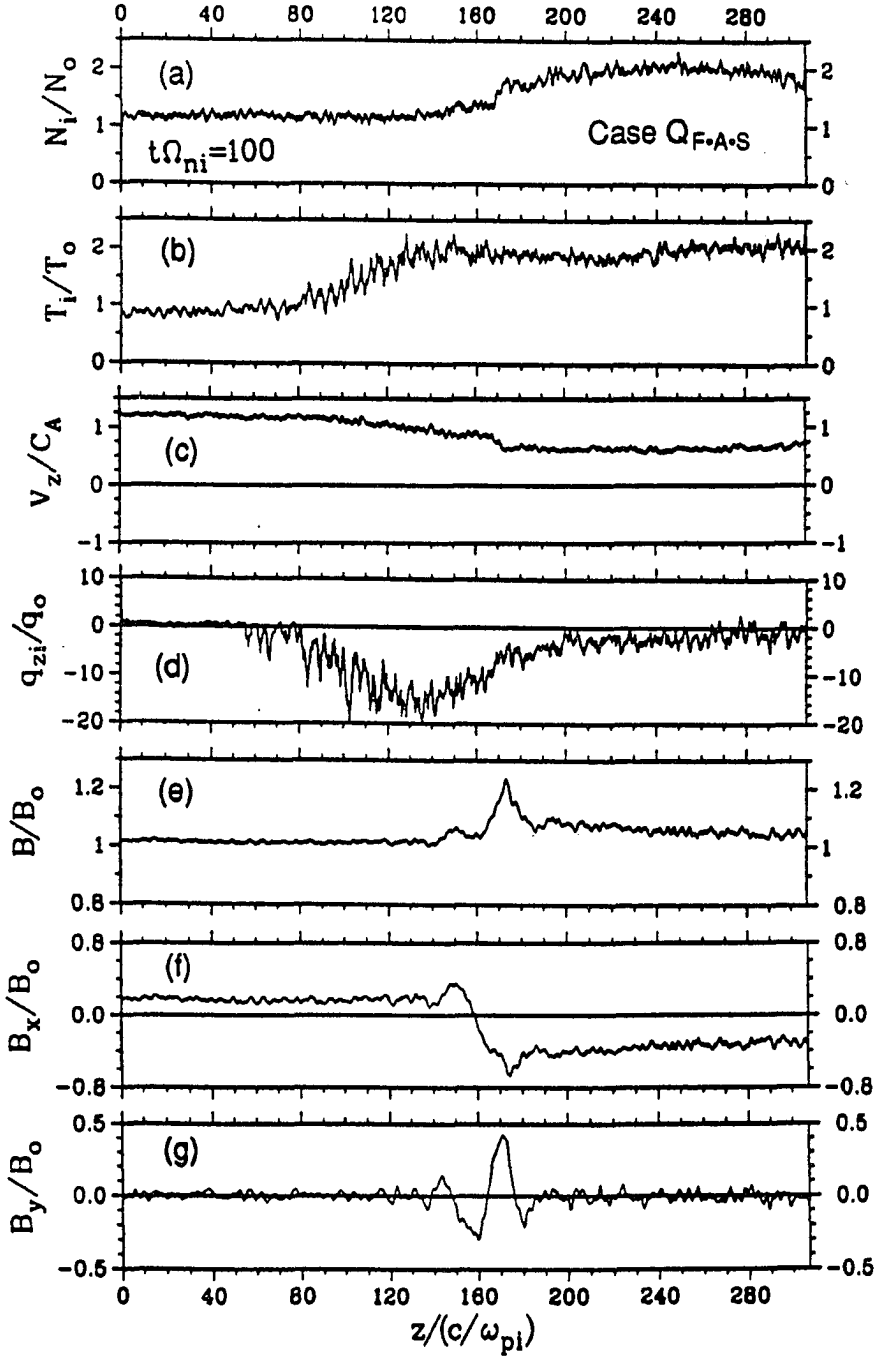

Figure 4.43 Spatial profiles of ion density N_i, ion temperature T_i, ion normal flow velocity V_z, ion heat flux q_{zi}, total magnetic field B, and tangential magnetic field B_x, B_y obtained from fast-Alfvén-slow shock simulation Case $Q_{F\cdot A\cdot S}$ at $t\Omega_{ni} = 100$.

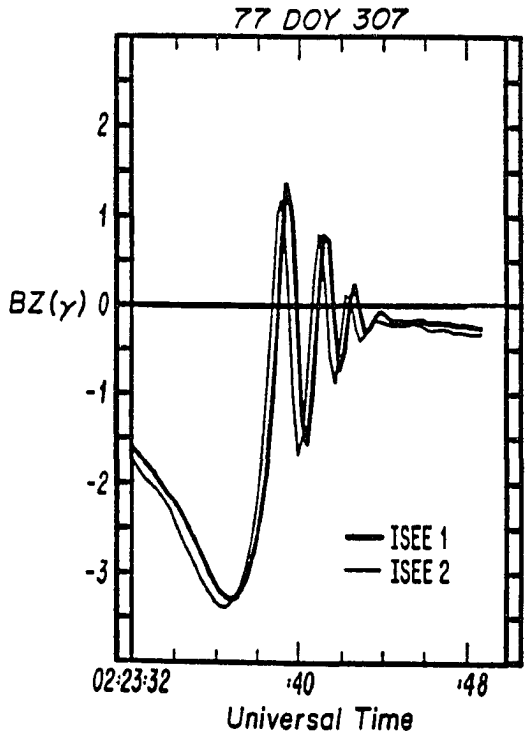

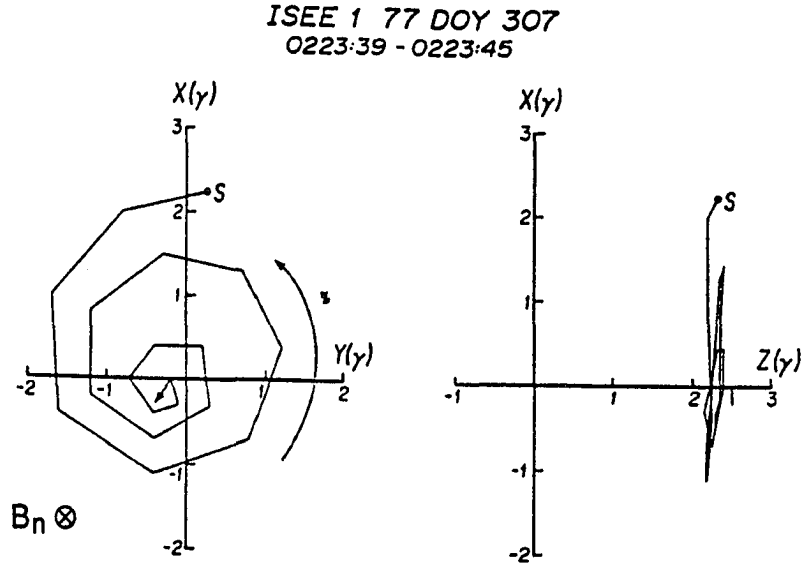

Figure 4.44 An example of discrete wave packet observed by ISEE 1 and 2 [after *Hoppe et al.*, 1981].

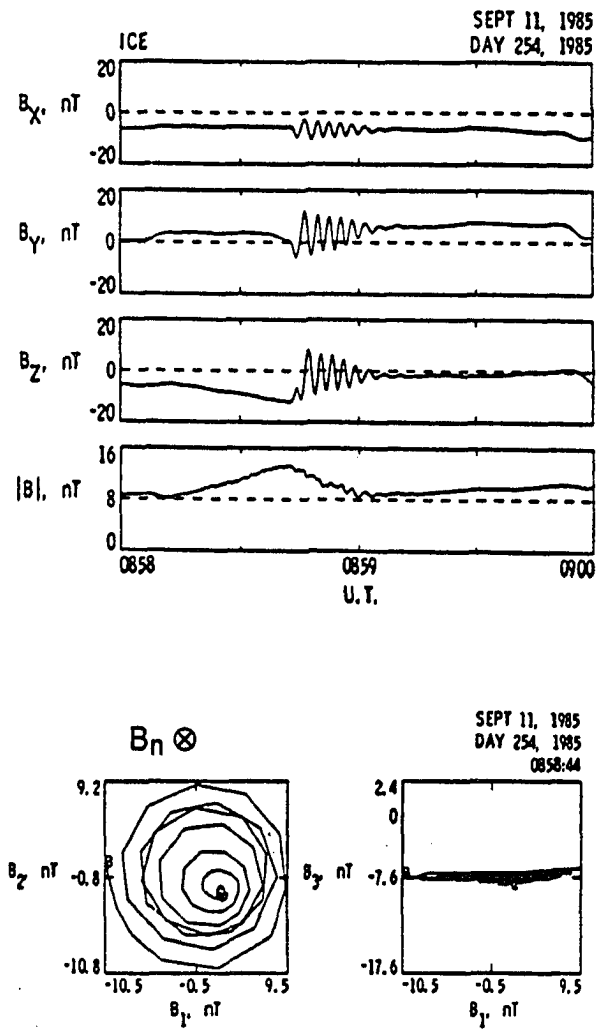

Figure 4.45 An example of steepened magnetosonic waves observed by ICE spacecraft [after *Tsurutani et al.*, 1986].

and 2 [*Hoppe et al.*, 1981]. Figure 4.45 shows an example of steepened magnetosonic waves observed by by ICE spacecraft [*Tsurutani and Smith*, 1986]. These observed nonlinear wave packets are plane waves with small θ_{BN}. *Le et al.* [1989] reported that 99% of all the discrete wave packets observed at comet Giacobini-Zinner and 82% of the discrete wave packets observed upstream from earth bow shock in the time interval they studied are propagating within 45° to the average magnetic field

and no waves are propagating at an angle larger than 60°. The propagation speed of these discrete wave packets are slower than the solar wind speed at 1 AU. Namely, if these observed discrete wave packets are shock waves, shocks with propagation speed slightly greater than the fast mode speed may be considered as the candidates of these observed nonlinear waves. Fast shock with structure similar to the $M_A = 2$ fast shock studied in Chapter 3 may be the best candidates of these observed nonlinear waves. However, with decreasing Mach number, no large amplitude upstream waves and large numbers of leakage ions can be found in the fast shock simulation of the $M_A = 1.2$ shock studied in Chapter 3. On the other hand, with the same Mach number ($M_A = 1.2$), large amplitude upstream waves and large numbers of leakage ions can be found in the fast-Alfvén shock Case $Q_{F\text{-}A}$ and the fast-Alfvén-slow shock Case $Q_{F\text{-}A\text{-}S}$ studied in this chapter. According to the Rankine-Hugoniot jump conditions, fast-Alfvén shocks and fast-Alfvén-slow shocks can only be found at small θ_{BN}, which is also consistent with the observational report given by *Le et al.* [1989]. Thus, we may conclude that if the observed discrete wave packets are shock waves, fast-Alfvén shocks, fast-Alfvén-slow shocks and fast shocks with structure similar to the $M_A = 2$ fast shock studied in Chapter 3 are the possible candidates of these observed nonlinear waves. Note that the $M_A = 2$ shock discussed in Chapter 3 is a quasi-parallel fast shock with Mach number greater than the first critical Mach number (M_{C1}) but less than the second critical Mach number (M_{C2}) as defined in Chapter 3; whereas, fast-Alfvén shocks and fast-Alfvén-slow shocks are mostly quasi-parallel shocks with a Mach number less than M_{C1}.

4.6 S-Shaped Rotational Structures

Since switch-off slow shock and Alfvén-slow shocks are neighboring solutions, we have considered them as a group of nonlinear wave solutions to compare with observations. Similar approaches can be applied to the neighboring solutions of S-shaped 180° rotational discontinuity and S-shaped Alfvén shocks. For convenience, they will be called the S-shaped rotational structure in the following discussions.

S-shaped rotational structures have been observed in the solar wind [e.g., *Neugebauer*, 1989] and at the magnetopause [e.g., *Berchem and Russell*, 1982] as have been discussed in Chapter 2. No large amplitude downstream (or upstream) wavetrain structure have been found to associate with these observed S-shaped rotational structures. Thus, we may conclude that these observed S-shaped rotational structures are not formed by an over-steepened rotational ramp (i.e., an extremely thin initial ramp). Instead, these rotational structures are likely be formed by a not purely Alfvénic disturbance. Rotational discontinuities simulations shown in Cases G3 and G4 and all the Alfvén shock simulations shown in this chapter may provide a possible cue on the formation of those observed S-shaped rotational structures in the solar wind and at the Earth magnetopause. Note that it is hard to determine the flow direction in observed low Mach number nonlinear waves. However, it can be shown that the polarization characteristics of an S-shaped rotational structure is independent to the normal flow direction. Thus, we can conclude that the S-shaped rotational structure observed at Earth magnetopause by *Berchem and Russell* [1982] as shown in Figure 2.31*a* is characterized by a right-hand polarized nonlinear wave structure followed by a left-hand polarized nonlinear wave structure. I strongly suggest that the sophisticated method introduced by *Neugebauer and Buti* [1990] to determine the normal flow direction should be widely used in future studies of planetary magnetopause structures

and other nonlinear hydromagnetic waves observed upstream from quasi-parallel bow shocks.

4.7 Summary

Structures of rotational discontinuities, switch-off shock and intermediate shocks are studied in this chapter using hybrid simulations. New results obtained in this chapter are listed below.

(1) *Non-S-Shaped RDs at Small θ_{BN}.* Non-S-shaped rotational discontinuities with upstream $\gamma\beta/2 < \cos^2\theta_{BN}$ are obtained in this chapter for the first time from hybrid simulation. The simulation results shown by Cases G1 and G2 in Sections 4.3 are consistent with the theoretical predictions obtained in Chapter 2. Namely, for upstream $\gamma\beta/2 < \cos^2\theta_{BN}$ (or $C_A < V_{AX}$) the magnetic hodogram is highly circularly polarized for a left-hand polarized RD, but relatively flat for a right-hand polarized RD.

(2) *Quasi-Laminar S-Shaped Rotational Structures.* For both $\gamma\beta/2 < \cos^2\theta_{BN}$ and $\gamma\beta/2 > \cos^2\theta_{BN}$, S-shaped rotational structures without large amplitude upstream or downstream wavetrain structure have been obtained in this chapter for the first time from hybrid simulation with a non-Alfvénic initial ramp field.

(3) *Quasi-Laminar Subcritical Switch-Off Shock.* Subcritical switch-off shock without a large amplitude downstream wavetrain has been obtained in this chapter for the first time from hybrid simulation as shown by Case Z2 in Section 4.4. The subcritical switch-off shock is characterized by a linearly polarized nonlinear wave in the upstream shock transition region followed by a right-hand polarized nonlinear wave in the downstream shock transition region. We have also shown that the magnetic hodogram of the Uranian magnetopause observed by Voyager 2 [*Russell et al.*, 1989]

is similar to the magnetic hodograms obtained in the simulation studies of subcritical switch-off shock Case Z2 and its neighboring solution Alfvén-slow shock Case $Z_{A,S}2$.

(4) *Stable Intermediate Shocks.* Intermediate shocks with stable structures are obtained in this chapter for the first time from hybrid simulations. Intermediate shocks obtained in this chapter include quasi-perpendicular Alfvén shock and Alfvén-slow shock and quasi-parallel Alfvén shock, Alfvén-slow shock, fast-Alfvén shock and fast-Alfvén-slow shock. Systematic changes among switch-off shocks, RDs, and intermediate shocks have also been studied in this chapter for the first time from hybrid simulations.

Future studies on subjects related to those presented in this chapter should include the following:

(1) *Hybrid simulation study of RDs with rotational angle different from 180°.* Formation of the staple-shaped RDs, Ω-shaped RDs, and S-shaped RDs with left-hand polarized nonlinear waves followed by right-hand polarized nonlinear wave as predicted in Chapter 2 for both $\gamma\beta/2 < \cos^2\theta_{BN}$ and $\gamma\beta/2 > \cos^2\theta_{BN}$ plasmas should be studied based on hybrid simulation with a rotational angle different from 180°.

(2) *Hybrid simulation study of planetary magnetopause.* Simulation study of planetary magnetopause should be pursued based on the observed boundary conditions. The Earth magnetopause are often shown with two different plasma populations on two sides of the rotational structure. It is interesting to study the effect on the magnetic field configuration due to the different plasma temperature and plasma density imposed on the two sides of a rotational structure.

(3) *Comprehensive simulation study of intermediate shocks.* Comprehensive simulation study used in Sections 4.3, 4.4 and 4.5.1 should apply to the study of inter-

mediate shocks in Sections 4.5.2 and 4.5.3. Various types of shock structures are expected to be found in each intermediate shock shown in Sections 4.5.2 and 4.5.3.

(4) *Comprehensive simulation study of supercritical switch-off shocks and non-switch-off slow mode shocks.* Comprehensive simulation study used in Sections 4.3, 4.4 and 4.5.1 should apply to the study of supercritical switch-off shocks with $\gamma\beta/2 \ll \cos^2\theta_{BN}$ (or $\gamma\beta_i \ll \cos^2\theta_{BN}$) and non-switch-off slow mode shocks in the future. It may be noted that if ion reflection takes place in a supercritical slow shock, the number of reflected ions should be much greater than the one shown in Case Z2 due to a small thermal spread of incoming upstream ion distribution. As a result, the magnetic field configuration of a quasi-perpendicular supercritical slow shock may be more turbulent than the one shown in Case Z2.

(5) *Using Neugebauer-Buti method to determine the normal flow direction of low Mach number nonlinear waves.* The magnetic hodogram and the method of determining normal flow direction introduced by *Neugebauer and Buti* [1990] should be widely used in future observational data analysis. Hopefully, additional types of slow shocks, rotational structures, and intermediate shocks will be observed in the future to guide theoretical study and to bring understanding of nonlinear dispersion and dissipation processes in these low Mach number nonlinear waves in collisionless plasmas.

Chapter 5

Summary and Conclusions

5.1 Summary

One-dimensional nonlinear hydromagnetic waves and shocks with characteristic length of the order of 1–100 ion inertial length have been studied in this thesis based on two-fluid theoretical models and hybrid simulations. The main results of this thesis consist of three parts as presented in Chapters 2, 3, and 4.

Chapter 2 presents analytic solutions of various types of solitons, RDs, and wave-trains in dissipationless two-fluid plasmas using the classical pseudo potential method and the new multiple pseudo potential method. The pseudo potentials are obtained based on conservation of mass, momentum, and energy fluxes. Thus, all possible trajectories of the fictitious particle motion on the pseudo potential surface are self-consistent nonlinear constant-profile wave solutions of the two-fluid plasma equations. Nonlinear wave solutions obtained in Chapter 2 allowed us to understand the nonlinear wave dispersion due to the finite-ion-inertial-length effect in the collisionless two-fluid plasma. Important new results obtained in Chapter 2 are as follows:

(1) *Successful predictions of the structures of various types of RDs.* Theoretical solutions obtained in Chapter 2 predict that for upstream $C_S > V_{AX}$ the magnetic hodogram is highly circularly polarized for a right-hand polarized RD, but relatively flat for a left-hand polarized RD. For upstream $C_S < V_{AX}$ the magnetic hodogram is highly circularly polarized for a left-hand polarized RD, but relatively flat for a right-hand polarized RD. These conclusions are consistent with the simulation results of RDs with $C_S > V_{AX}$ obtained by *Swift and Lee* [1983] and the simulation results of RDs

with $C_S < V_{AX}$ presented in Section 4.3 of this thesis. These conclusions are also consistent with the observations by *Neugebauer and Buti* [1990], in which flat magnetic hodograms can be found in both left-hand polarized RDs and right-hand polarized RDs.

(2) *Solutions of constant-profile Ω-shaped RDs and staple-shaped RDs.* An Ω-shaped RD has been obtained in the hybrid simulation by *Swift and Lee* [1983]. Staple-shaped RDs have been observed in the solar wind by *Neugebauer* [1989] and *Neugebauer and Buti* [1990]. The theoretical solutions obtained in Chapter 2 indicate that for $C_S > V_{AX}$, Ω-shaped RD solutions and staple-shaped RD solutions can be found with a left-hand polarized principal rotational arc; whereas, for $C_S < V_{AX}$, Ω-shaped RD solutions and staple-shaped RD solutions can be found with a right-hand polarized principal rotational arc. These results are consistent with the simulation results obtained by *Swift and Lee* [1983] in which for $C_S > V_{AX}$, Ω-shaped RD can only be found when the principal rotation arc is left-hand polarized but not right-hand polarized. Our theoretical results show that the Ω-shaped RDs and the staple-shaped RDs belong to the same group of solutions.

(3) *Solutions of quasi-stationary S-shaped RDs.* S-shaped RDs have been observed at the magnetopause [e.g., *Berchem and Russell*, 1982] and in the solar wind [*Neugebauer*, 1989]. Constant-profile S-shaped RD solutions can be found in the presence of dissipations. Without dissipations, quasi-stationary S-shaped RD solutions can be found based on the multiple pseudo potential method. Our results indicate that the scale length of the S-shaped RDs is relatively shorter than the scale length of highly circularly polarized RDs. Our solutions also indicate that an S-shaped RD with right-hand polarized nonlinear structure followed by a left-hand polarized nonlinear structure may steepen into Alfvén shocks; whereas the ramp field of an S-shaped RD with left-hand

polarized nonlinear structure followed by a right-hand polarized nonlinear structure will not steepen, but gradually relax into a highly circularly polarized RD.

(4) *Solutions of quasi-stationary banana-shaped Alfvén wavetrains.* Banana-shaped wavetrains have been observed at the outer heliosphere [*Mavromichalaki et al.*, 1988]. Like the S-shaped RDs, constant-profile banana-shaped wavetrain solutions can be found in dissipative two-fluid plasmas. Without dissipation, quasi-stationary banana-shaped wavetrains can be found based on the multiple pseudo potential method shown in Chapter 2. Since the assumption of the presence of dissipation in these nonlinear Alfvénic wavetrains raises the issue of what is the cause of dissipation, the non-dissipative quasi-stationary banana-shaped wavetrain solution is a better choice to explain the observed Alfvénic nonlinear waves in the solar wind.

(5) *Multiple pseudo potential method.* The multiple pseudo potential method introduced in Chapter 2 allowed us to obtain various types of quasi-stationary nonlinear wave solutions without adding any dissipations into our two-fluid plasma model.

Additional nonlinear wave solutions obtained in Chapter 2 include the right-hand polarized rarefaction fast-mode soliton solutions, right-hand highly circularly polarized rarefaction Alfvén-mode soliton solutions, left-hand polarized compression slow-mode soliton solutions, and left-hand highly circularly polarized compression Alfvén-mode soliton solutions. These nonlinear wave structures can provide a possible explanation for the observed Alfvénic fluctuations in the solar wind with scale lengths of the order of 10–100 ion inertial lengths [*Lyu and Kan*, 1989*b*].

The method for determining normal flow direction in the Alfvénic nonlinear waves as proposed by *Neugebauer and Buti* [1990] allowed us to determine the polarization of the observed RD structures for the first time in the literature. The observations obtained by *Neugebauer* [1989] and *Neugebauer and Buti* [1990] provided

important information needed to improve the theoretical work shown in Chapter 2. This method should be applied to future observational studies of low Mach number nonlinear hydromagnetic waves.

Collisionless dissipation in the collisionless plasma are studied by carefully examining the hybrid simulation results of the quasi-parallel fast shock studies as shown in Chapter 3. A multiple-labeling diagnostic introduced in Chapter 3 is designed to help us understand the complicated wave structures and ion distributions in quasi-parallel shocks. To identify the source of upstream suprathermal ions, we carefully examined the ion leakage processes and ion reflection processes in the simulated quasi-parallel shocks. The heating process of leakage ions, reflected ions and transmitted ions are shown separately in Chapter 3 with the help of multiple labeling diagnostic, which allows us to study the dynamics of small sub-groups of ions. Our simulation results indicate that both shock-heated ions and initially loaded downstream hot ions can leakage across the shock front. The leakage ion density is greatly reduced by the large amplitude waves in the shock transition region. The nonlinear scattering by the large amplitude waves in the shock transition region and across the shock front can also energize the ions as they leak toward upstream. For high Mach number shocks, the leakage ion density is about one tenth of the leakage ion density estimated by *Edmiston et al.* [1982]. The temperature of the leakage ions is about ten times higher than the downstream ion temperature. Upstream suprathermal backstreaming ions for Alfvén Mach number less than or equal to 4 in our simulations of quasi-parallel shocks appear to come exclusively from the leakage ions. However, for higher Mach numbers, the suprathermal backstreaming ions are not exclusively due to the leakage ions. Highly field-aligned reflected ions can be heated at the shock ramp possibly by multiple Fermi accelerations. Some of these reflected ions can contribute to the upstream suprathermal

backstreaming ions without entering into the downstream side of the shock transition region. Reflected ions heated by the upstream waves and then directly contribute to the upstream suprathermal ions as suggested by observations [*Paschmann et al.*, 1981; *Gosling et al.*, 1982] are not found in our simulations. A gyro-reflection model is proposed to explain the different types of ion reflection events as observed at the quasi-parallel Earth's bow shock and obtained in the high Mach number simulation results shown in Chapter 3. Three critical Mach numbers are proposed based on the simulation results in Chapter 3 to show the Mach number dependence of ion leakage, ion reflection, shock front reformation, and structures of nonlinear waves in the shock transition region.

To show the possible existence of intermediate shocks, hybrid simulations of intermediate shocks as well as rotational discontinuities and switch-off shocks are presented in Chapter 4. Stable intermediate shocks are obtained for the first time in hybrid simulations. The intermediate shock solutions are found closely associated with its neighboring solutions of RDs and switch-off shocks. Non-unique shock structures and RD structures are found in these simulations. Non-unique RD structures have been discussed in previous simulations by *Swift and Lee* [1983] and in the theoretical results given in Chapter 2 of this thesis. Non-unique intermediate shock structures have been found in previous two-fluid simulation study by *Lyu and Kan* [1989*a*]. Non-unique switch-off shock structure is shown for the first time in this study. The non-unique switch-off shock structures indicate that the large-amplitude, left-hand polarized wavetrain structures are not necessarily present on the downstream of a subcritical switch-off shock. The structures of the shock ramps and RD ramps are found to depend on the initial magnetic field polarization, the initial velocity polarization and

the initial ramp thickness used in the simulations. The structure is non-unique because it depends on the initial condition of the simulation.

The theoretical predictions of RDs with $C_S < V_{AX}$ are confirmed by the RD simulations given in Section 4.3. This simulation result is obtained six months later after the proposed theoretical solutions given in Chapter 2. The result indicates that the consistency between the theoretical prediction and the previous simulation results of RDs with $C_S > V_{AX}$ [*Swift and Lee*, 1983] is not coincident.

Figure 5.1 sketches the analytical solutions for RD simulations in Cases G2 and G4. The top four panels show cross sections of pseudo potential Ψ at $B_z = 0$ and the constant Ψ contours for $\theta_{BN} = 80°$, $\beta = 0.5$, $M_A = 0.88$ and 0.9. Mach numbers of these two pseudo potentials are slightly greater than the initially assigned Mach number of Cases G2 and G4, which is $M_A = \cos\theta_{BN} \approx 0.8660254$. Simulation results of Cases G2 and G4 are shown in the bottom panel of Figure 5.1. Coordinate system (x, y, z) used in Figure 5.1 is the same as the one used in Chapter 2; whereas coordinate systems (x', y', z') and (x'', y'', z'') shown in Figure 5.1 are the coordinate systems corresponding to the simulation in Cases G2 and G4, respectively. It is shown that the simulation result of Case G2 can be modeled approximately by the analytical solution of curve S_1–T_1. The simulation result of Case G4 can be modeled approximately by the analytical quasi-stationary solution of curve S_2–C–T_2. Similar results can be obtained for simulation Cases G1, G3, and G5. The principal ramp of the RD structure shown in Cases G3 and G4 can be modeled by combining two pseudo potentials with Mach number slightly less than $\cos\theta_{BN}$ in the similar way as shown in the color plot of Figure 2.29. Additional pseudo potentials are needed to model the downstream structures in Cases G3 and G5 as show in Figures 4.5 and 4.8 in Chapter 4.

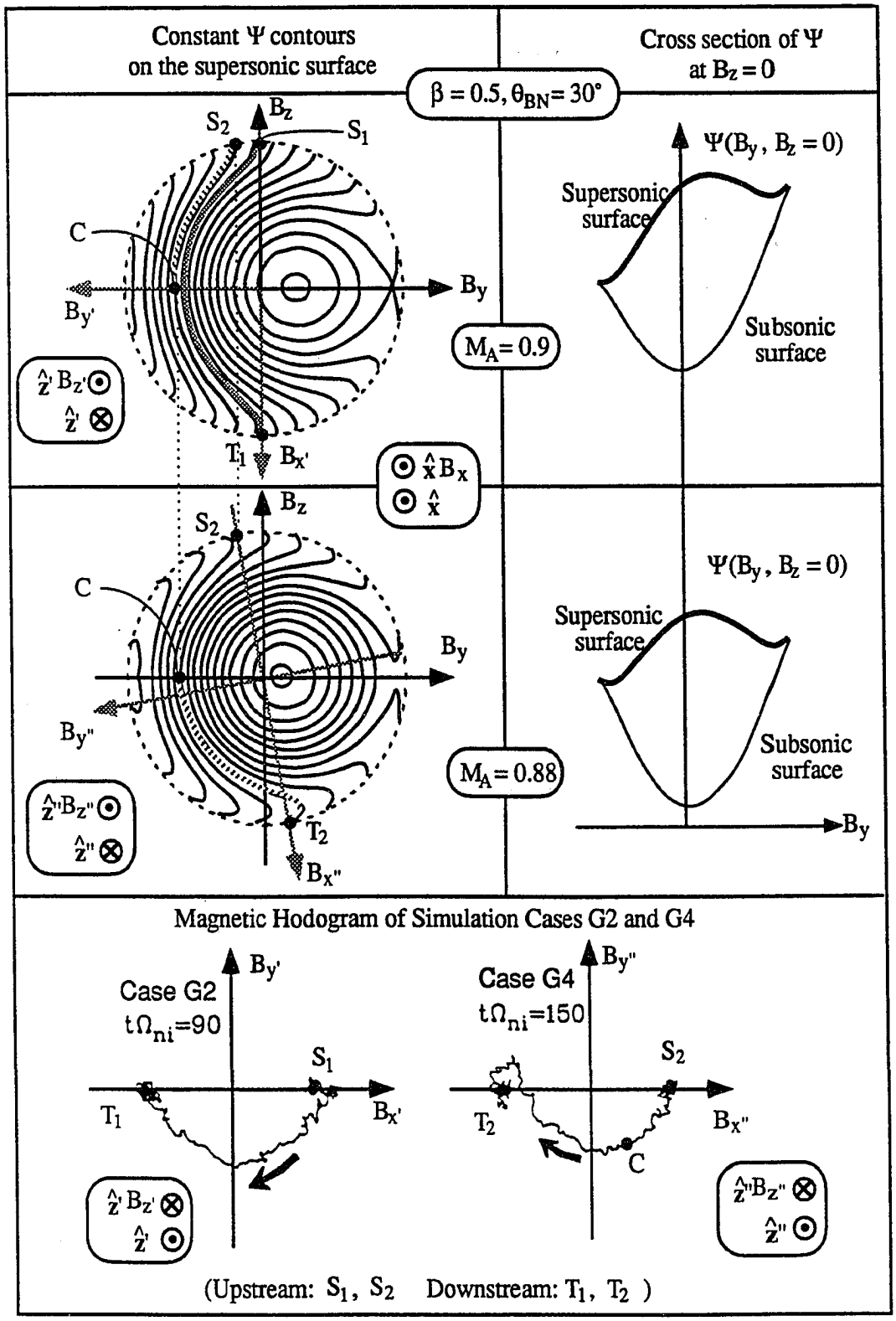

Figure 5.1 Analytical solutions for RD simulations in Cases G2 and G4. See text for discussion in detail.

Two different mechanisms for the formation of S-shaped rotational structures are found in this simulation study. The S-shaped RDs can develop from a very steep initial ramp field. Large amplitude nonlinear waves are dispersed from the steep ramp field and result in the S-shaped ramp field structure. S-shaped RDs without large amplitude upstream or downstream wavetrains can be found by a non-Alfvénic initial ramp field such as a circularly polarized magnetic field and a linearly polarized velocity field across the initial ramp. Observations of S-shaped RDs do not show large amplitude waves on either side of the RD. As a result, we propose that a non-Alfvénic initial disturbance may be responsible for the formation of the observed S-shaped RDs.

The cause of the non-unique ramp field structure is not yet clear at this time. It probably has something to do with nonlinear coupling of the fast, Alfvén and slow modes. Further study on this subject is needed to further improve our understanding of the formation of the various types of nonlinear Alfvénic structures observed in the solar wind and at the magnetopause.

5.2 Conclusion

Nonlinear hydromagnetic waves have been observed in the collisionless solar wind plasma. There are three characteristic modes of hydromagnetic waves, i.e., the Fast mode, the Alfvén mode and the Slow mode. A comprehensive theoretical study of nonlinear hydromagnetic waves, including rotational magnetic structures and collisionless shock waves, is carried out in this thesis by means of analytical solutions and numerical simulations. Results of this thesis shed new lights on the nonlinear behavior of hydromagnetic waves. The physics of nonlinear hydromagnetic waves are governed by the interplay of three fundamental processes. These are the dispersion process, the collisionless dissipation process and the nonlinear steepening process.

The dispersion process in nonlinear hydromagnetic waves is produced by the finite ratio of the ion inertial length to the wavelength. In the MHD limit as the ratio approaches zero, the dispersion vanishes. Thus, the MHD waves are nondispersive. This is demonstrated mainly by the analytic solutions of nonlinear two-fluid plasma equations obtained in this thesis for the rotational magnetic structures observed in the solar wind.

The collisionless dissipation process in hydromagnetic shock waves is governed by the wave structures produced by the dispersion process. The most important dissipation in a collisionless shock wave is the viscous dissipation which converts the flow energy into thermal energy. The collisionless viscous dissipation is produced by reflections and pitch-angle scattering of incoming ions as these ions move through the nonlinear waves in the shock transition region. This is demonstrated mainly by hybrid simulations of quasi-parallel fast shocks.

The nonlinear steepening process occurs when the wave phase speed increases with the wave amplitude. Thus, the large-amplitude portion of the wave profile propagates faster than the small-amplitude portion of the profile to result in steepening of the wavefront. Results of this thesis show that the collisionless dissipation process depends on the nonlinear wave structures produced by the dispersion process. The resulting collisionless dissipation in turn modifies the wave structures. The interplay between the dispersion and dissipation leads to spreading and smoothing the wave profile, which is needed to balance the nonlinear steepening of hydromagnetic waves. High Mach number collisionless shocks exhibit cyclic reformation behavior as observed in hybrid simulations. The shock front reformation can be explained in terms of momentary off-balance between the dispersion-dissipation on the one hand and the

nonlinear steepening on the other hand. The off-balance occurs after a significant fraction of incoming ions are reflected at a small pitch-angle ϕ with respect to the upstream average magnetic field $\mathbf{B}_1$ in the de Hoffman-Teller frame. The small pitch-angle on the upstream side keeps the reflected ions from reentering the shock ramp immediately after reflection. As a result, the mass flux and momentum flux getting into the shock layer decrease during the highly field-aligned (small pitch-angle) ion reflection event, so that the rate of nonlinear steepening decreases. At the same time, the dissipation increases due to ion reflections. Thus, the nonlinear steepening is too weak to balance the dissipation during the highly field-aligned ion reflection event, so that the shock front retreats and the shock ramp widens. Since it takes time for shock front to re-steepen, each off-balance lasts a few ion gyro periods. However, a momentarily stable shock front can also be found in the high Mach number quasi-parallel shocks, which occurs when the reflected ions have a large pitch-angle with respect to $\mathbf{B}_1$. The large pitch-angle on the upstream side enables the reflected ions to reenter the shock ramp immediately after reflection. As a result, the mass flux and momentum flux can be almost conserved across the shock ramp, and nonlinear steepening is balanced by dispersion-dissipation processes at the shock front during each reflect-reentering ion reflection event. The upstream pitch-angle of different types of reflected ion beams depends strongly on the orientation of the ramp field $\mathbf{B}^*$. A gyro-reflection model is proposed in Section 3.4, to explain the dependence between the ramp field $\mathbf{B}^*$ and the upstream pitch-angle of reflected ion beams. Thus, a circularly polarized ramp field $\mathbf{B}^*$ can lead to alternative occurrence of different types of ion reflection events, which then leads to cyclically shock-front reformation in very high Mach number quasi-parallel shocks.

References

Anagnostopoulos, G. C., E. T. Sarris, and S. M. Krimigis, Magnetospheric origin of energetic (E $\geq$ 50 keV) ions upstream of the bow shock: The October 31, 1977, event, *J. Geophys. Res., 91,* 3020, 1986.

Barnes, A., Interplanetary Alfvénic fluctuations: A stochastic model, *J. Geophys. Res., 86,* 7498, 1981.

Barnes, A., Hydromagnetic turbulence in the interplanetary medium, in *Solar Terrestrial Physics, Principles and Theoretical Foundations,* edited by R. L. Carovillano and J. M. Forbes, p. 172, D. Reidel, Hingham, Mass., 1983.

Belcher, J. W., and L. Davis, Jr., Large-amplitude Alfvénic waves in the interplanetary medium, *J. Geophys. Res., 76,* 3534, 1971.

Berchem, J. W., and C. T. Russell, Magnetic field rotation through the magnetopause: ISEE 1 and 2 observations, *J. Geophys. Res., 87,* 8139, 1982.

Berezin, Y. A., Formation of solitons, *Sov. Phys. Tech. Phys., 13,* 16, 1968.

Berezin, Y. A., and V. I. Karpman Nonlinear evolution of disturbances in plasmas and other dispersive media, *Sov. Phys. JETP, 24,* 1049, 1967.

Biskamp, D., Collisionless Shock Waves in Plasmas, *Nucl. Fusion, 13,* 719, 1973.

Burgess, D., Cyclic behavior at quasi-parallel collisionless shocks, *Geophys. Res. Lett., 16,* 345, 1989.

Burgess, D., W. P. Wilkinson, and S. J. Schwartz, Ion distributions and thermalization at perpendicular and quasi-perpendicular collisionless shocks, *J. Geophys. Res., 94,* 8783, 1989.

Burlaga, L. F., and J. M. Turner, Microscale 'Alfvén wave' in the solar wind at 1 AU, *J. Geophys. Res., 81,* 73, 1976.

Burlaga, L. F., J. F. Lemaire, and J. M. Turner, Interplanetary current sheets at 1 AU, *J. Geophys. Res.*, *82*, 3191, 1977.

Buti, B., Stochastic and coherent process in space plasmas, in *Cometary and Solar Plasma Physics*, edited by B. Buti, p. 221, World Scientific, Singapore, 1988.

Chao, J. K., Interplanetary collisionless shock waves, *Rep. CSR TR-70-3*, Mass. Inst. of Technol. Cent. for Space Res., Cambridge, Mass., 1970.

Chen, F. F., *Introduction to Plasma Physics*, Plenum Press, New York, 1974.

Chen, F. F., *Introduction to Plasma Physics and Controlled Fusion, Volume 1: Plasma Physics*, Plenum Press, New York, 1984.

Coroniti, F. V., Dissipation discontinuities in hydromagnetic shock waves, *J. Plasma Phys.*, *4*, 265, 1970.

Coroniti, F. V., Laminar wave-train structure of collisionless magnetic slow shocks, *Nucl. Fusion*, *11*, 261, 1971.

Crevier, W. F., and D. A. Tidman, Oblique shocks in finite-beta plasmas, *Phys. Fluids*, *13*, 2275, 1970.

Daily, W. D., Alfvén wave refraction by interplanetary inhomogeneities, *J. Geophys. Res.*, *78*, 2043, 1973.

Davis, L., R. Lüst, and A. Schlüter, The structure of hydromagnetic shock waves, I, Nonlinear hydromagnetic waves in a cold plasma, *Z. Naturforsch.*, *13a*, 916, 1958.

Dawson, S. P., and C. F. Fontán, Soliton decay of nonlinear Alfvén waves: Numerical studies, *Phys. Fluid*, *31*, 83, 1988.

Denskat, K. U., and F. M. Neubauer, Statistical properties of low-frequency magnetic field fluctuations in the solar wind from 0.29 to 1.0 AU during solar minimum conditions: Helios 1 and Helios 2, *J. Geophys. Res.*, *87*, 2215, 1982.

Edmiston, J. P., C. F. Kennel, and D. Eichler, Escape of heated ions upstream of quasi-parallel shocks, *Geophys. Res. Lett., 9,* 531, 1982.

Feldman, W. C., S. J. Schwartz, S. J. Bame, D. N. Baker, J. Birn, J. T. Gosling, E. W. Hones, Jr., D. H. McComas, J. A. Slavin, E. J. Smith, and R. D. Zwickl, Evidence for slow-mode shocks in the deep geomagnetic tail, *Geophys. Res. Lett., 11,* 599, 1984.

Feldman, W. C., D. N. Baker, S. J. Bame, J. Birn, J. T. Gosling, E. W. Hones, Jr., and S. J. Schwartz, Slow-mode shocks: A semipermanent feature of the distant geomagnetic tail, *J. Geophys. Res., 90,* 233, 1985.

Feldman, W. C., R. L. Tokar, J. Birn, E. W. Hones, Jr., S. J. Bame, and C. T. Russell, Structure of a slow mode shock observed in the plasma sheet boundary layer, *J. Geophys. Res., 92,* 83, 1987.

Formisano, V., and C. F. Kennel, Small amplitude waves in high β plasmas, *J. Plasma Phys., 3,* 55, 1969.

Friedman, M. A., C. T. Russell, J. T. Gosling, and M. F. Thomsen, Noncoplanar component of the magnetic field at low Mach number shocks, *J. Geophys. Res., 95,* 2441, 1990.

Goodrich, C. C., and J. D. Scudder, The adiabatic energy change of plasma electrons and the frame dependence of the cross-shock potential at collisionless magnetosonic shock waves, *J. Geophys. Res., 89,* 6654, 1984.

Goodrich, C. C., and J. D. Scudder, Reply, *J. Geophys. Res., 91,* 7135, 1986.

Goodrich, C. C., and P. J. Cargill, An investigation of the structure of rotational discontinuities, *Geophys. Res. Lett., 18,* 65, 1991.

Gosling, J. T., M. F. Thomsen, S. J. Bame, W. C. Feldman, G. Paschmann, and N. Sckopke, Evidence for specularly reflected ions upstream from the quasi-parallel bow shock, *Geophys. Res. Lett.*, *9*, 1333, 1982.

Gosling, J. T., D. Winske, and M. F. Thomsen, Noncoplanar magnetic fields at collisionless shocks: A test of a new approach, *J. Geophys. Res.*, *93*, 2735, 1988.

Gosling, J. T., M. F. Thomsen, S. J. Bame, and C. T. Russell, On the source of diffuse, suprathermal ions observed in the vicinity of the Earth's bow shock, *J. Geophys. Res.*, *94*, 3555, 1989*a*.

Gosling, J. T., M. F. Thomsen, S. J. Bame, and C. T. Russell, Ion reflection and downstream thermalization at the quasi-parallel bow shock, *J. Geophys. Res.*, *94*, 10,027, 1989*b*.

Greenstadt, E. W., Oblique, parallel, and quasi-parallel morphology of collisionless shocks, *Collisionless Shocks in the Heliosphere: Reviews of Current Research, AGU Monogr. Ser.*, Vol. *35*, edited by B. T. Tsurutani and R. G. Stone, p. 169, AGU, Washington, D. C., 1985.

Greenstadt, E. W., and R. W. Fredricks, Shock systems in collisionless space plasmas, in *Solar System Plasma Physics*, vol. III, edited by L. J. Lanzerotti, C. F. Kennel, and E. N. Parker, p.3, North-Holland, Amsterdam, 1979.

Greenstadt, E. W., I. M. Green, G. T. Inoye, A. J. Hundhausen, S. J. Bame, and I. B. Strong, Correlated magnetic field and plasma observations of the Earth's bow shock, *J. Geophys. Res.*, *73*, 51, 1968.

Hada, T., C. F. Kennel, and B. Buti, Stationary nonlinear Alfvén waves and solitons, *J. Geophys. Res.*, *94*, 65, 1989.

Hain, K., R. Lüst, and A. Schlüter, Hydromagnetic waves of finite amplitude in a plasma with isotropic and nonisotropic pressure perpendicular to a magnetic field, *Rev. Mod. Phys., 32,* 967, 1960.

Hollweg, J. V., Alfvén wave refraction in high-speed solar wind streams, *J. Geophys. Res., 80,* 908, 1975.

Hoppe, M. M., C. T. Russell, L. A. Frank, T. E. Eastman, and E. W. Greenstadt, Upstream hydromagnetic waves and their association with backstreaming ion populations: ISEE 1 and 2 observations, *J. Geophys. Res., 86,* 4471, 1981.

Hudson, P. D., Rotational discontinuities in an anisotropic plasma, *Planet. Space Sci., 19,* 1693, 1971.

Hudson, P. D., Rotational discontinuities in an anisotropic plasma–II, *Planet. Space Sci., 21,* 475, 1973.

Hudson, P. D., The reflection of charged particles by rotational discontinuities, *Planet. Space Sci., 22,* 1571, 1974.

Jones, F. C., and D. C. Ellison, Noncoplanar magnetic fields, shock potentials and ion deflection, *J. Geophys. Res., 92,* 11,205, 1987.

Kakutani, T., T. Kawahara, and T. Taniuti, Nonlinear hydromagnetic solitary waves in a collision-free plasma with isothermal electron pressure, *J. Phys. Soc. Jpn., 23,* 1138, 1967.

Kan, J. R., and D. W. Swift, Structure of the quasi-parallel bow shock: Results of numerical simulations, *J. Geophys. Res., 88,* 6919, 1983.

Kantrowitz, A., and H. E. Petschek, MHD characteristics and shock waves, in *Plasma Physics in Theory and Application,* edited by W. B. Kunkel, p. 148, McGraw-Hill Inc., New York, 1966.

Kellogg, P. J., Solitary waves in cold collisionless plasma, *Phys. Fluids, 7,* 1555, 1964.

Kennel, C. F., and R. Z. Sagdeev, Collisionless shock waves in high β plasma, 1, *J. Geophys. Res.*, *72*, 3303, 1967*a*.

Kennel, C. F., and R. Z. Sagdeev, Collisionless shock waves in high β plasma, 2, *J. Geophys. Res.*, *72*, 3327, 1967*b*.

Kennel, C. F., F. L. Scarf, F. V. Coroniti, C. T. Russell, K. P. Wenzel, T. R. Sanderson, P. Van Nes, W. C. Feldman, G. K. Parks, E. J. Smith, B. T. Tsurutani, F. S. Mozer, M. Temerin, R. R. Anderson, J. D. Scudder, and M. Scholer, Plasma and energetic particle structure upstream of a quasi-parallel interplanetary shock, *J. Geophys. Res.*, *89*, 5419, 1984*a*.

Kennel, C. F., J. P. Edmiston, F. L. Scarf, F. V. Coroniti, C. T. Russell, E. J. Smith, B. T. Tsurutani, J. D. Scudder, W. C. Feldman, R. R. Anderson, F. S. Mozer, and M. Temerin, Structure of the November 12, 1978, quasi-parallel interplanetary shock, *J. Geophys. Res.*, *89*, 5436, 1984*b*.

Kennel, C. F., J. P. Edmiston, and T. Hada, A quarter century of collisionless shock research, in *Collisionless Shocks in the Heliosphere: A Tutorial Review, AGU Monogr. Ser.*, Vol. *34*, edited by R. G. Stone and B. T. Tsurutani, p. 1, AGU, Washington, D. C., 1985.

Kennel, C. F., B. Buti, T. Hada, and R. Pellat, Nonlinear, dispersive, elliptically polarized Alfvén waves, *Phys. Fluids*, *31*, 1949, 1988.

Kennel, C. F., R. D. Blandford, and P. Coppi, MHD intermediate shock discontinuities. Part 1. Rankine-Hugoniot conditions, *J. Plasma Phys.*, *42*, 299, 1989.

Kennel, C. F., R. D. Blandford, and C. C. Wu, Structure and evolution of small-amplitude intermediate shock waves, *Phys. Fluids, B2*, 253, 1990.

Kortweg, D. J., and G. de Vries, *Phil. Mag.*, *39*, 5, 442, 1895.

Krall, N. A., and A. W. Trivelpiece, *Principles of Plasma Physics*, McGraw-Hill, New York, 1973.

Krimigis, S. M., R. D. Zwickl, and D. N. Baker, Energetic ions upstream of Jupiter's bow shock, *J. Geophys. Res., 90*, 3947, 1985.

Le, G., C. T. Russell, and E. J. Smith, Discrete wave packets upstream from the Earth and comets, *J. Geophys. Res., 94*, 3755, 1989.

Lee, L. C., L. Huang, and J. K. Chao, On the stability of rotational discontinuities and intermediate shocks, *J. Geophys. Res., 94*, 8813, 1989*a*.

Lee, L. C., Y. Lin, Y. Shi, and B. T. Tsurutani, Slow shock characteristics as a function of distance from the X-line in the magnetotail, *Geophys. Res. Lett., 16*, 903, 1989*b*.

Lembege, B., and J. M. Dawson, Self-consistent plasma heating and acceleration by strong magnetosonic waves for $\theta = 90°$. Part 1: Basic mechanisms, *Phys. Fluids, 29*, 821, 1986.

Lembege, B., and J. M. Dawson, Self-consistent study of a perpendicular collisionless and nonresistive shock, *Phys. Fluids, 30*, 1767, 1987.

Lepping, R. P., and K. W. Behannon, Magnetic field directional discontinuities: Characteristics between 0.46 and 1.0 AU, *J. Geophys. Res., 91*, 8725, 1986.

Leroy, M. M., Structure of perpendicular shocks in collisionless plasma, *Phys. Fluids, 26*, 2742, 1983.

Leroy, M. M., C. C. Goodrich, D. Winske, C. S. Wu, and K. Papadopoulos, Simulation of a perpendicular bow shock, *Geophys. Res. Lett., 8*, 1269, 1981.

Leroy, M. M., D. Winske, C. C. Goodrich, C. S. Wu, and K. Papadopoulos, The structure of perpendicular bow shocks, *J. Geophys. Res., 87*, 5081, 1982.

Liberman, M. A., and A. L. Velikovich, *Physics of Shock Waves in Gases and Plasmas*, Springer-Verlag, New York, 1986.

Liu, A., and K. B. Quest, Simulations of perpendicular shocks including electron inertia, *EOS Trans. AGU, Vol. 71, No. 43,* 1516, 1990.

Lyu, L. H., and J. R. Kan, Shock jump conditions modified by pressure anisotropy and heat flux for Earth's bowshock, *J. Geophys. Res., 91,* 6771, 1986.

Lyu, L. H., and J. R. Kan, Structures of Alfvén shocks: S-shaped magnetic hodogram observed at the magnetopause, *Geophys. Res. Lett., 16,* 349, 1989*a*.

Lyu, L. H., and J. R. Kan, Nonlinear two-fluid hydromagnetic waves in the solar wind: Rotational discontinuity, soliton, and finite-extent Alfvén wave train solutions, *J. Geophys. Res., 94,* 6523, 1989*b*.

Lyu, L. H., and J. R. Kan, Ion leakage, ion reflection, ion heating and shock-front reformation in a simulated supercritical quasi-parallel collisionless shock, *Geophys. Res. Lett., 17,* 1041, 1990.

Mandt, M. E., The quasi-parallel collisionless shock waves: A simulation study. Ph.D. Thesis, University of Alaska Fairbanks, 1988.

Mandt, M. E., and J. R. Kan, Effects of electron pressure in quasi-parallel collisionless shocks, *J. Geophys. Res., 90,* 115, 1985.

Mandt, M. E., and J. R. Kan, Ion equation of state in quasi-parallel shocks: A simulation result, *Geophys. Res. Lett., 15,* 1157, 1988.

Mandt, M. E., J. R. Kan, and C. T. Russell, Comparison of magnetic field structures in quasi-parallel interplanetary shocks: Observations versus simulations, *J. Geophys. Res., 91,* 8981, 1986.

Martin, R. N., J. W. Belcher, and A. J. Lazarus, Observations and analysis of abrupt changes in the interplanetary plasma velocity and magnetic field, *J. Geophys. Res., 78,* 3653, 1973.

Matthaeus, W. H., and M. L. Goldstein, Measurement of the rugged invariants of magnetohydrodynamic turbulence in the solar wind, *J. Geophys. Res., 87,* 6011, 1982.

Mavromichalaki, H., X. Moussas, J. J. Quenby, J. F. Valdes-Galicia, E. J. Smith, and B. T. Thomas, Relatively stable, large-amplitude Alfvénic waves seen at 2.5 and 5.0 AU, *Solar Phys., 116,* 377, 1988.

Mio, K., T. Ogino, K. Minami, and S. Takeda, Modified nonlinear Schrödinger equation for Alfvén waves propagating along the magnetic field in cold plasmas, *J. Phys. Soc. Japan, 41,* 265, 1976.

Moiseev, S. S., and R. Z. Sagdeev, Collisionless shock waves in a plasma in a weak magnetic field, in *Plasma Phys. J. Nucl. Energy, Part C, 5,* 43, 1963.

Montgomery, D., Nonlinear Alfvén waves in a cold ionized gas, *Phys. Fluids, 2,* 585, 1959.

Neugebauer, M., The enhancement of solar wind fluctuations at the proton thermal gyroradius, *J. Geophys. Res., 80,* 998, 1975.

Neugebauer, M., Corrections to and comments on the paper "The enhancement of solar wind fluctuations at the proton thermal gyroradius," *J. Geophys. Res., 81,* 2447, 1976.

Neugebauer, M., The structure of Rotational Discontinuities, *Geophys. Res. Lett., 16,* 1261, 1989.

Neugebauer, M., and B. Buti, A search for evidence of the evolution of rotational discontinuities in the solar wind from nonlinear Alfvén waves, *J. Geophys. Res., 95,* 13, 1990.

Neugebauer, M., C. S. Wu, and J. D. Huba, Plasma fluctuations in the solar wind, *J. Geophys. Res., 83,* 1027, 1978.

Nicholson, D. R., *Introduction to Plasma Theory,* John Wiley & Sons, New York, 1983.

Omidi, N., and D. Winske, Structure of slow magnetosonic shocks in low beta plasmas, *Geophys. Res. Lett., 16,* 907, 1989.

Omidi, N., and D. Winske, Electromagnetic ion/ion cyclotron instability at slow shocks: 2. Ion heating, *EOS Trans. AGU, Vol. 71, No. 43,* 1534, 1990.

Omidi, N., K. B. Quest, and D. Winske, Low Mach number parallel and quasi-parallel shocks, *J. Geophys. Res., 95,* 20,717, 1990.

Onsager, T. G., M. F. Thomsen, J. T. Gosling, S. J. Bame, and C. T. Russell, Survey of coherent ion reflection at the quasiparallel bow shock, *J. Geophys. Res., 95,* 2261, 1990.

Parker, E. N., A quasi-linear model of plasma shock structure in a longitudinal magnetic field, *J. Nucl. Energy, C2,* 146, 1961.

Paschmann, G., N. Sckopke, J. R. Asbridge, S. J. Bame, and J. T. Gosling, Engerization of solar wind ions by reflection from the earth's bow shock, *J. Geophys. Res., 85,* 4689, 1980.

Paschmann, G., N. Sckopke, I. Papamastorakis, J. R. Asbridge, S. J. Bame, and J. T. Gosling, Characteristics of reflected and diffuse ions upstream from the earth's bow shock, *J. Geophys. Res., 86,* 4355, 1981.

Quest, K. B., Theory and simulation of collisionless parallel shocks, *J. Geophys. Res., 93,* 9649, 1988.

Quest, K. B., D. W. Forslund, J. U. Brackbill, and K. Lee, Collisionless dissipation processes in quasi-parallel shocks, *Geophys. Res. Lett., 10,* 471, 1983.

Richter, P., and M. Scholer, On the stability of rotational discontinuities, *Geophys. Res. Lett., 16,* 1257, 1989.

Richtmyer, R. D., and K. W. Morton, *Difference Methods for Initial-Value Problems*, second edition, John Wiley & Sons, New York, 1967.

Russell, C. T., P. Song, and R. P. Lepping, The Uranian magnetopause: Lesson from Earth, *Geophys. Res. Lett., 16*, 1485, 1989.

Sagdeev, R. Z., Cooperative phenomena and shock waves in collisionless plasmas, in *Reviews of Plasma Physics*, Vol. *4*, edited by A. M. A. Leontovich, p. 23, Consultants Bureau, New York, 1966.

Sarris, E. T., G. C. Anagnostopoulos, and S. M. Krimigis, Simultaneous measurements of energetic ion ($\geq$ 50 keV) and electron ($\geq$ 220 keV) activity upstream of Earth's bow shock and inside the plasma sheet: Magnetospheric source for the November 3, and December 3, 1977, upstream events, *J. Geophys. Res., 92*, 12,083, 1987.

Schwartz, S. J., M. F. Thomsen, and J. T. Gosling, Ion upstream of Earth's bow shock: A theoretical comparison of alternative source populations, *J. Geophys. Res., 88*, 2039, 1983.

Scudder, J. D., L. F. Burlaga, and E. W. Greenstadt, Scale lengths in quasi-parallel shocks, *J. Geophys. Res., 89*, 7545, 1984.

Sibeck, D. G., R. W. McEntire, S. M. Krimigis, and D. N. Baker, The magnetosphere as a sufficient source for upstream ions on November 1, 1984, *J. Geophys. Res., 93*, 14,328, 1988.

Solodyna, C. V., and J. W. Belcher, On the minimum variance direction of magnetic field fluctuations in the azimuthal velocity structure of the solar wind, *Geophys. Res. Lett., 3*, 565, 1976.

Sonnerup, B. U. Ö., Acceleration of particles reflected at a shock front, *J. Geophys. Res., 74*, 1301, 1969.

Sonnerup, B. U. Ö., and L. J. Cahill, Jr., Magnetopause structure and attitude from Explorer 12 observations, *J. Geophys. Res., 72,* 171, 1967.

Sonnerup, B. U. Ö., and L. J. Cahill, Jr., Explorer 12 observations of the magnetopause current layer, *J. Geophys. Res., 73,* 1757, 1968.

Sonnerup, B. U. Ö., and B. G. Ledley, Magnetopause rotational forms, *J. Geophys. Res., 79,* 4309, 1974.

Spangler, S. R., and J. P. Sheerin, Properties of Alfvén solitons in a finite-beta plasma, *J. Plasma Phys., 27,* 193, 1982.

Spangler, S. R., J. P. Sheerin, and G. L. Payne, A numerical study of nonlinear Alfvén waves and solitons, *Phys. Fluids, 28,* 104, 1985.

Stringer, T. E., Low-frequency waves in an unbounded plasma, *Plasma Phys. J. Nucl. Energy, Part C, 5,* 89, 1963.

Swift, D. W., On the structure of the magnetic slow switch-off shock, *J. Geophys. Res., 88,* 5685, 1983.

Swift, D. W., and L. C. Lee, Rotational discontinuities and the structure of the magnetopause, *J. Geophys. Res., 88,* 111, 1983.

Taha, T. R., and M. J. Ablowitz, Analytical and numerical aspects of certain nonlinear evolution equations. I. Analytical, *J. Comp. Phys., 55,* 192, 1984*a*.

Taha, T. R., and M. J. Ablowitz, Analytical and numerical aspects of certain nonlinear evolution equations. II. Numerical, nonlinear Schrödinger equation, *J. Comp. Phys., 55,* 203, 1984*b*.

Taha, T. R., and M. J. Ablowitz, Analytical and numerical aspects of certain nonlinear evolution equations. III. Numerical, Korteweg-de Vries equation, *J. Comp. Phys., 55,* 231, 1984*c*.

Thomas, V. A., D. Winske, and N. Omidi, Re-forming supercritical quasi-parallel shocks: 1, One- and two-dimensional simulations, *J. Geophys. Res., 95,* 18,809, 1990.

Thomsen, M. F., Upstream suprathermal ions, in *Collisionless Shocks in the Heliosphere: Reviews of Current Research, AGU Monogr. Ser.,* Vol. *35,* edited by B. T. Tsurutani and R. G. Stone, p. 253, AGU, Washington, D. C., 1985.

Thomsen, M. F., J. T. Gosling, S. J. Bame, T. G. Onsager, and C. T. Russell, Two-state ion heating at quasi-parallel shocks, *J. Geophys. Res., 95,* 6363, 1990.

Tsurutani, B. T., and P. Rodriguez, Upstream waves and particles: An overview of ISEE results, *J. Geophys. Res., 86,* 4319, 1981.

Tsurutani, B. T., and E. J. Smith, Hydromagnetic waves and instabilities associated with cometary ion pickup: ICE observations, *Geophys. Res. Lett., 13,* 263, 1986.

Unti, T., and C. T. Russell, On the causes of spectral enhancements in solar wind power spectra, *J. Geophys. Res., 81,* 469, 1976.

Unti, T. W. J., M. Neugebauer, and B. E. Goldstein, Direct measurements of solar-wind fluctuations, *Astrophys. J., 180,* 591, 1973.

Whitham, G. B., Linear and nonlinear dispersive waves, *J. Fluid Mech., 22,* 273, 1965.

Winske, D., E. K. Stover, and S. P. Gary, The structure and evolution of slow mode shocks, *Geophys. Res. Lett., 12,* 295, 1985.

Winske, D., N. Omidi, K. B. Quest, and V. A. Thomas, Re-forming supercritical quasi-parallel shocks: 2, Mechanism for wave generation and front re-formation, *J. Geophys. Res., 95,* 18,821, 1990.

Wu, C. C., On the MHD intermediate shock, *Geophys. Res. Lett., 14,* 668, 1987.

Wu, C. C., The MHD intermediate shock interaction with an intermediate wave: Are intermediate shocks physical? *J. Geophys. Res., 93,* 987, 1988*a*.

Wu, C. C., Effects of dissipation on rotational discontinuities, *J. Geophys. Res.*, *93*, 3969, 1988*b*.

Zabusky, N. J., and M. D. Kruskal, Interaction of "solitons" in a collisionless plasma and the recurrence of initial states, *Phys. Rev. Lett.*, *15*, 240, 1965.